

DIRECT NUMERICAL SIMULATION OF COMPRESSIBLE AND INCOMPRESSIBLE WALL BOUNDED TURBULENT FLOWS WITH PRESSURE GRADIENTS

by

LIANG WEI

A thesis submitted to the
Department of Mechanical and Materials Engineering
in conformity with the requirements for
the degree of Doctor of Philosophy

Queen's University
Kingston, Ontario, Canada
December 2009

Copyright © Liang Wei, 2009

Abstract

This thesis is focused on direct numerical simulation (DNS) of compressible and incompressible fully developed and developing turbulent flows between isothermal walls using a discontinuous Galerkin method (DGM).

Three cases ($Ma = 0.2, 0.7$ and 1.5) of DNS of turbulent channel flows between isothermal walls with $Re \sim 2800$, based on bulk velocity and half channel width, have been carried out. It is found that a power law seems to scale mean streamwise velocity with Ma slightly better than the more usual log-law. Inner and outer scaling of second-order and higher-order statistics have been analyzed. The linkage between the pressure gradient and vorticity flux on the wall has been theoretically derived and confirmed and they are highly correlated very close to the wall. The correlation coefficients are influenced by Ma , and viscosity when Ma is high. The near-wall spanwise streak spacing increases with Ma . Isosurfaces of the second invariant of the velocity gradient tensor are more sparsely distributed and elongated as Ma increases.

DNS of turbulent isothermal-wall bounded flow subjected to favourable and adverse pressure gradient (FPG, APG) at $Ma \sim 0.2$ and $Re_{\text{ref}} \sim 428000$, based on the inlet bulk velocity and the streamwise length of the bottom wall, is also investigated. The FPG/APG is obtained by imposing a concave/convex curvature on the top wall of a plane channel. The flows on the bottom and top walls are tripped turbulent and

laminar boundary layers, respectively. It is observed that the first and second order statistics are strongly influenced by the pressure gradients. The cross-correlation coefficients of the pressure gradients and vorticity flux remain constant across the FPG/APG regions of the flat wall. High correlations between the streamwise/wall-normal pressure gradient and the spanwise vorticity are found near the separation region close to the curved top wall. The angle of inclined hairpin structure to streamwise direction of the bottom wall is smaller (flatter) in the FPG region than the APG region.

Acknowledgments

First and foremost, I would like to express my deepest gratitude to my supervisor, Prof. Andrew Pollard, for his guidance, encouragement, patience, and support throughout the course of this thesis work, especially during both the highs and lows of the process. His vision, expertise, experience, and passion for research have inspired me and enriched my growth as a student and researcher.

I would also like to thank other members of my thesis committee for their reviews. I am grateful to Prof. Ugo Piomelli for his helpful comments and insightful criticism of my work along the way. Additionally I'd like to thank Prof. Xiaohua Wu (Royal Military College) for his help on the coding of spectra and correlations. I would also thank Prof. Gary N. Coleman (University of Southampton), Prof. Robert Moser (The University of Texas at Austin), and Dr. Philippe R. Spalart (Boeing Commercial Airplanes) for the use of their DNS data.

Moreover, I would like to thank Prof. George Karniadakis (Brown University) & his CRUNCH group members (Prof. Suchuan Dong, Dr. Guang Lin, and Dr. Vasileios Symeonidis) and Prof. Mike Kirby (University of Utah) for providing the original compressible Nektar code and related helpful email discussions. Prof. Spencer Sherwin (Imperial College) is acknowledged for providing the incompressible Nektar code with additional libraries. Although the incompressible code was not used in

this thesis, its related documents and simulations promoted my understanding and improvements to the compressible Nektar code.

In addition, I am thankful to my former and current members of Computational and Experimental Fluid Dynamics Laboratory: Christopher Ball, Dustin Bespalko, Andrew Duncan, Dr. Hachimi Fellouah, Dr. Matthew Ford, Dr. Guillaume Fournier, Dr. François Golanski, Alireza MahdaviFar, Peter Massaro, Seyd Mohammad Mojab, Hassan Raiesi, Frank Secretain, Emily Sheridan, Dr. Abdul-Monsif Shinneeb, Ben Turnbull, Prof. Mesbah Uddin (The University of North Carolina at Charlotte), and Dominik Wyss for helpful and/or interesting discussions and activities on research, sports, life, etc during the past years.

Furthermore, I would also like to acknowledge the financial support from Department of Mechanical and Materials Engineering, School of Graduate Studies of Queen's University, High Performance Computing Virtual Laboratory (HPCVL). The research was funded through grants from NSERC Canada. Computing resources were provided by HPCVL, West-Grid and C3.ca. Special thanks are given to HPCVL Computing Specialists: Tony Curtis, Dr. Gang Liu, Chris MacPhee and Dr. Hartmut Schmider for the timely and helpful responses on the issues involved with the computing on HPCVL.

Finally, I would like to dedicate this work to my parents for their unconditional love, support, encouragement, and sacrifice over the years. I am deeply indebted to them.

Table of Contents

| | |
|---|--------------|
| Abstract | i |
| Acknowledgments | iii |
| Table of Contents | v |
| List of Tables | viii |
| List of Figures | ix |
| Nomenclature | xviii |
| Chapter 1: | |
| Introduction | 1 |
| 1.1 Background and motivation | 1 |
| 1.2 Literature review | 5 |
| 1.3 Research objectives | 12 |
| 1.4 Major contributions | 12 |
| 1.5 Outline | 14 |
| Chapter 2: | |
| Numerical Methodology | 16 |

| | | |
|-----|---|----|
| 2.1 | Direct numerical simulation (DNS) | 16 |
| 2.2 | Discontinuous Galerkin method (DGM) | 17 |
| 2.3 | 1D hyperbolic formulation | 18 |
| 2.4 | 3D compressible Navier-Stokes formulation | 22 |
| 2.5 | Compressible DGM code | 31 |

Chapter 3:

| | | |
|------|---|-----------|
| | DNS of turbulent compressible channel flows | 35 |
| 3.1 | Introduction | 35 |
| 3.2 | Computational details | 42 |
| 3.3 | Grid resolution and domain size | 46 |
| 3.4 | Mean profiles of velocity, density and temperature | 52 |
| 3.5 | Second-order statistics | 64 |
| 3.6 | Higher-order statistics | 80 |
| 3.7 | Turbulent kinetic energy budget | 85 |
| 3.8 | Reynolds stress and velocity-temperature cross-correlations | 92 |
| 3.9 | Relations between pressure gradient and vorticity flux | 94 |
| 3.10 | Near-wall turbulence structures | 100 |
| 3.11 | Concluding remarks | 104 |

Chapter 4:

| | | |
|-----|---|------------|
| | DNS of turbulent flow with FPG & APG | 111 |
| 4.1 | Introduction | 111 |
| 4.2 | Computational details | 120 |
| 4.3 | Global quantities | 123 |

| | | |
|---------------------------------------|---|------------|
| 4.4 | Transition | 126 |
| 4.5 | Local profiles | 128 |
| 4.6 | Vorticity and pressure gradients correlations | 145 |
| 4.7 | Near-wall turbulence structures | 151 |
| 4.8 | Concluding remarks | 161 |
| Chapter 5: | | |
| | Conclusion and future work | 166 |
| 5.1 | Conclusion | 166 |
| 5.2 | Future work | 170 |
| Bibliography 172 | | |
| Appendix A: | | |
| | Favre average and TKE budget | 183 |
| Appendix B: | | |
| | The Database | 189 |

List of Tables

| | | |
|-----|--|----|
| 2.1 | The scaling test for DGM on Sun SPARC Enterprise M9000 | 33 |
| 2.2 | The scaling test for DGM on SGI Origin 3900 | 33 |
| 3.1 | Physical and numerical parameters | 45 |

List of Figures

| | | |
|-----|---|----|
| 2.1 | 1-D grid of continuous Galerkin method | 20 |
| 2.2 | 1-D grid of discontinuous Galerkin method | 21 |
| 2.3 | Speedup of DGM on Sun SPARC Enterprise M9000 and SGI Origin 3900 respectively. | 34 |
| 3.1 | Computational domain for turbulent channel flow | 45 |
| 3.2 | Kolmogorov microscale of length (η) versus grid resolution (Δy^+) in wall units | 48 |
| 3.3 | One dimensional energy spectra for the case Ma02 for density, velocities and temperature. | 49 |
| 3.4 | One dimensional energy spectra for the case Ma07 for density, velocities and temperature. | 50 |
| 3.5 | One dimensional energy spectra for the case Ma15 for density, velocities and temperature. | 51 |
| 3.6 | Two-point correlations for the case Ma02 for density, velocities and temperature. | 53 |
| 3.7 | Two-point correlations for the case Ma07 for density, velocities and temperature. | 54 |

| | | |
|------|---|----|
| 3.8 | Two-point correlations for the case Ma15 for density, velocities and temperature. | 55 |
| 3.9 | Mean streamwise velocity, density and temperature profiles for the case Ma02 and Ma15 versus the case MKM and CKM respectively. | 57 |
| 3.10 | Mean streamwise velocity profiles for the cases Ma02, Ma07, and Ma15 in global coordinates. | 58 |
| 3.11 | Mean density $\langle \rho \rangle$, normalized by bulk density (ρ_m), and temperature $\langle T \rangle$, normalized by wall temperature (T_w) for the cases Ma02, Ma07, and Ma15 in global coordinates. | 58 |
| 3.12 | Mean density $\langle \rho \rangle$, normalized by bulk density (ρ_m), and temperature $\langle T \rangle$, normalized by wall temperature (T_w) for the case Ma02 in global coordinates. | 59 |
| 3.13 | Mean streamwise velocity normalized by friction velocity and its Van Driest transformation for the cases Ma02, Ma07, and Ma15 versus the law of the wall and the case MKM. | 60 |
| 3.14 | A power law quantity (β) and a log law quantity (γ) for the cases Ma02, Ma07, and Ma15 in wall coordinates. | 63 |
| 3.15 | Local Mach number $Ma_y = \frac{u(y)}{a(y)}$ for the cases Ma02, Ma07, and Ma15 | 64 |
| 3.16 | Mean pressure profile for the cases Ma02, Ma07, and Ma15. | 65 |
| 3.17 | Mean viscosity profile normalized by the viscosity at wall ($\langle \mu \rangle / \mu_w$) for the cases Ma02, Ma07, and Ma15 | 66 |
| 3.18 | RMS velocity fluctuations normalized by the friction velocity for the case Ma02 and Ma15 versus the case MKM and CKM respectively in wall coordinates. | 67 |

| | | |
|------|--|----|
| 3.19 | RMS velocity fluctuations normalized by the friction velocity (u_τ) and the mean bulk velocity (U_m) respectively for three cases Ma02, Ma07, and Ma15. | 69 |
| 3.20 | RMS density and temperature fluctuations normalized by $\langle \rho \rangle$ and $\langle T \rangle$, as well as ρ_m and U_m^2/c_v respectively for three cases Ma02, Ma07, and Ma15. | 71 |
| 3.21 | RMS vorticity fluctuations normalized by the mean shear at the wall τ_w/μ_w for Ma=0.2 versus the incompressible case MKM in wall coordinates. | 72 |
| 3.22 | RMS vorticity fluctuations normalized by the mean shear at the wall τ_w/μ_w and U_m/h respectively for the cases Ma02, Ma07, and Ma15. . | 73 |
| 3.23 | Top: RMS pressure fluctuations normalized by the wall shear stress $\rho_w u_\tau^2$ versus the incompressible case MKM. | 74 |
| 3.24 | RMS pressure fluctuations normalized by the wall shear stress $\rho_w u_\tau^2$ and the mean bulk quantity $\rho_m U_m^2$ respectively for the cases Ma02, Ma07, and Ma15. | 75 |
| 3.25 | RMS streamwise (top), wall-normal (middle) and spanwise (bottom) pressure gradient fluctuations normalized by $\rho_m U_m^2/h$ for three cases Ma02, Ma07, and Ma15. | 77 |
| 3.26 | Decomposition of shear stresses normalized by the wall shear stress τ_w for the case Ma02 versus the incompressible case MKM, the case Ma07, and the case Ma15. | 78 |

| | | |
|------|--|----|
| 3.27 | Turbulence and viscous shear stresses normalized by the wall shear stress τ_w Shear stresses for all three cases Ma02, Ma07, and Ma15 in global coordinates (top) and wall coordinates (bottom) | 79 |
| 3.28 | Skewness factors of velocity and pressure fluctuations for the case Ma02 in wall coordinates versus the case MKM | 81 |
| 3.29 | Skewness factors of velocity and pressure fluctuations for all three cases in wall and global coordinates respectively. | 82 |
| 3.30 | Skewness factors of density and temperature fluctuations for all three cases in wall and global coordinates respectively. | 84 |
| 3.31 | Flatness factors of velocity and pressure fluctuations for the case Ma02 in wall coordinates versus the case MKM | 85 |
| 3.32 | Flatness factors of velocity and pressure fluctuations for all three cases in wall and global coordinates respectively. | 86 |
| 3.33 | Flatness factors of density and temperature fluctuations for all three cases in wall and global coordinates respectively. | 87 |
| 3.34 | Turbulent kinetic energy budget normalized by wall variables $\tau_w u_\tau / \delta_v$ and bulk variables $\rho_m U_m^3 / h$ respectively. | 90 |
| 3.35 | Compressibility terms of TKE equation normalized by wall variables $\tau_w u_\tau / \delta_v$ and bulk variables $\rho_m U_m^3 / h$ respectively. | 91 |
| 3.36 | Cross-correlation coefficients of velocities and temperature: $\rho_{u:T}$ (top); $\rho_{v:T}$, $\rho_{w:T}$ (middle); $\rho_{u:v}$ (bottom) | 93 |
| 3.37 | Cross-correlation coefficients between streamwise pressure gradient and spanwise vorticity fluxes in the wall normal direction including the influence of viscosity very near the wall. | 98 |

| | | |
|------|---|-----|
| 3.38 | Cross-correlation coefficients between spanwise pressure gradient and streamwise vorticity fluxes in the wall normal direction including the influence of viscosity very near the wall. | 99 |
| 3.39 | Cross-correlation coefficients between wall normal pressure gradient and streamwise vorticity fluxes in the spanwise direction including the influence of viscosity very near the wall. | 101 |
| 3.40 | Correlations of streamwise velocity fluctuations at different y locations for the cases Ma02 (top), Ma07 (middle) and Ma15 (bottom). | 103 |
| 3.41 | Near-wall streak spacing for the cases Ma02 , Ma07 and Ma15. | 104 |
| 3.42 | A snapshot of streamwise velocity fluctuations at $y/h = 0.03$ ($y^+ \approx 5$) for the case Ma02 (top), Ma07 (middle), and Ma15 (bottom) respectively. | 105 |
| 3.43 | Iso-surfaces of second invariant of the velocity gradient tensor ($Q=0.5$) in the bottom half channel for the case Ma02. | 106 |
| 3.44 | Iso-surfaces of second invariant of the velocity gradient tensor ($Q=0.5$) in the bottom half channel for the case Ma07. | 107 |
| 3.45 | Iso-surfaces of second invariant of the velocity gradient tensor ($Q=0.5$) in the bottom half channel for the case Ma15. | 108 |
| 4.1 | Flow configuration comparing with the SW case in 2D (top) and Computational domain in 3D (bottom) | 122 |
| 4.2 | strength of the forcing function $F(x)$ | 123 |
| 4.3 | Wall pressure coefficients compared with the experiment and DNS data of the SW case | 124 |
| 4.4 | Skin friction coefficient scaled by $0.5\rho_{\text{ref}}U_{\text{ref}}^2$ | 125 |
| 4.5 | Nondimensional pressure gradient parameter | 126 |

| | | |
|------|---|-----|
| 4.6 | Iso-surfaces of streamwise velocity $u/U_{\text{ref}} = 0.8$ close to the transition at the bottom wall. | 127 |
| 4.7 | Iso-surfaces of streamwise velocity $u/U_{\text{ref}} = 0.8$ for the top wall (top) and bottom wall (bottom). | 129 |
| 4.8 | Mean inlet streamwise velocity close to the bottom wall and the Blasius boundary layer velocity profile. | 130 |
| 4.9 | Mean streamwise velocities close to the bottom plane wall versus the log law and the SW case. (a) $x = 0.55$; (b) $x = 0.60$; (c) $x = 0.70$. . . | 132 |
| 4.10 | Mean streamwise velocity profiles close to the bottom plane wall versus the log law at different streamwise locations. | 133 |
| 4.11 | Mean streamwise velocity profiles at different streamwise locations . . | 134 |
| 4.12 | Mean pressure coefficients at different streamwise locations | 134 |
| 4.13 | Mean streamwise pressure gradients at different streamwise locations. | 135 |
| 4.14 | Mean wall-normal and spanwise velocity profiles at different streamwise locations | 136 |
| 4.15 | RMS velocity fluctuations, scaled by u_τ , close to the bottom plane wall versus the DNS data of the SW case in wall units. (a) $x = 0.55$; (b) $x = 0.60$; (c) $x = 0.70$ | 138 |
| 4.16 | RMS streamwise (top), wall-normal (middle), and spanwise (bottom) velocity fluctuations, scaled by u_τ , close to the bottom wall at different streamwise locations in wall units. | 139 |
| 4.17 | RMS streamwise (top), wall-normal (middle), and spanwise (bottom) velocity fluctuations, scaled by U_{ref} , between the bottom and top walls at different streamwise locations. | 140 |

| | | |
|------|---|-----|
| 4.18 | RMS pressure fluctuations between the bottom and top walls, normalized by $\rho_{\text{ref}} U_{\text{ref}}^2$ in global units (top); RMS pressure fluctuations close to the bottom plane wall, normalized by the local wall shear stress in wall units (bottom). | 141 |
| 4.19 | RMS streamwise (top), wall-normal (middle), and spanwise (bottom) vorticity fluctuations close to the bottom plane wall, normalized by the mean shear at the wall τ_w/μ_w in wall units. | 143 |
| 4.20 | RMS streamwise (top), wall-normal (middle), and spanwise (bottom) vorticity fluctuations between the bottom and top walls, normalized by the U_{ref}/L_x in global units. | 144 |
| 4.21 | Turbulence, viscous, and total shear stresses normalized by the wall shear stress τ_w . (a) $x = 0.55$; (b) $x = 0.60$; (c) $x = 0.70$ | 146 |
| 4.22 | Turbulence, viscous, and total shear stresses normalized by the wall shear stress τ_w . (d) $x = 0.80$; (e) $x = 0.90$; (f) $x = 1.00$ | 147 |
| 4.23 | Cross-correlation coefficients between pressure gradients and vorticity fluxes on the wall. (a) bottom wall; (b) top wall. | 150 |
| 4.24 | Cross-correlation coefficients between streamwise pressure gradient and spanwise vorticity fluxes in the wall normal direction at different streamwise locations, very near the wall in wall units (top), and global units (bottom). | 152 |
| 4.25 | Cross-correlation coefficients between spanwise pressure gradient and streamwise vorticity fluxes in the wall normal direction at different streamwise locations, very near the wall in wall units (top), and global units (bottom). | 153 |

| | | |
|------|--|-----|
| 4.26 | Cross-correlation coefficients between wall normal pressure gradient and streamwise vorticity fluxes in the spanwise direction at different streamwise locations, very near the wall in wall units (top), and global units (bottom). | 154 |
| 4.27 | Cross-correlation coefficients between wall normal pressure gradient and spanwise vorticity fluxes in the streamwise direction at different streamwise locations, very near the wall in wall units (top), and global units (bottom). | 155 |
| 4.28 | Cross-correlation coefficients between pressure gradients and spanwise vorticity at different streamwise locations. (top) streamwise pressure gradient; (middle) wall-normal pressure gradient; (bottom) spanwise pressure gradient. | 156 |
| 4.29 | Correlations of streamwise velocity fluctuations close to the wall at different x locations: (a) $x = 0.50$; (b) $x = 0.60$; (c) $x = 0.70$ | 158 |
| 4.30 | Correlations of streamwise velocity fluctuations close to the wall at different x locations: (d) $x = 0.80$; (e) $x = 0.90$; (f) $x = 1.00$ | 159 |
| 4.31 | A snapshot of streamwise velocity fluctuations close to the bottom plane wall ($y^+ \approx 8$), in the FPG region (top), and APG region (bottom).160 | |
| 4.32 | Iso-surfaces of the second invariant of the velocity gradient tensor (Q) in the FPG region. The smaller figure at the bottom right is the side view of a thin slice in the z direction to show the inclined angle of the structures. | 162 |

| | |
|---|-----|
| 4.33 Iso-surfaces of the second invariant of the velocity gradient tensor (Q) | |
| in the APG region. The smaller figure at the bottom right is the side | |
| view of a thin slice in the z direction to show the inclined angle of the | |
| structures. | 163 |

Nomenclature

Acronyms

| | |
|-------|---------------------------------|
| APG | Adverse Pressure Gradient |
| CFD | Computational Fluid Dynamics |
| CGM | Continuous Galerkin Method |
| CKM | Coleman, Kim and Moser (1995) |
| DG | Discontinuous Galerkin |
| DGM | Discontinuous Galerkin Method |
| DNS | Direct Numerical Simulation |
| FEM | Finite Element Method |
| FPG | Favourable Pressure Gradient |
| FVM | Finite Volume Method |
| KMM | Kim, Moin, and Moser (1987) |
| LES | Large Eddy Simulation |
| LETOT | Large Eddy Turn Over Time |
| MKM | Moser, Kim, and Mansour (1999) |
| MPI | Message Passing Interface |
| RANS | Reynolds Averaged Navier-Stokes |

| | |
|-----|-------------------------------|
| RMS | Root-Mean-Square |
| SMP | Shared-memory Multi-Processor |
| SW | Spalart and Watmuff (1993) |
| TKE | Turbulent Kinetic Energy |
| TVB | Total Variation Bounded |
| 1D | One Dimensional |
| 2D | Two Dimensional |
| 3D | Three Dimensional |

Greek Symbols

| | |
|--------------------------------------|--|
| $\Delta x^+, \Delta y^+, \Delta z^+$ | Grid spacing in wall units |
| Δt | Time-step |
| δ | Boundary layer thickness |
| δ_{max} | Maximum boundary layer thickness |
| δ_{ij} | Kronecker delta |
| ϵ | Turbulence dissipation rate per unit mass |
| ε_{ijk} | Permutation symbol |
| η | Kolmogorov length scale |
| Φ | Approximation and weighting function space |
| κ | Thermal conductivity |
| κ | Von Kármán constant |
| λ | Bulk viscosity |
| $\lambda(x)$ | Forcing strength |
| μ | Dynamic viscosity |

| | |
|-------------------------|---|
| μ_{ref} | Reference dynamic viscosity |
| ν | Kinematic viscosity |
| ν | Variable coefficient |
| ω | Vorticity |
| ω_x, ω_{-x} | streamwise vorticity |
| ω_y, ω_{-y} | wall normal vorticity |
| ω_z, ω_{-z} | spanwise vorticity |
| $d\omega_{-x}/dy$ | $\partial\omega_x/\partial y$ (in figures only) |
| $d\omega_{-x}/dz$ | $\partial\omega_y/\partial z$ (in figures only) |
| $d\omega_{-z}/dy$ | $\partial\omega_z/\partial y$ (in figures only) |
| $d\omega_{-z}/dx$ | $\partial\omega_z/\partial x$ (in figures only) |
| Ω | The whole computational domain |
| Ω^e | The e -th element |
| $\partial\Omega$ | The boundary of the domain |
| ρ | Fluid density |
| $\rho_{a:b}$ | Cross-correlation coefficient between a and b |
| ρ_{ref} | Reference fluid density |
| τ, τ_{ij} | Shear stress |
| τ_w | Wall shear stress |
| Θ | Dilatation |

Latin Symbols

| | |
|-----|-----------------|
| A | Jacobian matrix |
| c | Speed of sound |

| | |
|--------------------------|--|
| C_f | Skin friction coefficient |
| c_p | Specific heat constant for constant pressure |
| C_p | Pressure coefficient |
| c_v | Specific heat constant for constant volume |
| D | Diagonal matrix of the eigenvalues |
| dp/dx | $\partial p/\partial x$ (in figures only) |
| dp/dy | $\partial p/\partial y$ (in figures only) |
| dp/dz | $\partial p/\partial z$ (in figures only) |
| E | Total energy per unit volume |
| E_i | A cell of the computational domain |
| e | Total energy per unit mass |
| F_x | Driving force function in the fringe region |
| f | Driving force per unit mass |
| $\widehat{f(u)}$ | Interface numerical flux |
| $f(u)_x$ | Derivative of $f(u)$ with respect to x |
| \mathbf{F}_B | Body force terms |
| \mathbf{F}^I | Inviscid flux |
| $\widehat{\mathbf{F}}^I$ | Numerical boundary flux for convection |
| \mathbf{F}^V | Viscous flux |
| $\widehat{\mathbf{f}}^V$ | Numerical boundary flux for diffusion |
| h | Half channel width |
| k | Turbulence kinetic energy per unit mass |
| K_p | Acceleration (pressure gradient) parameter |
| L | Left eigenvector |

| | |
|---------------------|--|
| \hat{n} | Unit normal vector |
| P | Negative dilatation $-\partial u_i/\partial x_i$ |
| p | Pressure |
| p | The order of the approximation polynomials |
| Q | Second invariant of the velocity gradient tensor |
| q | Heat flux |
| R | Specific gas constant |
| R | Right eigenvector |
| R_{ij} | $0.5(\partial u_i/\partial x_j - \partial u_j/\partial x_i)$ |
| S_{ij} | $0.5(\partial u_i/\partial x_j + \partial u_j/\partial x_i)$ |
| T | Fluid temperature |
| T_w | Wall temperature |
| $\langle T \rangle$ | Reynolds-averaged fluid temperature |
| T' | Fluctuating fluid temperature with respect to Reynolds average |
| T'' | Fluctuating fluid temperature with respect to Favre average |
| T'_{rms} | Root-mean-square temperature fluctuation |
| t | Time |
| \mathbf{U} | Conserved variables $\mathbf{U} = [\rho, \rho u, \rho v, \rho w, E]^t$ |
| \tilde{U}_i | Inflow laminar velocity |
| U_c | Mean centerline velocity |
| U_B, U_m | Mean bulk velocity |
| U_{ref} | Reference velocity |
| U_∞ | Freestream velocity |
| U_- | Internal value at element boundary |

| | |
|--------------------------------|--|
| U_+ | External value at element boundary |
| $\langle u \rangle$ | Reynolds-averaged fluid velocity |
| u', v', w' | Fluctuating fluid velocity with respect to Reynolds average |
| u'', v'', w'' | Fluctuating fluid velocity with respect to Favre average |
| u_τ | Friction velocity, $u_\tau = \sqrt{\tau_w/\rho}$ |
| u_p | Velocity scale based on pressure gradient |
| u^+ | Fluid velocity normalized by the friction velocity |
| $u'_{rms}, v'_{rms}, w'_{rms}$ | Root-mean-square velocity fluctuation |
| u_t | Derivative of u with respect to t |
| v_x | Derivative of v with respect to x |
| $\mathbf{W}, \mathbf{w}, v$ | Weighting functions |
| x, y, z | streamwise, wall-normal, and spanwise global coordinates |
| y^+ | Distance from the wall in wall units, $y^+ = y/(\nu/u_\tau)$ |

Non-dimensional Numbers

| | |
|-------------------|---|
| Ma | Mach number $Ma = u/c$ |
| Re | Reynolds number $Re = \rho u L / \mu$ |
| Re_τ | Friction Reynolds number $Re = \rho u_\tau L / \mu$ |
| Pr | Prandtl number $Pr = \mu c_p / \kappa$ |
| Pr_{ref} | Reference Prandtl number $Pr_{\text{ref}} = \mu_{\text{ref}} c_p / \kappa_{\text{ref}}$ |

Superscripts, Subscripts and Other Symbols

| | |
|-------------------|--|
| $\langle \rangle$ | Mean quantity based on Reynolds average |
| $()'$ | Fluctuating quantity based on Reynolds average |

| | |
|--------------|--|
| $\{\}$ | Mean quantity based on Favre average |
| $()''$ | Fluctuating quantity based on Favre average |
| $()^-$ | Left limit of the discontinuous function |
| $()^+$ | Right limit of the discontinuous function |
| $()^+$ | Variable given in wall units, or normalized by friction velocity |
| $()_{rms}$ | Root-Mean-Square of a variable |
| $()_{ref}$ | Reference variable |
| $()_{ij}$ | 9-component tensor; $i = 1, 2, 3, \quad j = 1, 2, 3$ |
| $()_{ijk}$ | 27-component tensor; $i = 1, 2, 3, \quad j = 1, 2, 3, \quad k = 1, 2, 3$ |
| $()_w$ | Variable value at wall |
| $()_c$ | Variable value at center |
| $()_m$ | Bulk Variable |
| $()_t$ | Time derivative of a variable |
| $()^*$ | Nondimensionalized variables |
| $()_{trans}$ | A variable at transition |
| $()_{trip}$ | A variable at trip |

Chapter 1

Introduction

1.1 Background and motivation

Wall bounded turbulent flows, referred to as turbulent flows bounded by one or more solid surfaces, are important. The main practical reason why they are important is that wall bounded turbulent flows are broadly used in practical engineering applications, such as the external flow around airplanes, ships and buildings, the internal flow through turbine blades, pipes and channels. Many of these flows involve compressibility effects and/or favourable/adverse pressure gradients (the pressure decreases/increases in the direction of fluid flow) where a strong adverse pressure gradient would lead to flow separation. The pressure gradient and compressibility increase the complexity of the flow and as well as the difficulty to understand and predict the flows using models. A further understanding of compressible and incompressible wall bounded turbulent flows with pressure gradients is needed, which is the main theoretical reason. The focus of this thesis is to study compressible and incompressible wall bounded turbulent flows with zero, favourable, and adverse pressure gradients.

The effect of pressure gradients on wall bounded turbulent flows is of great theoretical and practical significance. Theoretically, pressure gradients have significant effects on the wall vorticity generation (Lighthill, 1963; Wu, Wu & Wu, 1993) and wall shear stress does not dominate in adverse pressure gradient (APG) flows (Spalart & Watmuff, 1993). Practically, besides flow separation, the relation between pressure gradient and wall vorticity generation can be employed for wall vorticity-generation control, drag reduction aerodynamic diagnostic and optimization (Wu *et al.*, 1993; Wu & Wu, 1998; Koumoutsakos, 1999; Lee & Kim, 2002). To the best of the author's knowledge, however, there is little work that has been done on compressible turbulent flows between isothermal walls, especially when subjected to an adverse pressure gradient. One of the motivations of this thesis is to study the effects of pressure gradient on wall vorticity flux for compressible turbulent flows between isothermal walls.

An adverse pressure gradient, if strong enough, would cause a flow to separate. The ability to accurately predict the location and extent of flow separation is of crucial importance in aerodynamic applications including airfoils, turbine blades and many other aerodynamic devices, particularly in the design of aircraft wings. Some researchers have attempted to describe turbulent structures in the separation region (Tobak & Peake, 1982; Rogallo & Moin, 1984; Simpson, 1989; Détery, 2001); even so, the structure of the flow in the separated region still remains shrouded with uncertainty. Part of the reason was the lack of proper instrumentation in early studies (Simpson, Chew & Shivaprasad, 1981*a,b*; Na & Moin, 1998). More importantly, due to the effect of adverse pressure gradient, there could probably be a high angle between the instantaneous velocity and the mean velocity, which would degrade the accuracy of the hot-wire measurements, and moreover, there are significant pressure fluctuations

produced in the separation region that cannot be readily measured experimentally . Therefore numerical methods have become an ideal tool for analyzing flows subjected to adverse pressure gradient.

Direct numerical simulation (DNS), whereby the Navier-Stokes equations are solved numerically without using any models, is the only way to get a complete description of turbulent flows (Moin & Mahesh, 1998), and thus it has become the tool of choice for computational turbulence research. Traditional RANS based approaches, which solve the Reynolds averaged Navier-Stokes equations, lose a lot of flow information; this is particularly troublesome for the near wall region. Thus, these methods have significant shortcomings for the prediction of most complex turbulent flows, and separated flows being an extreme example (Na & Moin, 1996). Another approach, called large eddy simulation (LES), resolves large scales in the flow and models are applied to the unresolved small scales; thus LES suffers from a central closure problem, where, the filtered Navier-Stokes equations requires additional modeling of the Reynolds stress tensor to close the system of equations (Geurts, 2004).

The computing resources have evolved to allow DNS of wall-bounded turbulent flows. Kim, Moin & Moser (1987) performed the first DNS of plane channel flow. Spalart (1988) calculated the turbulent flat-plate boundary layer under zero and favorable pressure gradients. Spalart & Watmuff (1993) studied turbulent flat-plate boundary layer under favorable-to-adverse pressure gradients both experimentally and numerically. Na & Moin (1998) investigated a separated turbulent flow over a flat plate with a forced adverse-to-favorable pressure gradient using DNS. However, wall bounded turbulent flows subjected to adverse pressure gradient, is still not fully understood, especially for low Mach number turbulent flows with adverse

pressure gradient. Another motivation is to study the physics of low Mach number wall bounded turbulent flow subjected to adverse pressure gradient using DNS and to provide a database for turbulence studies.

The application of DNS has continued to evolve to include the increased flow complexity, broader flow regime (compressible flows) and more efficient numerical methods to achieve these solutions. DNS demands accurate numerical methods to fully capture a wide range of length and time scales. The classical finite difference, finite volume and finite element methods have been often used in DNS. With the evolving complexity of geometry, application in aerodynamics and needs to capture the structures around discontinuities and/or high gradients, the discontinuous Galerkin method (DGM), has been proposed and developed into a class of methods. Originating from the classical Galerkin finite element method, the DGM uses discontinuous approximate solutions, which is borrowed from the finite volume method. The DGM can achieve a high order of accuracy if a high degree of the approximating polynomials is used. More importantly, DGM is highly parallelizable and can handle complex geometries very well (Cockburn, Karniadakis & Shu, 2000). It seems to be well suited to meet the stringent requirements of DNS of turbulence.

The main motivations of the present work are to study the effects of pressure gradients and its fluctuations on vorticity generation in compressible and incompressible fully developed turbulent flows between isothermal walls and developing turbulent wall-bounded flows subjected to favourable and adverse pressure gradients through direct numerical simulation using discontinuous Galerkin method, and to study the physics of these flows and provide a database for turbulence studies. The verification of the compressible discontinuous Galerkin code is to make comparisons with

published experimental and numerical data.

1.2 Literature review

Much work has been done to understand turbulent wall bounded flows with zero or adverse pressure gradient and separation, through theoretical & experimental analysis, and numerical approximations.

1.2.1 Theoretical analysis

In most theoretical analysis of turbulent wall flows, it was of great importance to determine the relevant velocity scales (Skote & Henningson, 2002). Friction velocity $u_\tau = \sqrt{\tau_w/\rho}$, where τ_w and ρ are wall shear stress and density, is usually chosen as the velocity scale for near-wall turbulence, especially for a zero pressure gradient (ZPG) boundary layer.

But there are some limitations. On one hand, Reynolds stresses did not scale with u_τ because large eddies contribute a significant fraction to the Reynolds stresses (Morrison, 2007). This phenomenon was explained differently by many different researchers.

Townsend (1961) proposed a concept 'inactive motion' to explain the wall scaling failures. Inactive motion was essentially a first-order approximation of the effect of large eddies close to the wall that acted as a quasi-inviscid, linear, low frequency modulation of shear-stress-bearing motion (Morrison, 2007). In other words, large eddies close to the wall were "inactive" and the inner-outer interaction between the large eddies and small shear-stress-bearing motion of turbulent wall flows was linear.

Morrison (2007) investigated the inner and outer layer interactions of turbulent wall-bounded flows and claimed that it was probable that the interaction was inherently nonlinear, so that the assumption of the hypothesis of energy equilibrium close to the wall (Townsend, 1956, 1976), which was identified as a no-interaction condition and inactive motion, was invalidated.

Zhao & Smits (2007) studied the scaling of the wall-normal turbulence component in high-Reynolds-number pipe flow and found that 'inactive motion' concept cannot explain their observation and confirmed that Morrison's arguments of near-wall motion was influenced by the outer flow.

On the other hand, u_τ cannot be used as the relevant velocity scale when it approaches zero in a boundary layer under APG, especially a strong APG. Many studies (Stratford, 1959; Kader & Yaglom, 1978) on separated flows chose another velocity scale $u_p = (\nu/\rho \, dP/dx)^{1/3}$ based on pressure gradient.

Lately, Durbin & Belcher (1992) and Melnik (1989) obtained a three-layer structure of the turbulent boundary layer with an APG.

Some other velocity scales were also brought up. For example, Perry & Schofield (1973) proposed a universal velocity defect law for a developing turbulent boundary layer under adverse pressure gradient. The velocity scale they used was related to the local maximum in the Reynolds stress profile, which is neither u_τ nor u_p . It is also found that the theory had a half-power distribution. Schofield (1981) analyzed equilibrium boundary layers under moderate and strong adverse pressure gradient, based on this defect law. It was found that the predicted shear-stress profiles using the expression derived from the law, was in good agreement with experimental data.

Even so, there seems to be no evidence that the earlier work considered the fact

that flow with APG and separation is highly three dimensional. The following theory of pressure gradient and wall vorticity flux would probably shed some lights.

Lighthill (1963) proposed a simple relation between the streamwise vorticity flux and the spanwise pressure gradient, at least for a incompressible laminar flow over a stationary plane wall. x, y, z was taken as the streamwise, wall-normal, and spanwise directions respectively, and if $y = 0$ denotes the wall surface, then the simple relation followed,

$$\nu \frac{\partial \omega_x}{\partial y} = \nu \frac{\partial}{\partial y} \left(\frac{\partial w}{\partial y} - \frac{\partial v}{\partial z} \right) = \nu \frac{\partial^2 w}{\partial y^2} = \nu \nabla^2 w = \frac{1}{\rho} \frac{\partial p}{\partial z} \quad (1.1)$$

where ω_x is the streamwise vorticity, $\partial p / \partial z$ is the spanwise pressure gradient.

Wu *et al.* (1993) proposed a more general relationship between the vorticity and pressure gradient:

$$-\hat{n} \times \left(\frac{\nabla p}{\rho} \right)_W - \nu \hat{n} \times (\nabla \times \vec{\omega})_W = \hat{n} \times a_W \quad (1.2)$$

where \hat{n} denotes the unit normal vector and the suffix W denotes the wall surface. a is the wall acceleration. So for a stationary plane wall surface, eq.(1.2) becomes

$$\hat{n} \times \left(\frac{\nabla p}{\rho} \right)_W + \nu \hat{n} \times (\nabla \times \vec{\omega})_W = 0 \quad (1.3)$$

Vorticity flux was also considered for the active control of turbulent flows on a solid surface. Koumoutsakos (1999) proposed a control algorithm based on the measurement and manipulation of the wall vorticity flux (or equivalently pressure gradient) and applied this algorithm to a low Reynolds number turbulent incompressible channel flow. The simulation showed that the resulting skin friction drag reduction could reach an order of 40% through out-of-phase control (implying cancellation of the induced vorticity flux).

Lee & Kim (2002) also investigated vortices in a viscous sublayer of a turbulent boundary layer and found that a significant generation of vorticity there. A significant amount of drag reduction could be achieved through a suppression of spanwise disturbances in the sublayer which caused suppression of near-wall turbulence structures.

1.2.2 Experimental investigations

Many experimental studies on boundary layer separation have been carried out, even though there are some variables that cannot be obtained through experiment, such as the pressure fluctuations within the separation region (Na & Moin, 1996).

Simpson, Strickland & Barr (1977), Simpson *et al.* (1981*a*) and Simpson *et al.* (1981*b*) studied separating turbulent boundary layer for an airfoil-type flow in which the flow was accelerated and then decelerated until separation and determined the distribution of mean profiles, the Reynolds stress, and higher-order statistics. It was found that the velocity profile correlations of Perry & Schofield (1973) were supported upstream of separation within the uncertainty of the data and the similarity of the streamwise velocity and streamwise component of turbulence intensity throughout the shear flow was found downstream of separation. They also found that the separated turbulent boundary layer consisted of three layers: viscous layer nearest the wall; a rather flat intermediate layer, an overlap region between the viscous wall and outer regions; and outer backflow region, the farthest from the wall. The logarithmic law were found not valid when the turbulent boundary layer approached separation, and mixing length and eddy viscosity models were physically meaningless in the backflow and had reduced values in the outer region of the separated flow. It was found that

the skewness factor for streamwise velocity was positive upstream of separation near the wall, but negative downstream of separation. They claimed that the large-scale eddies in the outer region flow, which provided the mechanism for turbulence-energy diffusion, controlled the back flow.

Nagano, Tagawa & Tsuji (1993) investigated the characteristics of mean flow and turbulent statistics of a turbulent boundary layer with moderate to strong adverse pressure gradients. It was found that the influence of adverse pressure gradient caused the velocity profile to fall below the standard log-law. Adverse pressure gradient also had a strong effect on higher-order statistics of velocity fluctuations.

Na & Moin (1996) claimed in their DNS of turbulent boundary layers with APG and separation, that the accuracy of the hot-wire measurements is degraded by two characteristics of the flow: the tendency of not remaining two-dimensional in the mean and the high sensitivity to the upstream conditions, which also cause discrepancies among experiments.

1.2.3 Numerical simulations

DNS has become an important tool for the turbulence research community. DNS can provide accurate, complete and detailed data, especially in the near wall regions and/or separation regions, where it is still difficult for experimental methods to get reliable data for certain variables, especially for compressible flows, despite improvements in experimental techniques.

Reynolds-averaged Navier-Stokes (RANS) based methods are not reliable in separated flows because they are not good at the treatment of the near-wall turbulent flow, which is argued here to be the main focus for separation. With the development

of powerful computers and DNS, the effects of APG and separated flows can be investigated.

The foundations of DNS were laid at the National Center for Atmospheric Research in the United States (Fox & Lilly, 1972). The first computation using DNS was performed by Orszag & Patterson (1972). Although it was just a 32^3 grid computation of isotropic turbulence, it showed how spectral methods can be used to perform detailed computations of 3D turbulence. The first DNS of incompressible turbulent plane channel flow was performed by Kim *et al.* (1987). The Reynolds number based on friction velocity was around 180 ($Re_\tau \approx 180$). A large number of turbulence statistics including turbulence intensities, Reynolds shear stress, vorticity, high order statistics, etc were compared with experimental data with good agreement.

DNS of turbulent compressible plane channel flow between isothermal walls was performed by Coleman, Kim & Moser (1995). The Mach numbers based on the bulk velocity and sound speed at the walls were 1.5 and 3. The Reynolds numbers were of order 3000, based on the centre line velocity and channel half width. They found that the mean density and temperature gradients caused enhanced streamwise coherence of near-wall streaks. The density-weighted Van Driest transformation (Van Driest, 1951) of mean streamwise velocity generated curves of similar slopes. It was also claimed that the compressibility effects caused by the mean property variations were dominant, compared with those caused by thermodynamic fluctuations.

Na & Moin (1998) investigated a separated turbulent flow over a flat plate with a forced adverse-to-favorable pressure gradient using DNS to consider the effect of APG on separated flows. The Reynolds number based on momentum thickness upstream of separation and free stream velocity $Re_\theta = 300$. They found that the locations

of instantaneous spanwise-averaged detachment and reattachment points both fluctuate significantly in the streamwise direction, and turbulent structures emanating upstream of separation move upwards into the shear layer in the detachment region and turn around the separation bubble, and that the largest pressure fluctuations are located in the middle of the shear layer.

Huttl *et al.* (2001) performed a low Reynolds number modeling work. They claimed that none of the models can accurately capture the distribution of turbulent kinetic energy. The models they used are standard $k - \omega$ model and Menter's SST model (Menter, 1993). Both models perform well in the region with strong APG & FPG and the mean velocities are in good agreement with the DNS data. However, deviations become visible for the predication of Reynolds shear stress, turbulent kinetic energy and the development of the skin friction coefficient in the region of smaller APG. The reason remains unknown and needs further detailed investigation.

Morinishi *et al.* (2004) performed a DNS of compressible turbulent channel flow between adiabatic and isothermal walls. The main difference between adiabatic and isothermal walls were explained. The energy transfer was analysed. It was found that Morkovin's hypothesis (Morkovin, 1964), which generally claimed that the compressible shear flow dynamics would follow the incompressible pattern, was not applicable to the near wall asymptotic behaviour of the wall normal turbulence intensity.

Shan, Jiang & Liu (2005) performed a two-dimensional and a three-dimensional DNS of flow separation around a NACA 0012 airfoil with an attack angel of 4° and a Reynolds number of 10^5 based on the free stream velocity and the chord length. They solved the full compressible Navier-Stokes equations in the curvilinear coordinate systems using an implicit scheme with a high order compact central difference scheme

and non-reflecting boundary conditions. The 2D simulation was started from the uniform flow field and 3D simulation from the 2D simulation results. They claimed that the disturbance in the near wake region may propagate upstream and cause three dimensional instability, which seems to be self-sustained and leads to transition to turbulence.

1.3 Research objectives

There are three main objectives of this research.

- 1). To apply and assess to see suitability of the discontinuous Galerkin method to calculate, via DNS, compressible turbulent channel flows and complex turbulent flows under favourable and adverse pressure gradients.
- 2). To compute and study the effects of pressure gradients on vorticity generation from a solid wall for compressible and incompressible turbulent flows under zero, favourable, and adverse pressure gradients.
- 3). To provide a database for low Mach number turbulent flows subjected to favourable and adverse pressure gradients. This database may then be used to develop and test modifications to models of turbulence that can accurately predict aircraft-wing-type APG and separated flows.

1.4 Major contributions

This study involves the application of discontinuous Galerkin method to direct numerical simulation of complex compressible and incompressible wall bounded flows

under zero, favourable, and adverse pressure gradients at different Mach numbers.

The major contributions are:

- The first to apply DGM to DNS of compressible and incompressible wall bounded turbulent flows under favourable, zero, and adverse pressure gradients at different Mach numbers
- Addition of a fringe region technique to DGM in the application of turbulent boundary layer under FPG and APG
- Derivation of the relation between pressure gradients and wall vorticity flux for compressible turbulent flows between isothermal walls (variable viscosity for fluid flow)
- Analysis of the effects of pressure gradient on vorticity generation and the influence of Mach number, viscosity gradient, dilatation on the correlation between pressure gradient and vorticity flux. It has demonstrated that the Mach number has a great effect on the pressure-gradient and vorticity-flux correlation in the near wall region. The effect of viscosity on this correlation becomes significant for supersonic turbulent flows.
- Analysis of the influence of pressure gradients through FPG and APG regions in a transitional turbulent flow on the correlations between pressure gradients and vorticity flux and other statistics.
- Analysis of the influence of flow separation on correlations and statistics of a transitional turbulent flow with FPG and APG.

- Construction of database for compressible and incompressible wall-bounded flows ($Ma = 0.2, 0.7$ and 1.5) that include mean profiles, second order and higher-order statistics, shear stresses, turbulent kinetic energy budget, correlations between velocities and temperature, correlations between pressure gradients and vorticity flux, one dimensional spectra and correlations etc. See Appendix B.
- Construction of database for low Mach number wall-bounded flows with pressure gradients and separation that include global quantities, such as wall pressure coefficient, skin friction, nondimensional acceleration parameter, and local profiles, such as mean profiles, second-order statistics, shear stresses, correlations between pressure gradient and vorticity flux, correlations between pressure gradient and vorticity, spanwise autocorrelations of streamwise velocities, etc. See Appendix B.

1.5 Outline

This thesis is laid out as follows. Chapter 2 is an introduction of the numerical methods being used in this thesis. First it is a general introduction of direct numerical simulation. Then it is followed by an introduction, formulation of discontinuous Galerkin method for 1D hyperbolic and 3D Navier-Stokes equations. Implementation related issues are discussed last. Chapter 3 provides a complete documentation of direct numerical simulation of fully developed turbulent channel flow at three different Mach numbers ($0.2, 0.7$, and 1.5) using discontinuous Galerkin method. Results that

include 1D spectra and correlations, mean profiles, low and high order statistics, energy balance, turbulent structures, cross-correlations, and relations between pressure gradient and vorticity gradient are presented and discussed. Chapter 4 documents the details of direct numerical simulation of transitional turbulent flows with favourable and adverse pressure gradients and separation. A fringe region technique is introduced in the section of computational details which follows the introduction and literature review sections. The result section presents global quantities, transition, local mean profiles, second order statistics, correlations between pressure gradients and vorticity (gradient), near-wall turbulent structures. It is then followed by the conclusions drawn from all results presented in this thesis, together with recommendations for future work, which are presented in Chapter 5.

Chapter 2

Numerical Methodology

2.1 Direct numerical simulation (DNS)

DNS solves the full system of established flow equations, i.e. Navier-Stokes equations, without using any further approximation or modeling except those associated with their numerical implementations. All the flow aspects at all time and spatial locations can be obtained through DNS. Those data that DNS provides are numerically accurate and complete.

DNS requires a much higher computation power and memory as it solves all the details of a turbulent flow. Parallel computation methods are often used in DNS to decrease the computation time. Efficient numerical methods suitable for parallel computing will be a further improvement in the arsenal of the computational turbulence community.

Most turbulent flows in real world involves complex geometries. This adds additional difficulties to DNS. Moreover, flows have to be considered compressible in many aerodynamic situations, in which compressible Navier-Stokes equations are required

to solve.

The Discontinuous Galerkin Method is one method that can accommodate all the above requirements.

2.2 Discontinuous Galerkin method (DGM)

The first DGM was introduced by Reed & Hill (1973). Various schemes based on the DGM have been proposed since then, (check Cockburn *et al.* (2000), Karniadakis & Sherwin (2005) for reviews)

The DGM has several attractive features. First, using completely discontinuous piecewise polynomial space with no global continuity requirement between the element interfaces, the DGM combines the features in the standard Galerkin finite element method and finite volume method (FVM). It can capture physical discontinuities, such as shock wave, without producing spurious oscillations around them (Cockburn *et al.*, 2000). The lack of global continuity constraints enables discrete approximations characterized by the great geometrical flexibility, which makes it suitable for simulating flow with complex geometries, one of the main attractive features.

Its high order accuracy can be accomplished by using high order approximation polynomials and/or refinement of the mesh without considering the inter-element continuity restraint, and it also allows using different degrees of approximation polynomials in different elements, which makes it more efficient and flexible, especially for the case of wall bounded flows, such as turbulent flows with adverse pressure gradients or separated flows. For this case, extremely fine scales in the near wall region require fine grid and high order accurate computation, which can be achieved in DGM by using locally high order polynomials and fine grid elements.

The DGM is compact and highly parallelizable. In DGM each element uses its own approximation polynomial without considering the inter-element continuity constraints, that is, the resulting system of equations is local to the element. Solving the equation system in an element does not need the data of its neighboring elements except for some boundary data, as will be shown in the following sections. This compactness makes DGM ideally suited for parallel computations (Baggag *et al.*, 1999).

The DGM has a good stability. Proper numerical fluxes and slope limiters are often employed in high-resolution finite difference and finite volume methods to guarantee that the appearance of a discontinuity in the approximate solution does not induce spurious oscillations, but DGM assumes discontinuous solutions and naturally incorporates the ideas of numerical fluxes and slope limiters (Cockburn *et al.*, 2000). For example, DGM uses Riemann solvers (Toro, 1997; Rider & Lowrie, 2002) as the numerical fluxes on element interfaces and total variation bounded (TVB) nonlinear limiters (Shu, 1987) to eliminate oscillations for strong discontinuities.

As illustrated above, the DGM has many attractive features that are needed by DNS of complex turbulent flows.

The formulation and implementation of DGM discussed in the following sections are mainly based on the method developed by Karniadakis & Sherwin (2005) & Warburton & Karniadakis (1999).

2.3 1D hyperbolic formulation

The formulation and discretization of DGM will start from its origin: standard continuous Galerkin method (CGM) (Galerkin, 1915). The CGM (also called the Bubnov-Galerkin method) is a class of finite element methods (FEM) that uses the same

continuous piecewise polynomial space for the approximation solution and the weighting functions. There exists another class of Galerkin method called Petrov-Galerkin method, which uses similar, but not identical, polynomial space for the approximation and the weighting functions. Since DGM originates from standard Bubnov-Galerkin method (CGM) instead of Petrov-Galerkin method, only CGM will be considered here.

The analysis will start from one dimensional non-linear hyperbolic laws for simplicity, since Euler equations of gas dynamics are the bottleneck to deal with the compressible Navier-Stokes equations (Cockburn, 2003).

One-dimensional case of hyperbolic conservation law is given in equation 2.1:

$$u_t + f(u)_x = 0 \quad (2.1)$$

where u_t is denoted as $\frac{\partial u}{\partial t}$; similarly, $f(u)_x$ is denoted as $\frac{\partial f(u)}{\partial x}$. It is same for the variable v_x hereafter.

The CGM uses the same approximation and weighting function space:

$$\Phi = \{v \mid v = \sum_{k=0}^p a_k x^k \quad \text{for } x \in E_i, \quad i = 1, \dots, N\}$$

where p is the order of the approximation polynomials, and $a_k (k = 0, \dots, p)$ is the coefficient. $E_i = [x_{i-\frac{1}{2}}, x_{i+\frac{1}{2}}]$ (for $i = 1, \dots, N$), is a cell of the computational domain (total N cells). The cell size is $\Delta x_i = \frac{1}{2}(x_{i+\frac{1}{2}} - x_{i-\frac{1}{2}})$ with its centre located at: $x_i = \frac{1}{2}(x_{i+\frac{1}{2}} + x_{i-\frac{1}{2}})$, as illustrated in figure (2.1).

The approximation function $u \in \Phi$ (the same function space as the weighting function v). Eq.(2.1) becomes

$$\int_{E_i} v u_t dx + \int_{E_i} v f(u)_x dx = 0 \quad \text{for } i = 1, \dots, N \quad (2.2)$$

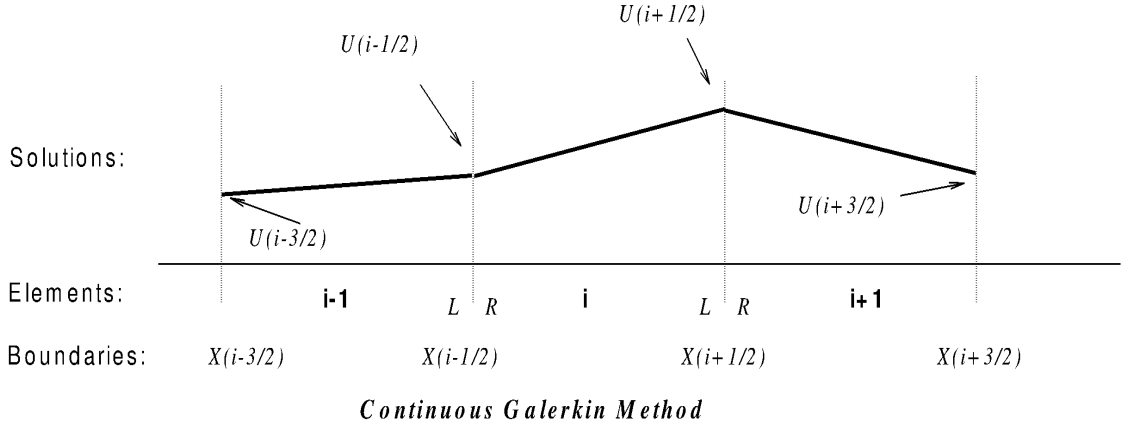


Figure 2.1: 1-D grid of continuous Galerkin method

for $u, v \in \Phi$.

According to Green's theorem:

$$\int_{\Omega} v \nabla \cdot \overrightarrow{F(u)} d\Omega = - \int_{\Omega} \nabla v \cdot \overrightarrow{F(u)} d\Omega + \oint_{\Gamma} v \overrightarrow{n} \cdot \overrightarrow{F(u)} ds. \quad (2.3)$$

It follows that for the one-dimensional case, eq.(2.2) becomes:

$$\int_{E_i} v u_t dx - \int_{E_i} v_x f(u) dx + \int_{x_{i-\frac{1}{2}}}^{x_{i+\frac{1}{2}}} v f(u) ds = 0 \quad \text{for } i = 1, \dots, N \quad (2.4)$$

for all weighting functions $v \in \Phi$.

This is the CGM formulation.

DGM develops from CGM and also has the same functional space for the approximate and the weighting functions, so the previous formulations also apply to DGM. But the difference is that in DGM the approximation polynomials (u) are only continuous within elements, that is, the values of variables are discontinuous on the interfaces of neighboring elements, i.e. a variable has two separate values at the interface of two neighboring elements. Terms involving the values on the interface,

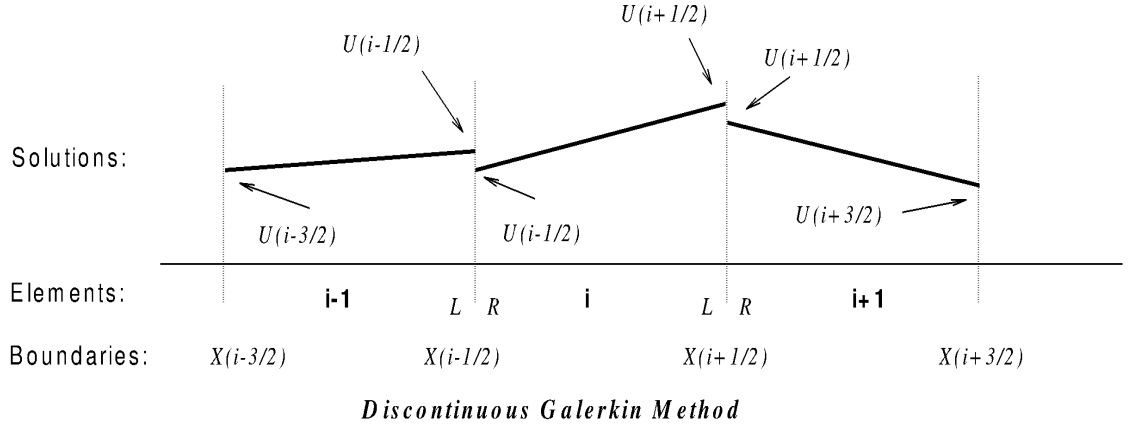


Figure 2.2: 1-D grid of discontinuous Galerkin method

such as the third term $(\int_{x_{i-\frac{1}{2}}}^{x_{i+\frac{1}{2}}} v f(u) ds)$ in eq.(2.4), must be treated with some special means.

Then in DGM, eq.(2.4) becomes

$$\int_{E_i} v u_t dx - \int_{E_i} v_x f(u) dx + v_{i+\frac{1}{2}}^- \widehat{f(u)}_{i+\frac{1}{2}} - v_{i-\frac{1}{2}}^+ \widehat{f(u)}_{i-\frac{1}{2}} = 0 \quad \text{for } i = 1, \dots, N \quad (2.5)$$

where v^- denotes the left limit of the discontinuous function v at the interface and v^+ denotes the right limit of v at the interface, as shown in figure (2.2) and $\widehat{f(u)} = f(u^-, u^+)$ is an interface numerical flux, which can be obtained by using an approximate Riemann solver (Toro, 1997).

Time discretization of eq. (2.5) will involve using explicit Adams-Bashforth or Runge-Kutta methods which have a low cost for each time step and a relatively large stability region. A wide range of length scales exists in turbulent flows, bounded from below by the diffusive action of molecular viscosity, to above by the dimensions of the flow field and the small eddies in turbulence have very short time scales (Tennekes & Lumley, 1972). DNS demands fine resolution of grids and a large number of tiny time

steps to be able to successfully capture all the time and spatial scales. It is argued to be no need to employ an implicit time discretization method that can accommodate larger time steps.

This is just a basic introduction of DGM on one dimensional hyperbolic system. DGM on three dimensional compressible Navier-Stokes equations will be explained in the next section.

2.4 3D compressible Navier-Stokes formulation

Three dimensional compressible Navier-Stokes equations with Stokes hypothesis will be considered in this section. The conservation form of continuity, momentum, and energy equations with an addition of a driving force can be written as equations (2.6) (2.7) (2.8) respectively.

$$\frac{\partial \rho}{\partial t} + \frac{\partial \rho u_j}{\partial x_j} = 0 \quad (2.6)$$

$$\frac{\partial \rho u_i}{\partial t} + \frac{\partial (\rho u_i u_j + p \delta_{ij})}{\partial x_j} = \frac{\partial \tau_{ij}}{\partial x_j} + \rho f_i \quad (2.7)$$

$$\frac{\partial E}{\partial t} + \frac{\partial (E + p) u_j}{\partial x_j} = \frac{\partial (\tau_{ij} u_i - q_j)}{\partial x_j} + \rho f_i u_i \quad (2.8)$$

where,

δ_{ij} is Kronecker's delta;

τ_{ij} is the viscous stress tensor: $\tau_{ij} = \mu \left(\frac{\partial u_i}{\partial x_j} + \frac{\partial u_j}{\partial x_i} \right) - \frac{2}{3} \mu \delta_{ij} \frac{\partial u_k}{\partial x_k}$;

f_i is the driving force (e.g. $f_i = \tau_{w_{av}} \delta_{i1} / (h \rho_m)$ for fully developed turbulent plane channel flow);

E is the total energy, defined as $E = \rho c_v T + \frac{1}{2} \rho u_i u_i = \frac{p}{\gamma-1} + \frac{1}{2} \rho u_i u_i$;

q_j is the heat flux: $q_j = -\kappa \frac{\partial T}{\partial x_j}$.

The equation of state for a perfect gas is

$$p = \rho R T \quad (2.9)$$

where R is the gas constant: $R = c_p - c_v$ and $\gamma = \frac{c_p}{c_v}$.

The Mach number is

$$Ma = \frac{u}{c} = \frac{u}{\sqrt{\gamma R T}} = \frac{u}{\sqrt{\gamma p / \rho}}. \quad (2.10)$$

The temperature can be written as:

$$T = \frac{u^2}{\gamma R Ma^2}. \quad (2.11)$$

The total energy E can also be written as:

$$E = \frac{\rho u^2}{\gamma(\gamma-1) Ma^2} + \frac{1}{2} \rho u_i u_i. \quad (2.12)$$

The equations (2.6) (2.7) (2.8) can be expanded in 3D as equation (2.13) for nondimensionalization

$$\begin{aligned}
& \frac{\partial}{\partial t} \begin{pmatrix} \rho \\ \rho u \\ \rho v \\ \rho w \\ E \end{pmatrix} + \frac{\partial}{\partial x} \begin{pmatrix} \rho u \\ \rho uu + p \\ \rho uv \\ \rho uw \\ (E + p)u \end{pmatrix} + \frac{\partial}{\partial y} \begin{pmatrix} \rho v \\ \rho vu \\ \rho vv + p \\ \rho vw \\ (E + p)v \end{pmatrix} + \frac{\partial}{\partial z} \begin{pmatrix} \rho w \\ \rho wu \\ \rho wv \\ \rho ww + p \\ (E + p)w \end{pmatrix} = \\
& \frac{\partial}{\partial x} \begin{pmatrix} 0 \\ \frac{2}{3}\mu(2\frac{\partial u}{\partial x} - \frac{\partial v}{\partial y} - \frac{\partial w}{\partial z}) \\ \mu(\frac{\partial u}{\partial y} + \frac{\partial v}{\partial x}) \\ \mu(\frac{\partial u}{\partial z} + \frac{\partial w}{\partial x}) \\ u\frac{2}{3}\mu(2\frac{\partial u}{\partial x} - \frac{\partial v}{\partial y} - \frac{\partial w}{\partial z}) + v\mu(\frac{\partial u}{\partial y} + \frac{\partial v}{\partial x}) + w\mu(\frac{\partial u}{\partial z} + \frac{\partial w}{\partial x}) + \kappa\frac{\partial T}{\partial x} \end{pmatrix} + \\
& \frac{\partial}{\partial y} \begin{pmatrix} 0 \\ \mu(\frac{\partial u}{\partial y} + \frac{\partial v}{\partial x}) \\ \frac{2}{3}\mu(2\frac{\partial v}{\partial y} - \frac{\partial u}{\partial x} - \frac{\partial w}{\partial z}) \\ \mu(\frac{\partial v}{\partial z} + \frac{\partial w}{\partial y}) \\ u\mu(\frac{\partial u}{\partial y} + \frac{\partial v}{\partial x}) + v\frac{2}{3}\mu(2\frac{\partial v}{\partial y} - \frac{\partial u}{\partial x} - \frac{\partial w}{\partial z}) + w\mu(\frac{\partial v}{\partial z} + \frac{\partial w}{\partial y}) + \kappa\frac{\partial T}{\partial y} \end{pmatrix} + \\
& \frac{\partial}{\partial z} \begin{pmatrix} 0 \\ \mu(\frac{\partial u}{\partial z} + \frac{\partial w}{\partial x}) \\ \mu(\frac{\partial v}{\partial z} + \frac{\partial w}{\partial y}) \\ \frac{2}{3}\mu(2\frac{\partial w}{\partial z} - \frac{\partial u}{\partial x} - \frac{\partial v}{\partial y}) \\ u\mu(\frac{\partial u}{\partial z} + \frac{\partial w}{\partial x}) + v\mu(\frac{\partial v}{\partial z} + \frac{\partial w}{\partial y}) + w\frac{2}{3}\mu(2\frac{\partial w}{\partial z} - \frac{\partial u}{\partial x} - \frac{\partial v}{\partial y}) + \kappa\frac{\partial T}{\partial z} \end{pmatrix} + \\
& \begin{pmatrix} 0 \\ \rho f_x \\ \rho f_y \\ \rho f_z \\ \rho(f_x u + f_y v + f_z w) \end{pmatrix} \quad (2.13)
\end{aligned}$$

All the variables in the equation 2.13 can be nondimensionalized in the following way.

$$x = \frac{x}{L_{\text{ref}}}, y = \frac{y}{L_{\text{ref}}}, z = \frac{z}{L_{\text{ref}}}, \rho = \frac{\rho}{\rho_{\text{ref}}}, u = \frac{u}{U_{\text{ref}}}, v = \frac{v}{U_{\text{ref}}}, w = \frac{w}{U_{\text{ref}}}, E = \frac{E}{\rho_{\text{ref}} U_{\text{ref}}^2}$$

$$p = \frac{p}{\rho_{\text{ref}} U_{\text{ref}}^2}, \mu = \frac{\mu}{\mu_{\text{ref}}}, \kappa = \frac{\kappa}{\kappa_{\text{ref}}}, T = \frac{T}{U_{\text{ref}}^2 / c_v}, t = \frac{t}{L_{\text{ref}} / U_{\text{ref}}}, f = \frac{f}{U_{\text{ref}}^2 / L_{\text{ref}}}$$

where

L_{ref} —reference Length;

ρ_{ref} —reference density;

U_{ref} —reference velocity;

μ_{ref} —reference dynamic viscosity;

κ_{ref} —reference thermal conductivity.

Thus the reference Reynolds number is $Re_{\text{ref}} = \frac{\rho_{\text{ref}} U_{\text{ref}} L_{\text{ref}}}{\mu_{\text{ref}}}$. And the reference Prandtl number $Pr_{\text{ref}} = \frac{\mu_{\text{ref}} c_p}{\kappa_{\text{ref}}}$.

Eq. 2.13 is multiplied by terms in 2.14 respectively. Then eq. 2.15 can be obtained.

$$\begin{pmatrix} L_{\text{ref}} / (\rho_{\text{ref}} U_{\text{ref}}) \\ L_{\text{ref}} / (\rho_{\text{ref}} U_{\text{ref}}^2) \\ L_{\text{ref}} / (\rho_{\text{ref}} U_{\text{ref}}^2) \\ L_{\text{ref}} / (\rho_{\text{ref}} U_{\text{ref}}^2) \\ L_{\text{ref}} / (\rho_{\text{ref}} U_{\text{ref}}^3) \end{pmatrix} \quad (2.14)$$

$$\begin{aligned}
& \frac{\partial}{\partial t} \begin{pmatrix} \rho \\ \rho u \\ \rho v \\ \rho w \\ E \end{pmatrix} + \frac{\partial}{\partial x} \begin{pmatrix} \rho u \\ \rho u u + p \\ \rho u v \\ \rho u w \\ (E + p)u \end{pmatrix} + \frac{\partial}{\partial y} \begin{pmatrix} \rho v \\ \rho v u \\ \rho v v + p \\ \rho v w \\ (E + p)v \end{pmatrix} + \frac{\partial}{\partial z} \begin{pmatrix} \rho w \\ \rho w u \\ \rho w v \\ \rho w w + p \\ (E + p)w \end{pmatrix} = \\
& \frac{1}{Re_{\text{ref}}} \left[\frac{\partial}{\partial x} \begin{pmatrix} 0 \\ \frac{2}{3}\mu(2\frac{\partial u}{\partial x} - \frac{\partial v}{\partial y} - \frac{\partial w}{\partial z}) \\ \mu(\frac{\partial u}{\partial y} + \frac{\partial v}{\partial x}) \\ \mu(\frac{\partial u}{\partial z} + \frac{\partial w}{\partial x}) \\ u\frac{2}{3}\mu(2\frac{\partial u}{\partial x} - \frac{\partial v}{\partial y} - \frac{\partial w}{\partial z}) + v\mu(\frac{\partial u}{\partial y} + \frac{\partial v}{\partial x}) + w\mu(\frac{\partial u}{\partial z} + \frac{\partial w}{\partial x}) + \frac{\kappa\gamma}{Pr_{\text{ref}}}\frac{\partial T}{\partial x} \end{pmatrix} + \right. \\
& \frac{\partial}{\partial y} \begin{pmatrix} 0 \\ \mu(\frac{\partial u}{\partial y} + \frac{\partial v}{\partial x}) \\ \frac{2}{3}\mu(2\frac{\partial v}{\partial y} - \frac{\partial u}{\partial x} - \frac{\partial w}{\partial z}) \\ \mu(\frac{\partial v}{\partial z} + \frac{\partial w}{\partial y}) \\ u\mu(\frac{\partial u}{\partial y} + \frac{\partial v}{\partial x}) + v\frac{2}{3}\mu(2\frac{\partial v}{\partial y} - \frac{\partial u}{\partial x} - \frac{\partial w}{\partial z}) + w\mu(\frac{\partial v}{\partial z} + \frac{\partial w}{\partial y}) + \frac{\kappa\gamma}{Pr_{\text{ref}}}\frac{\partial T}{\partial y} \end{pmatrix} + \\
& \left. \frac{\partial}{\partial z} \begin{pmatrix} 0 \\ \mu(\frac{\partial u}{\partial z} + \frac{\partial w}{\partial x}) \\ \mu(\frac{\partial v}{\partial z} + \frac{\partial w}{\partial y}) \\ \frac{2}{3}\mu(2\frac{\partial w}{\partial z} - \frac{\partial u}{\partial x} - \frac{\partial v}{\partial y}) \\ u\mu(\frac{\partial u}{\partial z} + \frac{\partial w}{\partial x}) + v\mu(\frac{\partial v}{\partial z} + \frac{\partial w}{\partial y}) + w\frac{2}{3}\mu(2\frac{\partial w}{\partial z} - \frac{\partial u}{\partial x} - \frac{\partial v}{\partial y}) + \frac{\kappa\gamma}{Pr_{\text{ref}}}\frac{\partial T}{\partial z} \end{pmatrix} \right] + \\
& \begin{pmatrix} 0 \\ \rho f_x \\ \rho f_y \\ \rho f_z \\ \rho(f_x u + f_y v + f_z w) \end{pmatrix} \quad (2.15)
\end{aligned}$$

All variables in eq. 2.15 are nondimensionalized and the state equation for perfect gas (2.9) becomes $p = \rho(\gamma - 1)T$. Nondimensional temperature can be therefore obtained from:

$$T = \frac{E - 0.5\rho(u^2 + v^2 + w^2)}{\rho} \quad (2.16)$$

Nondimensionalization of eq. 2.10 becomes

$$Ma = u / \sqrt{\gamma(\gamma - 1)T} \quad (2.17)$$

Then Mach number can be obtained from

$$1 = Ma_{\text{ref}}^2 \gamma(\gamma - 1)T_{\text{ref}} \quad (2.18)$$

Eq. 2.15 looks a bit complicated. We can rewrite it in a compact form as:

$$\mathbf{U}_t + \nabla \cdot \mathbf{F}^I = \frac{1}{Re_{\text{ref}}} \nabla \cdot \mathbf{F}^V + \mathbf{F}_B \quad (2.19)$$

where the vector $\mathbf{U} = [\rho, \rho u, \rho v, \rho w, E]^t$ denotes the conserved variables; $\mathbf{F}^I = \mathbf{F}^I(\mathbf{U})$ and $\mathbf{F}^V = \mathbf{F}^V(\mathbf{U}, \nabla \mathbf{U})$ are inviscid and viscous fluxes respectively; $\mathbf{F}_B = [0, \rho f_x, \rho f_y, \rho f_z, \rho(f_x u + f_y v + f_z w)]^t$ represents the body force terms.

Discontinuous Galerkin method treats these terms differently. The treatment of the inviscid flux term $(\nabla \cdot \mathbf{F}^I)$ will be considered first. The contribution of viscous fluxes and body force terms will be treated as an correction.

2.4.1 Discontinuous Galerkin method for convection

The convection part of the equation 2.19 or the Euler equation is:

$$\mathbf{U}_t + \nabla \cdot \mathbf{F}^I = 0. \quad (2.20)$$

Let Ω denote the whole computational domain and $\partial\Omega$ the boundary. The whole domain Ω is divided into N subdomains (or elements). $\Omega^e (e = 1, 2, \dots, N)$ represents the e -th element with boundary $\partial\Omega^e$. Elements are only overlapping on element interfaces. Let \mathbf{W} be the weighting function, which is continuous in Ω^e and zero outside.

DGM treats each element separately. After multiplying the weighting function \mathbf{W} and integrating over the element Ω^e , eq. 2.20 becomes,

$$\int_{\Omega^e} \mathbf{W} \mathbf{U}_t d\mathbf{x} + \int_{\Omega^e} \mathbf{W} \nabla \cdot \mathbf{F}^I d\mathbf{x} = 0 \quad \text{for } e = 1, \dots, N. \quad (2.21)$$

Integrating by parts gives:

$$\int_{\Omega^e} \mathbf{W} \mathbf{U}_t d\mathbf{x} - \int_{\Omega^e} \nabla \mathbf{W} \cdot \mathbf{F}^I d\mathbf{x} + \int_{\partial\Omega^e} \mathbf{W} \hat{\mathbf{n}} \cdot \mathbf{F}^I d\mathbf{s} = 0 \quad \text{for } e = 1, \dots, N. \quad (2.22)$$

All the operations in eq. 2.22 are within the element Ω^e so far. As DGM allows discontinuous solutions at element boundaries, however, some elemental coupling is required to connect adjacent elements, enforce boundary conditions and keep the solution within a certain bounded variation. The coupling at boundaries between adjacent elements is employed in DGM by the computation of the flux \mathbf{F}^I in the third term of the equation 2.22. Two possible values of \mathbf{U} at the boundary of element Ω^e can be denoted as \mathbf{U}_- (internal) and \mathbf{U}_+ (external), and the numerical boundary flux can be written as $\hat{\mathbf{F}}^I(\mathbf{U}_-, \mathbf{U}_+)$. Eq. 2.22 then becomes:

$$\int_{\Omega^e} \mathbf{W} \mathbf{U}_t d\mathbf{x} - \int_{\Omega^e} \nabla \mathbf{W} \cdot \mathbf{F}^I d\mathbf{x} + \int_{\partial\Omega^e} \mathbf{W} \hat{\mathbf{n}} \cdot \hat{\mathbf{F}}^I d\mathbf{s} = 0 \quad \text{for } e = 1, \dots, N. \quad (2.23)$$

Integrating the second term of the equation 2.23 by parts once more, gives another implementation of DGM which is employed in the current code:

$$\int_{\Omega^e} \mathbf{W} \mathbf{U}_t d\mathbf{x} + \int_{\Omega^e} \mathbf{W} \nabla \cdot \mathbf{F}^I d\mathbf{x} + \int_{\partial\Omega^e} \mathbf{W} \hat{\mathbf{n}} \cdot (\hat{\mathbf{F}}^I - \mathbf{F}^I) d\mathbf{s} = 0 \quad \text{for } e = 1, \dots, N. \quad (2.24)$$

The calculation of numerical boundary flux $\hat{\mathbf{F}}^I$ can use a simple upwind approach or an approximate Riemann solver. Three approaches based on Riemann solver are available in the current implementation of the code. The first is the upwind flux calculated in the following way:

$$\hat{\mathbf{F}}^I(\mathbf{U}_-, \mathbf{U}_+) = \mathbf{F}^I(\mathbf{R}\mathbf{D}^+ \mathbf{L}\mathbf{U}_- + \mathbf{R}\mathbf{D}^- \mathbf{L}\mathbf{U}_+) \quad (2.25)$$

where $\mathbf{A} = \mathbf{R}\mathbf{D}\mathbf{L}$ is the Jacobian matrix of \mathbf{F}^I ;

$$\mathbf{A} = \mathbf{R}\mathbf{D}\mathbf{L} = \frac{\partial \mathbf{F}^I}{\partial \mathbf{U}} \quad (2.26)$$

where \mathbf{R} and \mathbf{L} are its right and left eigenvectors; \mathbf{D} is the diagonal matrix of its eigenvalues and $\mathbf{D}^\pm = \frac{1}{2}(\mathbf{D} \pm |\mathbf{D}|)$.

The second is Roe splitting flux:

$$\hat{\mathbf{F}}^I(\mathbf{U}_-, \mathbf{U}_+) = \frac{1}{2}[\mathbf{F}^I(\mathbf{U}_-) + \mathbf{F}^I(\mathbf{U}_+)] - \frac{1}{2}\mathbf{R}|\mathbf{D}|\mathbf{L}(\mathbf{U}_+ - \mathbf{U}_-). \quad (2.27)$$

The Lax-Friedrichs flux is implemented as follows:

$$\hat{\mathbf{F}}^I(\mathbf{U}_-, \mathbf{U}_+) = \frac{1}{2}[\mathbf{F}^I(\mathbf{U}_-) + \mathbf{F}^I(\mathbf{U}_+) - \alpha_{max}(\mathbf{U}_+ - \mathbf{U}_-)] \quad (2.28)$$

where α_{max} is the maximum absolute value of the eigenvalues.

2.4.2 Discontinuous Galerkin method for diffusion

The diffusion part of the equation 2.19 is:

$$\mathbf{U}_t = \frac{1}{Re_{\text{ref}}} \nabla \cdot \mathbf{F}^V + \mathbf{F}_B. \quad (2.29)$$

where $\mathbf{F}^V = \mathbf{F}^V(\mathbf{U}, \nabla \mathbf{U})$ is the viscous flux.

The problem can be simplified as:

$$u_t = \nabla \cdot (\nu \nabla u) + s \quad (2.30)$$

where ν is a variable coefficient $\nu = \nu(\mathbf{x}, t)$; The field variable u is a scalar $u = u(\mathbf{x}, t)$; and s is the source term.

A flux variable is introduced:

$$\mathbf{f}^V = \nu \nabla u. \quad (2.31)$$

Then the equation 2.30 can be rewritten as:

$$u_t = \nabla \cdot \mathbf{f}^V + s \quad (2.32)$$

$$\frac{1}{\nu} \mathbf{f}^V = \nabla u. \quad (2.33)$$

Weighting functions \mathbf{w} and v is introduced, so that, for the element Ω^e , it has

$$\int_{\Omega^e} v u_t d\mathbf{x} = \int_{\Omega^e} v \nabla \cdot \mathbf{f}^V d\mathbf{x} + \int_{\Omega^e} v s d\mathbf{x} \quad (2.34)$$

$$\int_{\Omega^e} \frac{1}{\nu} \mathbf{w} \cdot \mathbf{f}^V d\mathbf{x} = \int_{\Omega^e} \mathbf{w} \cdot \nabla u d\mathbf{x}. \quad (2.35)$$

As in the previous convection section, Integrating the above equation by parts

gives:

$$\int_{\Omega^e} vu_t d\mathbf{x} = - \int_{\Omega^e} \nabla v \cdot \mathbf{f}^V d\mathbf{x} + \int_{\partial\Omega^e} v \hat{\mathbf{n}} \cdot \hat{\mathbf{f}}^V d\mathbf{s} + \int_{\Omega^e} v s d\mathbf{x} \quad (2.36)$$

$$\int_{\Omega^e} \frac{1}{\nu} \mathbf{w} \cdot \mathbf{f}^V d\mathbf{x} = - \int_{\Omega^e} u \nabla \cdot \mathbf{w} d\mathbf{x} + \int_{\partial\Omega^e} \hat{u} \hat{\mathbf{n}} \cdot \mathbf{w} d\mathbf{s}. \quad (2.37)$$

Integrating the above equation by parts once more, it follows,

$$\int_{\Omega^e} vu_t d\mathbf{x} = \int_{\Omega^e} v \nabla \cdot \mathbf{f}^V d\mathbf{x} + \int_{\partial\Omega^e} v \hat{\mathbf{n}} \cdot (\hat{\mathbf{f}}^V - \mathbf{f}^V) d\mathbf{s} + \int_{\Omega^e} v s d\mathbf{x} \quad (2.38)$$

$$\int_{\Omega^e} \frac{1}{\nu} \mathbf{w} \cdot \mathbf{f}^V d\mathbf{x} = \int_{\Omega^e} \mathbf{w} \cdot \nabla u d\mathbf{x} + \int_{\partial\Omega^e} \mathbf{w} \cdot \hat{\mathbf{n}} (\hat{u} - u) d\mathbf{s} \quad (2.39)$$

where $\hat{\mathbf{f}}^V$, \hat{u} denotes the viscous boundary fluxes.

Bassi & Rebay (1997) calculated the fluxes by averaging the values from two sides of the boundary.

$$\hat{\mathbf{f}}^V = \frac{1}{2}(\mathbf{f}_+^V + \mathbf{f}_-^V) \quad (2.40)$$

$$\hat{u} = \frac{1}{2}(u_+ + u_-) \quad (2.41)$$

There are also many other methods available, such as, local discontinuous Galerkin method (Cockburn & Shu, 1998), Baumann-Oden method (Baumann & Oden, 1999), etc.

2.5 Compressible DGM code

The original compressible DG code is the 3D compressible Nektar code from Dr. Karniadakis' CRUNCH Group at Brown University. The code is written in C++ (with MPI). It can correctly solve the conservative form of Navier-stokes equations without driving force by using discontinuous Galerkin method and Adams-Bashforth

time scheme. But it has problems of getting incorrect density and temperature field for simulations with a driving force.

My key contributions/modifications to the code are:

- Fixed an important bug of not considering the introduced additional term in the total energy equation due to the addition of driving force. The original DG code has a section for adding drive force to Navier-Stokes equations, but the addition is only done on momentum equations. This causes a total energy loss in the total energy equation due to the missing term, that is, energy is losing as time/simulation goes. Consequently, this would lead to a maximum temperature and a minimum density at the channel walls for the simulation fully developed turbulent isothermal-wall channel flow, which is opposite to the correct result: maximum temperature and the minimum density happens at the channel center for turbulent isothermal-wall channel flow.
- Upgraded the driving force to driving force function. The original code can only use fixed values, which is the same for the whole computation domain. The new implementation can allow the use of a driving force function, which can be different at different locations of the computational domain.
- Implemented fringe region technique. Henningson's fringe region technique was implemented in the code.
- Fixed several output and limit bugs and made some improvements, such as several newly added functions, etc.
- Implemented over-integration and added new utilities for the post-processing code, such as combining all elements into one, creating (Tecplot) binary files.

| No. of CPUs | Seconds per time-step | Speedup |
|-------------|-----------------------|---------|
| 8 | 11.08 | 8 |
| 16 | 5.71 | 15.53 |
| 32 | 3.12 | 28.41 |
| 64 | 1.67 | 53.08 |

Table 2.1: The scaling test for DGM on Sun SPARC Enterprise M9000

| No. of CPUs | Seconds per time-step | Speedup |
|-------------|-----------------------|---------|
| 64 | 5.66 | 64 |
| 100 | 3.81 | 95.0 |
| 120 | 3.01 | 120.4 |
| 180 | 2.06 | 175.7 |

Table 2.2: The scaling test for DGM on SGI Origin 3900

2.5.1 Scaling test

The scaling tests of the discontinuous Galerkin method have been conducted on different architectures: (1) A channel flow simulation of 4320 elements ($24 \times 15 \times 12$) and 10th order polynomial with over-integration was carried out on Sun SPARC Enterprise M9000 at HPCVL (total 64 quad-core 2.52 Ghz Sparc64 VII processors, total Memory size: 2 TBytes) with 8, 16, 32 and 64 processors respectively; (2) A channel flow simulation of 41400 elements ($100 \times 18 \times 23$) and 7th order polynomial was performed on SGI Origin model 3900 at West-Grid (total 256 processors of 700 MHz IP35, total memory size: 256 GBytes) with 64, 100, 120, 180 processors respectively. The scaling results are shown in tables (2.1) and (2.2) respectively. The speedup is presented in figure (2.3). It can be easily seen that DGM achieves very good speed-up for this problem on these architectures, although both are shared-memory multi-processor (SMP) machines.

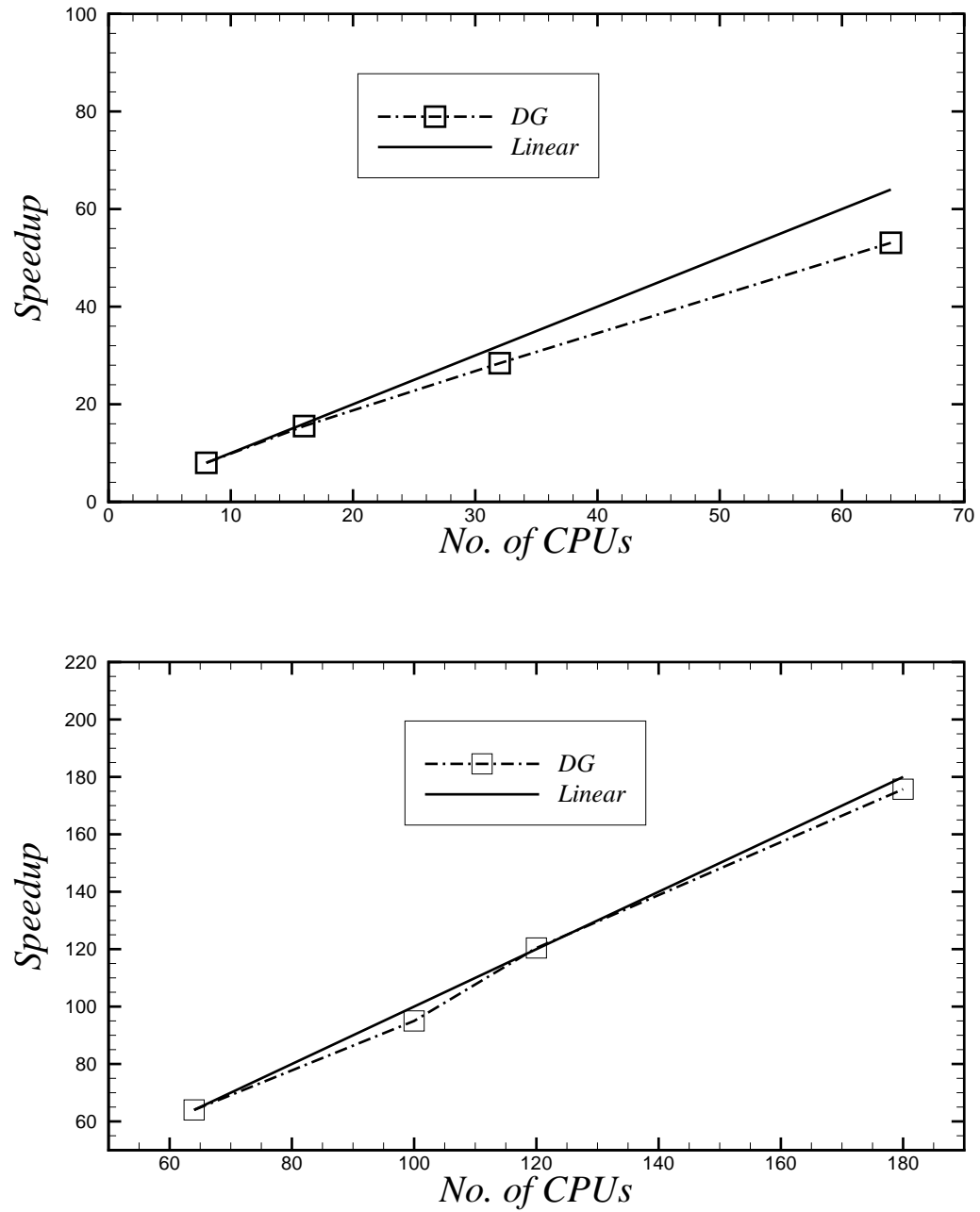


Figure 2.3: Top: Speedup of DGM on Sun SPARC Enterprise M9000; Bottom: Speedup of DGM on SGI Origin 3900

Chapter 3

DNS of turbulent compressible channel flows

3.1 Introduction

It has been demonstrated that incompressible turbulent channel flow is extremely useful for the study of wall-bounded turbulence (Moin & Mahesh, 1998). Direct numerical simulation (DNS) of wall-bounded compressible turbulent flow is equally useful because it provides 3D and time-dependent data that are very difficult or even impossible to obtain experimentally (Morinishi, Tamano & Nakabayashi, 2004). Here, DNS of fully developed compressible and incompressible turbulent channel flows are investigated to study the effects of Mach number, compressibility and pressure gradient on turbulence scaling, near-wall vorticity dynamics, turbulence structures, and the related turbulence physics. In addition, the present work seeks to verify the application of discontinuous Galerkin method (DGM) to DNS of turbulent flows.

There are two type of compressibility effects. One is caused by variations of the

mean properties such as density and viscosity, and the other the fluctuation of thermodynamic quantities (Morinishi *et al.*, 2004). Lele (1994) has reviewed compressibility effects on turbulence. He summarized many facets of compressibility effects on turbulence and discussed several homogeneous and inhomogeneous compressible flows. He argued that the density gradient in a compressible turbulent boundary layer is mainly responsible for a decreased skin-friction coefficient, smaller turbulence intensity, viscous effects, and for modifications to the incompressible law of the wall. Smits (1991) also argued that a single Reynolds number is not sufficient to characterize the flow with large gradients of fluid properties.

The first DNS of incompressible turbulent plane channel flow was performed by Kim, Moin & Moser (1987), referred to hereafter as KMM. The Reynolds number based on friction velocity was around 180 ($Re_\tau \approx 180$). A large number of turbulence statistics including turbulence intensities, Reynolds shear stress, vorticity, high order statistics, etc were compared with experimental data with good agreement.

New simulations of the KMM $Re_\tau \approx 180$ case were performed by Moser, Kim & Mansour (1999), referred to hereafter as MKM. A comprehensive database was provided including mean profiles, Reynolds stress, skewness, and flatness profiles, etc. Besides this, two higher Reynolds number ($Re_\tau \approx 395$ and $Re_\tau \approx 590$) fully developed turbulent channel flow simulations were conducted (Moser *et al.*, 1999), in which fewer low Reynolds number effects were observed than the $Re_\tau \approx 180$ case. For example, near-wall scaling of mean streamwise velocity profile for the case $Re_\tau \approx 180$ has a larger intercept in the log-law region than higher Reynolds number flows.

The first application of the discontinuous Galerkin method (DGM) to DNS of

turbulent flows was performed by Collis (2002). Collis applied the DGM to a low-Reynolds-number DNS of compressible turbulent channel flow with isothermal walls. The Reynolds number based on the friction velocity (Re_τ) was 100. The centre-line Mach number (Ma_c) was 0.3. Mean and RMS velocity profiles were obtained and compared with the incompressible cases. To the best of the author’s knowledge, this is the only application of DG method to DNS of turbulent flows.

DNS of turbulent compressible plane channel flow between isothermal walls was performed by Coleman, Kim & Moser (1995), referred to henceforth as CKM. The Mach numbers based on the bulk velocity and sound speed at the walls were 1.5 and 3. The Reynolds numbers were of order 3000 and 4880, based on the centre line velocity and channel half width. They found that the mean density and temperature gradients caused enhanced streamwise coherence of near-wall streaks. The density-weighted Van Driest transformation (Van Driest, 1951) of mean streamwise velocity generated curves of similar slopes. It was also claimed that the compressibility effects caused by the mean property variations were dominant, compared with those caused by thermodynamic fluctuations.

Huang, Coleman & Bradshaw (1995) analysed DNS results of fully developed supersonic isothermal wall channel flow and found that the difference between Reynolds and Favre averages was small and any difference mainly existed in the region close to the wall. Their DNS results did not support the “strong Reynolds analogy”, which built a relation between temperature and streamwise velocity fluctuations, as proposed by Morkovin (1964). Instead, they proposed a new Reynolds analogy that had good agreement with their DNS data.

Morinishi *et al.* (2004) performed a DNS of compressible turbulent channel flow

between adiabatic and isothermal walls. The main difference between adiabatic and isothermal walls were explained. The energy transfer was analysed. It was found that Morkovin's hypothesis (Morkovin, 1964), which generally claimed that the compressible shear flow dynamics would follow the incompressible pattern, was not applicable to the near wall asymptotic behaviour of the wall normal turbulence intensity.

Foysi, Sarkar & Friedrich (2004) used DNS to study Reynolds shear stress scaling in turbulent supersonic channel flow with isothermal walls. It was found that the outer scaling (scaling with global variables) of Reynolds stresses worked well for the region far away from the wall, but inner scaling (scaling with wall variables) failed. An effective density was proposed based on an integral of local mean density over the vertical extent of turbulent eddy. They claimed that the difference between effective density and local mean density was the reason why local-mean-density-based turbulence inner scaling law failed.

Recently Brun *et al.* (2008) performed a large eddy simulation of compressible turbulent channel flow with isothermal walls. The Reynolds numbers were 3000 and 4800 and Mach number $0.3 < Ma < 3$. Low Reynolds number effects and compressibility effects were analyzed. An improved Van Driest transformation with an addition of the influence of viscosity was proposed. The density and viscosity weighted RMS velocity fluctuation profiles collapsed well.

3.1.1 Turbulence scaling

Turbulence inner and outer scaling as well as inner-outer layer interactions have been studied in an effort to separate near wall from outer region effects.

Townsend (1976) proposed the concept of inactive motion, referred to as low-frequency large-scale swirling motion in a turbulent boundary layer. In other words, large eddies close to the wall were “inactive”. He explained the influence of inactive motion on the inner scaling of wall parallel components of turbulence intensities (square of RMS velocity fluctuations in the streamwise and spanwise directions). He also claimed that the scaling of wall-normal turbulence intensity and the shear stress was little affected by inactive motion.

Morrison *et al.* (2004) investigated Reynolds number effects on the streamwise turbulence intensities and higher order moments of streamwise velocity in fully developed pipe flow over a range of high Reynolds numbers ($5.5 \times 10^4 \leq Re_D \leq 5.7 \times 10^6$). It was shown that streamwise turbulence intensities had two maxima. The first maximum was at $y^+ \approx 15$ where the production of turbulence kinetic energy is maximized; however, this maximum was Reynolds number dependent. The second maximum was found at $y^+ \approx 500$ with $Re_D > 2 \times 10^5$. They argued that the inactive motion concept was inappropriate, although it could provide qualitative explanation of low-wavenumber motion near the wall.

Morrison (2007) investigated the inner and outer layer interactions of turbulent wall-bounded flows and suggested that it was probable that the interaction was inherently nonlinear. He also argued that large eddies contributed a significant fraction to the Reynolds stresses, which was the reason that Reynolds stress do not scale with wall friction velocity. It was then concluded that the assumption of the hypothesis of energy equilibrium close to the wall (Townsend, 1956, 1976), which was identified as a no-interaction condition and inactive motion, was invalid.

Zhao & Smits (2007) studied the scaling of the wall-normal turbulence component in high-Reynolds-number pipe flow and found that 'inactive motion' concept cannot explain their observations and confirmed that Morrison's arguments of near-wall motion was influenced by the outer flow.

3.1.2 Near-wall vorticity dynamics

It is well known that vorticity generation occurs at the wall; however, large near-wall viscosity variations can also influence the generation of vorticity. How these variations influence the near wall pressure gradients for compressible channel flow has not been explored.

Lighthill (1963) proposed that the vorticity flux (kinematic viscosity times vorticity gradient for incompressible flows) was dominated by tangential pressure gradients in an incompressible laminar boundary layer. A flow over a stationary plane wall was considered, with x, y, z denoted as the streamwise, wall-normal, and spanwise directions respectively, and the wall surface taken as $y = 0$. A relation between vorticity and pressure was derived:

$$\nu \frac{\partial \omega_x}{\partial y} = \nu \frac{\partial}{\partial y} \left(\frac{\partial w}{\partial y} - \frac{\partial v}{\partial z} \right) = \nu \frac{\partial^2 w}{\partial y^2} = \nu \nabla^2 w = \frac{1}{\rho} \frac{\partial p}{\partial z} \quad (3.1)$$

where ω_x is the streamwise vorticity, $\partial p / \partial z$ is the spanwise pressure gradient.

Wu *et al.* (1988) extended the vorticity-pressure relation to a viscous compressible flow under the assumption of a constant viscosity. A general theory on the interaction between vorticity-dilatation field and the solid surface was outlined. Actually, vorticity flux can be affected by the wall normal gradient of the kinematic viscosity as result of surface heating, chemical reaction, etc, shown by Gad-El-Hak (1990).

Wu *et al.* (1993) studied vorticity generation on an oscillating wall. It was found that the the wall oscillation could generate additional vorticity flux, which could affect the existing vorticity field either positively or negatively. They claimed that this effect was partially responsible for the mechanism of vortex flow control by waves. Developments of boundary vorticity dynamics theory were reviewed by Wu & Wu (1998).

Vorticity flux was also considered for the active control of turbulent flows on a solid surface. Koumoutsakos (1999) proposed a control algorithm based on the measurement and manipulation of the wall vorticity flux (or equivalently pressure gradient) and applied this algorithm to a low Reynolds number turbulent incompressible channel flow. The simulation showed that the resulting skin friction drag reduction could reach an order of 40% through out-of-phase control (implying cancellation of the induced vorticity flux).

Lee & Kim (2002) also investigated vortices in a viscous sublayer of a turbulent boundary layer and found that a significant generation of vorticity there. A significant amount of drag reduction could be achieved through a supression of spanwise disturbances in the sublayer which caused supression of near-wall turbulence structures.

The near wall vorticity, viscosity and pressure correlations will be explored in further detail in section (3.9)

3.2 Computational details

3.2.1 Numerical methods

DNS of fully developed turbulent flow between two isothermal parallel plates at different Mach numbers is considered. The fluid is assumed to be an ideal gas with constant specific heats ($c_p = \gamma R/(\gamma - 1)$, $c_v = R/(\gamma - 1)$; $\gamma = 1.4$, R is the gas constant) and Prandtl number (Pr).

The discontinuous Galerkin method (DGM) was used for the DNS. DGM is a finite element based method that uses numerical fluxes on element boundaries, which draws from finite volume method, so that it can accommodate discontinuous solutions on element boundaries. It has many attractive features including: high order accuracy, highly parallelizable, well suitable for complex geometries, local conservation, etc (Cockburn, Karniadakis & Shu, 2000). The first DGM was introduced by Reed & Hill (1973). It is only recently that DGM has been made suitable for computational fluid dynamics related applications (Cockburn *et al.*, 2000; Karniadakis & Sherwin, 2005), see chapter 2 for details.

The nondimensionalized conservation form of continuity, momentum, and energy equations with an addition of a driving force can be written as equations (3.2) (3.3) (3.4) respectively.

$$\frac{\partial \rho^*}{\partial t^*} + \frac{\partial \rho^* u_j^*}{\partial x_j^*} = 0 \quad (3.2)$$

$$\frac{\partial \rho^* u_i^*}{\partial t^*} + \frac{\partial (\rho^* u_i^* u_j^* + p^* \delta_{ij})}{\partial x_j^*} = \frac{1}{Re} \frac{\partial \tau_{ij}^*}{\partial x_j^*} + \rho^* f_i^* \quad (3.3)$$

$$\frac{\partial E^*}{\partial t^*} + \frac{\partial(E^* + p^*)u_j^*}{\partial x_j^*} = \frac{1}{Re} \frac{\partial(\tau_{ij}^* u_i^* + \frac{\gamma^* \kappa^*}{Pr} \frac{\partial T^*}{\partial x_j^*})}{\partial x_j^*} + \rho^* f_i^* u_i^* \quad (3.4)$$

where all the variables with superscript "*" were nondimensionalized by the reference variables (half channel width h , mean bulk density ρ_m , mean bulk velocity U_m , dynamic viscosity at wall μ_w , thermal conductivity at wall κ_w , specific heat at constant volume c_v) in the following way: $x_i^* = x_i/h$, $\rho^* = \rho/\rho_m$, $u_i^* = u_i/U_m$, $E^* = E/(\rho_m U_m^2)$, $p^* = p/(\rho_m U_m^2)$, $\mu^* = \mu/\mu_w$, $\kappa^* = \kappa/\kappa_w$, $T^* = T/(U_m^2/c_v)$, $t^* = t/(h/U_m)$, $f_i^* = f_i/(U_m^2/h)$; where $f_i = \tau_{w_{av}} \delta_{i1}/(h\rho_m)$.

The ideal gas law then becomes,

$$p^* = \rho^*(\gamma - 1)T^* \quad (3.5)$$

Re is the reference Reynolds number: $Re = \rho_m U_m h / \mu_w$;

δ_{ij} is Kronecker's delta: $\delta_{ij} = 1$ if $i = j$; $\delta_{ij} = 0$ if $i \neq j$

τ_{ij}^* is the viscous stress tensor:

$$\tau_{ij}^* = \mu^* \left(\frac{\partial u_i^*}{\partial x_j^*} + \frac{\partial u_j^*}{\partial x_i^*} \right) - \frac{2}{3} \mu^* \delta_{ij} \frac{\partial u_k^*}{\partial x_k^*}; \quad (3.6)$$

f_i^* is the driving force: $f_i^* = 0.5(\langle \tau_{12}^* \rangle|_{x_2^*=0} - \langle \tau_{12}^* \rangle|_{x_2^*=2})\delta_{i1}/Re$; the angle brackets $\langle \rangle$ denote the average over time (t) and streamwise (x_1) & spanwise (x_3) directions.

E is the total energy: $E^* = \rho^* T^* + 1/2 \rho^* u_i^* u_i^* = p^*/(\gamma - 1) + 1/2 \rho^* u_i^* u_i^*$.

The relation between the bulk Mach number and the nondimensionalized wall temperature is

$$Ma = \frac{1}{\sqrt{\gamma(\gamma - 1)T_w^*}} \quad (3.7)$$

Prandtl number is defined as:

$$Pr = \frac{c_p \mu_w}{\kappa_w} = \frac{c_p \mu}{\kappa} \quad (3.8)$$

Pr and C_p are constants by assumption. It follows

$$\kappa^* = \mu^* \quad (3.9)$$

The calculation of dynamic viscosity was based on Sutherland's theory of viscosity, for which interpolation formula can be written as (Schlichting, 1979) :

$$\mu^* = \frac{\mu}{\mu_w} = \left(\frac{T}{T_w} \right)^{\frac{3}{2}} \frac{T_w + S_1}{T + S_1} = \left(\frac{T^*}{T_w^*} \right)^{\frac{3}{2}} \frac{T_w^* + S_1^*}{T^* + S_1^*} \quad (3.10)$$

where μ_w denotes the reference dynamics viscosity at the reference wall temperature T_w , S_1 is a constant with a value of $S_1 = 110K$ for air, and $S_1^* = S_1/(U_m^2/c_v)$.

DGM was employed for both convection and diffusion terms in the Navier-Stokes equations (3.2, 3.3, 3.4) and Adams-Bashforth scheme for time integration. Numerical boundary flux for convection was computed using upwind flux (Karniadakis & Sherwin, 2005) and numerical viscous boundary flux was evaluated using Bassi-Rebay method (Bassi & Rebay, 1997).

3.2.2 Physical and numerical parameters

Three DNS cases with Mach numbers $Ma = 0.2$, $Ma = 0.7$, and $Ma = 1.5$ (referred to as Ma02, Ma07, and Ma15 hereafter) based on the bulk velocity U_m are considered. They share the same computational domain and coordinate system: streamwise (x) : $12h$, wall-normal (y) : $2h$, spanwise (z) : $6h$, as illustrated in figure (3.1). The domain size was large enough to include the largest eddies in the flow, as will be discussed in the next section. The flow was assumed to be periodic in the streamwise and spanwise directions as the flow was fully developed.

The Reynolds number was ≈ 2800 based on the mean bulk density ρ_m , mean bulk velocity U_m , dynamic viscosity at wall μ_w and the channel half-width h (180

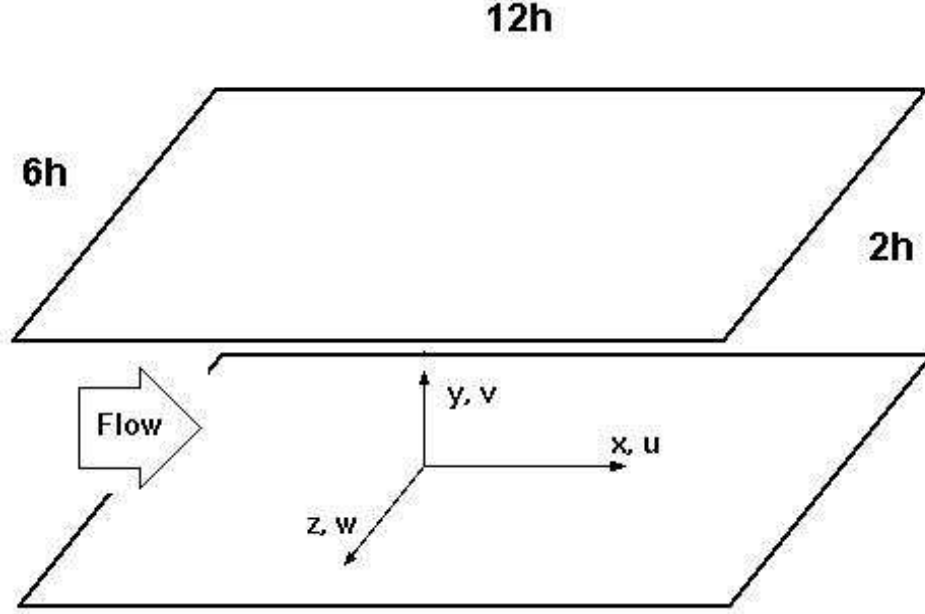


Figure 3.1: Computational domain for turbulent channel flow

| Case | Ma | Re | Re_τ | Pr | γ | L_x | L_y | L_z | Δx^+ | $\Delta y_{min}^+/\Delta y_{max}^+$ | Δz^+ |
|------|------|------|-----------|------|----------|----------|-------|--------------------|--------------|-------------------------------------|--------------|
| MKM | 0 | 2800 | 178 | / | / | $4\pi h$ | $2h$ | $\frac{4}{3}\pi h$ | 17.7 | 0.1/4.4 | 5.9 |
| CKM | 1.5 | 3000 | 222 | 0.7 | 1.4 | $4\pi h$ | $2h$ | $\frac{4}{3}\pi h$ | 19 | 0.1/5.9 | 12 |
| Ma02 | 0.2 | 2772 | 180 | 0.72 | 1.4 | $12h$ | $2h$ | $6h$ | 4.74 | 0.19/2.81 | 4.74 |
| Ma07 | 0.7 | 2795 | 186 | 0.72 | 1.4 | $12h$ | $2h$ | $6h$ | 4.89 | 0.19/2.89 | 4.89 |
| Ma15 | 1.5 | 2811 | 208 | 0.72 | 1.4 | $12h$ | $2h$ | $6h$ | 5.42 | 0.22/3.24 | 5.42 |

Table 3.1: Physical and numerical parameters

based upon the friction velocity u_τ and h for $Ma = 0.2$). A summary of the physical parameters of current simulations and two reference databases (MKM, CKM) is given in the table (3.1). Although there is slight difference in some parameters (such as Reynolds number and Prandtl number) between the case CKM and the current cases, the comparison is still useful.

Uniform grid elements were employed in the streamwise and spanwise directions.

A hyperbolic tangent function was used to distribute grids in the wall-normal direction. The number of grid elements are $24 \times 15 \times 12$, in x, y, z directions respectively.

The initial field of the current simulations consisted of a uniform density profile ($\langle \rho^* \rangle = 1$), a laminar parabolic velocity profile with a superimposition of random fluctuations ($\langle u^* \rangle = 1.5(1 - (1 - y^*)^2)$, $\langle v^* \rangle = 0$, $\langle w^* \rangle = 0$), and a total energy profile that makes the mean fluid temperature field uniform ($\langle T^* \rangle = T_w^*$). The simulation started with a polynomial expansion order of $P = 5^{th}$ per element and over-integration was applied to avoid aliasing errors; that is, $10 \times 10 \times 10$ quadrature in each element. Then the simulation was restarted with $p = 10^{th}$ order with over-integration, that is $20 \times 20 \times 20$ quadrature in each element, to collect the flow statistics. A second-order Adams-Bashforth scheme was used for time discretization.

The statistics for all three cases Ma02, Ma07, and Ma15 were obtained by an average over 120 non-dimensional time units ($t^* = t/(h/U_m)$), or ≈ 8 large eddy turn-over time (LETOT, based on $t/(h/u_\tau)$).

3.3 Grid resolution and domain size

This section addresses grid resolution and the size of the computational domain. Grid resolution should be fine enough to capture the smallest length scales in turbulent flow and the computational domain should be large enough to accommodate the largest length scales.

Kolmogorov microscales of length, which characterizes the smallest scales, is defined as:

$$\eta = (\nu^3/\epsilon)^{1/4} \quad (3.11)$$

where the dissipation rate per unit mass is:

$$\epsilon = \frac{1}{2}\nu\langle(\frac{\partial u'_i}{\partial x_j} + \frac{\partial u'_j}{\partial x_i})(\frac{\partial u'_i}{\partial x_j} + \frac{\partial u'_j}{\partial x_i})\rangle \quad (3.12)$$

$$= \nu\langle\frac{\partial u'_i}{\partial x_j}\frac{\partial u'_i}{\partial x_j}\rangle + \langle\frac{\partial u'_i}{\partial x_j}\frac{\partial u'_j}{\partial x_i}\rangle \quad (3.13)$$

where angle brackets $\langle \rangle$ denote Reynolds average. Although these definitions are taken from incompressible flows, they are used here for comparison purpose.

Grid resolution in wall units in the wall-normal direction for all three cases Ma02, Ma07, and Ma15 versus Kolmogorov microscales of length scaled in wall units is shown in figure (3.2). The mean grid spacings in the wall normal directions are: $\Delta y_{min}^+ \approx 0.2$ ($y^+ = y/(\nu/u_\tau)$, where u_τ is the friction velocity.) at the wall, and $\Delta y_{max}^+ \approx 3$ at the centre of channel, which is smaller than the Kolmogorov length scale for all y (here y denotes the nondimensionalized variable y/h for convenience, which is the same for the rest figures).

Grid spacings based on wall units in the streamwise and spanwise directions for three cases are ≈ 5 , as shown in the table (3.1), which is a little higher than the value of Kolmogorov microscales of length, but it does not mean that the resolution is not enough because measuring grid spacing in terms of friction velocity and viscosity at the wall does not yield a straightforward indication of resolution quality due to the rapid variations of mean properties near the wall (Coleman *et al.*, 1995; Huang *et al.*, 1995). Another way to check grid resolution in a homogeneous direction is to consider the one-dimensional energy spectra.

The streamwise and spanwise one-dimensional energy spectra of density, velocities, and temperature at the channel centre and near the walls for all three cases Ma02, Ma07, and Ma15 are shown in figures (3.3), (3.4), and (3.5) respectively, where kx, kz are the wavenumbers in the streamwise and spanwise directions respectively. It can

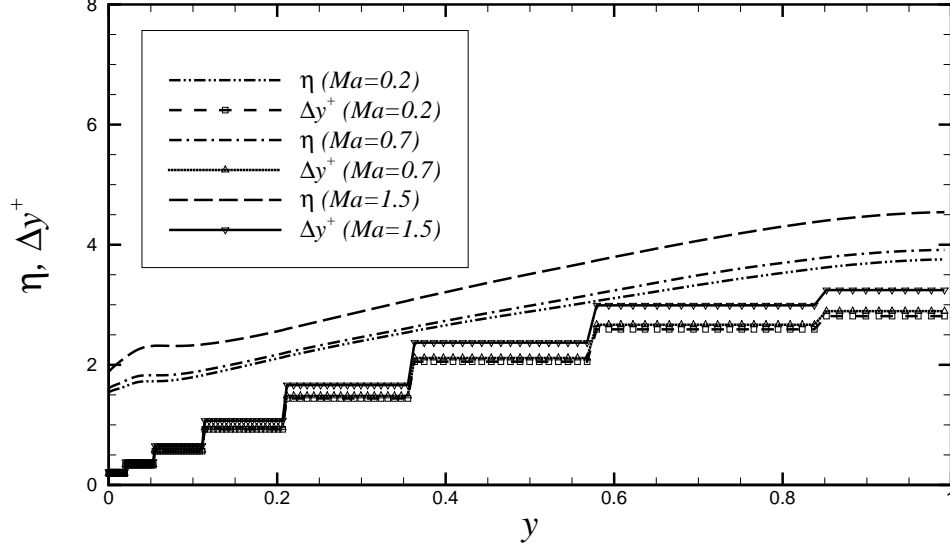


Figure 3.2: Kolmogorov microscale of length (η) versus grid resolution (Δy^+) in wall units

be seen from these figures that all cases share similar trends: rapid fall-off at high wave numbers. Turbulence energy is dissipated and no energy is piled up at high wavenumbers, as the inertial subrange where the Kolmogorov five-thirds law applies is passed, shown in the above three figures. This verifies that the grid resolution in x and z direction is also adequate.

Two point streamwise and spanwise correlations of a certain quantity $a(x, y, z, t)$ are defined as:

$$R_{(\Delta x)} = \frac{\langle a'(x, y, z, t) a'(x + \Delta x, y, z, t) \rangle}{\langle a'(x, y, z, t) a'(x, y, z, t) \rangle} \quad (3.14)$$

$$R_{(\Delta z)} = \frac{\langle a'(x, y, z, t) a'(x, y, z + \Delta z, t) \rangle}{\langle a'(x, y, z, t) a'(x, y, z, t) \rangle} \quad (3.15)$$

Two point steamwise and spanwise correlations of density, velocities, and temperature at the channel centre and near the wall for three cases Ma02, Ma07, and Ma15 are shown in figures (3.6),(3.7), and (3.8) respectively. Figures (3.6) and (3.7)

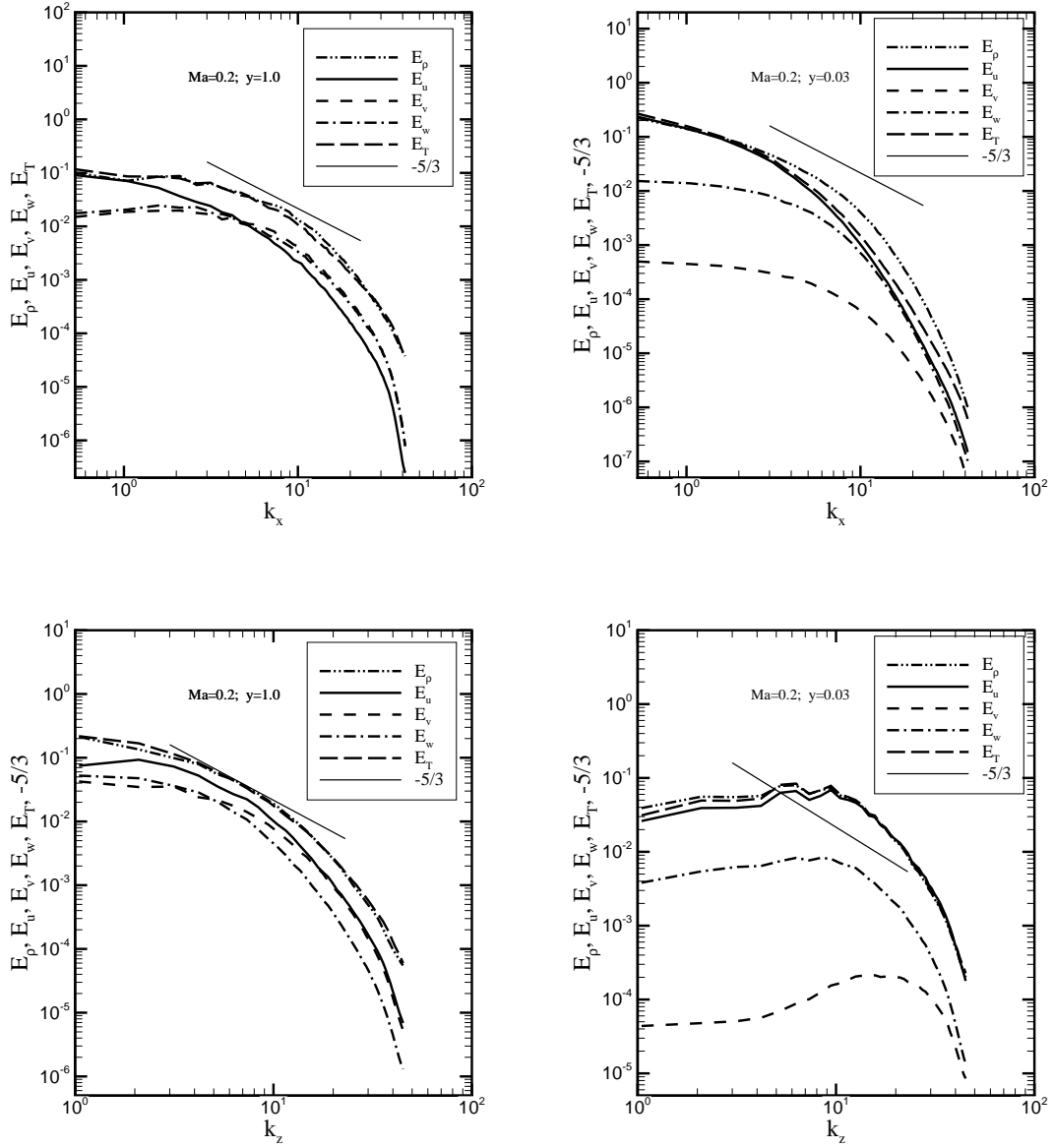


Figure 3.3: One dimensional energy spectra for $Ma=0.2$ for density (ρ), three velocity components (u, v, w) and temperature (T); top left: at the channel centre in the streamwise direction; top right: close to the wall in the streamwise direction; bottom left: at the channel centre in the spanwise direction; bottom right: close to the wall in the spanwise direction. Note the thin solid line is $-5/3$ slope.

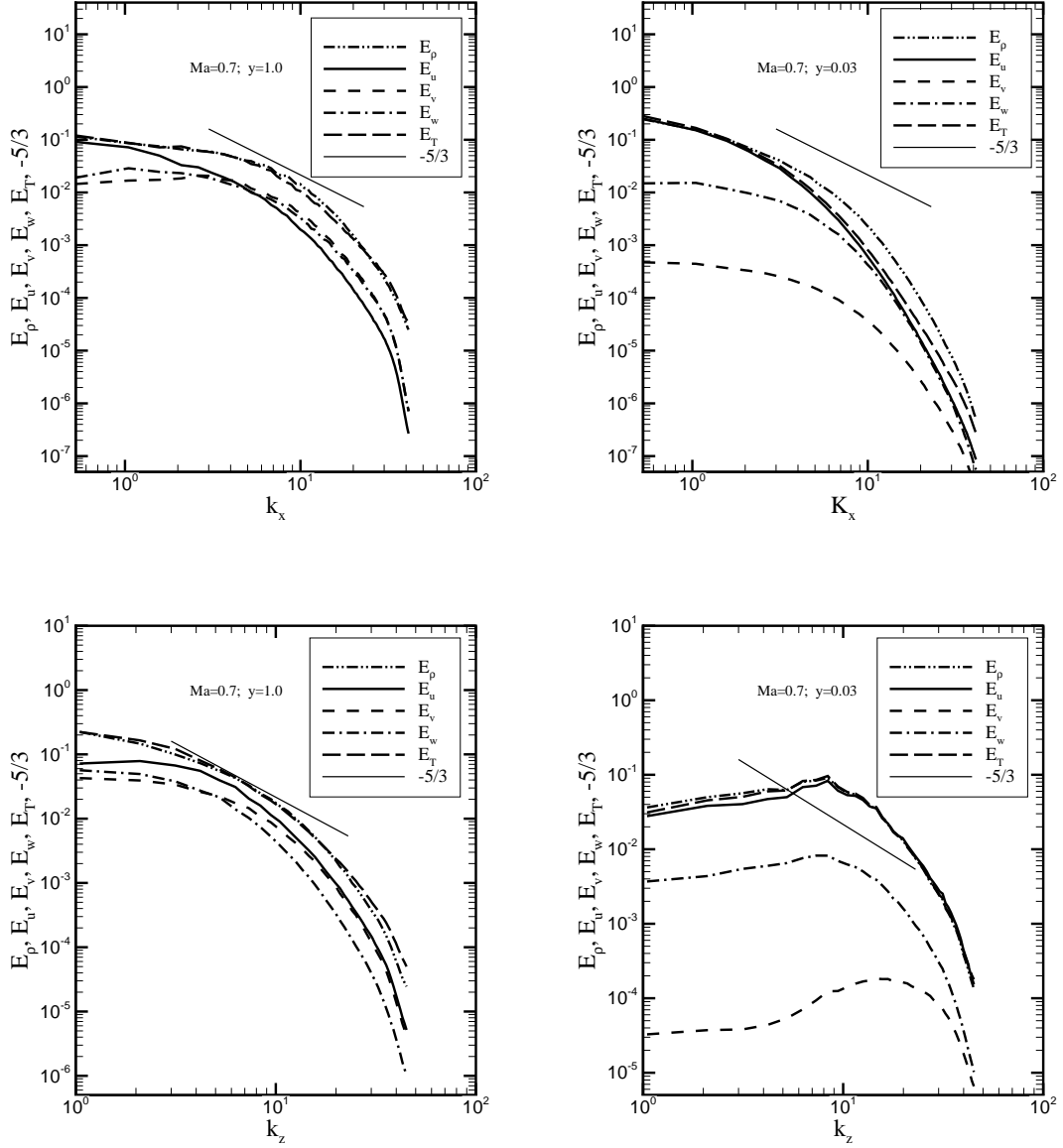


Figure 3.4: One dimensional energy spectra for Ma=0.7 for density (ρ), three velocity components (u, v, w) and temperature (T); top left: at the channel centre in the streamwise direction; top right: close to the wall in the streamwise direction; bottom left: at the channel centre in the spanwise direction; bottom right: close to the wall in the spanwise direction. Note the thin solid line is $-5/3$ slope.

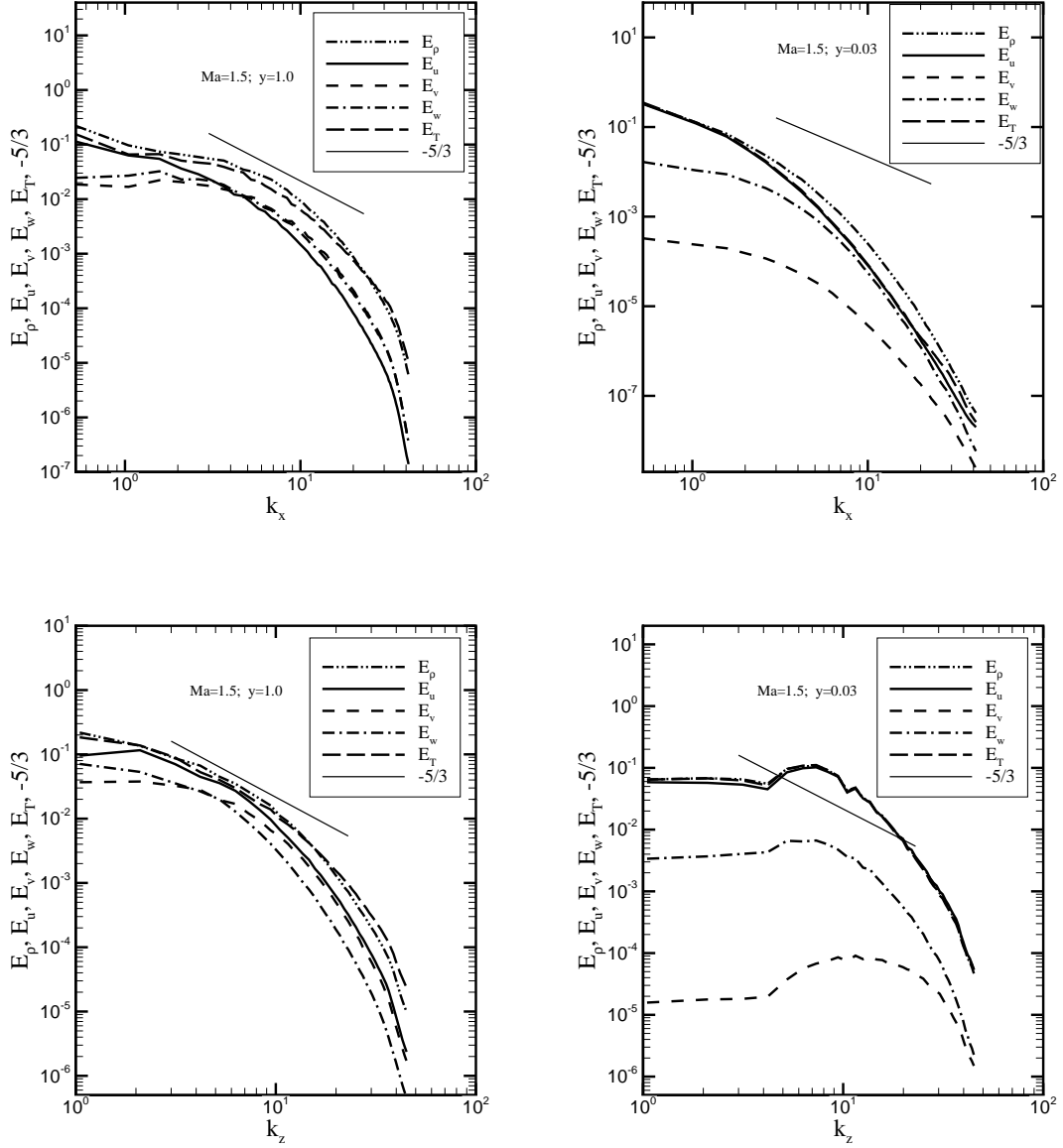


Figure 3.5: One dimensional energy spectra for $Ma=1.5$ for density (ρ), three velocity components (u, v, w) and temperature (T); top left: at the channel centre in the streamwise direction; top right: close to the wall in the streamwise direction; bottom left: at the channel centre in the spanwise direction; bottom right: close to the wall in the spanwise direction. Note the thin solid line is $-5/3$ slope.

show that the correlations of velocities for the cases $Ma=0.2$ and 0.7 are similar to the incompressible results (see the figure 2 of KMM). The results given in figure (3.8) are in good agreement with the case CKM (see the figure 3 of CKM).

It can be seen from figures (3.6),(3.7), and (3.8) that the streamwise correlation of density, temperature and streamwise velocity close to the wall is similar in each case but it increases with increase of Mach number, especially when the flow is in the supersonic region. This indicates that the near-wall streaks become more coherent as Mach number increases. Spanwise coherence of density and temperature at the channel centre line is also observed to increase with increase of Mach number. The large coherence is due to the effect of acoustic disturbances in the channel because the perfectly rigid channel walls in the DNS are not replicated in an experiment; however, this does not significantly affect the turbulent statistics, according to Coleman *et al.* (1995).

3.4 Mean profiles of velocity, density and temperature

The mean streamwise velocity, density and temperature profiles for the cases Ma02 and Ma15, compared with the incompressible case MKM (Moser *et al.*, 1999) and the compressible case CKM (Coleman *et al.*, 1995) respectively, are shown in figure (3.9). The velocity, density and temperature are nondimensionalized by the bulk velocity, bulk density, and the wall temperature respectively. The wall-normal coordinate y is nondimensionalized by the channel half width. The agreement between the current simulations and those of MKM and CKM is observed to be very good. The slight

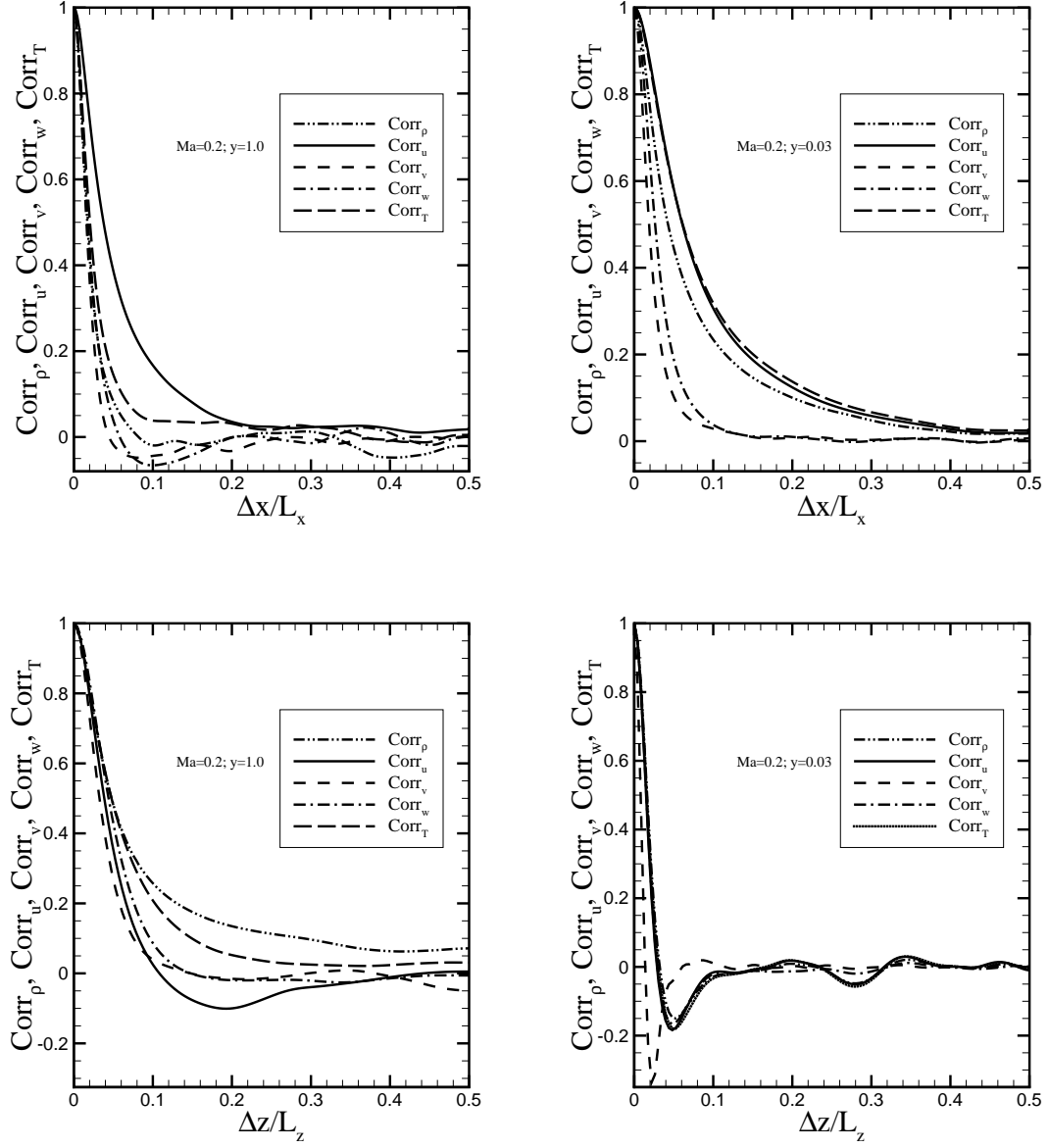


Figure 3.6: Two-point correlations for $Ma=0.2$ for density (ρ), three velocity components (u, v, w) and temperature (T); top right: close to the wall in the streamwise direction; bottom left: at the channel centre in the spanwise direction; bottom right: close to the wall in the spanwise direction.

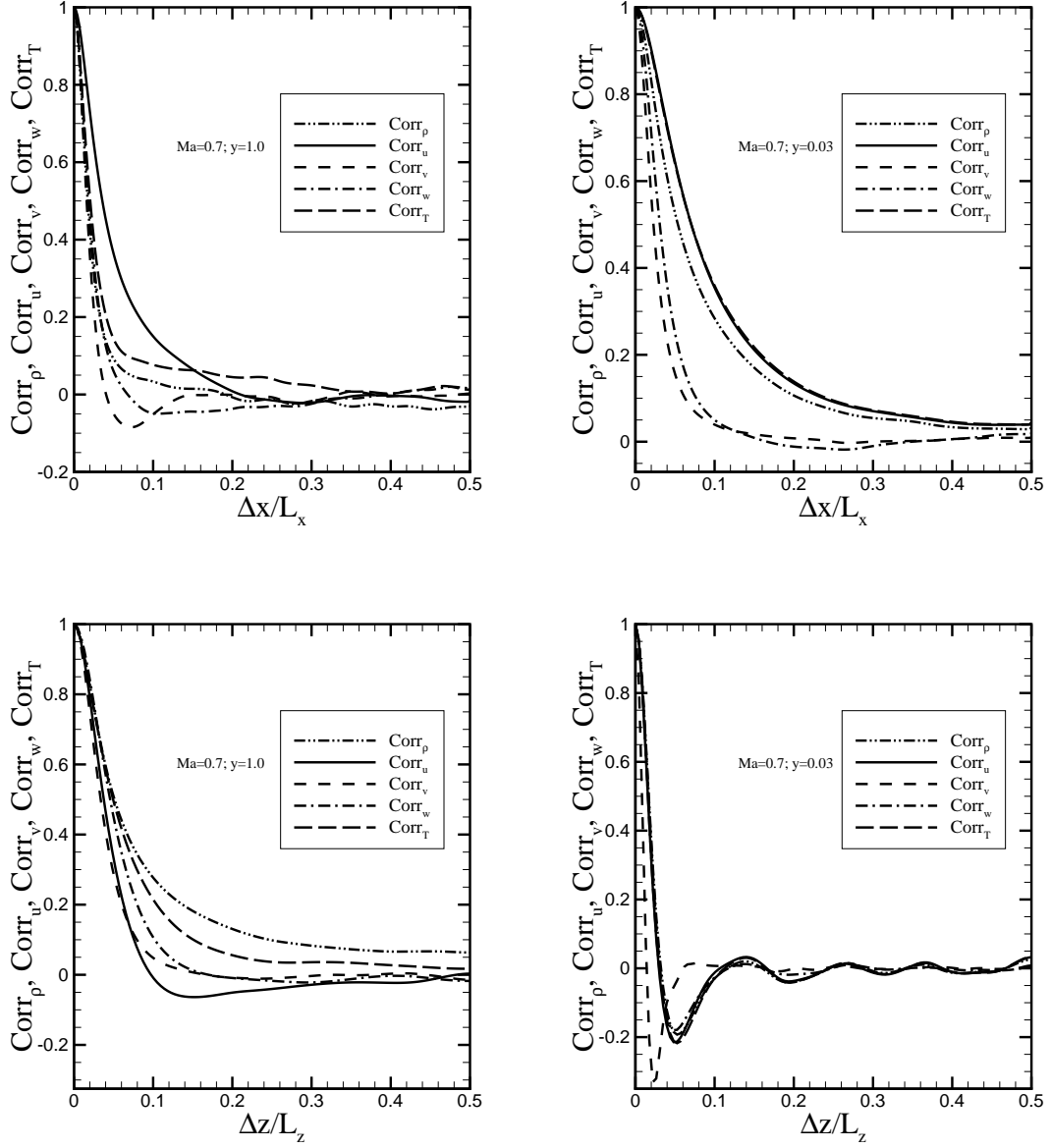


Figure 3.7: Two-point correlations for $\text{Ma}=0.7$ for density (ρ), three velocity components (u, v, w) and temperature (T); top left: at the channel centre in the streamwise direction; top right: close to the wall in the streamwise direction; bottom left: at the channel centre in the spanwise direction; bottom right: close to the wall in the spanwise direction.

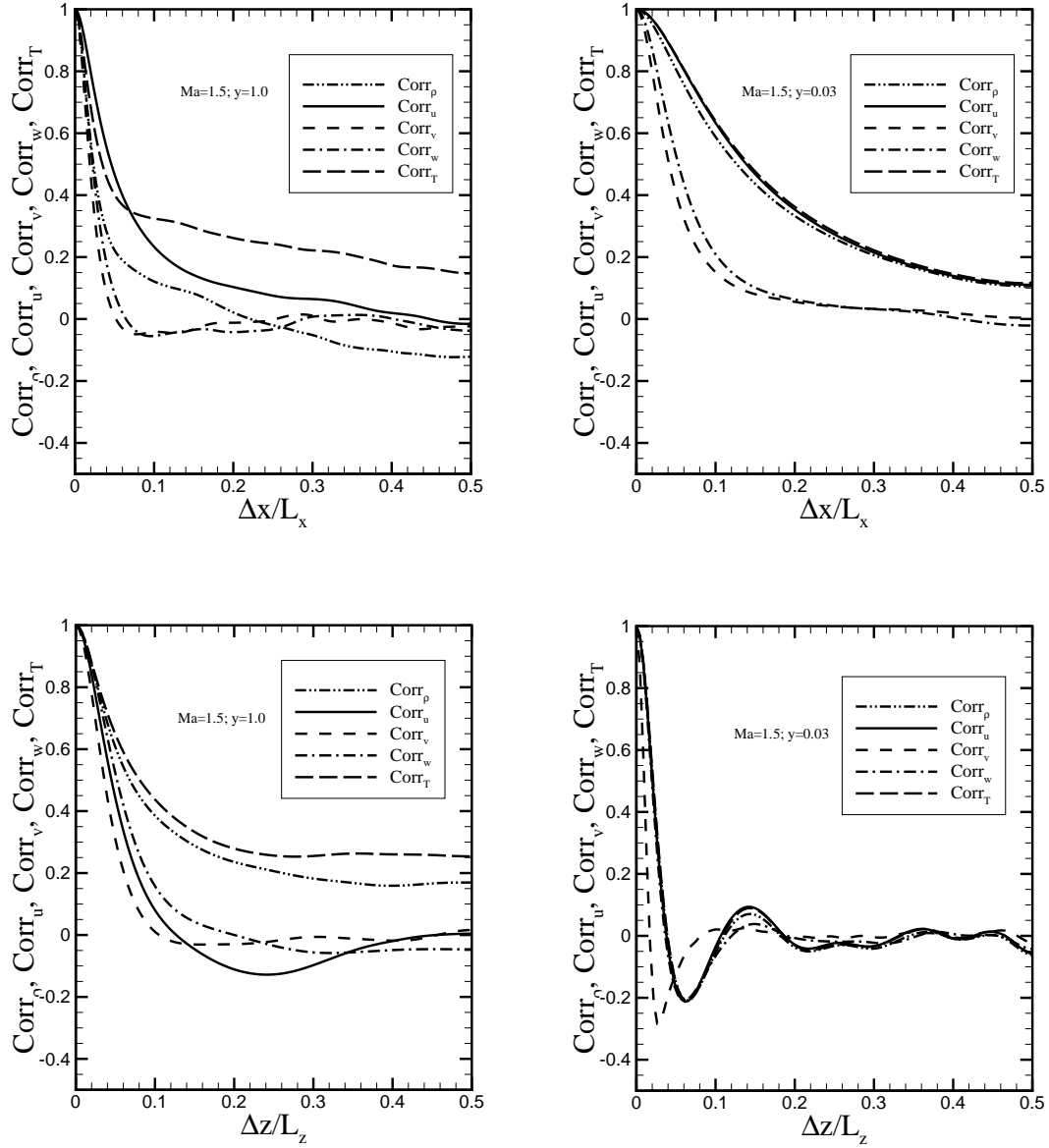


Figure 3.8: Two-point correlations for $Ma=1.5$ for density (ρ), three velocity components (u, v, w) and temperature (T); top left: at the channel centre in the streamwise direction; top right: close to the wall in the streamwise direction; bottom left: at the channel centre in the spanwise direction; bottom right: close to the wall in the spanwise direction.

difference in the mean temperature between the case Ma15 and the case CKM is probably due to the slight difference in the parameters (see table 3.1).

The comparison of the mean velocity profiles for three cases Ma02, Ma07, and Ma15 is presented in figure (3.10). It can be seen that the difference between the cases Ma02 and Ma07 is negligible. But the velocity profile for the case Ma15 is slightly lower in the region $y < \approx 0.17$ and slightly higher in the region $y > \approx 0.17$ than the other two cases.

The comparison of the mean density and temperature profiles for three cases Ma02, Ma07, and Ma15 is shown in figure (3.11). The temperatures at the isothermal walls are lower than the fluid temperature. The maximum temperature is at the centre of the channel. The bigger the Mach number, the higher the temperature gradient close to the wall, and the higher the temperature difference between the wall and the centre. Although the temperature difference is marginal for the Ma02 case, it has a high temperature gradient close the wall, shown in the bottom of the figure 3.12.

The mean streamwise velocity normalized by the friction velocity and its Van Driest transformation for all three cases are displayed in figure (3.13). The top figure is a comparison for case Ma02, the incompressible case MKM and the incompressible law of the wall, which states that in the viscous sublayer region ($y^+ < 5$)

$$u_{sub} = y^+ \quad (3.16)$$

and in the log-law region ($y^+ > 30$)

$$u_{log} = \frac{1}{\kappa} \ln y^+ + B \quad (3.17)$$

where $\kappa = 0.41$ is the Von Kármán constant and $B = 5.2$ is a constant.

The Van Driest transformation of the mean velocity (Van Driest, 1951) accounts

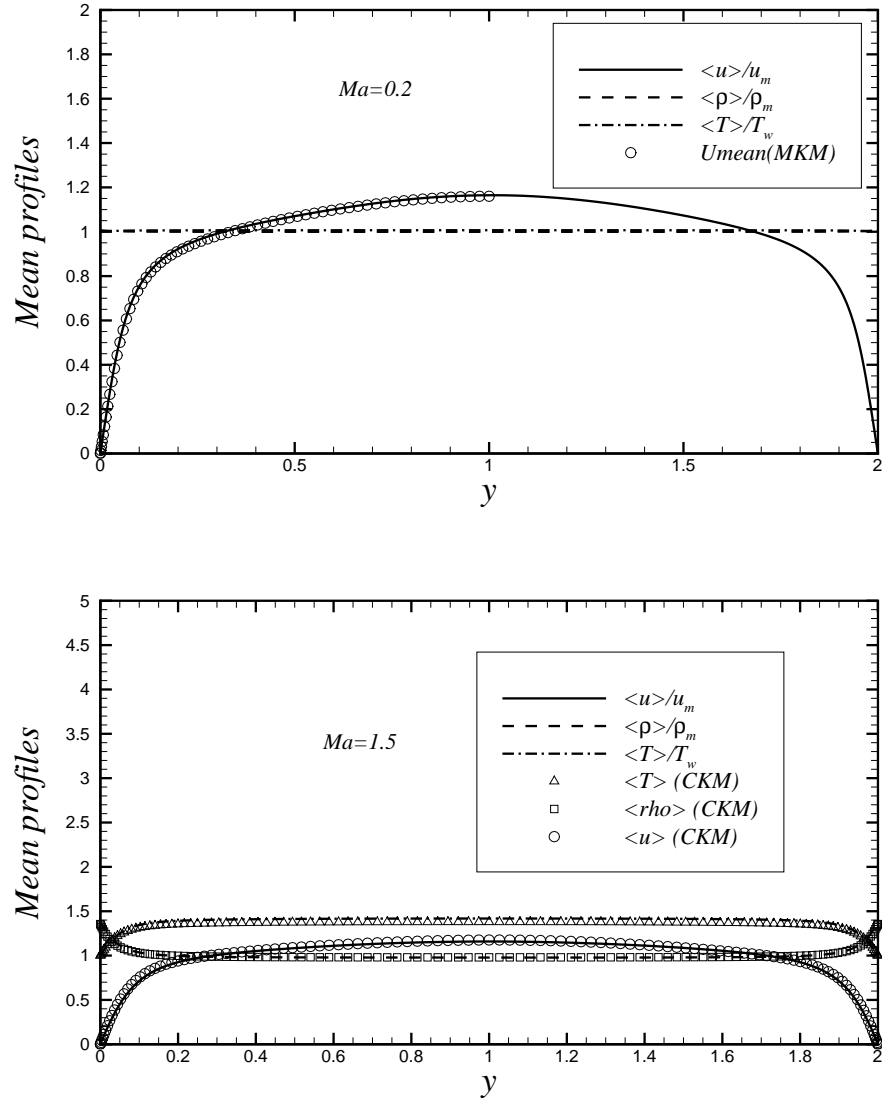


Figure 3.9: Top: Mean streamwise velocity, density and temperature profiles for $Ma=0.2$ versus incompressible case MKM (Moser *et al.*, 1999) in global coordinates ; Bottom: Mean streamwise velocity, density and temperature profiles for $Ma=1.5$ versus the case CKM (Coleman *et al.*, 1995) in global coordinates.

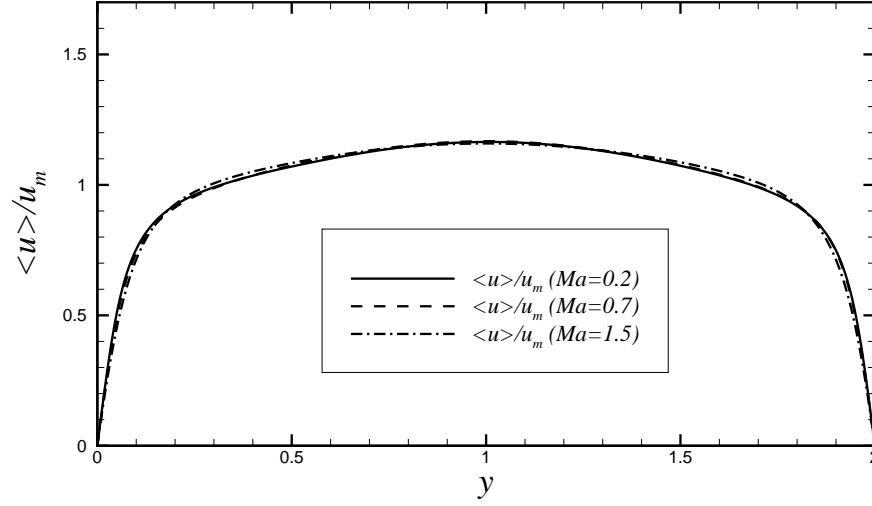


Figure 3.10: Mean streamwise velocity profiles for the cases Ma02, Ma07, and Ma15 in global coordinates.

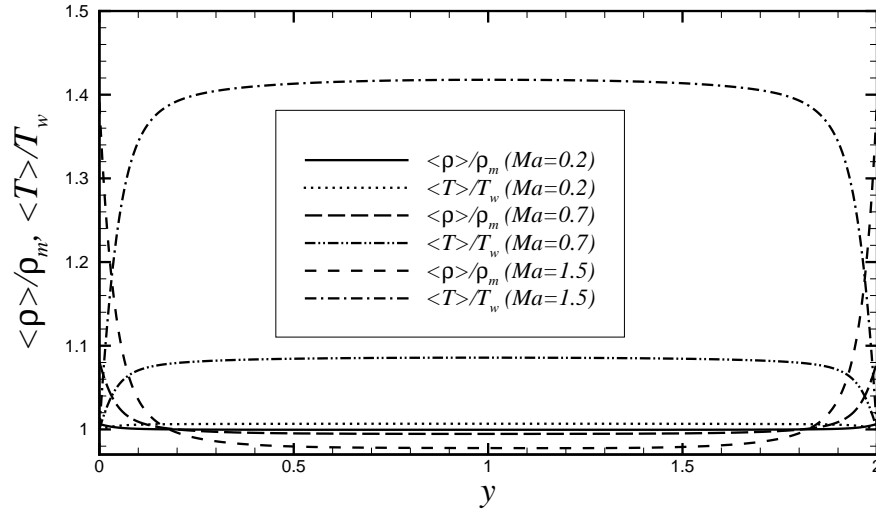


Figure 3.11: Mean density $\langle \rho \rangle$, normalized by bulk density (ρ_m), and temperature $\langle T \rangle$, normalized by wall temperature (T_w) for the cases Ma02, Ma07, and Ma15 in global coordinates.

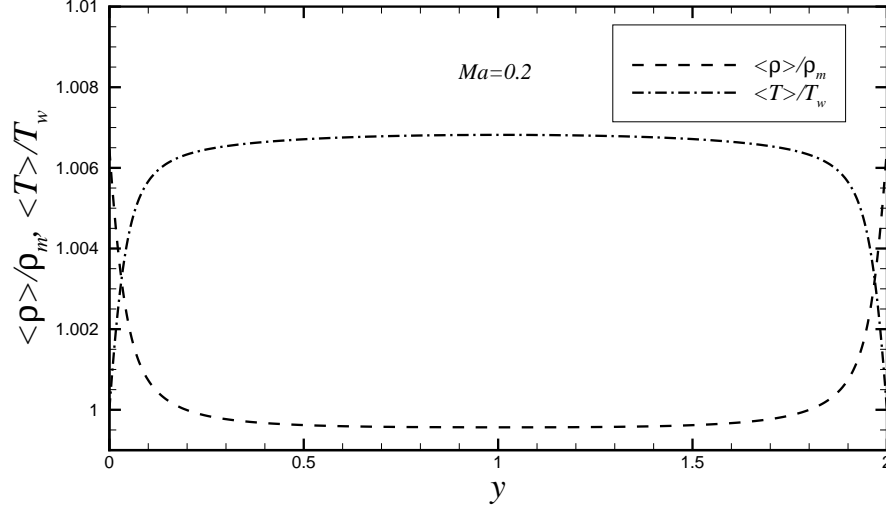


Figure 3.12: Mean density $\langle \rho \rangle$, normalized by bulk density (ρ_m), and temperature $\langle T \rangle$, normalized by wall temperature (T_w) for the case Ma02 in global coordinates.

for the influence of density variation:

$$\langle u \rangle_{VD}^+ = \int_0^{\langle u \rangle^+} \left(\frac{\langle \rho \rangle}{\rho_w} \right)^{1/2} d\langle u \rangle^+ \quad (3.18)$$

where ρ_w denotes the mean density at the wall. The $\langle u \rangle_{VD}^+$ supposedly satisfies the incompressible log law (Bradshaw, 1977):

$$\langle u \rangle_{VD}^+ = \frac{1}{\kappa} \ln y^+ + B \quad (3.19)$$

It can be seen from figure (3.13) that the Van Driest transformation of the mean velocity profile for the case Ma02 collapses on the mean velocity profile as changes in the mean density are negligible. The agreement between the case Ma02 and the incompressible case MKM is also satisfactory. However, both cases do not collapse onto the log law, which is due to the low Reynolds number effect, as discussed in Moser *et al.* (1999).

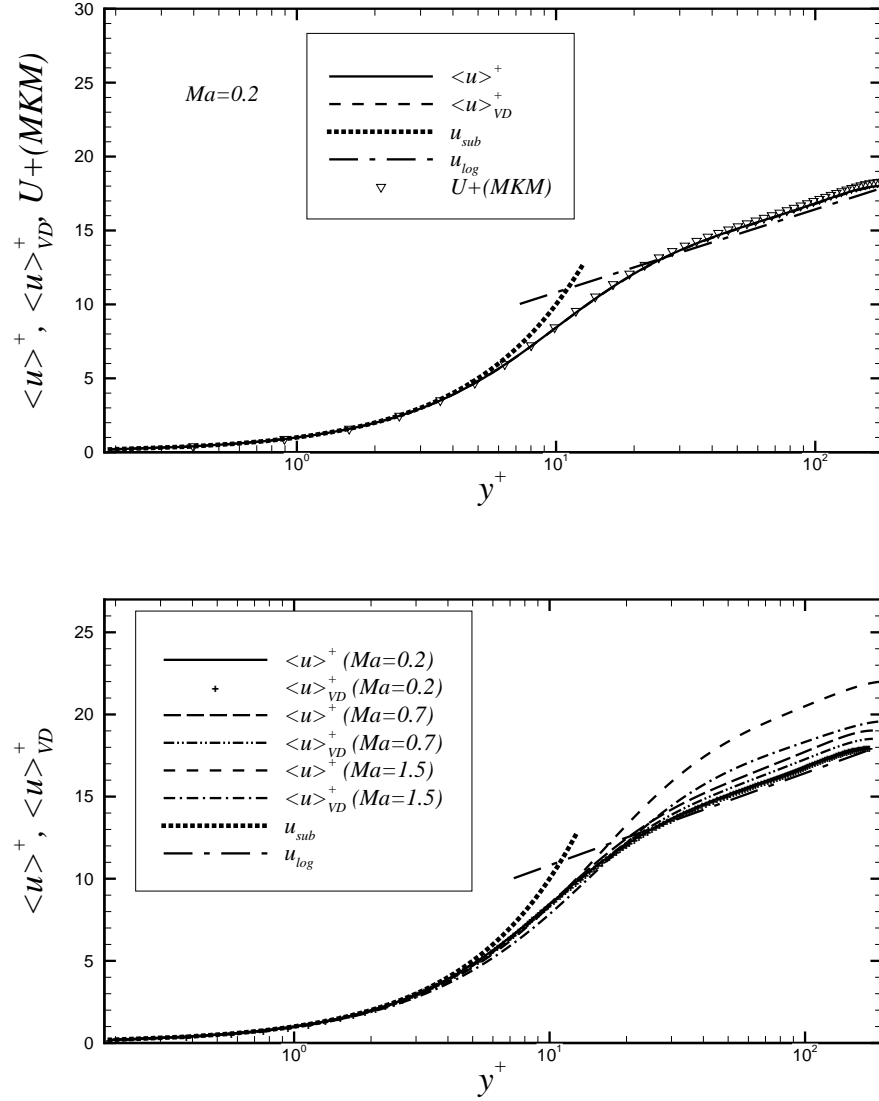


Figure 3.13: Top: Mean streamwise velocity normalized by friction velocity and its Van Driest transformation ($\langle u \rangle_{VD}^+$) for the case $Ma=0.2$ versus the incompressible case MKM and the law of the wall: $u_{sub} = y^+$, $u_{log} = 1/0.41 \ln(y^+) + 5.2$ in wall coordinates; Bottom: Mean streamwise velocity profiles and their Van Driest transformations for all three cases versus the law of the wall.

The bottom plot in figure 3.13 indicates that the velocity profile departs from the log law as the Mach number increases. However, there is a good fit in the viscous sublayer and buffer layer. The Van Driest transformation of the velocity profiles of compressible cases Ma07 and Ma15 causes the profiles to get closer to the incompressible log-law, but at the same time the velocity profile departs the incompressible profile in the buffer layer region.

Besides the traditional log-law for the intermediate region of turbulent wall-bounded flows and boundary layers, a power law:

$$u^+ = a(y^+)^b \quad (3.20)$$

was proposed by some researchers such as George & Castillo (1997) and Barenblatt, Chorin & Prostokishin (1997). Barenblatt and coworkers claimed a power law for the intermediate region of both boundary layer and wall-bounded flows; however, George and coworkers suggested that a power law was only applicable for boundary layers and the log law should be used for wall-bounded flows like channel and pipe flows (Wosnik *et al.*, 2000; Moser *et al.*, 1999). The scientific discussion arising from new observations from pipe, channel and boundary layer flows, reinforce the uncertainty as to what best describes these flows (Monty *et al.*, 2009).

Two quantities are often used to compare the performance of power law and log law to decide which one is more suitable for the scaling. They are defined as follows (Moser *et al.*, 1999):

$$\beta = \frac{y^+}{u^+} \frac{du^+}{dy^+} \quad (3.21)$$

$$\gamma = y^+ \frac{du^+}{dy^+} \quad (3.22)$$

β is supposed to be a constant (that is, b in eq. 3.20) in the region where a power law applies. γ should be $1/\kappa$ in the region where log law applies. β and γ for the current three cases Ma02, Ma07, and Ma15 are shown in figure (3.14). It can be seen that the power law displays a more consistent variation with y^+ than the log-law, as well as greater constancy between, say, $50 < y^+ < 150$. Moser *et al.* (1999) performed a similar study for the scaling of mean velocities with Reynolds number and found that neither the power law nor the log-law was obeyed exactly although β increased more slowly with y^+ than γ for the high Reynolds number cases. Similarly, it shows that the power law seems to be better than the log-law for the scaling of mean streamwise velocity with Mach number for the current cases.

Figure 3.15 presents the local Mach number (Ma_y):

$$Ma_y = \frac{\langle u(y) \rangle}{\langle a(y) \rangle} \quad (3.23)$$

where $\langle a(y) \rangle$ is the local mean sound speed and $\langle a(y) \rangle = \sqrt{\gamma R \langle T(y) \rangle}$. The sonic line ($Ma_y = 1$) is located at a distance of $y = 0.115$ from the wall, which exactly matches the CKM case (Coleman *et al.*, 1995).

The mean pressure nondimensionalized by the wall pressure for all three cases is shown in figure (3.16). It shows that the position of the minimum pressure shifts from $y \approx 0.3$ for the case Ma02 to $y \approx 0.4$ for the case Ma15, which is the same as the shift of positions of the maximum root-mean-square wall-normal velocity fluctuations, as will be shown in the next section. The value of the minimum pressure decreases with increasing Mach number.

The mean viscosity nondimensionalized by the viscosity at the wall is shown in figure (3.17). The difference between mean viscosity at the centre line and at the wall increases with increase of Mach number. It shares a similar trend with the mean

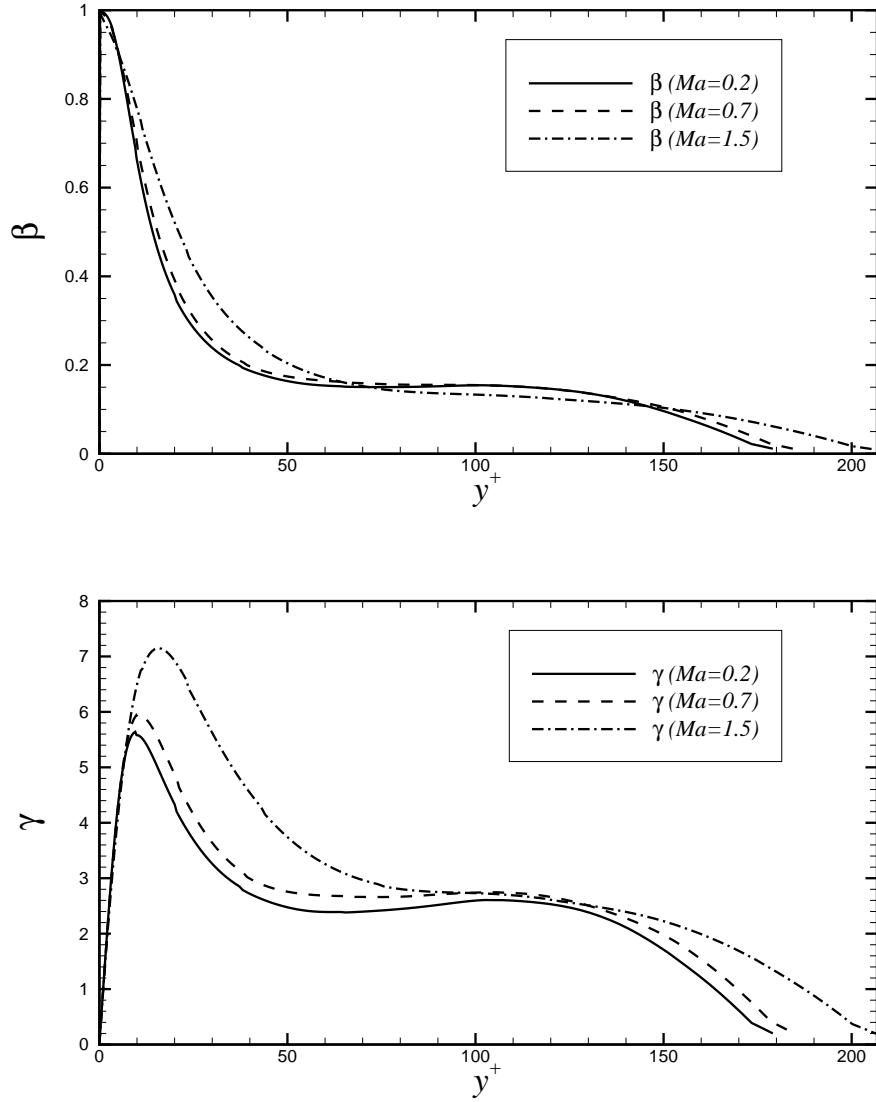


Figure 3.14: Top: A power law quantity (β) for the current three cases Ma02, Ma07, and Ma15 in wall coordinates; Bottom: A log law quantity (γ) for the current three cases Ma02, Ma07, and Ma15 in wall coordinates.

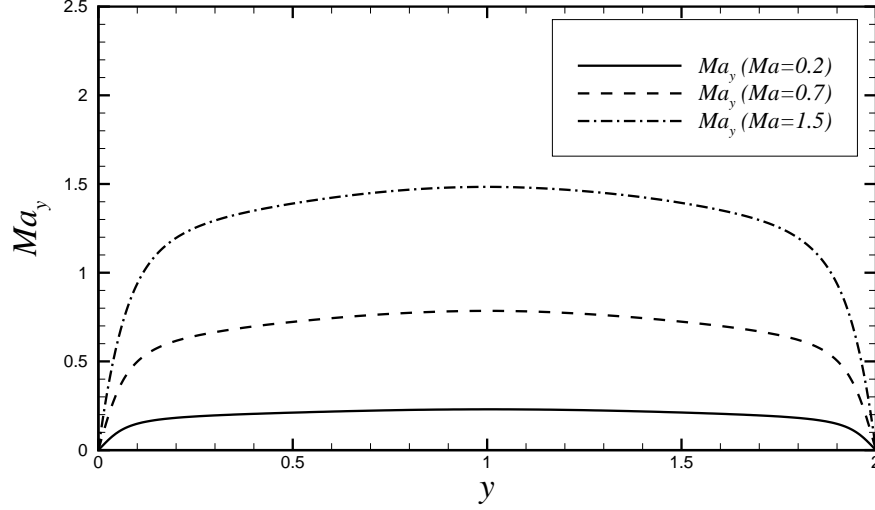


Figure 3.15: Local Mach number $Ma_y = \frac{u(y)}{a(y)}$ for the cases Ma02, Ma07, and Ma15

temperature profile, but the magnitude of the relative viscosity at the centre line is smaller.

3.5 Second-order statistics

The comparison of root-mean-square (RMS) velocity fluctuations normalized by the friction velocity between the case Ma02 and the incompressible case MKM (Moser *et al.*, 1999), and between the case Ma15 and the compressible case CKM (Coleman *et al.*, 1995), is shown in figure (3.18). The RMS profiles for the case Ma02 match almost perfectly with the incompressible case MKM in the top figure. The RMS profiles for the Ma15 case match well with the CKM case in the bottom figure except for a slight difference in the region around the peak values, which could be caused by the difference in parameters between the two cases, shown in the table (3.1).

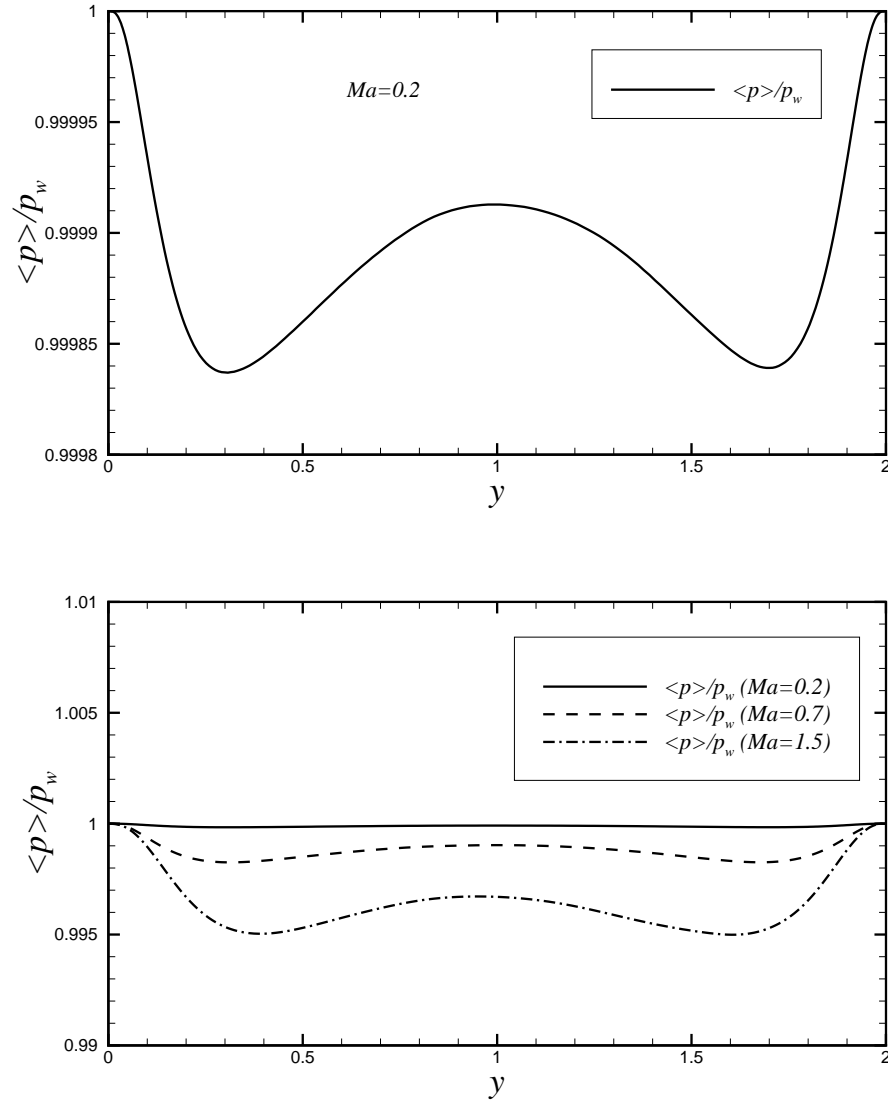


Figure 3.16: Top: Mean pressure profile for the case Ma02; Bottom: Mean pressure profile for the cases Ma02, Ma07, and Ma15. Note the scale difference between the top and the bottom figures

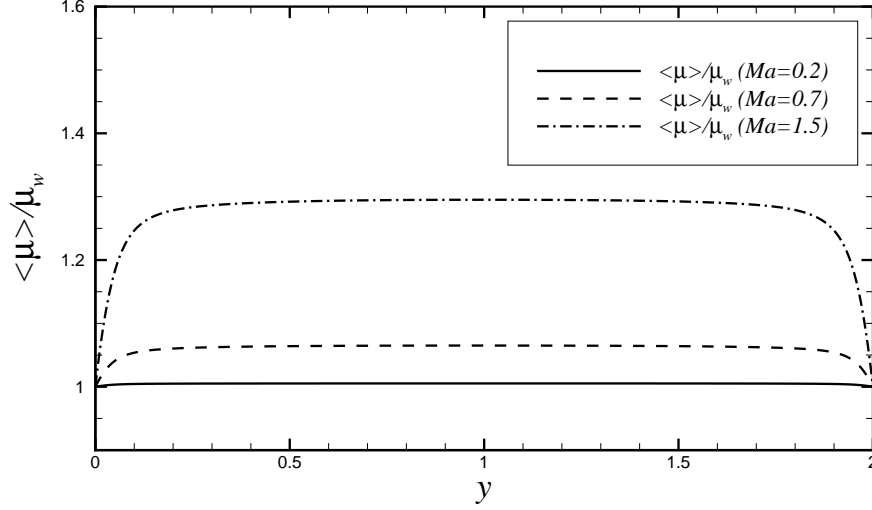


Figure 3.17: Mean viscosity profile normalized by the viscosity at wall ($\langle \mu \rangle / \mu_w$) for the cases Ma02, Ma07, and Ma15

The RMS velocity fluctuations normalized by the wall variables (velocity scale u_τ and length scale ν/u_τ) and the global variables (velocity scale u_m and length scale h), for all three cases Ma02, Ma07, and Ma15 are presented on figure (3.19), so as to study the influence of Mach numbers on turbulence scaling. The top figure, which uses wall variables for scaling, shows that the maximum value of RMS streamwise velocity fluctuation is increased and its location is shifted away from the wall, from $y^+ \approx 14$ at Ma=0.2 to $y^+ \approx 21$ at Ma=1.5. Similar trends are observed for the RMS wall-normal and spanwise velocity fluctuations. The congruence of the streamwise velocity fluctuations for the three cases is good at region $y^+ < 10$. However, no such region is found for spanwise and wall-normal velocity fluctuations. The outer scaling in the bottom figure shows a good collapse in the region around $y > 0.5$ for all components of RMS velocity fluctuations. The shift of the position of the maximum RMS wall-normal velocity fluctuation is similar to the shift of the position of the

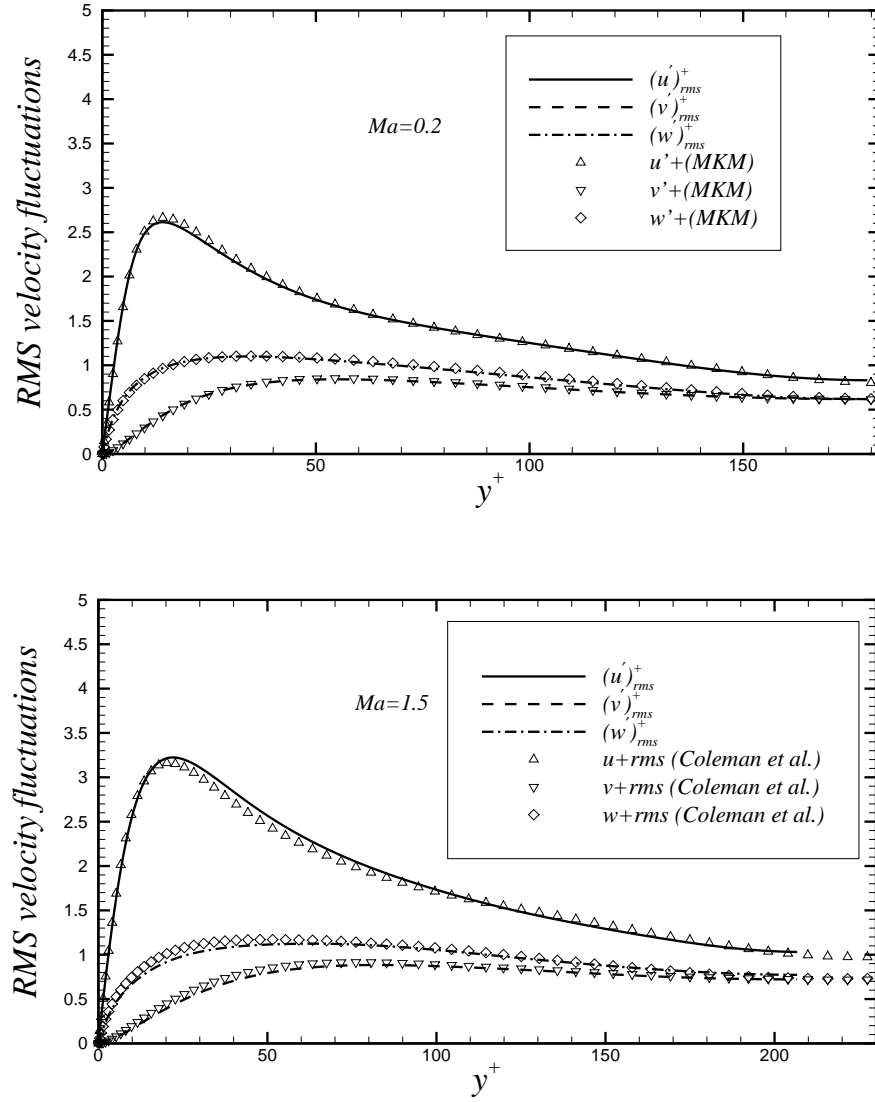


Figure 3.18: Top: RMS velocity fluctuations normalized by the friction velocity for the case $Ma=0.2$ in wall coordinates; Bottom: RMS velocity fluctuations normalized by the friction velocity for the case $Ma=1.5$ in wall coordinates.

minimum pressure, as indicated in the last section. This is due to the balance of the mean forces in the wall-normal direction that relates mean wall-normal pressure gradient and wall-normal gradient of RMS wall-normal velocity fluctuation, see Pope (2000).

The current cases consider similar Reynolds numbers but different Mach numbers and, as will be shown later, the Mach number does have an effect on large-scale motions near the wall. It is possible that this effect causes an inner scaling dependence on Mach numbers in the near-wall region, which in some sense agrees with Morrison's arguments about the influence of large scale motions (Morrison *et al.*, 2004; Morrison, 2007).

RMS density and temperature fluctuations normalized by local mean density $\langle \rho \rangle$ and local mean temperature $\langle T \rangle$ respectively for all three cases Ma02 Ma07 and Ma15 are illustrated in figure 3.20 (top) in wall units. RMS density and temperature fluctuations share a similar trend, including the location of the maximum $y^+ \approx 10$. Since the maximum turbulence kinetic energy production usually occurs at $y^+ \approx 15$, which can also be seen in the turbulence kinetic energy budget section, see section (3.7). It is interesting to see that the Prandtl number ($Pr = 0.72$) corresponds approximately to the ratio of this two values. There is a slight shift of the maximum position with increase of Mach number. The shift is not as significant as RMS velocity fluctuations. However, the maximum value of RMS density and temperature increases much more significantly with increasing Mach number.

Figure 3.20 (bottom) displays the RMS density and temperature fluctuations normalized by the mean bulk density ρ_m and the mean bulk velocity square over specific heat at constant volume U_m^2/c_v respectively scaled in global coordinates. The results

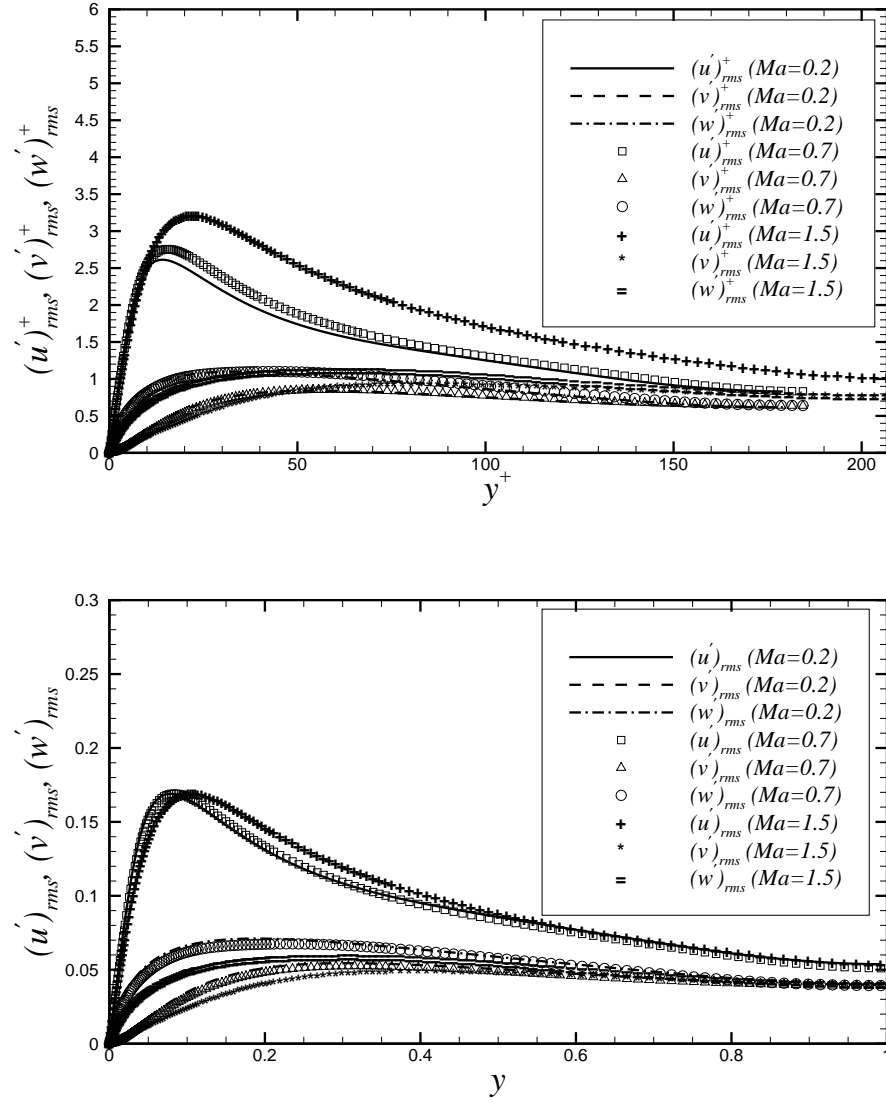


Figure 3.19: Top: RMS velocity fluctuations normalized by the friction velocity (u_τ) in wall coordinates; bottom figure: RMS velocity fluctuations normalized by the mean bulk velocity (U_m) in global coordinates

show a better collapse in the region $y \geq 0.5$ than the top figure.

The RMS vorticity fluctuations normalized by the mean shear at the wall τ_w/μ_w are given in figure (3.21) in wall coordinates. The collapse of the RMS vorticity fluctuations on the incompressible case MKM is good. However, there is a slight difference in collapse among the three components. The collapse of wall-parallel components of RMS vorticity fluctuations $(\omega_x)_{rms}$ (streamwise) and $(\omega_z)_{rms}$ (spanwise) is a little better than the collapse of RMS wall-normal vorticity fluctuation $(\omega_y)_{rms}$, in the region around $y^+ \approx 25$, although all three components of RMS vorticity fluctuations for the case Ma02 are slightly smaller than the case MKM.

Among three components of RMS vorticity fluctuations, the wall-normal component behaves differently from the other two wall-parallel components in many situations. For example, it is the only one that is independent of Reynolds number when scaled using wall variables for incompressible channel flows (Antonia & Kim, 1994; Moser *et al.*, 1999). However, the inner scaling of the RMS wall-normal and total vorticity fluctuations become smaller in the near wall region with increase of Mach number, as shown in figure 19 of Coleman *et al.* (1995). The difference in the Mach numbers of the current case ($Ma = 0.2$) and the case MKM ($Ma = 0$) is a possible reason for the slight deviation between the two profiles.

Three components of RMS vorticity fluctuations for three cases Ma02, Ma07, and Ma15 normalized by τ_w/μ_w and $\frac{U_m}{h}$ are compared in figure (3.22) in wall (top) and global (bottom) coordinates respectively. The top figure shows that $(\omega_x)_{rms}$ and $(\omega_z)_{rms}$ in the near wall region $y^+ < 30$ decreases with increase of Mach number. The local minimum of $(\omega_x)_{rms}$ close to the wall changes from $y^+ \approx 5$ for Ma=0.2 to $y^+ \approx 7$ for Ma=1.5. The local maximum of $(\omega_x)_{rms}$ shifts from $y^+ \approx 20$ for Ma=0.2

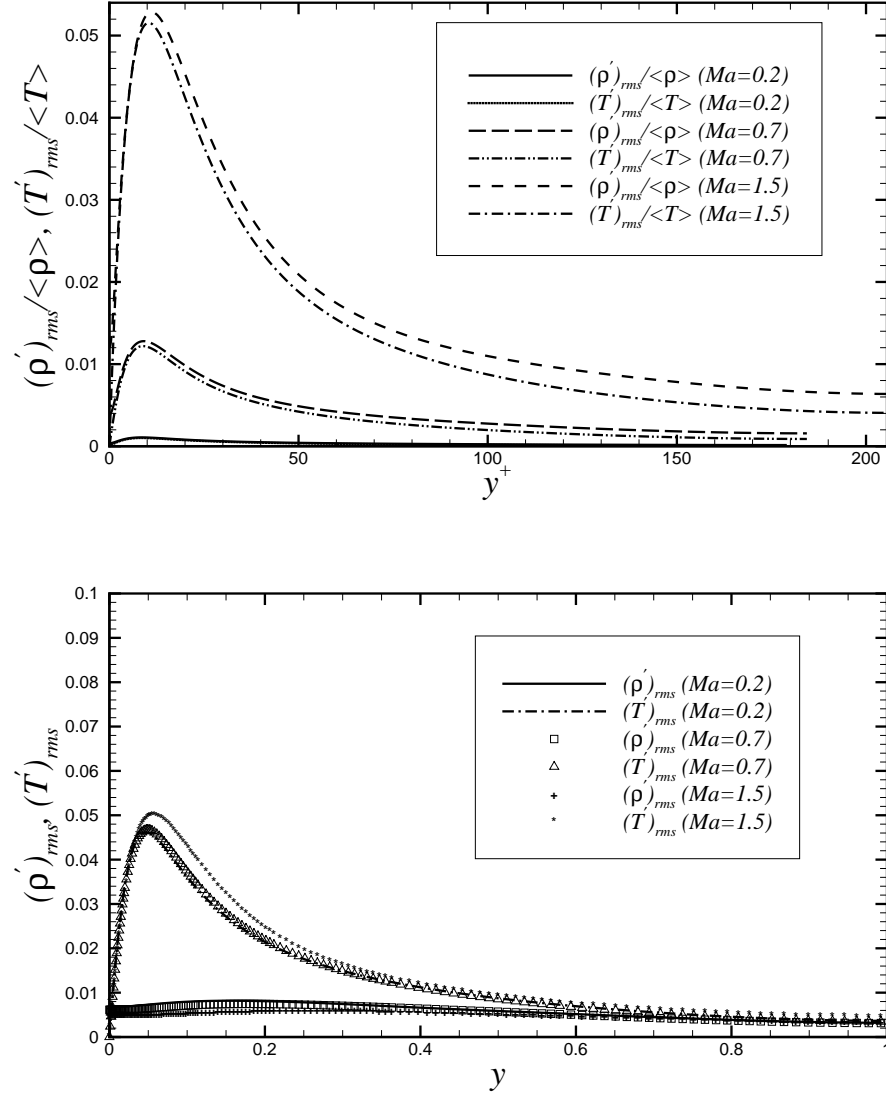


Figure 3.20: Top: RMS density and temperature fluctuations normalized by local mean density $\langle\rho\rangle$ and local mean temperature $\langle T\rangle$ respectively in wall coordinates; Bottom: RMS density and temperature fluctuations normalized by the mean bulk density ρ_m and the mean bulk velocity square over specific heat at constant volume U_m^2/c_v respectively in global coordinates

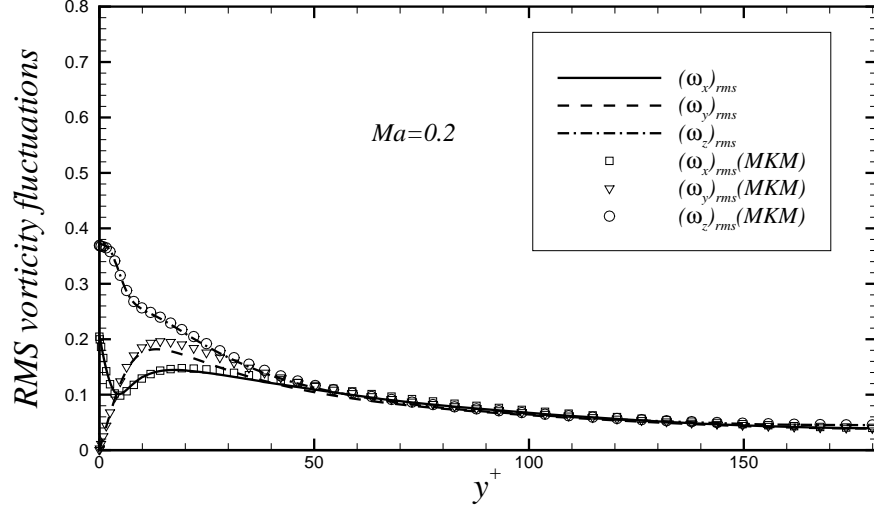


Figure 3.21: RMS vorticity fluctuations normalized by the mean shear at the wall τ_w/μ_w for $Ma=0.2$ versus the incompressible case MKM in wall coordinates.

to $y^+ \approx 36$ for $Ma=1.5$. As the local maximum of $(\omega_x)_{rms}$ denotes the averaged centre of the streamwise vortices and local minimum correspond to the averaged edge of the vortex (Moser & Moin, 1984; Kim *et al.*, 1987), the figure (3.22) indicates that the averaged streamwise eddy size increases with increase of Mach number, but its strength decreases with increasing Mach number. In other words, near-wall large-scale motions are affected by Mach number. It is interesting to note that all components roughly collapse into one line in the region $y^+ > 80$, which suggests that the influence of Mach numbers is almost negligible in this region. A similar trend can be observed in the bottom figure.

The RMS pressure fluctuation normalized by the wall shear stress $\tau_w = \rho_w u_\tau^2$ are shown in figure (3.23) in wall coordinates. It is a comparison between $Ma=0.2$ case and the case MKM's incompressible result. The general collapse is good except for a small deviation in the region close to the wall. This quantity is affected significantly

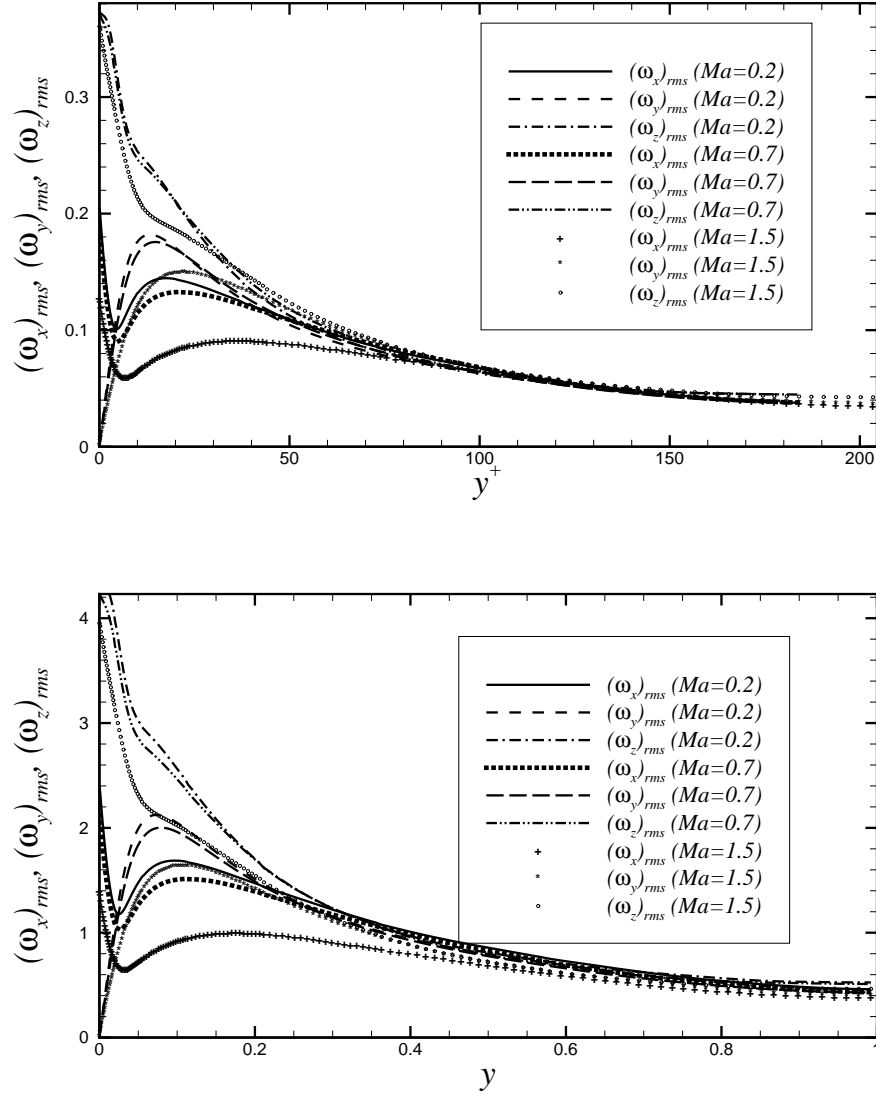


Figure 3.22: Top: RMS vorticity fluctuations normalized by the mean shear at the wall τ_w/μ_w for Ma02, Ma07, and Ma15 in wall coordinates; Bottom: RMS vorticity fluctuations normalized by the U_m/h for Ma02, Ma07, and Ma15 in global coordinates.

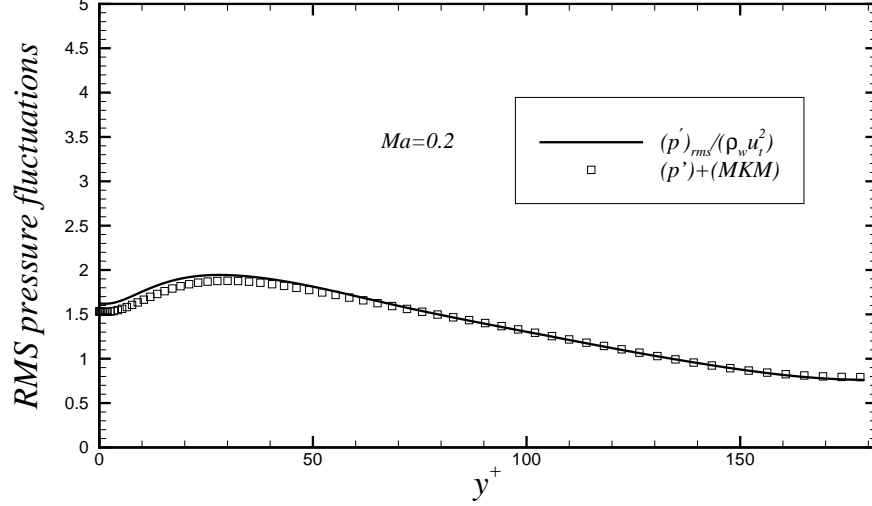


Figure 3.23: Top: RMS pressure fluctuations normalized by the wall shear stress $\rho_w u_\tau^2$ versus the incompressible case MKM.

by the quality of the statistics, which will be discussed in the next section.

For all three cases Ma02, Ma07, and Ma15, RMS pressure fluctuations normalized by $\rho_w u_\tau^2$ and $\rho_m U_m^2$ in wall and global coordinates respectively are presented in figure (3.24). The top figure shows that, with increase of Mach number, the RMS pressure fluctuations decrease in the region close to the wall, but increase in the region close to the centre of the channel, and the position of the maximum shifts away from the wall. The difference between pressure fluctuations in different regions becomes smaller with increasing Mach number. The scaling in the bottom figure indicates Mach number dependence in all regions.

The RMS pressure gradients fluctuations normalized by $\rho_m U_m^2/h$ for all three cases are shown in figures (3.25). The figure indicates that pressure gradient fluctuations decrease with increase of Mach number. The maximum value of the fluctuations is observed to happen within the region $y \in [0.1, 0.2]$. Among the values of the

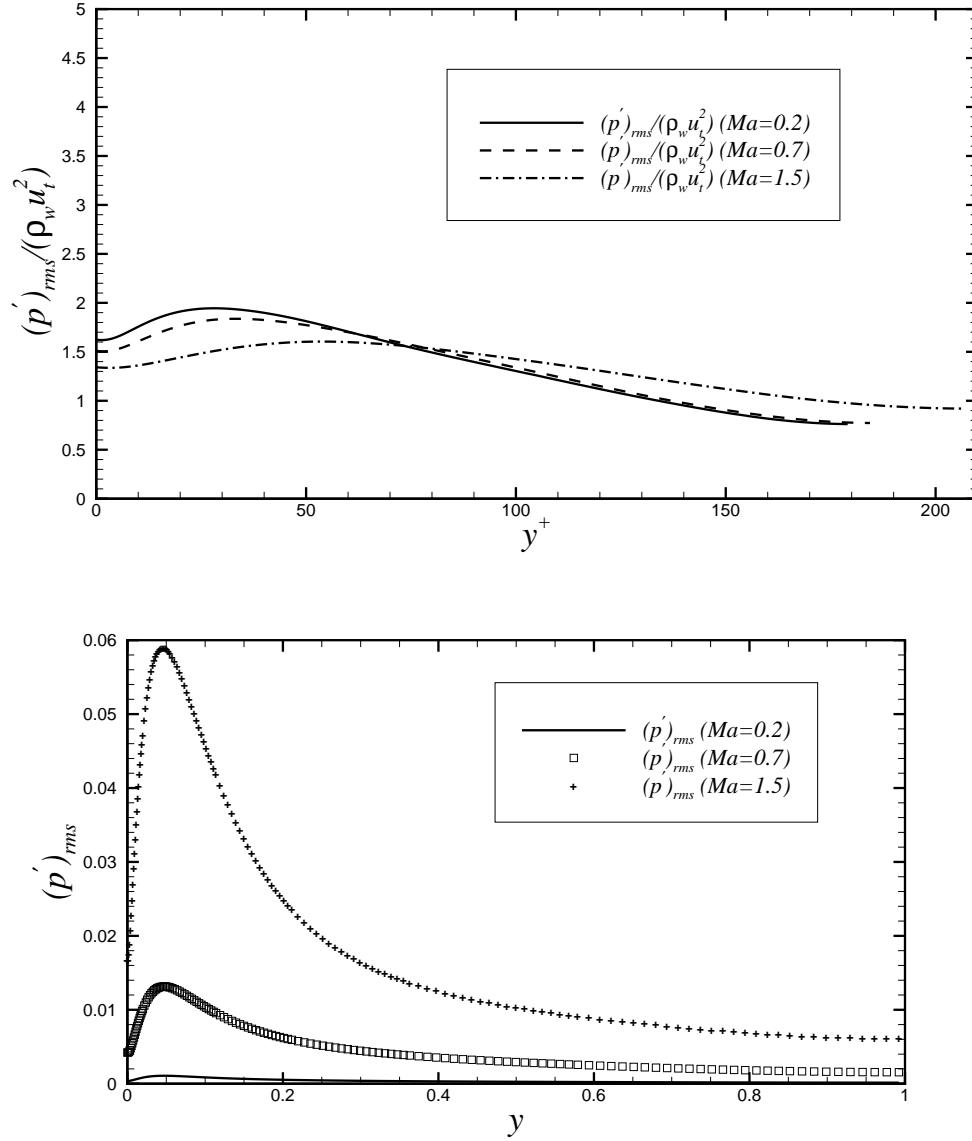


Figure 3.24: Top: RMS pressure fluctuations normalized by the wall shear stress $\rho_w u_\tau^2$ for Ma02, Ma07, and Ma15 in wall coordinates; Bottom: RMS pressure fluctuations normalized by the mean bulk quantity $\rho_m U_m^2$ for Ma02, Ma07, and Ma15 in global coordinates.

three gradients of pressure fluctuation on the wall, the spanwise pressure gradient fluctuation $(dp/dz)_{rms}$ is largest and the wall-normal pressure gradient fluctuation $(dp/dy)_{rms}$ is smallest. $(dp/dz)_{rms}$ is larger than $(dp/dx)_{rms}$ in the near-wall region, although both streamwise and spanwise directions are assumed homogenous.

Decomposition of the shear stresses and several different forms of turbulence stresses ($\langle \rho \rangle \langle u'v' \rangle$, $\langle \rho u'v' \rangle$, $\langle \rho \rangle \langle u''v'' \rangle$, where " denotes fluctuations based on Favre average, see Appendix A for details) normalized by the wall shear stress τ_w for the cases Ma02, Ma07, and Ma15 are shown in figure (3.26). Turbulence stresses are given in figure (3.26) and indicate excellent agreement with MKM. Different forms of turbulence stresses display little difference for the cases Ma02 and Ma07. The profile of $\langle \rho u'v' \rangle$ is slightly higher than $\langle \rho \rangle \langle u'v' \rangle$ in the region where the maximum turbulence stress is located. Almost no difference between $\langle \rho \rangle \langle u'v' \rangle$ and $\langle \rho \rangle \langle u''v'' \rangle$ is observed for the current cases, as one would probably expect, particularly for $Ma < 1$.

The comparison of the turbulence and viscous shear stresses for all three cases is illustrated in figure (3.27) in global coordinates (top) and wall coordinates (bottom) respectively. It can be seen from the top figure that the turbulence stress decrease as Mach number increases, and to the contrary, the viscous stresses increase with Mach number close to the wall. The increase of viscous stress should be due to the increase of dynamic viscosity, which is caused by the increase of temperature in this region as Mach number increases. The bottom figure is a plot of the profiles of the shear stresses in wall coordinates. The increase of turbulence stress with Mach number is limited to the region close to the wall, within approximately $y^+ < 70$. No collapse of turbulence stresses is found.

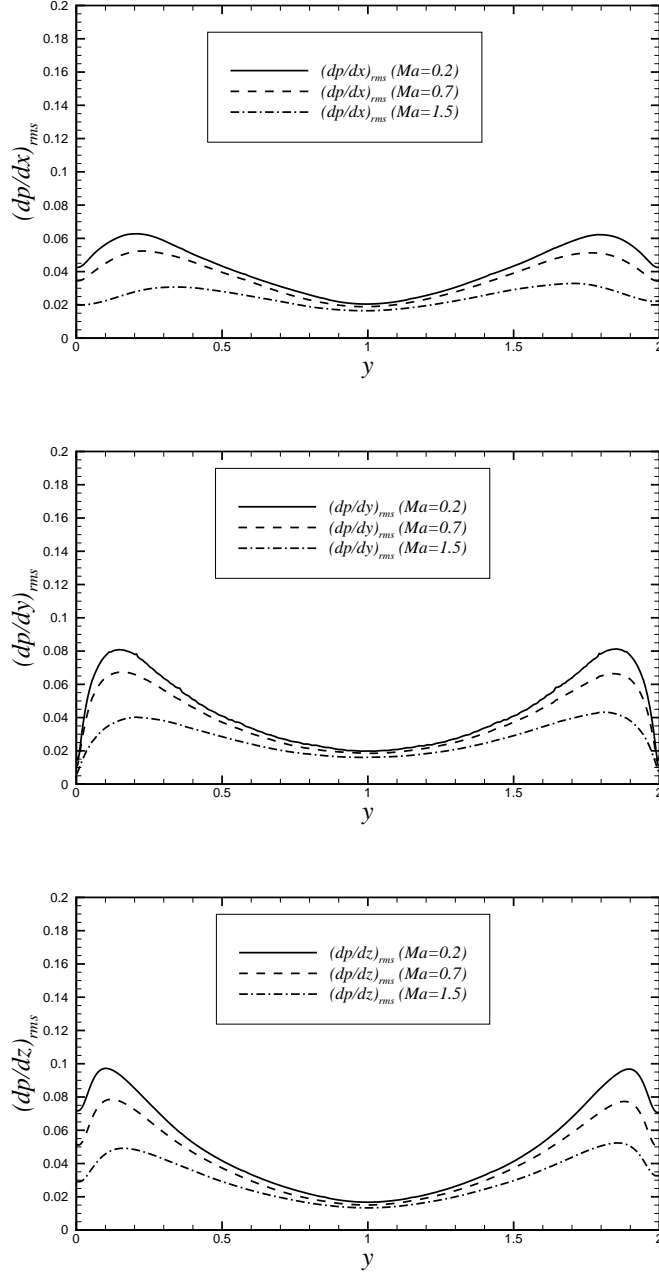


Figure 3.25: RMS streamwise (top), wall-normal (middle) and spanwise (bottom) pressure gradient fluctuations normalized by $\rho_m U_m^2 / h$. Note that d denotes ∂ here, for example, dp/dx means $\partial p / \partial x$.

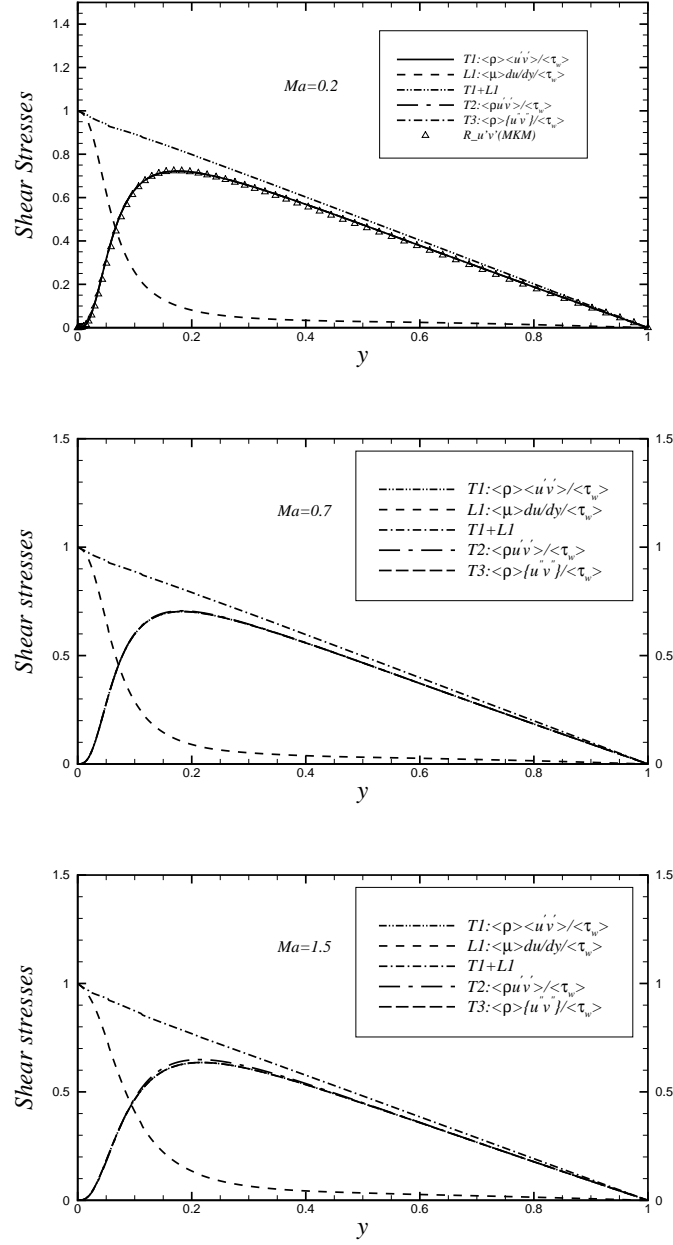


Figure 3.26: Decomposition of shear stresses normalized by the wall shear stress τ_w for the case Ma02 versus the incompressible case MKM (top), the case Ma07 (middle) and the case Ma15 (bottom). $L1$ represents viscous shear stress; $T1, T2, T3$ represent $\langle \rho \rangle \langle u'v' \rangle / \tau_w$, $\langle \rho u'v' \rangle / \tau_w$, $\langle \rho \rangle \langle u''v'' \rangle / \tau_w$ respectively

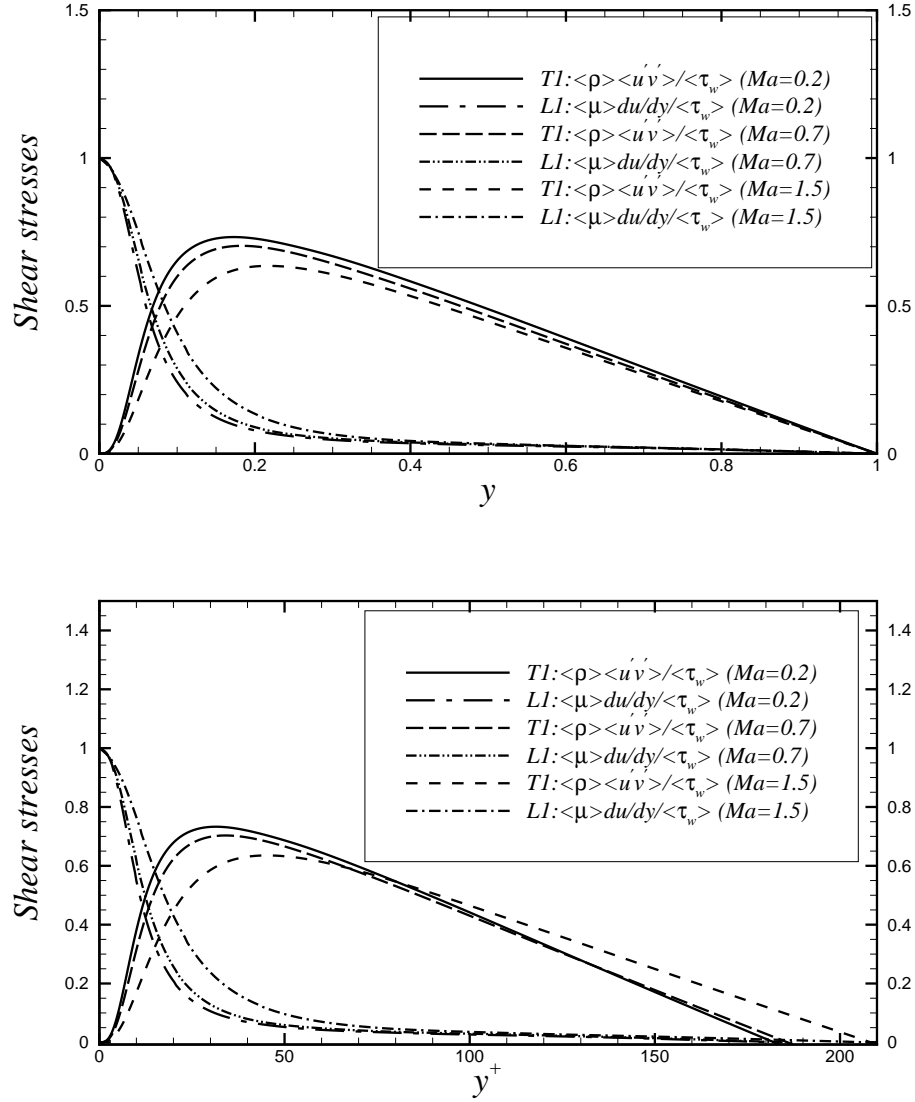


Figure 3.27: Turbulence and viscous shear stresses normalized by the wall shear stress τ_w Shear stresses for all three cases Ma02, Ma07, and Ma15 in global coordinates (top) and wall coordinates (bottom)

3.6 Higher-order statistics

Higher-order statistics considered here are the skewness and kurtosis (flatness) factors. The skewness (S) and flatness (F) factors of, for example, the velocity fluctuation u' , are defined as:

$$S(u') = \frac{\langle (u')^3 \rangle}{\langle u'u' \rangle^{3/2}} = \frac{\langle (u - \langle u \rangle)^3 \rangle}{\langle (u - \langle u \rangle)^2 \rangle^{3/2}} \quad (3.24)$$

$$F(u') = \frac{\langle (u')^4 \rangle}{\langle u'u' \rangle^2} = \frac{\langle (u - \langle u \rangle)^4 \rangle}{\langle (u - \langle u \rangle)^2 \rangle^2} \quad (3.25)$$

where $\langle \rangle$ denotes an average over time t and x, z directions.

Calculation of higher-order statistics usually requires more data than the second-order statistics. As indicated in Kim *et al.* (1987), oscillations and asymmetry in the skewness and flatness profiles suggest that the sample size used for the computation may not be adequate, and the skewness of spanwise velocity $S(w')$ should be zero due to the reflection symmetry of the solutions of Navier-Stokes equations. In other words, the oscillation, symmetry, and $S(w')$ may be used as the indicators of the quality of the statistics.

The skewness factor for velocity and pressure fluctuations for the case Ma02 in wall coordinates, compared with the case MKM, in figure (3.28). It can be seen from figure (3.28) that few oscillations are observed and the skewness of w' is essentially zero for the case Ma02. Although there seems to be a big difference in the sample size used here for the case Ma02 and those of MKM, the collapse of the profiles of $S(u')$ is good for almost the whole region, and $S(v')$ collapses well except for a small region close to the wall ($y^+ < 15$). In other words, compared with $S(v')$, $S(w')$, and

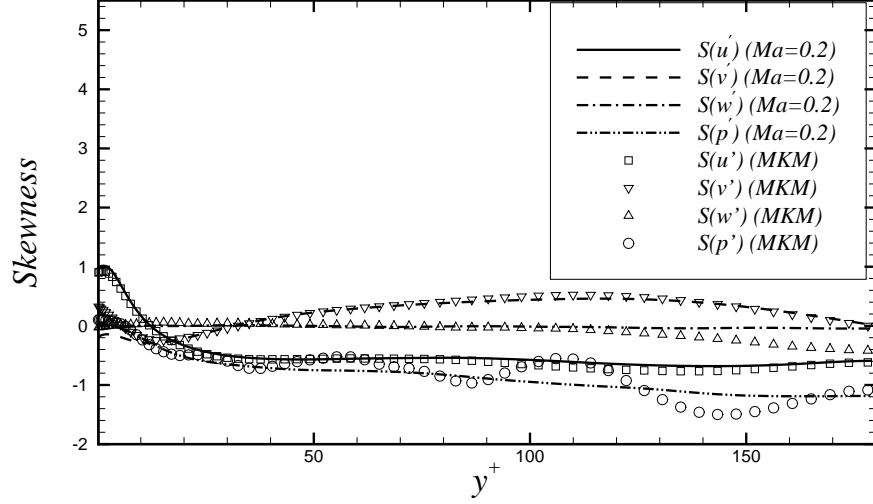


Figure 3.28: Skewness factors of velocity and pressure fluctuations for the case Ma02 in wall coordinates versus the case MKM

$S(p')$, $S(u')$ is less affected by the sample size. The figure also shows that the sample size has a great effect on $S(p')$.

The skewness factors of velocities and pressure fluctuations for the cases Ma02, Ma07 and Ma15 are compared in figure (3.29) including both wall coordinates (top) and global coordinates (bottom). Generally speaking, the influence of Mach number on the profiles is not significant in the current Mach number range ($0.2 < Ma < 1.5$). The bottom figure shows a slightly better collapse. It is interesting to note that the collapse of $S(v')$ agrees very well with those from the case MKM for the region ($y > \approx 0.4$), shown in the bottom figure.

The skewness factors of density and temperature fluctuations for the cases Ma02, Ma07 and Ma15 are given in figure (3.30). The profile of the skewness of temperature $S(T')$ is similar as $S(u')$ but with lower magnitude. This can be explained by the high correlations between velocity and temperature, as will be shown in the next section.

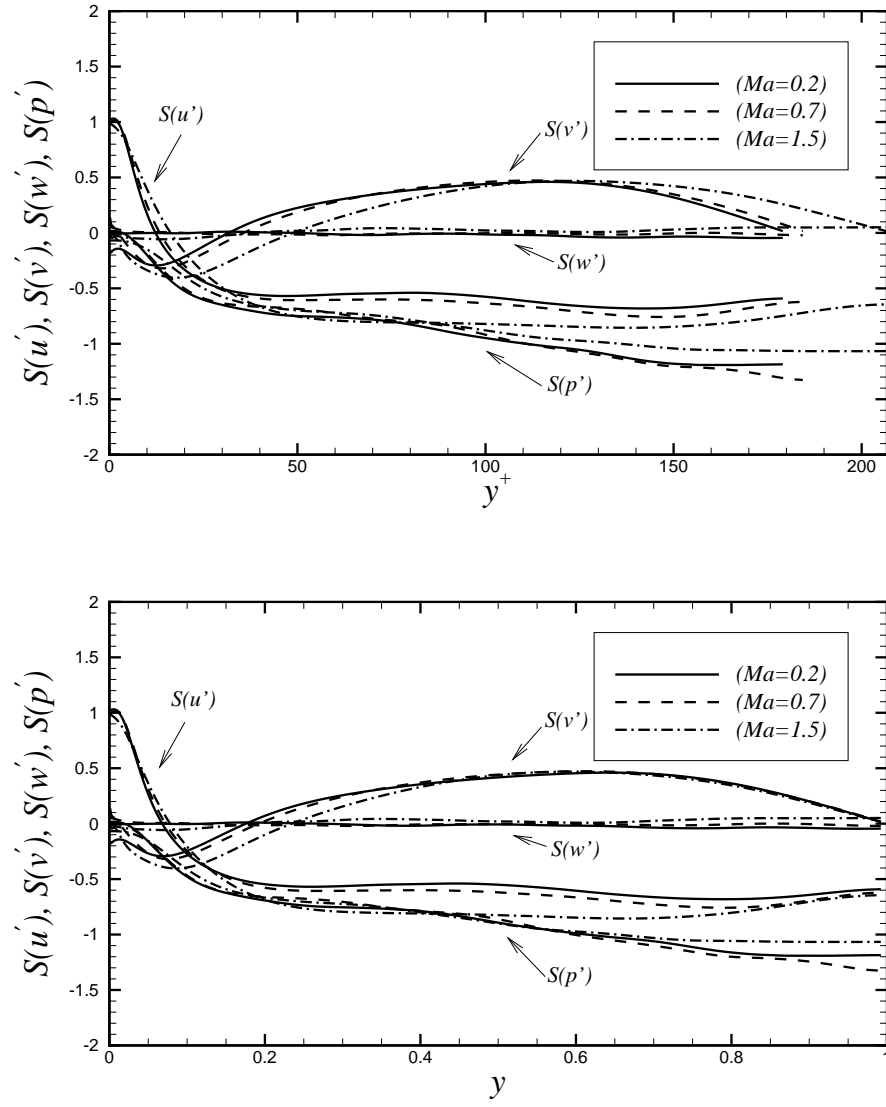


Figure 3.29: Top: Skewness factors of velocity and pressure fluctuations for all three cases in wall coordinates; Bottom: Skewness factors of velocity and pressure fluctuations for all three cases in global coordinates.

The scaling of $S(\rho')$ and $S(T')$ are satisfactory close to the wall, shown in the top figure. It is interesting to note that the location of the local minimum of $S(\rho')$ close to the wall and the local maximum of $S(\rho')$ is similar to the RMS streamwise vorticity fluctuation $(\omega_x)_{rms}$ shown in figure (3.22).

The flatness factors of velocity, pressure fluctuations for the cases Ma02, compared with the case MKM, are presented in figure (3.31). The general agreement is similar to that found for the skewness, figure (3.28). It is shown that flatness factors of velocities collapse onto one flat line at the central region of the channel ($y^+ > 50$). Flatness of pressure $F(p')$ is much larger than velocities in this region, which indicates that pressure fluctuations are more intermittent, so are the flatness of wall-normal velocity fluctuations $F(v')$ close to the wall.

The effect of scaling of the flatness factors of velocity, pressure fluctuations with Mach number is displayed in figure (3.32). It seems that $F(u')$ and $F(p')$ are not affected much by Mach number, whereas the profile of $F(v')$ near the wall for the case Ma15 behaves differently. The $F(v')$ profile for the case Ma15 first increases until $y^+ \approx 2.6$ and then drops suddenly as it moves from the centre of the channel to the wall, an effect also observed by Tamano & Morinishi (2006). They argued that it was due to the low Reynolds number and the compressibility effect. As this phenomenon is not observed for the cases Ma02 and Ma07, it is argued here that it is possibly due to effects of high gradients in the near-wall viscosity, as will be discussed in section (3.9).

The flatness factors of density and temperature fluctuations for the cases Ma02, Ma07, and Ma15 are illustrated in figures (3.33). The flatness of density $F(\rho')$ and temperature $F(T')$ show similar trend. The scaling with Mach number is very good

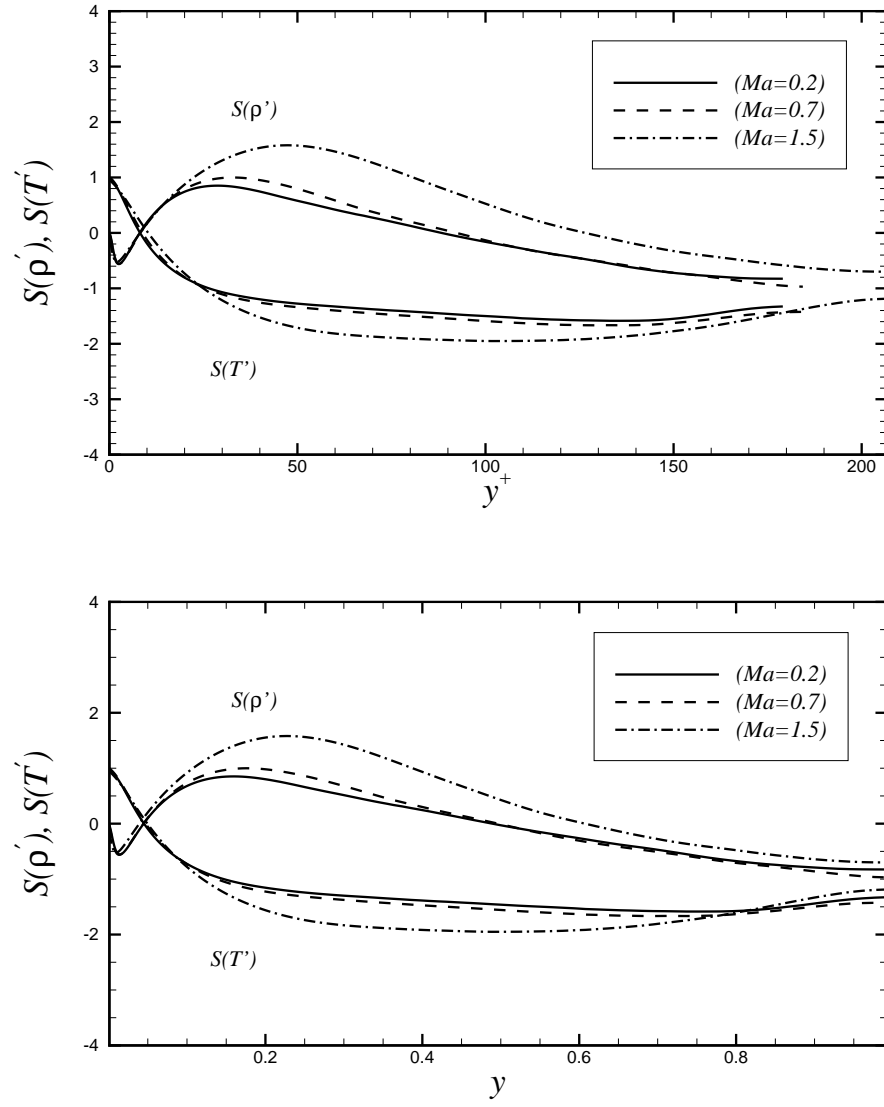


Figure 3.30: Top: Skewness factors of density and temperature fluctuations for all three cases in wall coordinates; Bottom: Skewness factors of density and temperature fluctuations for all three cases in global coordinates.

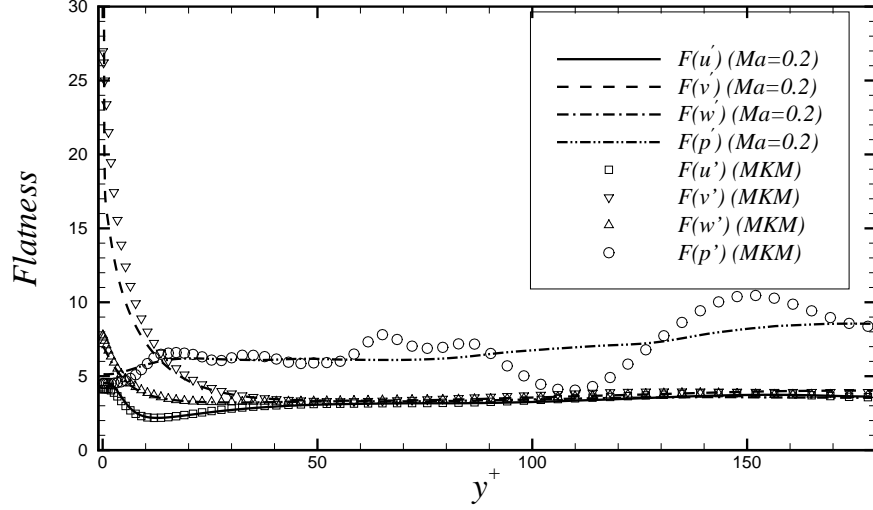


Figure 3.31: Flatness factors of velocity and pressure fluctuations for the case Ma02 in wall coordinates versus the case MKM

close to the wall. The higher value at the central region of channel indicates highly intermittent fluctuations.

3.7 Turbulent kinetic energy budget

The turbulent kinetic energy (TKE, $k = 0.5\langle\rho\rangle\{u_i''u_i''\}$) equation for compressible flows can be written as (Huang *et al.*, 1995):

$$\begin{aligned} \frac{\partial(\frac{1}{2}\langle\rho\rangle\{u_i''u_i''\}\{u_j\})}{\partial x_j} = & -\frac{\partial(\frac{1}{2}\langle\rho\rangle\{u_i''u_i''u_j''\} - \langle u_i'\tau_{ij}' \rangle + \langle u_j'p' \rangle)}{\partial x_j} \\ & -\langle\rho\rangle\{u_i''u_j''\}\frac{\partial\{u_i\}}{\partial x_j} - \langle u_i''\rangle\frac{\partial\langle p\rangle\delta_{ij}}{\partial x_j} + \langle u_i''\rangle\frac{\partial\langle\tau_{ij}\rangle}{\partial x_j} + \langle p'\rangle\frac{\partial u_j'}{\partial x_j} - \langle\tau_{ij}'\rangle\frac{\partial u_i'}{\partial x_j} \end{aligned} \quad (3.26)$$

This form is a little different from the traditional Favre-averaged TKE equation (Lele, 1994; Guarini *et al.*, 2000) as the Favre-averaging process was only used on the convective terms of compressible Navier-Stokes equations. However, this form of

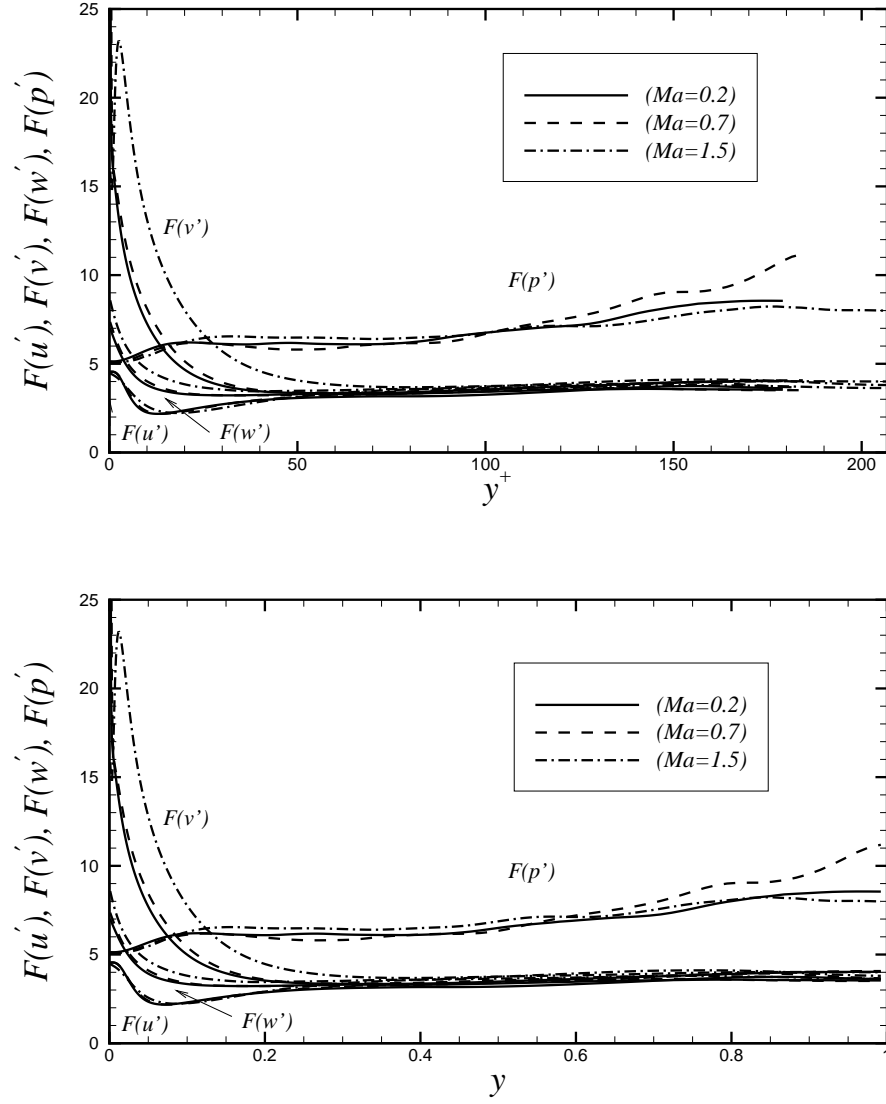


Figure 3.32: Top: Flatness factors of velocity and pressure fluctuations for all three cases in wall coordinates; Bottom: Flatness factors of velocity and pressure fluctuations for all three cases in global coordinates. Note the diminution in $F(v')$ for $y^+ < 3$ for the case $Ma = 1.5$.

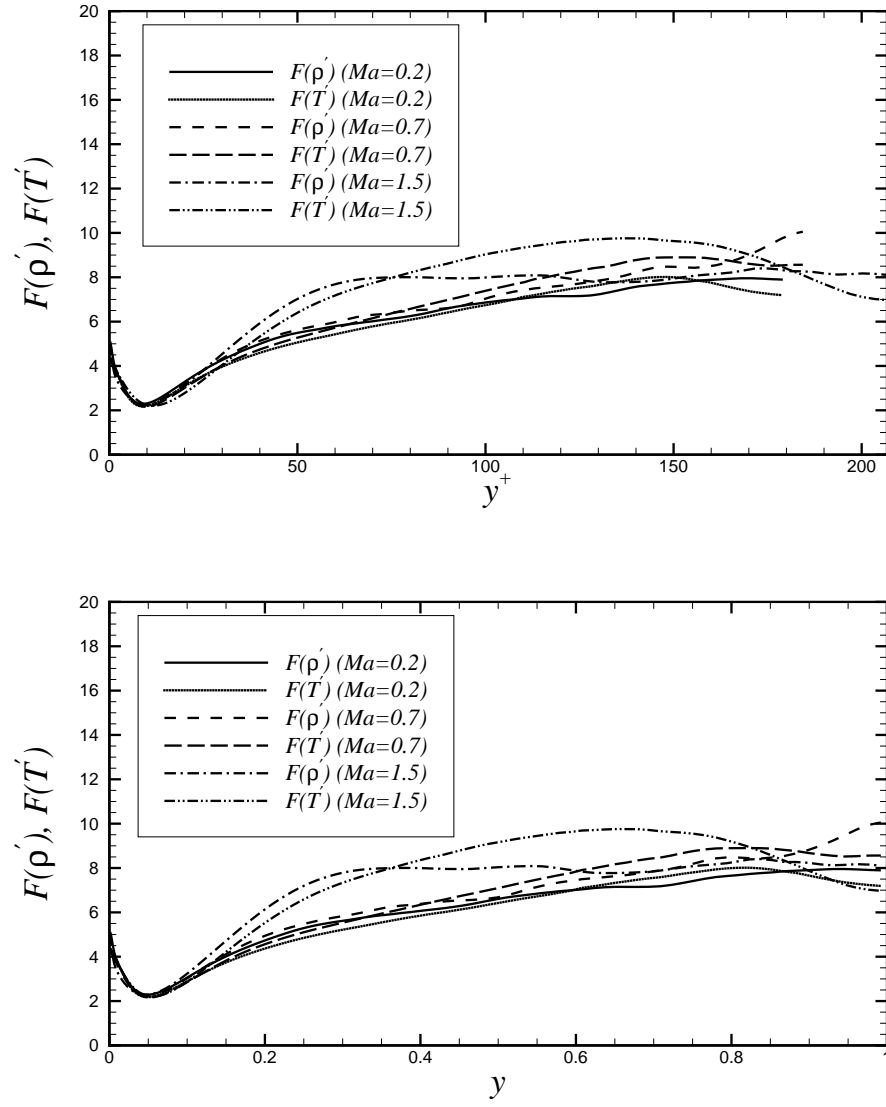


Figure 3.33: Top: Flatness factors of density and temperature fluctuations for all three cases in wall coordinates; Bottom: Flatness factors of density and temperature fluctuations for all three cases in global coordinates.

the TKE equation is equivalent to the traditional TKE form, as the different terms $\partial\langle u'_i \tau'_{ij} \rangle / \partial x_j$, $\partial\langle u'_j p' \rangle / \partial x_j$, $\langle p' \partial u'_j / \partial x_j \rangle$, $\langle \tau'_{ij} \partial u'_i / \partial x_j \rangle$ in equation (3.26) are equal to the respective terms of the traditional form: $\partial\langle u''_i \tau'_{ij} \rangle / \partial x_j$, $\partial\langle u''_j p' \rangle / \partial x_j$, $\langle p' \partial u''_j / \partial x_j \rangle$, $\langle \tau'_{ij} \partial u''_i / \partial x_j \rangle$, as $\langle a' b' \rangle = \langle a' b'' \rangle$.

The streamwise (x_1) and spanwise (x_3) directions may be averaged so that equation (3.26) can be simplified to,

$$\begin{aligned} \frac{\partial \frac{1}{2} \langle \rho \rangle \{u''_i u''_i\} \{u_2\}}{\partial x_2} = & - \frac{\partial (\frac{1}{2} \langle \rho \rangle \{u''_i u''_i u''_2\} - \langle u'_i \tau'_{i2} \rangle + \langle u'_2 p' \rangle)}{\partial x_2} \\ & - \langle \rho \rangle \{u''_i u''_2\} \frac{\partial \{u_i\}}{\partial x_2} - \langle u''_2 \rangle \frac{\partial \langle p \rangle}{\partial x_2} + \langle u''_i \rangle \frac{\partial \langle \tau_{i2} \rangle}{\partial x_2} + \langle p' \frac{\partial u'_j}{\partial x_j} \rangle - \langle \tau'_{ij} \frac{\partial u'_i}{\partial x_j} \rangle \end{aligned} \quad (3.27)$$

The terms in the TKE equation (3.27) are denoted as,

Advection:

$$A_k = \frac{\partial \frac{1}{2} \langle \rho \rangle \{u''_i u''_i\} \{u_2\}}{\partial x_2}; \quad (3.28)$$

Production:

$$P_k = - \langle \rho \rangle \{u''_i u''_2\} \frac{\partial \{u_i\}}{\partial x_2}; \quad (3.29)$$

Diffusion:

$$D_k = - \frac{\partial (\frac{1}{2} \langle \rho \rangle \{u''_i u''_i u''_2\} - \langle u'_i \tau'_{i2} \rangle + \langle u'_2 p' \rangle)}{\partial x_2}; \quad (3.30)$$

Dissipation:

$$\epsilon_k = \langle \tau'_{ij} \frac{\partial u'_i}{\partial x_j} \rangle; \quad (3.31)$$

Compressibility:

$$C_k = -C_{k1} + C_{k2} + C_{k3} \quad (3.32)$$

where $C_{k1} = \langle u''_2 \rangle \partial \langle p \rangle / \partial x_2$, $C_{k2} = \langle u''_i \rangle \partial \langle \tau_{i2} \rangle / \partial x_2$, $C_{k3} = \langle p' \partial u'_j / \partial x_j \rangle$ is the pressure-dilatation correlation term.

TKE budget normalized by wall variables $\tau_w u_\tau / \delta_v$ (viscous length scale $\delta_v = \nu / u_\tau$) for all three cases Ma02, Ma07, and Ma15 is given in the top of the figure (3.34) in wall coordinates. Advection terms should be zero for all cases, which is also shown in figure. The maximum turbulence production decreases with distance from the wall with increase in Mach number. A similar trend is observed for turbulence dissipation and diffusion terms. On the contrary, the absolute value of compressibility terms increase as Mach number increases. However, the influence of compressibility terms is small and mainly contained in the near-wall region. Further discussion of compressibility terms will be dealt with later. It can also be seen that the inner scaling for three cases do not collapse well in the near-wall region.

TKE budget normalized by bulk variables $\rho_m U_m^3 / h$ for all three cases Ma02, Ma07, and Ma15 is shown in the bottom of the figure (3.34) in global coordinates, to compare the performance of outer and inner scaling. The results indicate a better outer scaling: the collapse of the profiles is good in the region ($y/h > 0.2$).

Figure (3.35) provide plots for the three compressibility terms: C_{k1} , C_{k2} , C_{k3} for three cases using both inner and outer scaling as was presented for the term C_k in figure (3.34). It shows that the compressibility term C_k in the TKE equation is mainly affected by the term C_{k2} . The influence of the other two terms C_{k1} and C_{k3} is much smaller. This was also addressed in the work of Morinishi *et al.* (2004). The maximum of the absolute value of the term C_{k2} increases and moves further away from the wall with increasing Mach number. Again, the outer scaling shows a good collapse in the region close to the centre, especially for the term C_{k2} , shown in the bottom figure.

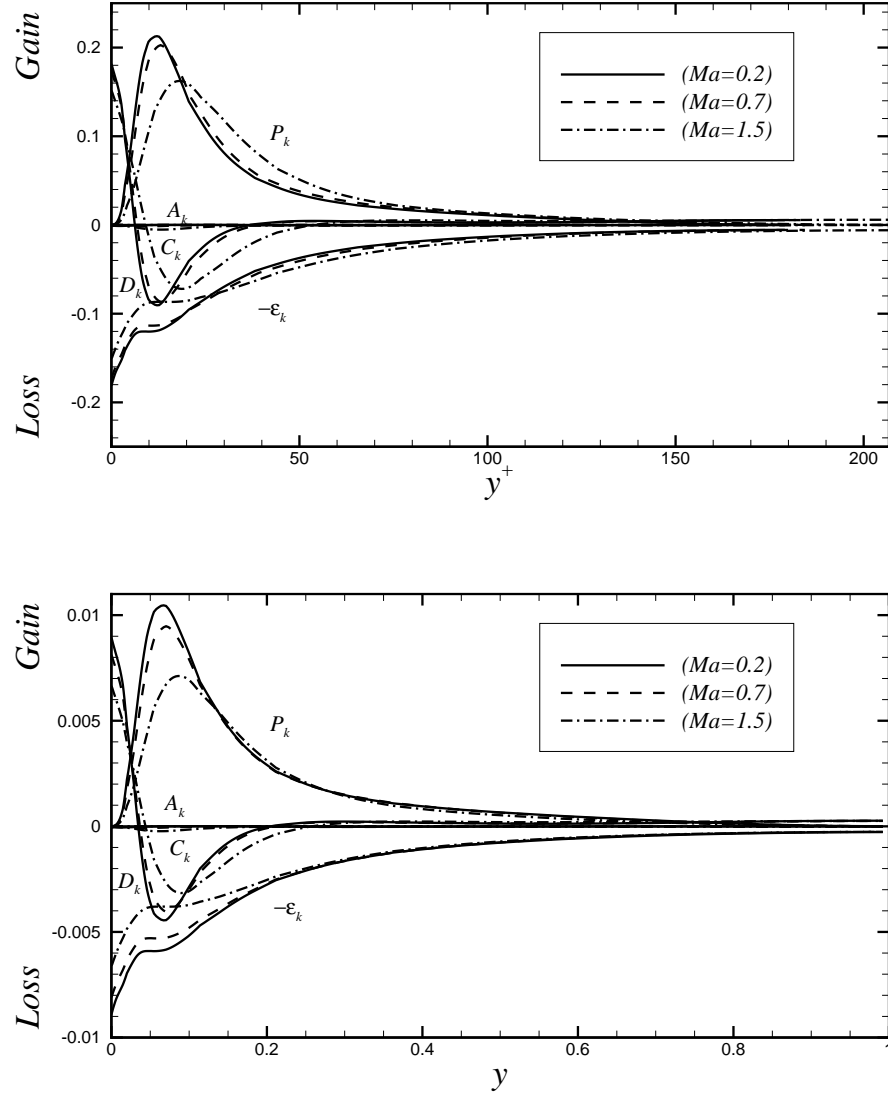


Figure 3.34: Top: Turbulent kinetic energy budget normalized by wall variables $\tau_w u_\tau / \delta_v$ in wall coordinates; Bottom: Turbulent kinetic energy budget normalized by bulk variables $\rho_m U_m^3 / h$ in global coordinates

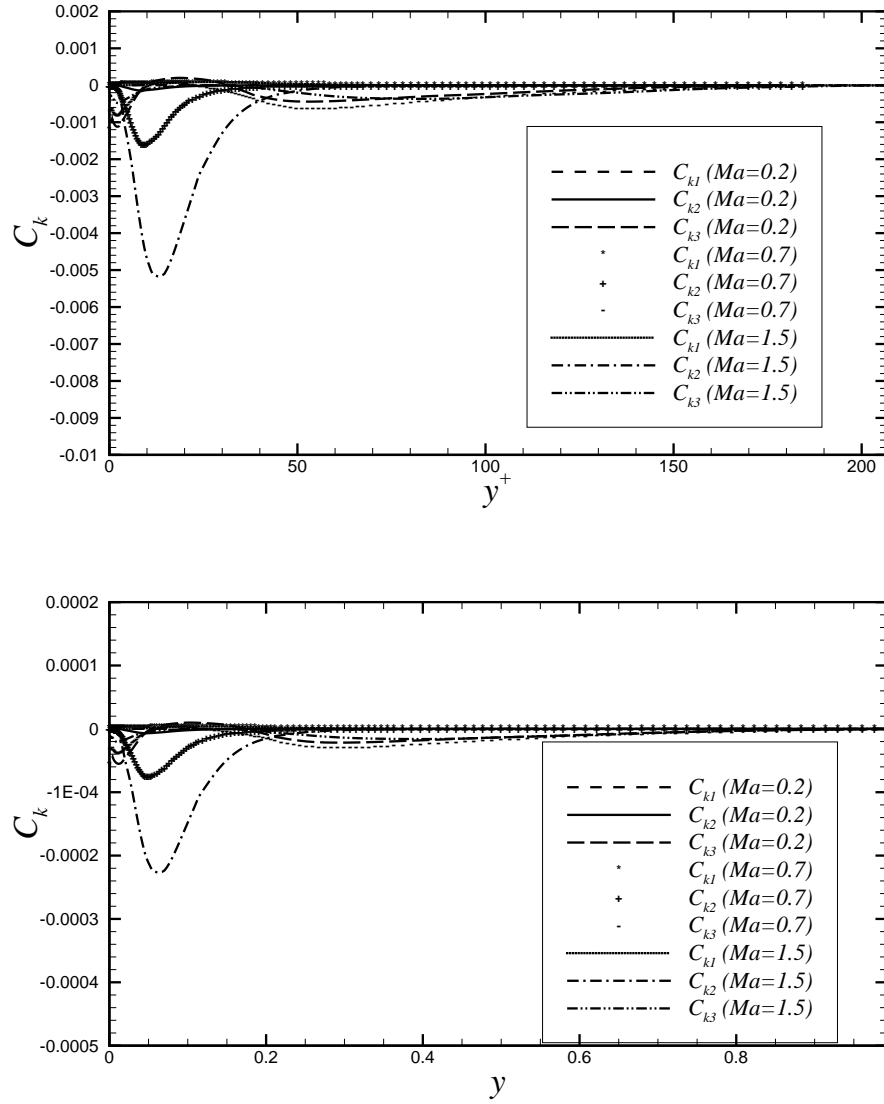


Figure 3.35: Top: Compressibility terms of TKE equation (eq. 3.7) normalized by wall variables $\tau_w u_\tau / \delta_v$ in wall coordinates; Bottom: Compressibility terms of TKE equation normalized by bulk variables $\rho_m U_m^3 / h$ in global coordinates

3.8 Reynolds stress and velocity-temperature cross-correlations

The cross-correlation coefficient (between variable a and variable b) is defined as:

$$\rho_{a:b} = \frac{\langle a'b' \rangle}{\langle a'a' \rangle^{0.5} \langle b'b' \rangle^{0.5}} \quad (3.33)$$

Cross-correlations between velocities and temperature for all three cases Ma02, Ma07, and Ma15 are presented in figure (3.36). The top figure shows that the cross-correlations between streamwise velocity and temperature $\rho_{u:T} \approx 1$ at the wall for all cases. At the central region of the channel, $\rho_{u:T}$ for the case Ma15 is slightly higher than the case Ma02, in other words, the influence of Mach number is small. However, the strong Reynolds analogy (SRA), proposed by Morkovin (1964) and supported by Morkovin's hypothesis, stated that the cross-correlation coefficient between velocity and temperature fluctuations should be -1 , in other words, velocity and temperature were highly correlated in a negative sense. The SRA can be applied to adiabatic compressible boundary layers, but the current results show that it is not applicable to fully developed turbulent channel flow with isothermal walls, as suggested by Huang *et al.* (1995) and Morrison *et al.* (2004). The middle figure indicates that $\rho_{v:T}$ and $\rho_{w:T}$ are little affected by the Mach number. The maximum of $\rho_{v:T}$ is around 0.5 at close to the wall. $\rho_{w:T} \approx 0$ are due to the symmetry of the spanwise velocity w . The cross-correlation coefficient between streamwise and wall normal velocity $\rho_{u:v}$, in other words, turbulent shear stress correlation coefficient, is shown in bottom figure. The profile of $\rho_{u:v}$ shares a similar trend as the one for $\rho_{v:T}$. It can be seen that Mach number has little effect on turbulent shear stress correlations.

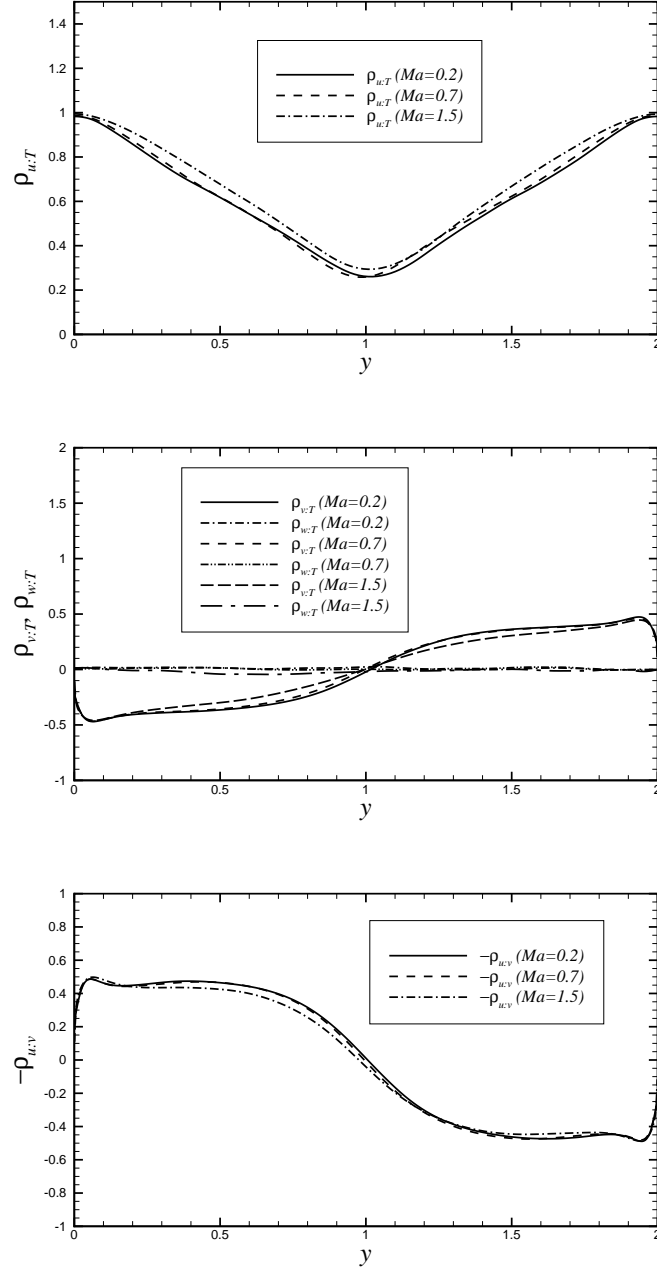


Figure 3.36: Cross-correlation coefficients of velocities and temperature: $\rho_{u:T}$ (top); $\rho_{v:T}$, $\rho_{w:T}$ (middle); $\rho_{u:v}$ (bottom)

3.9 Relations between pressure gradient and vorticity flux

Pressure gradient is believed to have a great effect on the generation of vorticity, which usually happens at the interface of fluid and solid surface. As noted in section (3.1.2), Lighthill (1963) considered incompressible laminar flow over a solid surface. Some researchers have further developed this vorticity dynamics theory, see for example, Wu & Wu (1998). However, there appears to be no existing relation and analysis of the connection between pressure gradient and vorticity flux for compressible non-isothermal turbulent flows over a solid surface. It is of both theoretical and practical importance to study the relationship between pressure gradient and vorticity flux. Theoretically the mechanism of this phenomenon needs further understanding and practically some light can be shed for the control of the compressible turbulent flows.

The deduction of relation between pressure gradient and vorticity flux for compressible non-isothermal turbulent flows over a solid surface starts from the momentum equation with the addition of a driving force.

$$\rho \frac{\partial u_i}{\partial t} + \rho u_j \frac{\partial u_i}{\partial x_j} + \frac{\partial p}{\partial x_i} = \frac{\partial \tau_{ij}}{\partial x_j} + \rho f_i, \quad (3.34)$$

where f_i is the driving force, density ρ is a function of space and time $\rho = \rho(x, y, z, t)$ and

$$\tau_{ij} = \mu \left(\frac{\partial u_i}{\partial x_j} + \frac{\partial u_j}{\partial x_i} \right) - \frac{2}{3} \mu \delta_{ij} \frac{\partial u_k}{\partial x_k}, \quad (3.35)$$

and viscosity μ is a function of temperature and also a function of space and time: $\mu = \mu(T) = \mu(x, y, z, t)$.

The diffusion term $\partial\tau_{ij}/\partial x_j$ in equation (3.34) can be expanded as

$$\frac{\partial}{\partial x_j} \left(\mu \left(\frac{\partial u_i}{\partial x_j} + \frac{\partial u_j}{\partial x_i} \right) - \frac{2}{3} \mu \delta_{ij} \frac{\partial u_k}{\partial x_k} \right) = -\mu \varepsilon_{ijk} \frac{\partial \omega_k}{\partial x_j} + \frac{4}{3} \mu \frac{\partial}{\partial x_i} \left(\frac{\partial u_k}{\partial x_k} \right) + \frac{\tau_{ij}}{\mu} \frac{\partial \mu}{\partial x_j}, \quad (3.36)$$

where ε_{ijk} is the permutation symbol (also called Levi-Civita symbol).

$$\varepsilon_{ijk} = \begin{cases} 1 & \text{if } (i, j, k) = (1, 2, 3), (2, 3, 1), \text{ or } (3, 1, 2) \\ -1 & \text{if } (i, j, k) = (3, 2, 1), (2, 1, 3), \text{ or } (1, 3, 2) \\ 0 & \text{if } i = j, j = k, \text{ or } k = i \end{cases}$$

and ω_k is the vorticity

$$\omega_k = \varepsilon_{klm} \frac{\partial u_m}{\partial x_l}. \quad (3.37)$$

The momentum equation (3.34) can be rewritten as:

$$\rho \frac{\partial u_i}{\partial t} + \rho u_j \frac{\partial u_i}{\partial x_j} + \frac{\partial p}{\partial x_i} = -\mu \varepsilon_{ijk} \frac{\partial \omega_k}{\partial x_j} + \frac{4}{3} \mu \frac{\partial}{\partial x_i} \left(\frac{\partial u_k}{\partial x_k} \right) + \frac{\tau_{ij}}{\mu} \frac{\partial \mu}{\partial x_j} + \rho f_i. \quad (3.38)$$

The unsteady term and convection terms of the momentum equation (3.38) vanish at the wall. It then follows, for on the wall, that

$$\frac{\partial p}{\partial x_i} = -\mu \varepsilon_{ijk} \frac{\partial \omega_k}{\partial x_j} + \frac{4}{3} \mu \frac{\partial}{\partial x_i} \left(\frac{\partial u_k}{\partial x_k} \right) + \frac{\tau_{ij}}{\mu} \frac{\partial \mu}{\partial x_j} + \rho f_i. \quad (3.39)$$

The right-hand side of equation (3.39) consists of four terms:

1. vorticity gradient term: $-\mu \varepsilon_{ijk} \partial \omega_k / \partial x_j$ which mainly involves vorticity fluxes in different directions
2. dilatation term: $4/3 \mu \partial (\partial u_k / \partial x_k) / \partial x_i$ which denotes compressibility effects. It is zero for incompressible flows.
3. viscosity gradient term: $\tau_{ij} / \mu \partial \mu / \partial x_j$ which denotes the effect of variations in viscosity mainly caused by the variations in temperatures (or heat flux).
4. driving force term: ρf_i .

Expand equation 3.39 to x, y, z directions (y denotes the wall normal direction) respectively

$$\frac{\partial p}{\partial x} = -\mu \frac{\partial \omega_z}{\partial y} + \mu \frac{\partial \omega_y}{\partial z} + \frac{4}{3} \mu \frac{\partial}{\partial x} \left(\frac{\partial u}{\partial x} + \frac{\partial v}{\partial y} + \frac{\partial w}{\partial z} \right) + \frac{\tau_{xx}}{\mu} \frac{\partial \mu}{\partial x} + \frac{\tau_{xy}}{\mu} \frac{\partial \mu}{\partial y} + \frac{\tau_{xz}}{\mu} \frac{\partial \mu}{\partial z} + \rho f_x. \quad (3.40)$$

$$\frac{\partial p}{\partial y} = -\mu \frac{\partial \omega_x}{\partial z} + \mu \frac{\partial \omega_z}{\partial x} + \frac{4}{3} \mu \frac{\partial}{\partial y} \left(\frac{\partial u}{\partial x} + \frac{\partial v}{\partial y} + \frac{\partial w}{\partial z} \right) + \frac{\tau_{yx}}{\mu} \frac{\partial \mu}{\partial x} + \frac{\tau_{yy}}{\mu} \frac{\partial \mu}{\partial y} + \frac{\tau_{yz}}{\mu} \frac{\partial \mu}{\partial z} + \rho f_y. \quad (3.41)$$

$$\frac{\partial p}{\partial z} = -\mu \frac{\partial \omega_y}{\partial x} + \mu \frac{\partial \omega_x}{\partial y} + \frac{4}{3} \mu \frac{\partial}{\partial z} \left(\frac{\partial u}{\partial x} + \frac{\partial v}{\partial y} + \frac{\partial w}{\partial z} \right) + \frac{\tau_{zx}}{\mu} \frac{\partial \mu}{\partial x} + \frac{\tau_{zy}}{\mu} \frac{\partial \mu}{\partial y} + \frac{\tau_{zz}}{\mu} \frac{\partial \mu}{\partial z} + \rho f_z. \quad (3.42)$$

Velocities u, v, w are zero on the wall ($y = 0$), and so are their first and higher order derivatives with respect to x and z .

The continuity equation for compressible flows is

$$\frac{\partial \rho}{\partial t} + \frac{\partial \rho u_j}{\partial x_j} = \frac{\partial \rho}{\partial t} + \rho \frac{\partial u_j}{\partial x_j} + u_j \frac{\partial \rho}{\partial x_j} = 0. \quad (3.43)$$

As $u_j = 0$ on the wall, it follows, for on the wall, that

$$\frac{\partial u_j}{\partial x_j} = -\frac{1}{\rho} \frac{\partial \rho}{\partial t} \neq 0. \quad (3.44)$$

Let Θ denote the dilatation $\Theta = \partial u_j / \partial x_j = \partial u / \partial x + \partial v / \partial y + \partial w / \partial z$. Then, $\Theta \neq 0$ (or $\partial v / \partial y \neq 0$) on the wall.

Compressible non-isothermal turbulent flows over an isothermal plane wall are considered here for simplicity. Derivatives of viscosity with respect to x and z are zero for an isothermal plane wall as temperature is constant at the wall. Then equations (3.40), (3.41), (3.42) can be rewritten as,

$$\frac{\partial p}{\partial x} = -\mu \frac{\partial \omega_z}{\partial y} + \frac{\partial u}{\partial y} \frac{\partial \mu}{\partial y} + \frac{4}{3} \mu \frac{\partial \Theta}{\partial x} + \rho f_x. \quad (3.45)$$

$$\frac{\partial p}{\partial y} = -\mu \frac{\partial \omega_x}{\partial z} + \mu \frac{\partial \omega_z}{\partial x} + \frac{4}{3} \mu \frac{\partial \Theta}{\partial y} + \frac{4}{3} \Theta \frac{\partial \mu}{\partial y} + \rho f_y. \quad (3.46)$$

$$\frac{\partial p}{\partial z} = \mu \frac{\partial \omega_x}{\partial y} + \frac{\partial w}{\partial y} \frac{\partial \mu}{\partial y} + \frac{4}{3} \mu \frac{\partial \Theta}{\partial z} + \rho f_z. \quad (3.47)$$

Further refinement of equations (3.45), (3.46), (3.47) gives,

$$\frac{\partial p}{\partial x} = -\frac{\partial \mu \omega_z}{\partial y} + \frac{4}{3} \frac{\partial \mu \Theta}{\partial x} + \rho f_x. \quad (3.48)$$

$$\frac{\partial p}{\partial y} = -\frac{\partial \mu \omega_x}{\partial z} + \frac{\partial \mu \omega_z}{\partial x} + \frac{4}{3} \frac{\partial \mu \Theta}{\partial y} + \rho f_y. \quad (3.49)$$

$$\frac{\partial p}{\partial z} = \frac{\partial \mu \omega_x}{\partial y} + \frac{4}{3} \frac{\partial \mu \Theta}{\partial z} + \rho f_z. \quad (3.50)$$

It can be seen from the above equations that the vorticity generation from the wall is affected by pressure gradients, driving force, dilatation gradients (compressibility effects), and viscosity gradients. Specifically, the vorticity flux in the wall normal direction may be determined by tangential pressure gradients/driving force, tangential dilatation gradients and wall normal viscosity gradients. On the other hand, the vorticity flux in the wall tangential directions may be determined by the wall normal pressure gradient, driving force, wall normal dilatation gradients and viscosity gradients.

The driving forces in the current simulations are constants: $f_i = -\tau_{w_{av}} \delta_{i1} / (h \rho_m)$ where h is the channel half width. $\tau_{w_{av}}$ is mean wall shear stress, that is,

$$f_x = -\tau_{w_{av}} / (h \rho_m), \quad f_y = 0, \quad f_z = 0.$$

The cross-correlations between pressure gradients and vorticity fluxes $\partial \mu \omega_i / \partial x_j$ and $\partial \omega_i / \partial x_j$ for three cases (Ma02, Ma07, and Ma15) were generated to investigate the influence of Mach numbers, viscosity, compressibilities, etc. It has been found that each pressure gradient is only highly correlated with a certain type of vorticity flux within the viscous sublayer region.

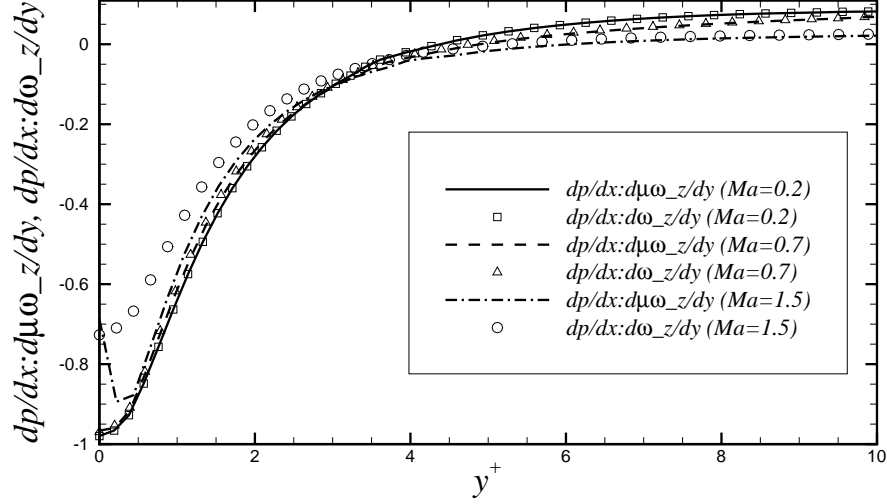


Figure 3.37: Cross-correlation coefficients between streamwise pressure gradient and spanwise vorticity fluxes in the wall normal direction including the influence of viscosity very near the wall. d denotes partial derivative, and $_$ denotes subscript.

The cross-correlation coefficients between streamwise pressure gradient ($\partial p/\partial x$) and two different spanwise vorticity fluxes ($\partial \omega_z/\partial y$ and $\partial \mu \omega_z/\partial y$) in the wall normal direction are shown in figure (3.37). High negative correlation coefficients are observed close to the wall, which match equations (3.45) and (3.48). The absolute value of the correlation coefficients decreases as Mach number increases because of the influence of the ρf_x term in which the RMS of density ρ increases with increasing Mach number. Although the difference between the correlations of pressure gradient with two different vorticity fluxes the two correlations on the wall is negligible, The difference between the two correlation very close to the wall increases with increasing Mach number, which denotes the influence of the viscosity and Mach number. It is interesting to see that the diminution for the case Ma15 very close to the wall is similar to flatness factor $F(v')$ profile for the case Ma15 in figure (3.32).

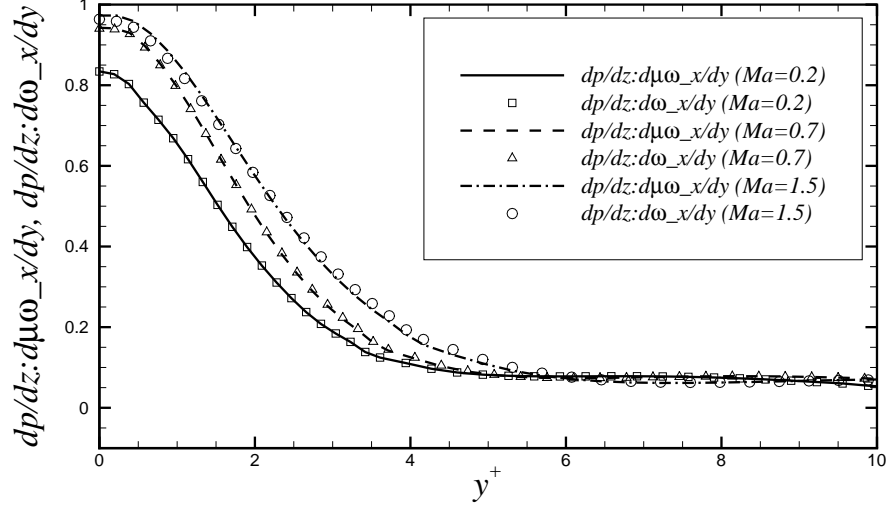


Figure 3.38: Cross-correlation coefficients between spanwise pressure gradient and streamwise vorticity fluxes in the wall normal direction including the influence of viscosity very near the wall. d denotes partial derivative, and $_x$ denotes subscript.

The cross-correlation coefficients between spanwise pressure gradient and two different streamwise vorticity fluxes in the wall normal direction are presented in figure (3.38). High positive correlation coefficients are observed close to the wall, which matches equations (3.47) and (3.50). Unlike figure 3.37, the absolute value of correlation coefficients in figure (3.38) approaches 1.0 as Mach number increases. The difference between the correlation of pressure gradient with two different vorticity fluxes is almost negligible for the current cases; but the trend shows that the difference slightly increases with increasing Mach number. Compared with the difference for the case $Ma=1.5$ observed in figure (3.37), the difference for the $Ma=1.5$ in figure (3.38) is negligible; and is because the term $\partial w / \partial y (\partial \mu / \partial y)$ is much smaller than $\partial u / \partial y (\partial \mu / \partial y)$ very near the wall, as are their fluctuations.

The cross-correlation coefficients between wall normal pressure gradient and two

different streamwise vorticity fluxes in the spanwise direction ($\partial\mu\omega_x/\partial z$) are given in figure (3.39). It shows that there is little difference between these correlations. This is obvious as the influence of additional term $\omega_x\partial\mu/\partial z = 0$. The correlation coefficients for all three cases are also high on the wall. However, it is interesting to note that the highest correlation occurs at $\text{Ma}=0.7$. It could be due to the combined effect of wall normal gradients of viscosity and dilatation.

Equations (3.46) and (3.49) suggest that wall normal gradient would possibly be correlated with spanwise vorticity fluxes in the streamwise direction ($\partial\mu\omega_z/\partial x$). The results show that their cross-correlation coefficients for all three cases are positive but below 0.2 on the wall, in other words, they are rather poorly correlated. It is mainly because $\partial\mu\omega_z/\partial x$ is much smaller than $\partial\mu\omega_x/\partial z$. The driving force in the streamwise direction leads to large streamwise shear stress close to the wall, which causes streaks and vortex lines close to the wall to be stretched in the streamwise direction, as will be shown later. This streamwise stretching makes streamwise gradients smaller than spanwise gradients.

Pressure gradients and other type of vorticity fluxes close to the wall are poorly correlated, and so are pressure gradients and vorticities, as well as pressure and vorticities. These results are not shown here.

3.10 Near-wall turbulence structures

Near-wall streaks, characteristics of wall-bounded turbulent flows (Robinson, 1991), are referred to as narrow regions of near-wall low speed fluid stretched in the streamwise direction (Smith & Metzler, 1983). Smith & Metzler (1983) studied characteristics of near-wall streaks in a turbulent boundary layer for a Reynolds number range

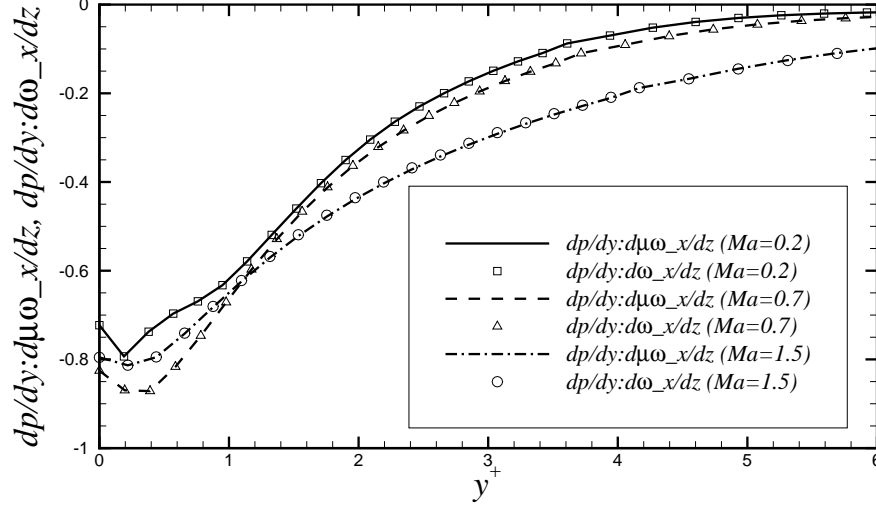


Figure 3.39: Cross-correlation coefficients between wall normal pressure gradient and streamwise vorticity fluxes in the spanwise direction including the influence of viscosity very near the wall. d denotes partial derivative, and $_-$ denotes subscript.

of $740 < Re_\theta < 5830$ and found that the near-wall low speed streaks had a mean spanwise spacing of $\Delta z^+ \approx 100$ in wall units, which was independent of Reynolds numbers, however, the spanwise streak spacing was found to increase with increasing distance from the wall. Numerical results of Kim *et al.* (1987) confirmed these findings through the indication of spanwise autocorrelations of streamwise velocity fluctuations. Morinishi *et al.* (2004) reported the spanwise streak spacing of around 100 in semi-local wall units ($\delta_{v^*} = \langle \mu \rangle / (\langle \rho \rangle u_{\tau^*})$, $u_{\tau^*} = (\tau_w / \langle \rho \rangle)^{0.5}$) for compressible channel flow.

The spanwise correlations of streamwise velocities at different y locations for all three cases Ma02, Ma07, and Ma15 are given in figure (3.40) in wall units. It can be seen that the location of the minimum of the correlations increases as the distance from wall increases for all cases. The minimum is more significant in the near wall

region ($y^+ < 30$). Comparison for three cases shows that the location of the minimum of the correlation in the near-wall region increases as Mach number increases, which indicates the trend of increased streak spacing.

The near-wall low speed streak spacings (twice of the location Δz^+ of minimum correlation of streamwise velocity fluctuations) for all cases are illustrated in figure (3.41). It is found that the spacing for the case $Ma=0.2$ increases from around 100 wall units at $y^+ \approx 5$ to around 140 at $y^+ \approx 27$, which agrees well with the incompressible experimental and numerical results reported by Kim *et al.* (1987); Smith & Metzler (1983). It is also found that the spacing at $y^+ \approx 5$ increases from around 100 wall units for the case $Ma = 0.2$ to around 150 for the case $Ma = 1.5$.

A snapshot of streamwise velocity fluctuations at $y/h = 0.03$ ($y^+ \approx 5$) for the case Ma02 (top), Ma07 (middle), and Ma15 (bottom) respectively is shown in figure (3.42). The streaks get longer in the streamwise direction and wider (or smaller in quantity) in the spanwise direction as the Mach number increases. In other words, the mean spanwise streak spacing increases with increasing Mach number, which confirms the previous predictions based on spanwise correlations of streamwise velocities.

Second invariant of the velocity gradient tensor (denoted as Q) is usually used for the visualization of turbulent coherent structures. It is defined as (Chong, Perry & Cantwell, 1990)

$$Q = \frac{1}{2}(P^2 - S_{ij}S_{ji} - R_{ij}R_{ji}) \quad (3.51)$$

where $P = -\partial u_i / \partial x_i$ is zero for incompressible flows, $S_{ij} = 0.5(\partial u_i / \partial x_j + \partial u_j / \partial x_i)$, and $R_{ij} = 0.5(\partial u_i / \partial x_j - \partial u_j / \partial x_i)$.

Iso-surfaces of $Q = 0.5$ (non-dimensionalized by bulk velocity and half channel width) in the bottom half channel (structures in the top half channel are removed for

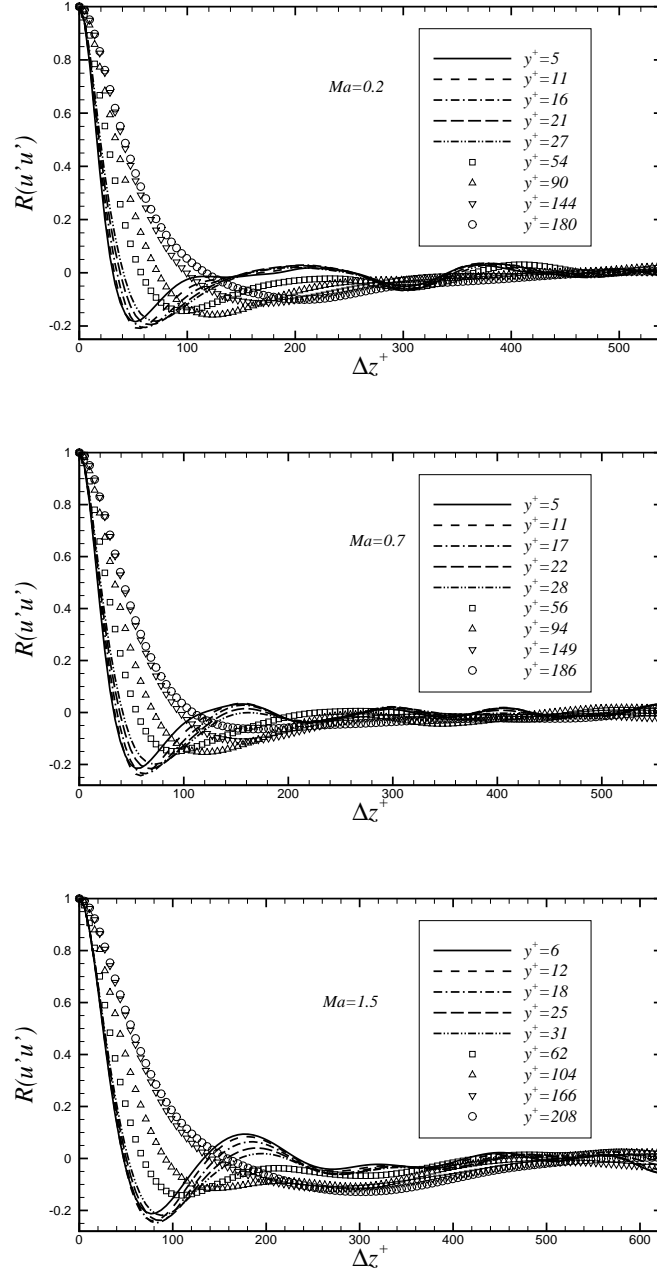


Figure 3.40: Correlations of streamwise velocity fluctuations at different y locations for the cases Ma02 (top), Ma07 (middle) and Ma15 (bottom).

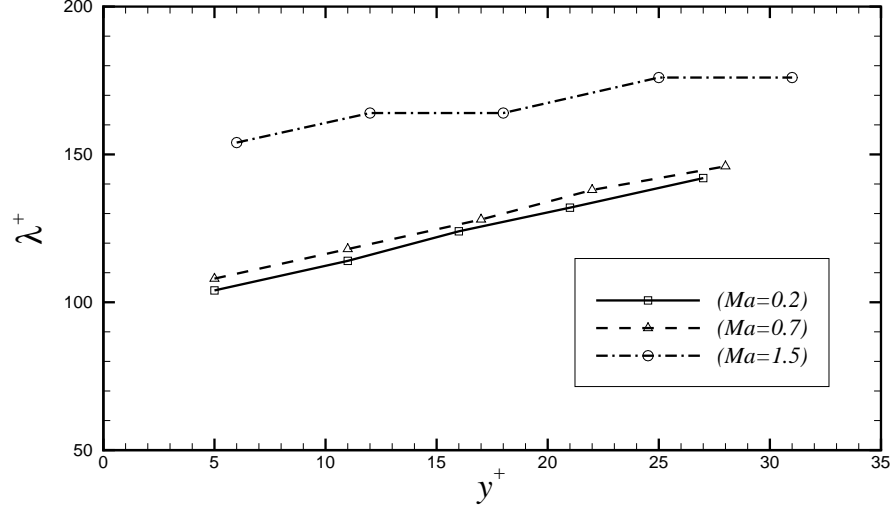


Figure 3.41: Near-wall streak spacing for the cases Ma02 , Ma07 and Ma15.

clarity) for the cases Ma02, Ma07, and Ma15 are presented in figures (3.43), (3.44), (3.45). The coloring of the iso-surfaces is based on the local streamwise velocity (blue to red, 0 to 1.2), which is similar to Wu & Moin (2009). It can be seen here that the structures are more sparsely distributed and elongated as Mach number increases, which is similar to the distribution of near-wall low speed streaks. The inclined hairpin-like structures with both one leg and two legs are observed, but only a few have two legs with heads, in other words, full hairpin structure.

3.11 Concluding remarks

Direct numerical simulation of fully developed, isothermal-wall, turbulent channel flow at Mach numbers $Ma = 0.2$, $Ma = 0.7$, and $Ma = 1.5$ and Reynolds number $Re \approx 2800$ has been performed. The agreement between the current simulation

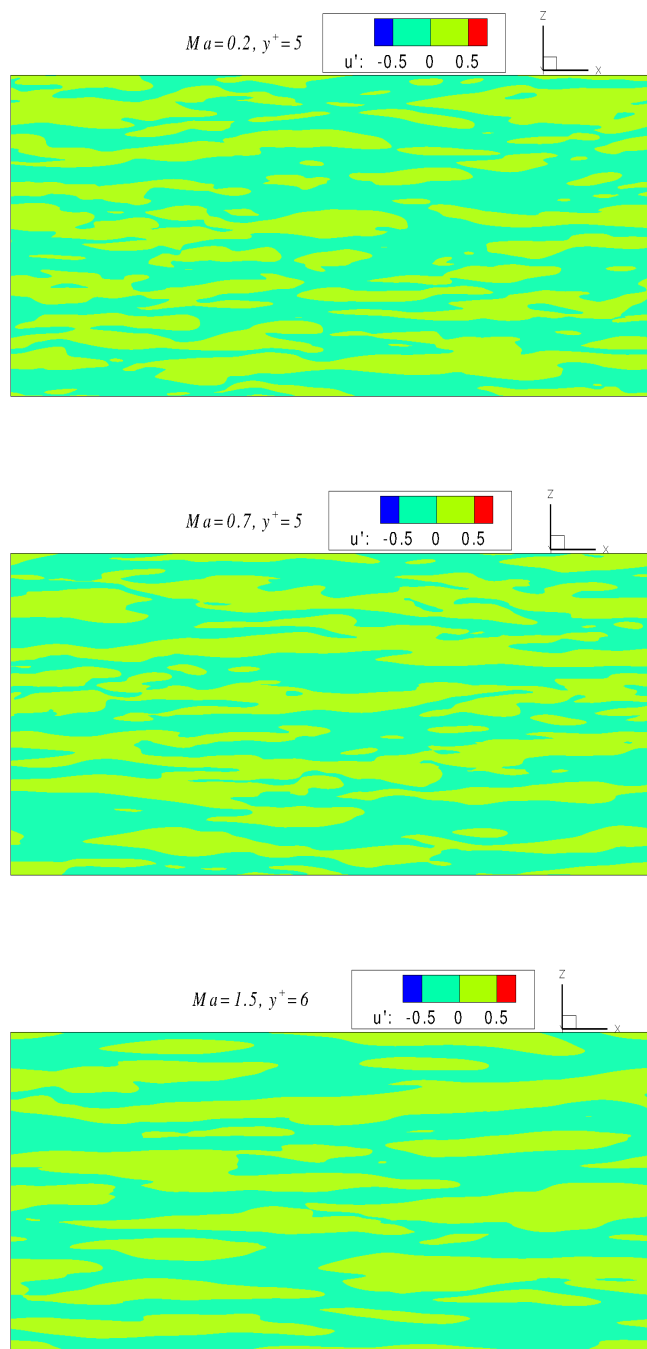


Figure 3.42: A snapshot of streamwise velocity fluctuations at $y/h = 0.03$ ($y^+ \approx 5$) for the case Ma02 (top), Ma07 (middle), and Ma15 (bottom) respectively.

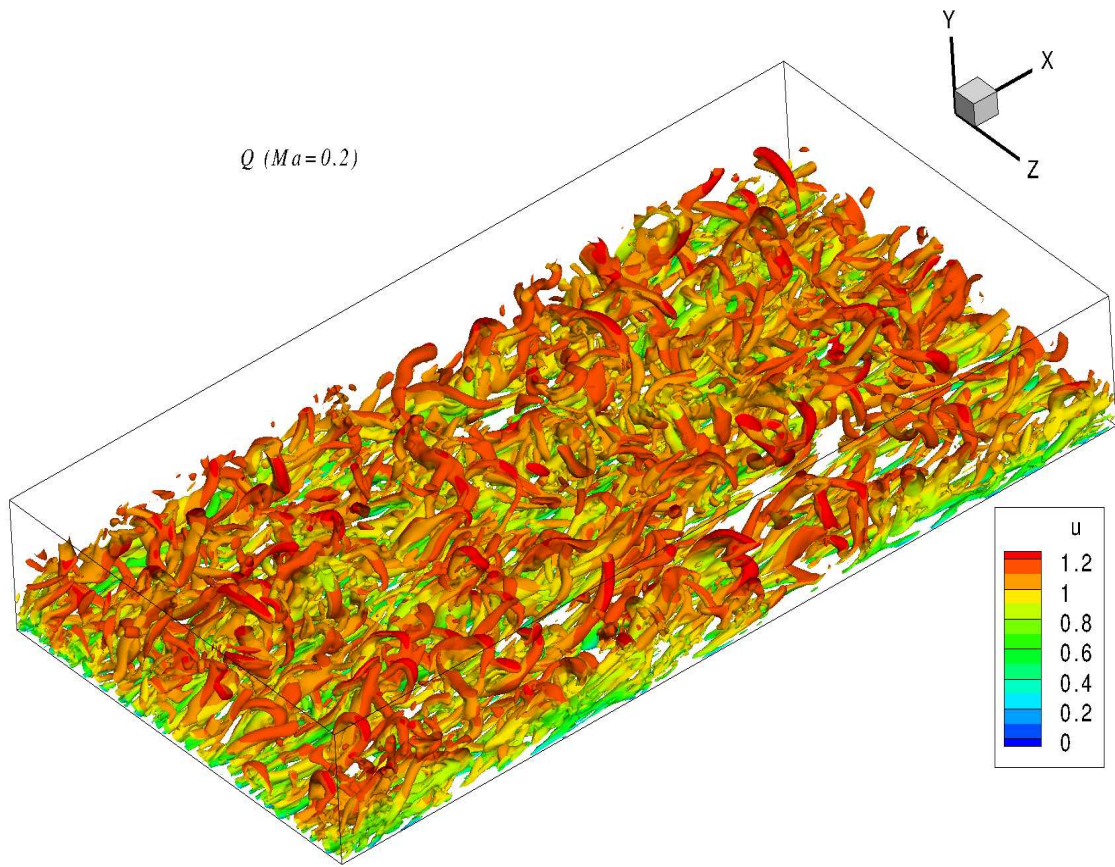


Figure 3.43: Iso-surfaces of second invariant of the velocity gradient tensor ($Q=0.5$) in the bottom half channel (structures in the top half channel are removed for clarity) for the case $Ma02$. The coloring is based on the local streamwise velocity.

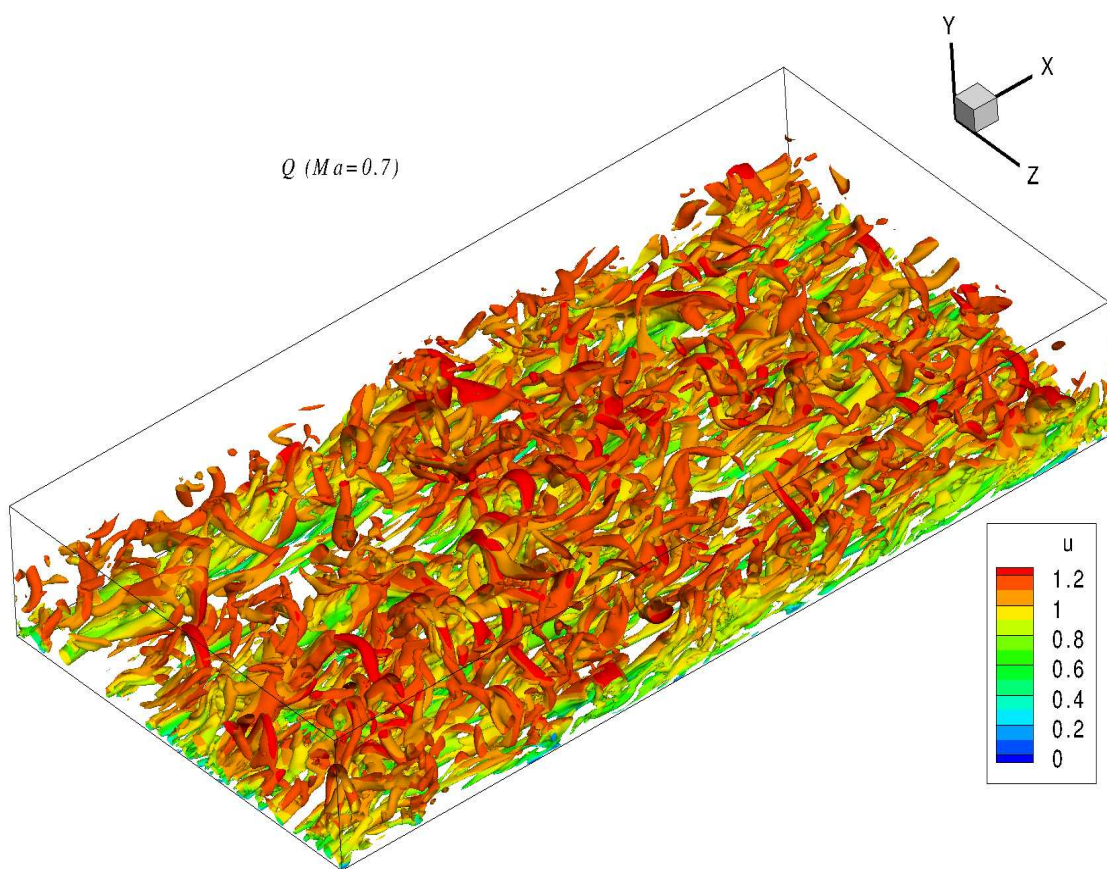


Figure 3.44: Iso-surfaces of second invariant of the velocity gradient tensor ($Q=0.5$) in the bottom half channel (structures in the top half channel are removed for clarity) for the case Ma07. The coloring is based on the local streamwise velocity.

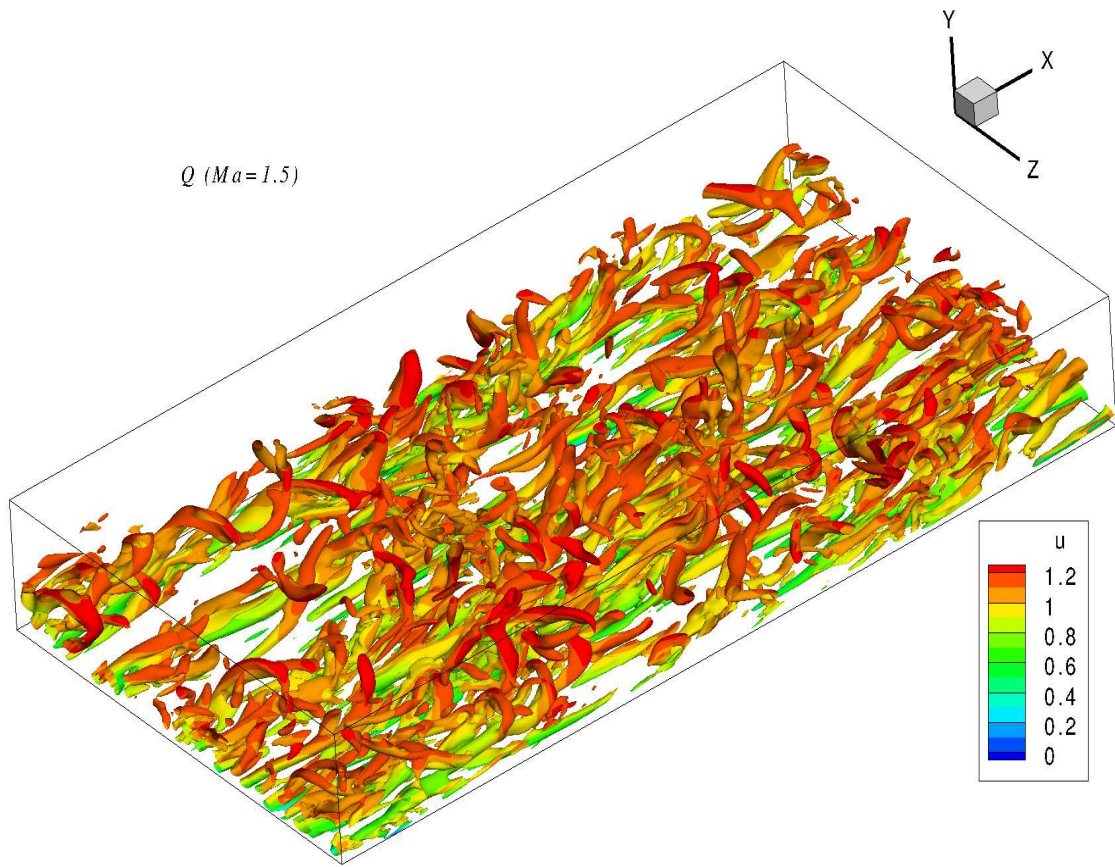


Figure 3.45: Iso-surfaces of second invariant of the velocity gradient tensor ($Q=0.5$) in the bottom half channel (structures in the top half channel are removed for clarity) for the case Ma15. The coloring is based on the local streamwise velocity.

results obtained using a discontinuous Galerkin method and the corresponding incompressible DNS data of Moser *et al.* (1999) and compressible DNS data of Coleman *et al.* (1995) is satisfactory, thereby demonstrating the utility of the DGM for DNS.

The mean velocity profile departs from the log law as the Mach number increases. However, there is a good fit in the viscous sublayer and buffer layer. The Van Driest transformation of the velocity profiles of compressible cases causes the profiles to get closer to the incompressible log law in the log-law region, but at the same time the velocity profile departs from the incompressible profile in the buffer layer region.

Compared with the log-law, a power law seems to represent the scaling of mean streamwise velocity with Mach number for the current cases, although the mean velocity profiles of the current cases do not exactly obey power law either.

Inner and outer scaling of second-order and higher-order statistics with Mach number have been compared. It is found that the inner scaling of second-order statistics, such as turbulence velocity, density, temperature, shear stress and vorticity fluctuations, is dependent of Mach numbers; but outer scaling with Mach number shows a better collapse. However, the scaling of some higher-order statistics, such as skewness and flatness of density and temperature fluctuations, seems to collapse better when inner scaling is used.

Turbulent kinetic energy (TKE) budget has been reported. The related scaling and analysis of compressibility terms have been analysed. The result shows that the inner scaling of TKE budget does not collapse well in the near-wall region, but the collapse of the outer scaling is satisfactory. The influence of compressibility terms on TKE budget is negligible.

The linkage between the pressure gradient and vorticity flux on the wall has been

theoretically derived and confirmed by their correlations of the current simulation results. The correlations between streamwise pressure gradient and spanwise vorticity flux in the wall normal direction, between spanwise pressure gradient and streamwise vorticity flux in the wall normal direction, and as well as the correlation between wall-normal pressure gradient and streamwise vorticity gradient in the spanwise direction, are very high on the wall. It is also found that both Mach number and viscosity affect the correlation between streamwise pressure gradient and spanwise vorticity flux in the wall normal direction very close to the wall.

Near-wall streaks, indicated by the spanwise correlation of streamwise velocity fluctuations and by the snapshot of streamwise velocity fluctuations close to the wall, have been analysed. The agreement of spanwise streak spacing between the case Ma02 and the incompressible data (Kim *et al.*, 1987) is good. The spanwise streak spacing which is independent of Reynolds numbers, however, increases with increasing Mach number, which is confirmed by the snapshot of near-wall streak contours. Isosurfaces of second invariant of the velocity gradient tensor are more sparsely distributed and elongated as Mach number increases, which is similar to the distribution of near-wall low speed streaks.

Chapter 4

DNS of turbulent flow with FPG & APG

4.1 Introduction

Flows with favorable pressure gradient (FPG) and adverse pressure gradient (APG) are of great importance theoretically and practically. In practice, many industrial applications, especially those in aerodynamics, such as aircraft and turbine designs, involve flows with pressure gradients and separation. In theory, wall shear stress does not dominate this type of flow (Spalart & Watmuff, 1993).

Much effort has been made to understand boundary layer flows with pressure gradients and separation, through theoretical analysis, experiments, and numerical approximations.

4.1.1 Theoretical analysis

It is important to determine the relevant velocity scales in most theoretical analysis of boundary layer flows (Skote & Henningson, 2002). The friction velocity $u_\tau = \sqrt{\tau_w/\rho}$, where τ_w and ρ are wall shear stress and density, is usually chosen as the velocity scale for a zero pressure gradient (ZPG) boundary layer.

However, u_τ cannot be used as the relevant velocity scale when it approaches zero in a boundary layer under APG, especially a strong APG. Many researchers (Stratford, 1959; Kader & Yaglom, 1978) chose another pressure-gradient based velocity scale $u_p = (\nu/\rho \, dp/dx)^{1/3}$ instead for separated flows.

Some other velocity scales were also brought up. For example, Perry & Schofield (1973) proposed a universal velocity defect law for a developing turbulent boundary layer under adverse pressure gradient. The velocity scale they used was related to the local maximum in the Reynolds stress profile, which is neither u_τ nor u_p . It is also found that the theory had a half-power distribution. Schofield (1981) analyzed equilibrium boundary layers under moderate and strong adverse pressure gradient, based on this defect law. It was found that the predicted shear-stress profiles using the expression derived from the law, was in good agreement with experimental data.

Melnik (1989) developed an two-parameter asymptotic theory for incompressible 2D turbulent boundary layer with prescribed pressure distributions and proposed a three-layer structure of the wall layer, the equilibrium layer and the outer layer based on the theory. Turbulent separated flows were treated by the two-parameter theory as it eliminated the small defect approximation of one-parameter theory. It was found that the variation of skin friction was linear near separation.

Durbin & Belcher (1992) obtained a three-layer structure of the turbulent boundary layer with strong APG: the wall layer, the wake layer and a transition layer. They found that the wall layer was not exponentially thinner than the wake layer and the wake layer had a large velocity deficit, and cannot be linearized. The mean velocity profile followed a power-law $y^{1/2}$ in the overlap region between the wall and transition layers.

George & Castillo (1993) studied equilibrium turbulent boundary layers with pressure gradients, referred to as a turbulent boundary layer subjected to a constant non-dimensional pressure gradient. They claimed that a power law should be used to describe the velocity profile in the matched layer and the friction law, and they also argued that the outer velocity scale should be the local freestream velocity, instead of the friction velocity.

Surana, Grunberg & Haller (2006) and Surana *et al.* (2008) developed a theory of three dimensional steady flow separation and attachment on fixed no-slip boundaries using nonlinear dynamical systems methods. Criteria for separation points and separation lines on no-slip boundaries at rest were proposed for compressible flows. Their theory led to four separation patterns, complementing the Lighthill's close separation (Lighthill, 1963) and Wang's open separation (Wang, 1972, 1974). They also claimed that separation and attachment surfaces originated from fixed lines on the boundary and the separation geometry could be determined by a weighted average of the wall shear stress and wall density fields.

4.1.2 Experimental investigation

Many experimental studies on flows subjected to APG have been carried out. Simpson, Strickland & Barr (1977) considered a two-dimensional separating boundary layer with an airfoil-type pressure distribution in which the flow was first accelerated and then decelerated until separation occurred. They showed that the velocity profile correlations of Perry & Schofield (1973) were supported upstream of separation within the uncertainty of the data and the similarity of the streamwise velocity and streamwise component of turbulence intensity throughout the shear flow was found downstream of separation.

Simpson, Chew & Shivaprasad (1981*a*) studied the structure of a separated turbulent boundary layer for an airfoil-type flow and determined the distribution of mean profiles and Reynolds stress. It was found that the separated turbulent boundary layer consisted of three layers. The first layer was a viscous layer nearest the wall that was dominated by the turbulent flow unsteadiness but with little Reynolds shearing stress effects; The second layer was a rather flat intermediate layer that seemed to act as an overlap region between the viscous wall and outer regions; and the third layer was outer backflow region, the farthest from the wall and part of the large-scaled outer region flow. They also found that the logarithmic law were not valid when the turbulent boundary layer approached separation, and mixing length and eddy viscosity models were physically meaningless in the backflow and had reduced values in the outer region of the separated flow.

Simpson, Chew & Shivaprasad (1981*b*) reported higher-order turbulence statistics for the separating turbulent boundary layer. It was found that the skewness factor for streamwise velocity was positive upstream of separation near the wall, but negative

downstream of separation. The flatness factor for streamwise velocity had a local maximum of about 4 at the minimum mean velocity location in the backflow. They claimed that the large-scale eddies in the outer region flow not only controlled the back flow but also provided the mechanism for turbulence-energy diffusion.

Nagano, Tagawa & Tsuji (1993) investigated the characteristics of mean flow and turbulent statistics of a turbulent boundary layer with moderate to strong adverse pressure gradients. It was found that the influence of adverse pressure gradient caused the velocity profile to fall below the standard log-law. Adverse pressure gradient also had a strong effect on higher-order statistics of velocity fluctuations.

Alving & Fernholz (1996) carried out an experiment on an axisymmetric body with a separated turbulent boundary layer. They found that the Reynolds stress is decreased in the inner region and reaches large peaks away from the wall. They also found that the large scale structures over the separation bubble do not interact with the near wall flow until after the flow reattaches.

Nagano, Tsuji & Houra (1998) performed experiments on the structure of a turbulent boundary layer subjected to APG. It was found that the characteristic time scales of velocity fluctuations of APG flow were extremely elongated in the near-wall region, compared with ZPG flow. They also claimed that the Taylor time scale ($\tau_E = \sqrt{2\langle u^2 \rangle / \langle (\partial u / \partial t)^2 \rangle}$) was the most appropriate to describe the temporal behaviour of turbulence quantities of APG flows.

Nagib, Christophorou & Monkewitz (2006) carried out experiments of high Reynolds number turbulent boundary layers with adverse, zero and favourable pressure gradients. The log-law parameter k was found to vary considerably for the non-equilibrium boundary layers under the various pressure gradients.

Na & Moin (1996) claimed in their DNS of turbulent boundary layers with APG and separation, that the accuracy of the hot-wire measurements was degraded by two characteristics of the flow: the tendency of not remaining two-dimensional in the mean and the high sensitivity to the upstream conditions, which thereby probably explained the discrepancies among experiments.

4.1.3 Numerical simulation and modeling

DNS has become an important tool for the turbulent research community since the 1980s. DNS can provide accurate, complete and detailed data, especially in the near wall regions and/or separation regions, where it is still difficult for experimental methods to get reliable data for certain variables, especially for compressible flows, despite improvements in experimental techniques.

Reynolds-averaged Navier-Stokes (RANS) based methods are not reliable in separated flows because they are not good at the treatment of the near-wall turbulent flow. With the development of powerful computers and DNS, the effects of APG and separated flows can be investigated.

Spalart & Watmuff (1993) performed both experiments and DNS of a turbulent boundary layer with pressure gradients, referred to as SW hereafter. The DNS used a part of the experimental domain and a prescribed velocity to generate the pressure gradients of their experiment instead of using a top curved wall like experiment. Good agreement between the experimental results and simulations was found for mean wall-pressure coefficients, displacement and momentum thicknesses. But moderate-to-large deviations were observed for quantities such as mean velocity profiles from the law of the wall, turbulence energy and dissipation rate. They also claimed that

the accuracy of the hot-wire measurements was degraded by higher probability of large angles between instantaneous velocity vector and the mean flow direction in the region of adverse pressure gradients.

Na & Moin (1998) conducted an incompressible DNS of turbulent APG & FPG flow with separation over a flat plate. The adverse-to-favorable pressure gradient was obtained using a suction-blowing velocity profile at the top boundary. The Reynolds number based on momentum thickness upstream of separation and free stream velocity $Re_\theta = 300$. They found that the locations of instantaneous spanwise-averaged detachment and reattachment points both fluctuated significantly in the streamwise direction, and turbulent structures emanating upstream of separation moved upwards into the shear layer in the detachment region and turned around the separation bubble, and that the largest pressure fluctuations were located in the middle of the shear layer. The maximum turbulent intensity occurred above the detachment region.

Skote, Henningson & Henkes (1998) performed an incompressible DNS of self-similar APG turbulent boundary layers. Comparison of turbulence statistics from the zero pressure gradient and the two APG cases showed that the development of a second peak in turbulence energy was in agreement with experiment.

Huttl *et al.* (2001) calculated a low Reynolds number flow by using the standard $k - \omega$ model and Menter's SST model (Menter, 1993). They claimed that none of the models can accurately capture the distribution of turbulent kinetic energy. Both models performed well in the region with strong APG & FPG and the mean velocities were in good agreement with the DNS data. However, deviations became visible for the predication of Reynolds shear stress, turbulent kinetic energy and the development of the skin friction coefficient in the region of smaller APG. The reason

remains unknown and further detailed investigation is warranted.

Shan, Jiang & Liu (2005) performed a two-dimensional and a three-dimensional DNS of flow separation around a NACA 0012 airfoil with an attack angle of 4° and a Reynolds number of 10^5 based on the free stream velocity and the chord length. They solved the full compressible form of the Navier-Stokes equations in curvilinear coordinates using an implicit scheme with a high order compact central difference scheme and non-reflecting boundary conditions. The 2D simulation was started from the uniform flow field and 3D simulation from the 2D simulation results. They claimed that the disturbance in the near wake region may propagate upstream and cause three dimensional instability, which seemed to be self-sustained and led to transition to turbulence. They did not analyze the spanwise effect in the flow separation, even though they showed the instantaneous spanwise vorticity contours in the midspan location.

Radhakrishnan, Piomelli & Keating (2008) conducted wall-modeled LES of flows with curvature and mild separation where RANS was used for the inner region and LES for the outer region. A stochastic forcing was employed to artificially perturb the RANS/LES interface to remove the buffer region where the velocity gradient was too high to get an accurate calculation of skin friction. They found that this method led to improved predictions of skin friction, mean velocity and Reynolds stresses for flows with APG despite the issues on CPU requirement and its application to strong FPG flows.

Marquillie, Laval & Dolganov (2008) performed an incompressible DNS of a separated channel flow. The pressure gradients were obtained by employing a wall curvature through a mathematical mapping from physical coordinates to Cartesian ones.

The inlet condition was taken from a highly resolved LES of plane channel flow. A thin separation bubble was found on the curved wall, and they presented data for stresses and turbulence kinetic energy budget.

Previous studies have made progress on turbulent flows with adverse pressure gradients. However, the physics of this type of flow is not completely understood and some issues have not been addressed, such as pressure gradient vorticity flux correlations. Most previous numerical work solved the incompressible form of the Navier-Stokes equations with/without modeling. Upstream turbulence or transition was mainly generated in numerical or non-physical ways. A DNS that solves compressible Navier-Stokes equations with laminar inflow and a physical transition to turbulence is therefore expected to provide a more accurate turbulent flow in aerodynamics.

A compressible DNS of turbulent flow with a physical trip element that transitions from laminar flow to turbulence and physical boundaries that prescribe favourable and adverse pressure gradients is more challenging. In the current work, a compressible form of the Navier-Stokes equations were solved using a discontinuous Galerkin method (see Karniadakis & Sherwin (2005), Cockburn, Karniadakis & Shu (2000).). In order to compare with incompressible results, the Mach number of approximately 0.2 based on the inlet bulk velocity was selected. The pressure gradients were obtained by using a curved top wall, similar to the experimental arrangement of Spalart & Watmuff (1993).

4.2 Computational details

The reference variables for the computation are the inlet bulk velocity (U_{ref}), inlet bulk density (ρ_{ref}), inlet viscosity at the wall (μ_w) and the streamwise length of the bottom plane wall (L_x), which leads to the reference Reynolds number of ~ 428000 .

The flow configuration of the current computation, similar to the SW case, is shown in figure 4.1. All the length units in the current simulation are non-dimensionalized by the streamwise length of the plate (L_x), as shown in the previous paragraph. The top figure provides the physical and computational domains in x - y plane in comparison with the SW case. The bottom figure shows the computational domain details in 3D where the periodic domain in x direction is $[0.1, 1.2]$.

At the computational inlet ($x = 0.1$), the inlet Reynolds number is ~ 42800 based on the inlet bulk velocity, inlet bulk density, inlet wall viscosity and inlet x . A trip wire with a shape of triangular prism (triangle base length: $\Delta x = 0.0344$; triangle height: $\Delta y = 0.0022$; depth: $\Delta z = 0.06$) at the bottom wall is used to trigger laminar-to-turbulence transition at $x = 0.15$. It is then followed by a FPG region $[0.2, 0.6]$ which is long enough for turbulence to develop and lose memory of inflow conditions (Spalart & Watmuff, 1993). The flow enters the APG region from $x = 0.6$. Note that the difference between the current computational domain and the experimental setup of the SW case is mainly located in the rear part of the APG region (approximately $[0.7, 1.0]$).

The region $[1.0, 1.2]$ is taken as a fringe region, where a fringe region technique (Skote *et al.*, 1998; Herbst & Henningson, 2006) is employed to drive the out-flow back to the inflow. It is implemented by the addition of a body force function, f , to the Navier-Stokes equations, in the following manner:

$$f = \lambda(x) * (\tilde{U}_i - U_i), \quad (4.1)$$

where \tilde{U}_i is the inflow laminar velocity profile that velocities in the fringe region U_i are forced to and $\lambda(x) = \lambda_{max}F(x)$ is the forcing strength, nonzero only in the fringe region. Function $F(x)$ is shown in figure 4.2.

Periodic boundary conditions are applied to the streamwise direction. The flow is assumed homogeneous in the spanwise (z) direction. In the wall normal (y) direction no-slip wall boundary conditions are applied to the bottom plane wall and the top curved wall which prescribes the streamwise pressure gradients.

There are $64 \times 16 \times 8$ body fitted non-orthogonal grid elements in the streamwise, wall-normal, spanwise directions respectively. 9th-order refinement with over-integration in each element (the number of quadrature points in each direction are twice the polynomial order to eliminate de-aliasing errors) makes a total of ~ 47 million quadrature points. Based on the highest value of friction velocity in turbulent region (around $x = 0.55$), the grid spacings in wall units are $\Delta x_{max}^+ \approx 27$, $\Delta z_{max}^+ \approx 12$. The first point away from the wall at $x = 0.55$, where the skin friction coefficient is maximum, is $\Delta y^+ \approx 0.5$. There are 20 quadrature points in the first 9 wall units away from the wall at $x = 0.55$.

The simulation was started from an isothermal laminar field superimposed by random fluctuations. After the simulation settled down, the statistics were obtained by an average over 0.5 non-dimensional time units (normalized by (L_x/U_{ref})), or about $15 \delta_{max}/U_{ref}$ (the maximum boundary layer thickness δ_{max} occurs near $x = 1.0$), which are enough as the data obtained are just a little smoother than the data averaged over 0.3 non-dimensional time units.

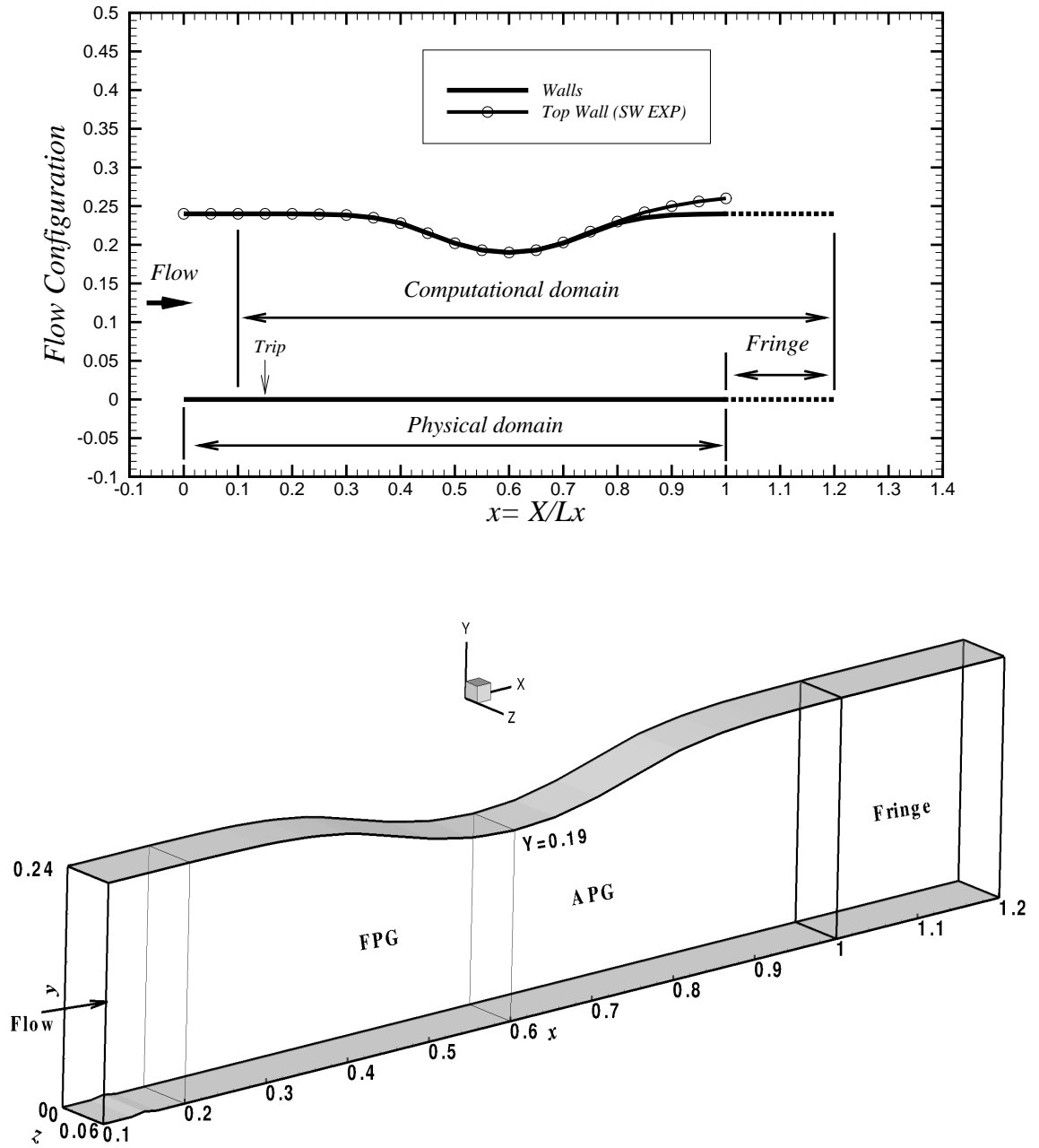
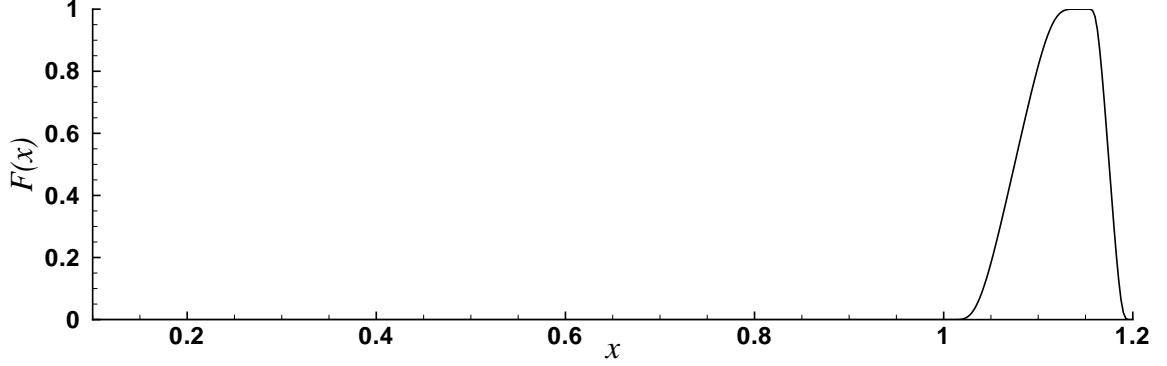


Figure 4.1: Flow configuration comparing with the SW case in 2D (top) and Computational domain in 3D (bottom)

Figure 4.2: strength of the forcing function $F(x)$

4.3 Global quantities

The wall pressure coefficient (C_p) of the current simulation is given in figure 4.3. The reference pressure was taken from wall pressure at ($x = 0.3$), in order to compare with the SW case. It indicates that the profile agrees well with experimental and DNS data of the SW case except for the rear part of the APG region where the curved top wall of the current case is different from the SW case, as shown in figure (4.1). A local minimum C_p occurs at $x = 0.15$, where the trip wire is located. The lowest pressure coefficient occurs near $x = 0.6$. The shape of the profile in the fringe region is caused by the additional driving force function that drives the turbulent flow back to a laminar state.

Skin friction coefficient is usually defined as $C_f = \tau_w / (0.5\rho_\infty u_\infty^2)$. This value is affected by the calculation of freestream velocity u_∞ , which is dependent on how to compute boundary layer thickness δ and u_∞ for compressible turbulent boundary layer with pressure gradients. However, there are no clear definition for calculating δ and u_∞ for this type of flow and different approximate calculation method would probably lead to different values. Spalart & Watmuff (1993) argued that the standard definition

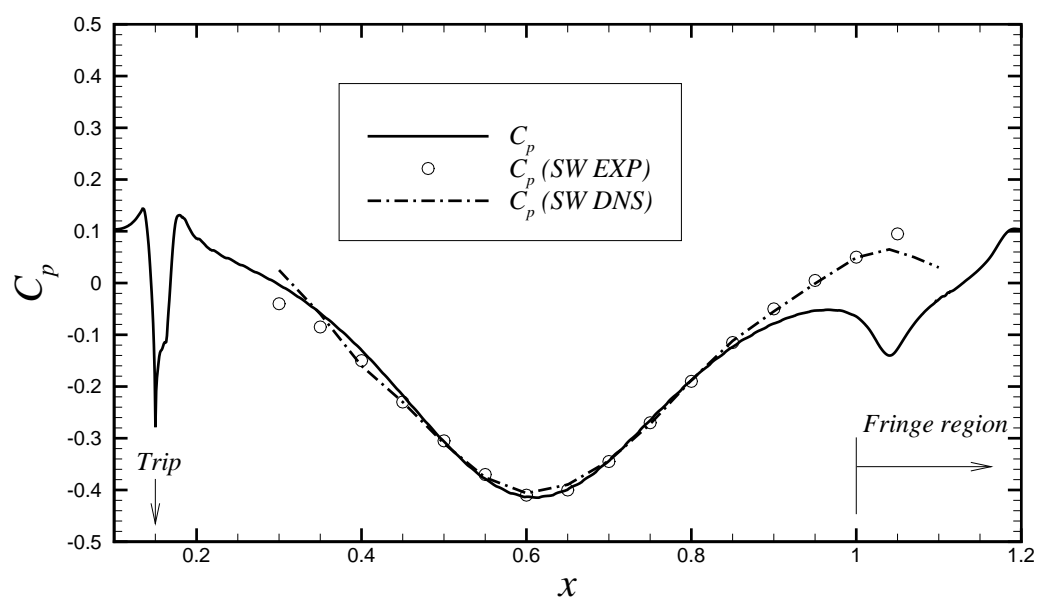


Figure 4.3: Wall pressure coefficients compared with the experiment and DNS data of the SW case

for boundary layer thickness δ where U is 99.5% of freestream velocity might fail completely for incompressible turbulent flow with pressure gradients. They proposed that δ could be decided manually to be 20% \sim 30% above the edge of the turbulent region, that is, the region with significant vorticity and turbulent shear stress, and the freestream velocity $U_\infty = \int_0^\infty \omega_z(y) dy$ etc. These definitions are used for the current case (U_∞ integration ends at the centre region instead of “ ∞ ”), although they are limited to incompressible flow (Spalart & Watmuff, 1993). Therefore, both $C_f = \tau_w / (0.5\rho_{\text{ref}}U_{\text{ref}}^2)$ and $C_f = \tau_w / (0.5\rho_\infty U_\infty^2)$ are calculated and shown in figure 4.4.

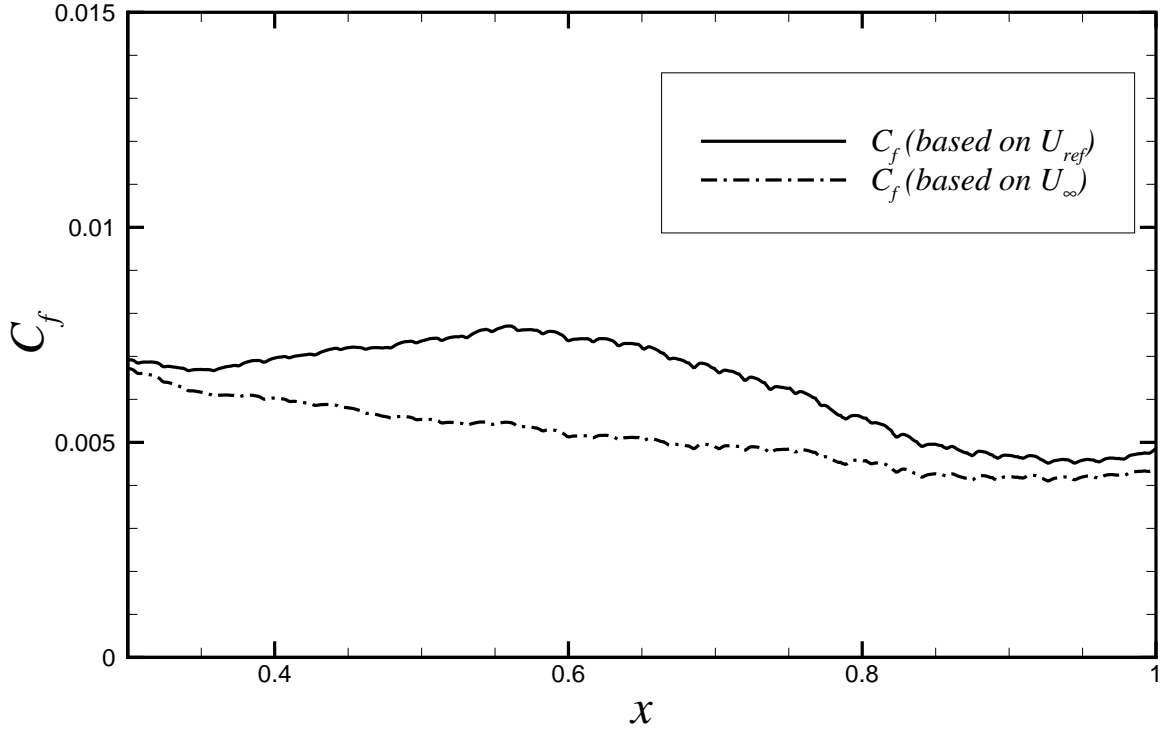


Figure 4.4: Skin friction coefficient scaled by $0.5\rho_{\text{ref}}U_{\text{ref}}^2$

Acceleration would cause flow relaminarization if the nondimensional acceleration (pressure gradient) parameter $K = \frac{\nu}{U_\infty^2} \frac{dU_\infty}{dx} \geq 3 \times 10^{-6}$. The maximum K in the

FPG region after the transition is $\sim 1.5 \times 10^{-6}$ for the current case, shown in figure 4.5.

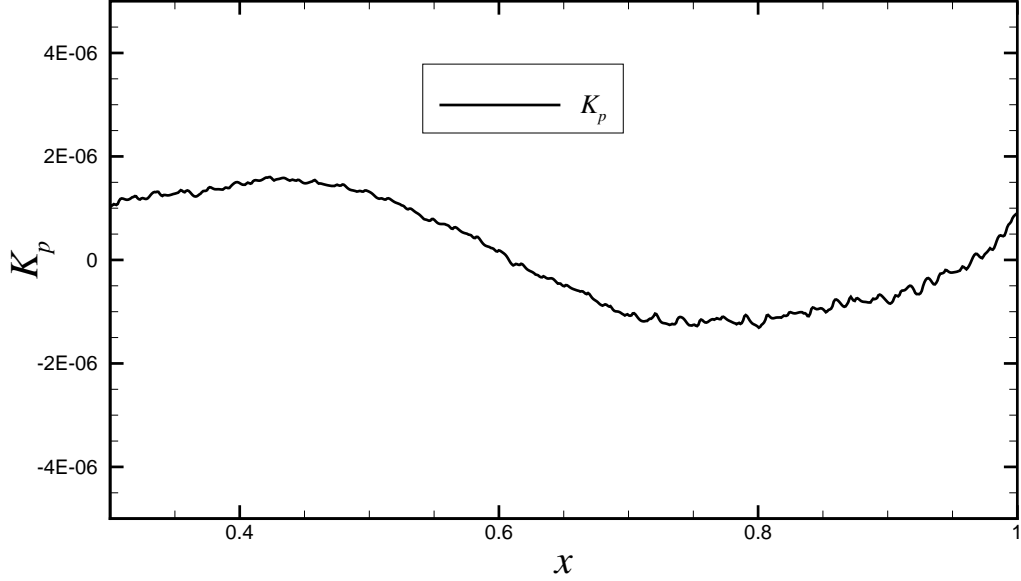


Figure 4.5: Nondimensional pressure gradient parameter

4.4 Transition

A close view of the transition at the bottom plane wall is given in figure (4.6) that shows a snapshot of iso-surfaces of streamwise velocity $u/U_{\text{ref}} = 0.8$. It can be seen that clear bulges are generated at $x \approx 0.17$, after the flow is tripped at $x = 0.15$. A bulge in the isosurfaces of streamwise velocity corresponds to transportation of low streamwise momentum away from the wall, or negative streamwise velocity fluctuations, as indicated in Wu & Moin (2009). The bulges are aligned well in the spanwise direction at $x \approx 0.17$ and then grow and become irregular and break down

to different shapes after that, in other words, turbulence is developing. The distance between the transition point and the cylinder tripping wire is $U(x_{trans} - x_{trip})/\nu = 2 \times 10^4$ (Schlichting, 1979), that is, $(x_{trans} - x_{trip})$ would be ~ 0.05 if a cylinder tripping wire were placed at $x = 0.15$. Here the trip device of the triangular prism seems to give an earlier transition than the cylinder.

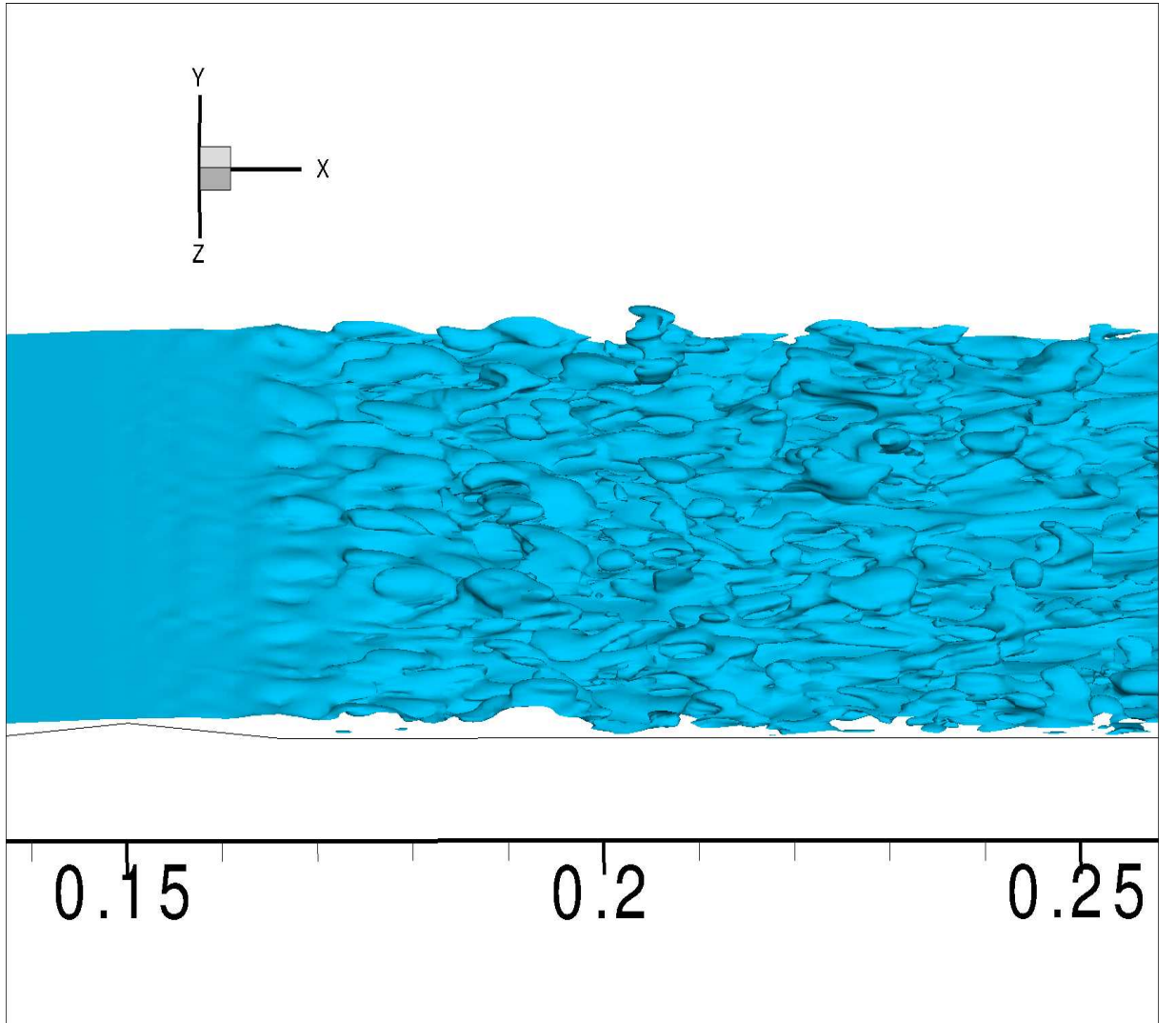


Figure 4.6: Iso-surfaces of streamwise velocity $u/U_{\text{ref}} = 0.8$ close to the transition at the bottom wall.

Figure (4.7) gives iso-surfaces of streamwise velocity $u/U_{\text{ref}} = 0.8$ for the whole computational domain. The top figure of (4.7) indicates that the flow close to the top wall remains laminar until after it enters the APG region. The transition to turbulence can be clearly seen. The bottom figure of (4.7) shows that the bulges are observed to grow after the trip ($x = 0.15$), then their sizes are getting smaller in the FPG region due to the acceleration. The structures are getting larger and more complex (more momentum transport) in the APG region due to the deceleration and finally returns to laminar in the fringe region.

4.5 Local profiles

4.5.1 Mean profiles

The mean inlet streamwise velocity close to the bottom plane wall versus the Blasius boundary layer velocity profile is presented in figure 4.8. It can be seen that the current profile is very close to the Blasius boundary layer profile, which is similar to the SW case. The slight difference is due to the presence of the top wall.

Mean streamwise velocities, scaled by local friction velocity u_τ , at different streamwise locations are compared with the DNS data of the SW case in figures (4.9) and (4.10). The agreement is satisfactory. A clear drop of the velocity profile at the region of log-layer can be seen as the flow develops from the FPG region to the APG region. It is mainly because of the influence of the pressure gradient that affects the low speed fluid in the lower log layer and also has an influence on downstream of the APG region (ie. $x = 1.0$), as indicated in figure (4.10).

Mean streamwise velocities, scaled by U_{ref} , at different streamwise locations are

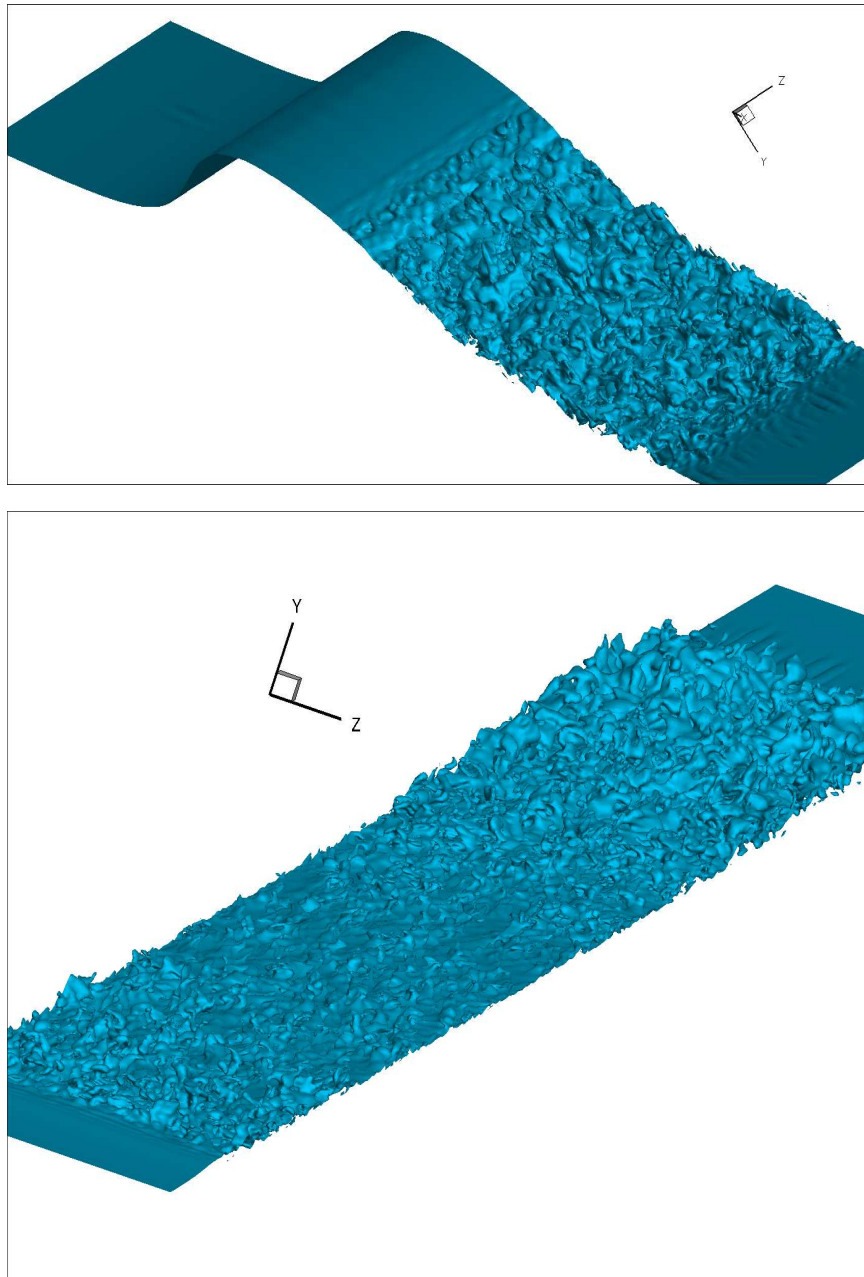


Figure 4.7: Iso-surfaces of streamwise velocity $u/U_{\text{ref}} = 0.8$ for the top wall (top) and bottom wall (bottom).

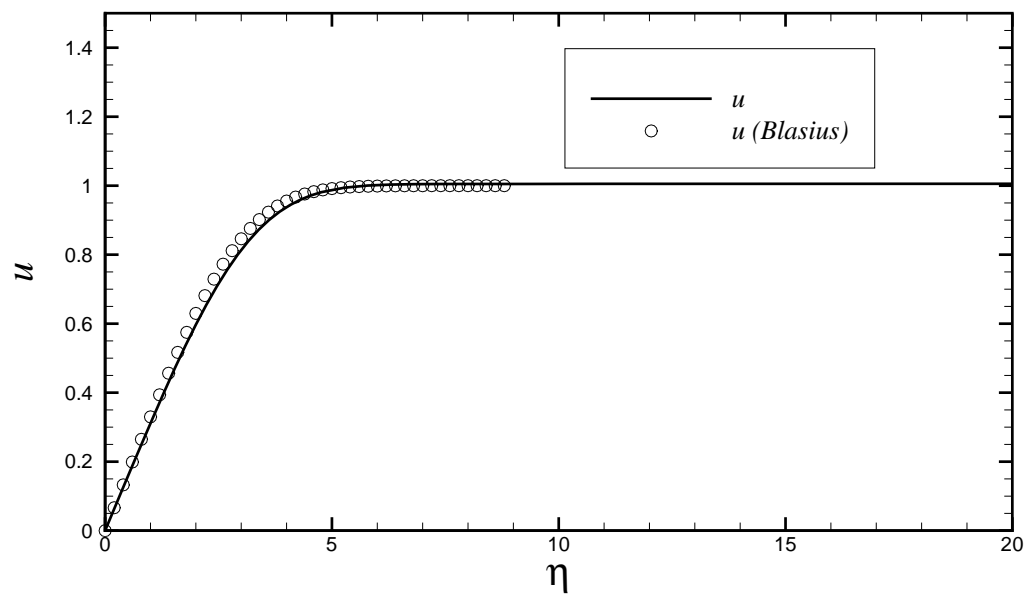


Figure 4.8: Mean inlet streamwise velocity close to the bottom wall and the Blasius boundary layer velocity profile.

given in figure (4.11). It can be seen that the velocities $U(y)$ at the centre region of each streamwise location are not constant, which makes the classical definition of boundary layer thickness at which U is 99.5% of free stream may fail completely (Spalart & Watmuff, 1993). The velocity profile at $x = 0.7$ shows a small separation region close to the top wall.

Mean pressure coefficients, scaled by $\rho_{\text{ref}}U_{\text{ref}}^2$, at different streamwise locations are provided in figure (4.12), compared with the SW case. The agreement is good. It indicates that the trend of pressure profiles in the wall-normal direction is nearly opposite to the trend of velocity profiles shown in figure (4.11), which can be roughly explained by the Bernoulli equation. It also indicates that the top wall has a much broader pressure range, for example, the pressure difference between $x = 0.6$ and $x = 0.8$ on the top wall is much higher than that on the bottom plane wall, which roughly explains the flow is separated close to the top wall instead of the bottom wall at around $x \approx 0.7$, shown in figure (4.11). In addition there is small local minimum of C_p at $x = 0.7$ close to the top wall, which corresponds to the location of separation bubble. It is interesting to note that the pressure coefficient on the top wall at $x = 0.9$ is smaller than $x = 0.8$.

Mean streamwise pressure gradients, scaled by $\rho_{\text{ref}}U_{\text{ref}}^2/L_x$, at different streamwise locations are presented in figure (4.13), in order to clearly indicate the FPG and APG regions. It can be seen that $dp/dx < 0$ is observed between the bottom and top walls for $x = 0.55$ and $x = 0.60$. It has a much lower value close to the top wall which provides stronger acceleration. $dp/dx > 0$ close to the bottom wall for $x = 0.70$, $x = 0.80$ and $x = 0.90$. The profiles for $x = 0.70$ and $x = 0.80$ are very close except for the region close to the top wall where $dp/dx < 0$ occurs around the flow separation

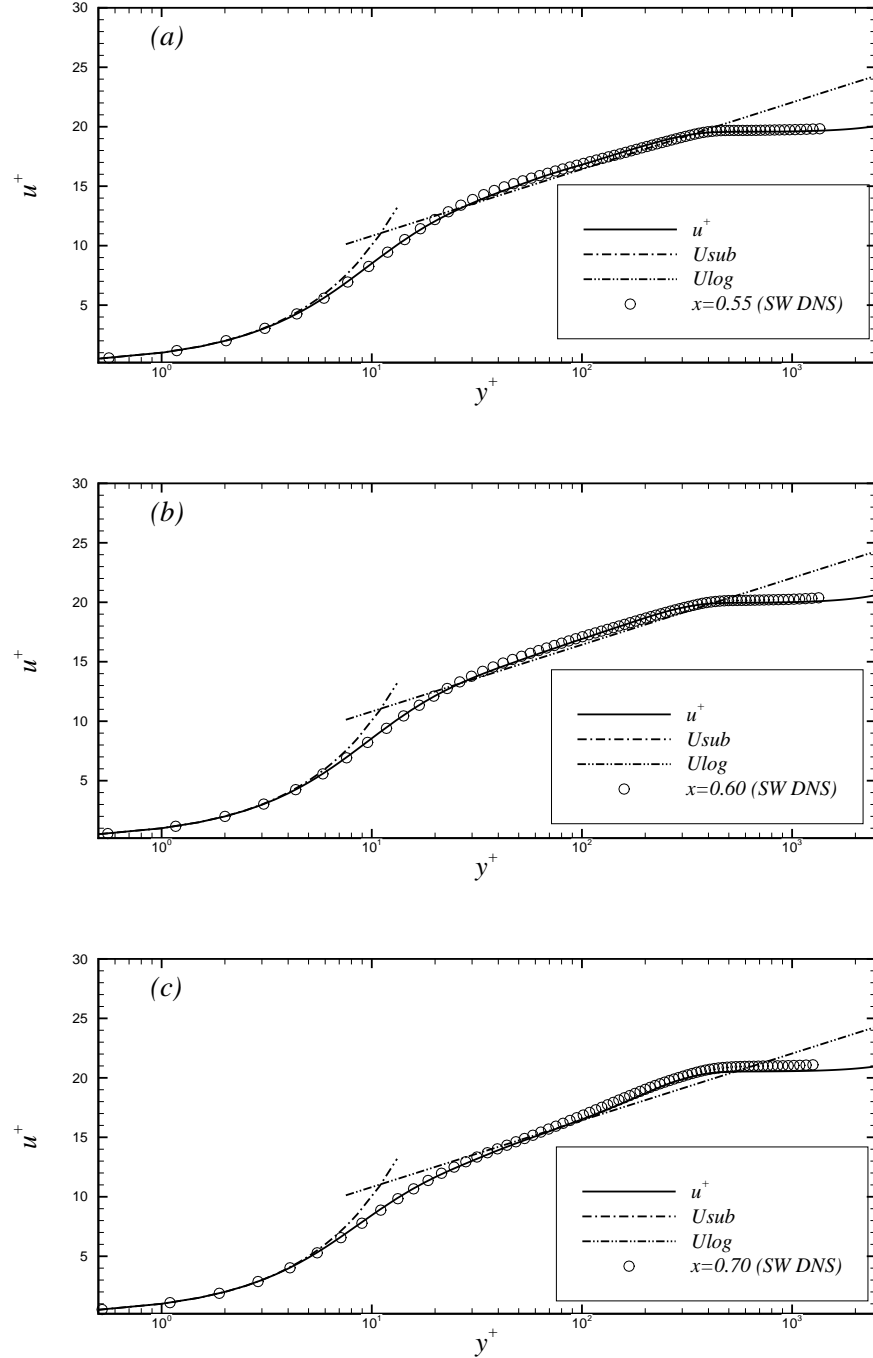


Figure 4.9: Mean streamwise velocities close to the bottom plane wall versus the log law and the SW case. (a) $x = 0.55$; (b) $x = 0.60$; (c) $x = 0.70$. $U_{sub} = y^+$; $U_{log} = 1/\kappa \ln(y^+) + B$, where $\kappa = 0.41$, $B = 5.2$.

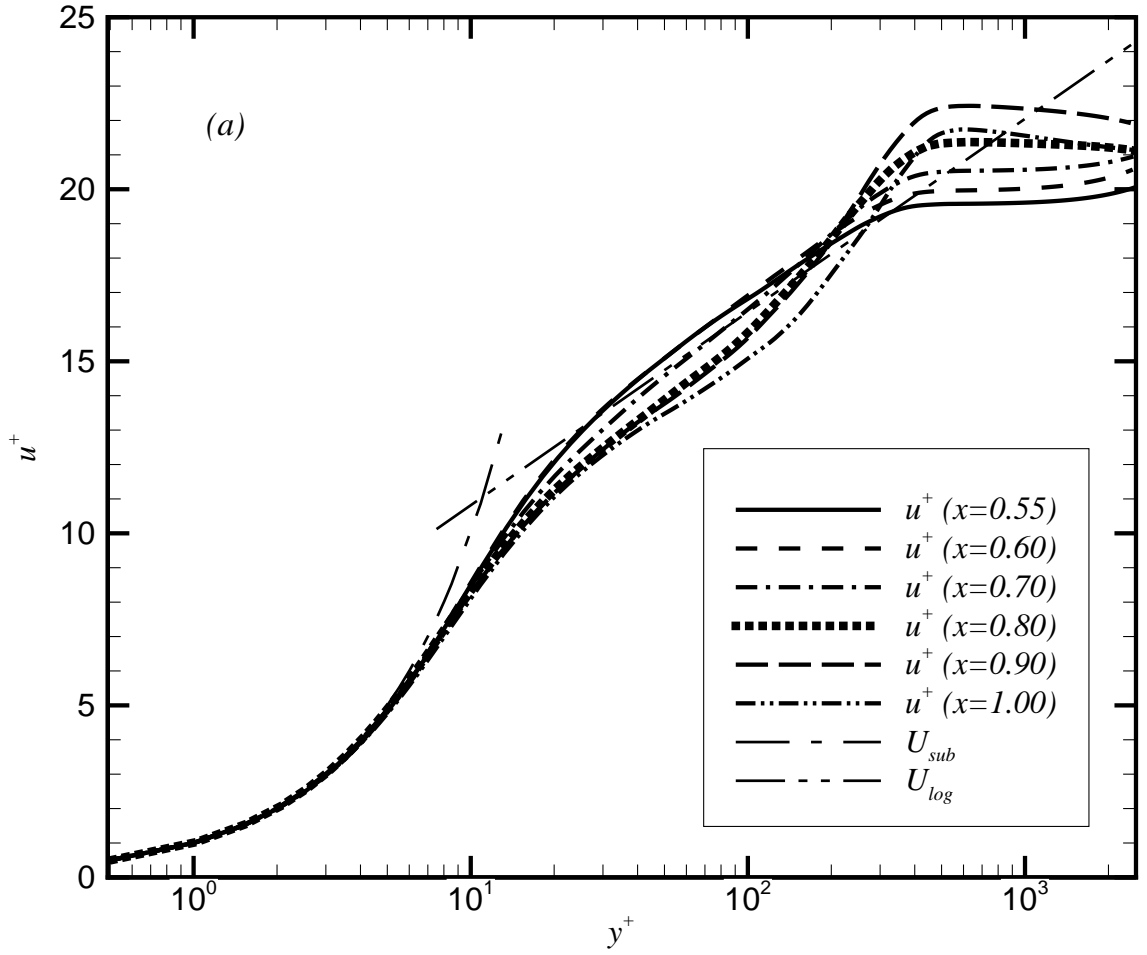


Figure 4.10: Mean streamwise velocity profiles close to the bottom plane wall versus the log law at different streamwise locations. $U_{sub} = y^+$; $U_{log} = 1/\kappa \ln(y^+) + B$, where $\kappa = 0.41$, $B = 5.2$.

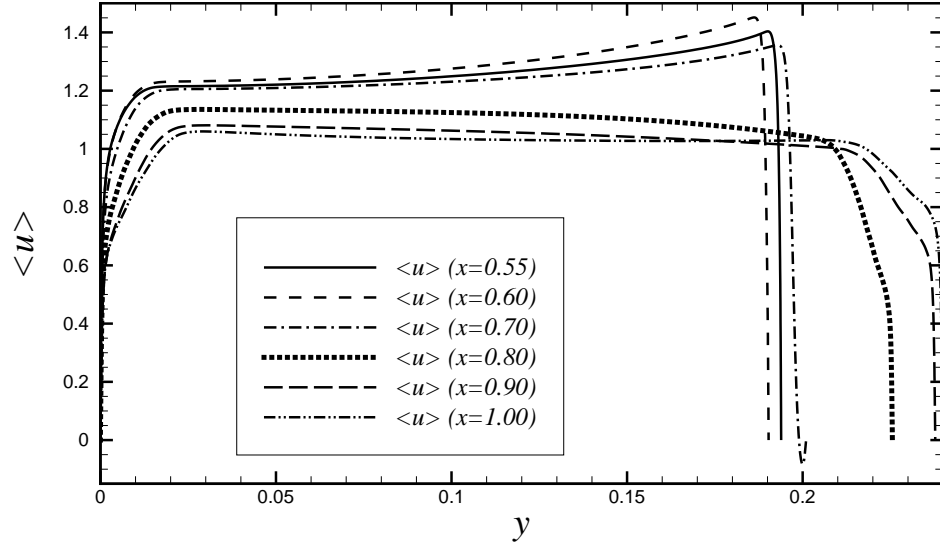


Figure 4.11: Mean streamwise velocity profiles at different streamwise locations

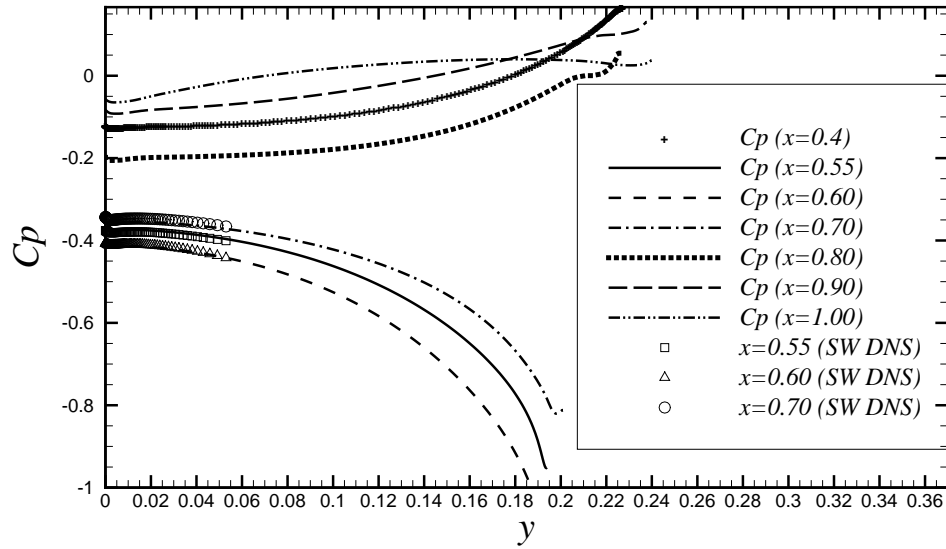


Figure 4.12: Mean pressure coefficients at different streamwise locations

region close to the top wall for $x = 0.70$. The profile at $x = 1.0$ behaves differently: $dp/dx < 0$ close to the both bottom and top walls, but $dp/dx > 0$ for the centre region. This also explains the complicated behaviour for the plots at $x = 1.0$ in the following sections.

Figure (4.14) displays the mean wall-normal and spanwise velocities scaled by U_{ref} at different streamwise locations. The mean wall-normal velocity profiles show a similar trend as figure (4.13) close to the bottom wall, such as, negative profile for $x = 0.55$, positive profiles for $x = 0.7$, $x = 0.8$ and $x = 0.9$. Again, small positive values are observed around the separation region close to the top wall at $x = 0.7$. The mean spanwise velocity profiles are essentially zero for all streamwise locations.

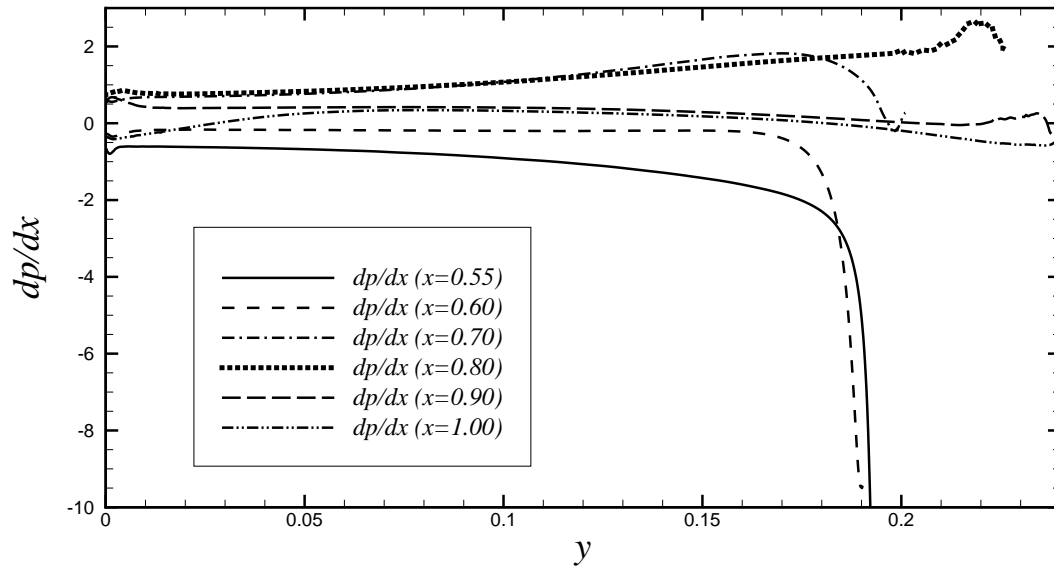


Figure 4.13: Mean streamwise pressure gradients at different streamwise locations. d denotes partial derivative, the same hereafter.

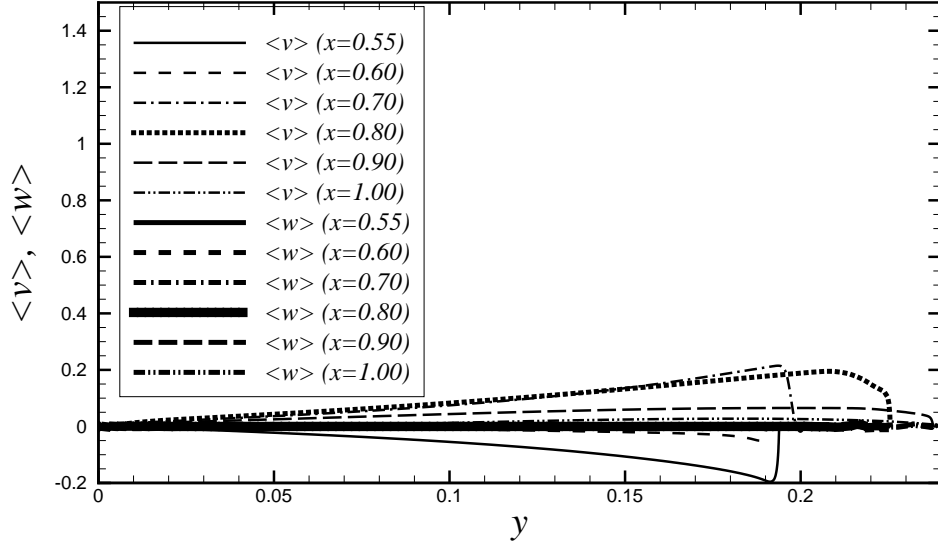


Figure 4.14: Mean wall-normal and spanwise velocity profiles at different streamwise locations

4.5.2 Second-order statistics

RMS streamwise, wall-normal, and spanwise velocity fluctuations close to the bottom plane wall at different streamwise locations, scaled in wall units, are compared with the DNS data of the SW case in figures (4.15) and (4.16). The general collapse of profiles in comparison is fair. The y location of peak values of RMS streamwise velocity fluctuations remains similar, although peak values slightly increase as the flow develops from FPG to APG regions, except for the wake of APG region, such as $x = 1.0$. Pressure gradient seems to have a stronger effect on the RMS wall-normal and spanwise velocity fluctuations: not only their peak values but also their locations of peak values increase significantly from FPG to APG. It also indicates a clear trend that the fluctuations in the region around $y^+ = 100 \sim 300$ increase and gradually to form a local peak as flow evolves from FPG to APG.

Figure (4.17) displays the RMS velocity fluctuations (scaled by U_{ref}) between the bottom and top walls at different streamwise locations. It indicates that all three components of RMS values close to the bottom wall increase as the flow evolves downstream except for the region $x = 1.0$, which can be explained by figure (4.13). RMS profiles close to the separation bubble at $x \approx 0.7$ close to the top wall behave differently: There are two local maxima on the RMS streamwise velocity profile and RMS spanwise velocity fluctuations are much smaller than the wall-normal velocity fluctuations. The first maximum close to the top wall occurs at $y \approx 0.2$, which corresponds to the largest negative mean velocity at $x = 0.7$, in other words, the edge of the separation bubble. The local minimum between the two maxima corresponds to the center of the separation bubble.

Figure (4.18) shows the RMS pressure fluctuations at different streamwise locations. The top figure shows that the peak RMS pressure fluctuations scaled by $\rho_{\text{ref}} U_{\text{ref}}^2$ close to the bottom plane wall do not change much except for the wake region at $x = 1.0$ as the flow evolves downstream; however, significant changes occur close to the location of flow separation at $x = 0.7$ close to the top wall where there is an extremely high value. This is due to the unstable separation bubble. The inner scaling of the RMS pressure fluctuation close to the bottom plane wall shown in the bottom figure, significantly increases as the flow develops downstream, which is mainly due to the decrease of skin friction.

The figure (4.19) gives RMS vorticity fluctuations, normalized by the mean shear at the bottom plane wall τ_w/μ_w , close to the bottom plane wall in wall units. It indicates for all three components of RMS vorticity fluctuations that the location of local maximum and minimum does not vary much with pressure gradient, although

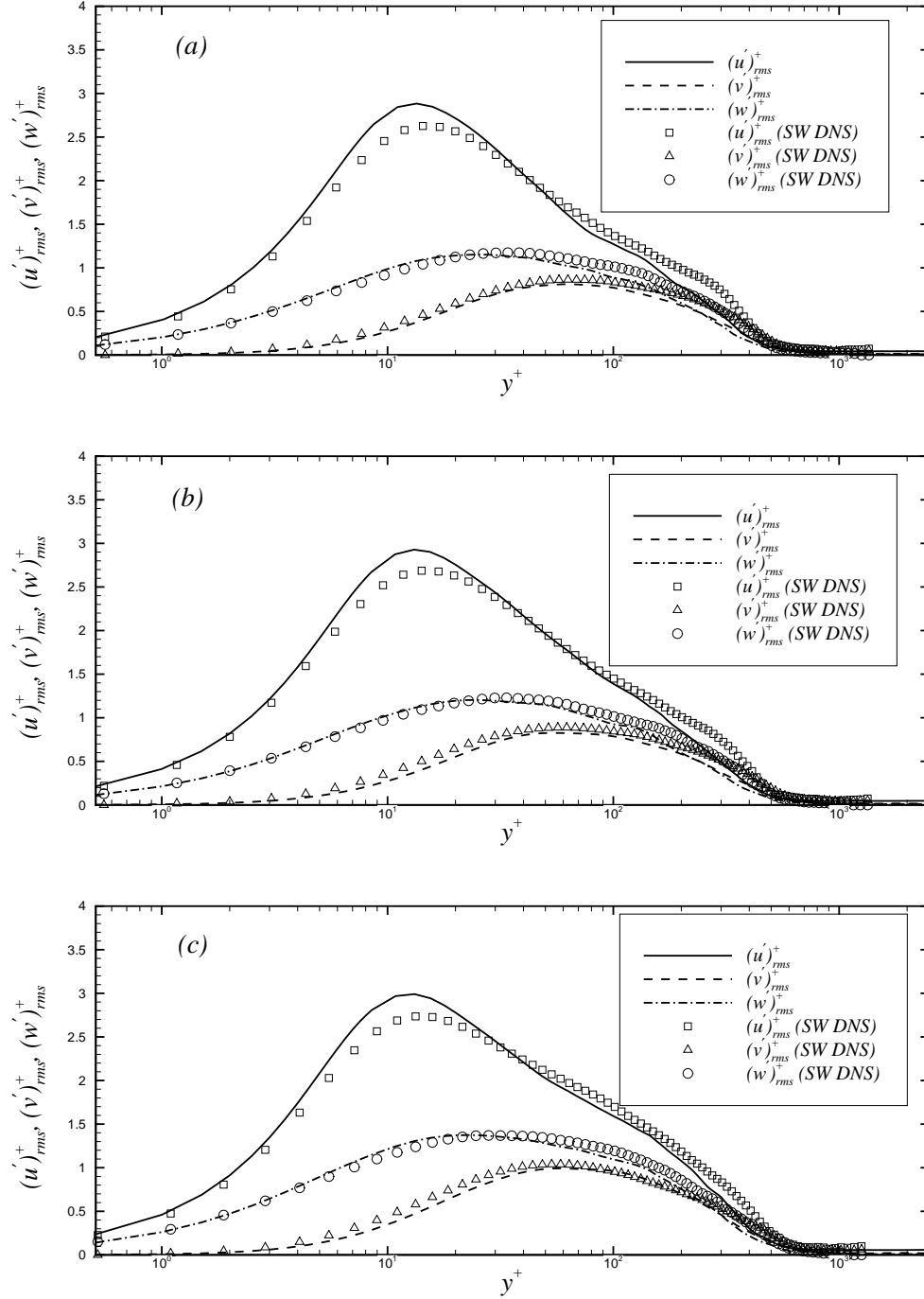


Figure 4.15: RMS velocity fluctuations, scaled by u_τ , close to the bottom plane wall versus the DNS data of the SW case in wall units. (a) $x = 0.55$; (b) $x = 0.60$; (c) $x = 0.70$.

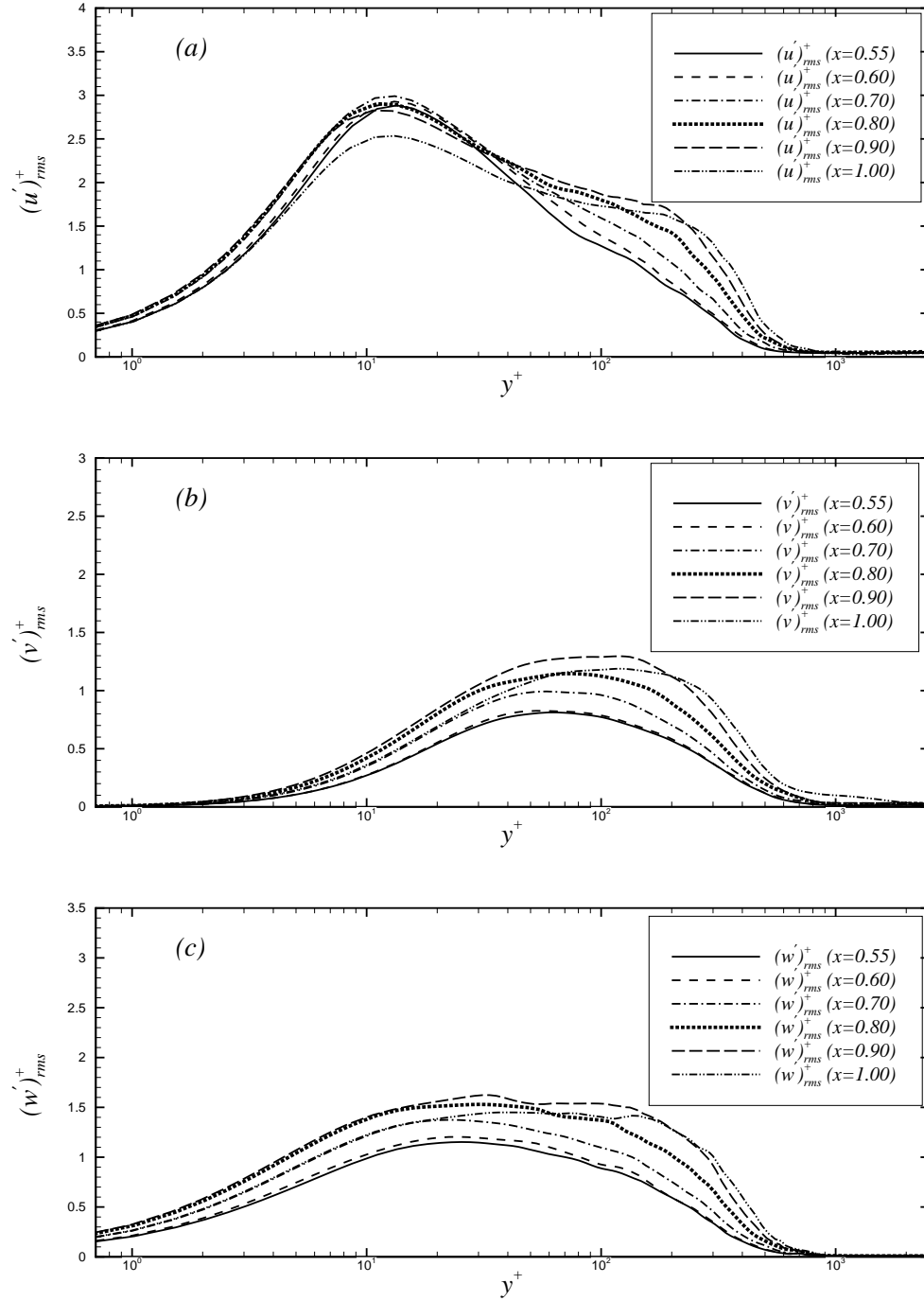


Figure 4.16: RMS streamwise (top), wall-normal (middle), and spanwise (bottom) velocity fluctuations, scaled by u_τ , close to the bottom wall at different streamwise locations in wall units.

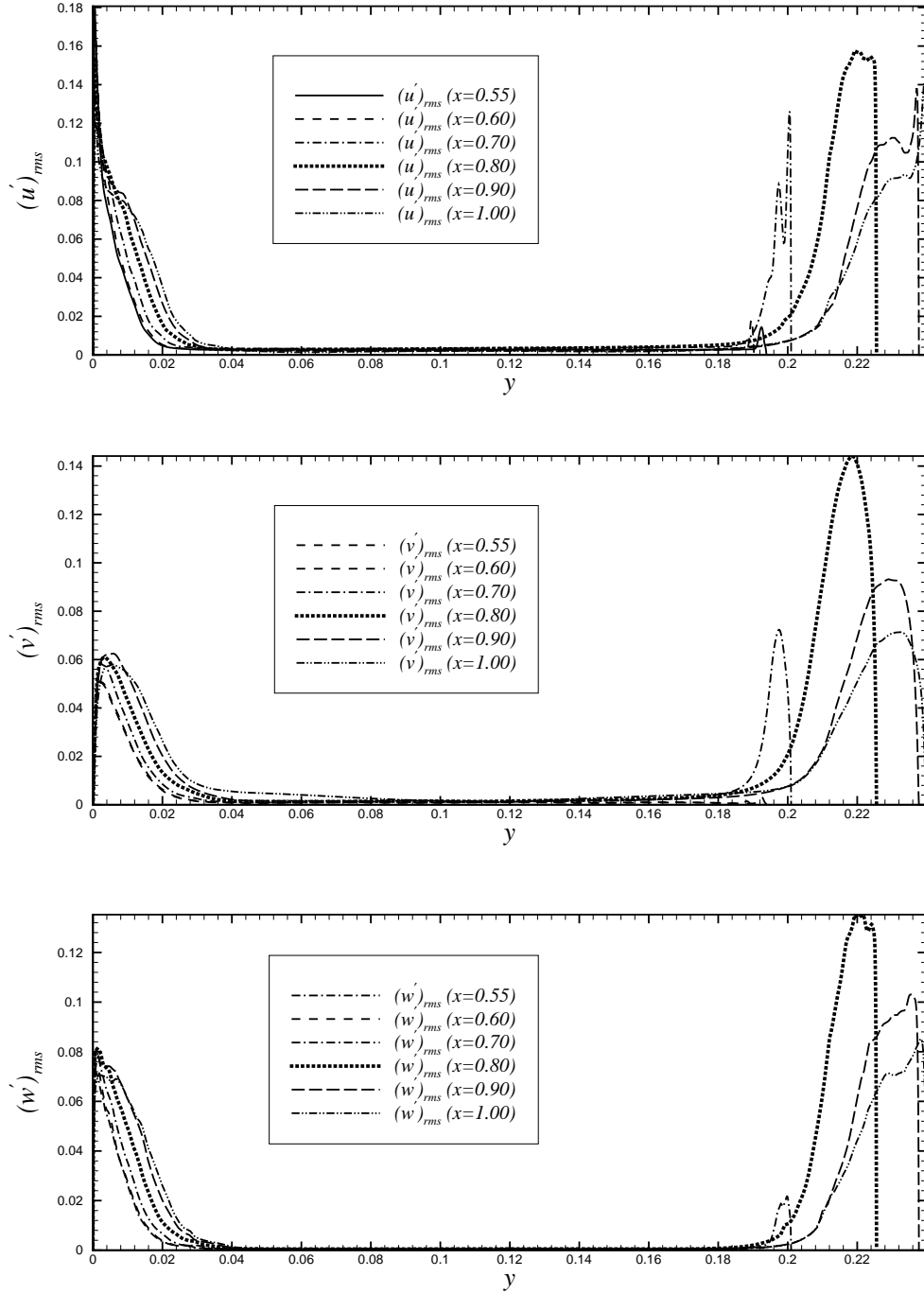


Figure 4.17: RMS streamwise (top), wall-normal (middle), and spanwise (bottom) velocity fluctuations, scaled by U_{ref} , between the bottom and top walls at different streamwise locations.

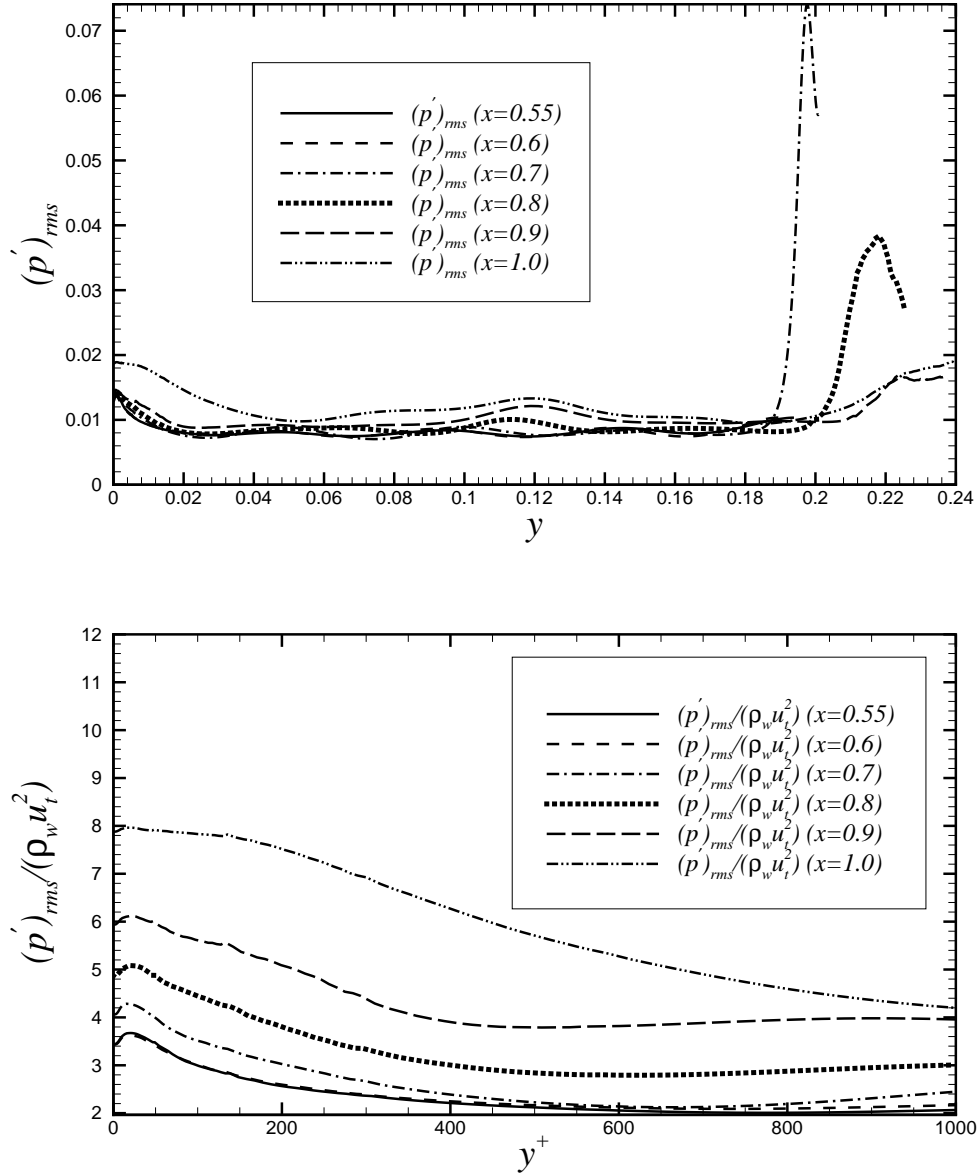


Figure 4.18: RMS pressure fluctuations between the bottom and top walls, normalized by $\rho_{\text{ref}} U_{\text{ref}}^2$ in global units (top); RMS pressure fluctuations close to the bottom plane wall, normalized by the local wall shear stress in wall units (bottom).

both the peak values and the general profiles increase as flow develops from FPG to APG regions except for the wake region around $x = 1.0$. The profiles at $x = 1.0$ close to wall ($y^+ < \sim 260$) is smaller than $x = 0.9$ because $dp/dx < 0$ close to the bottom wall at $x = 1.0$ (see figure 4.13), in other words, it is not in the APG region any more. However, upstream APG flow still has an influence on the region away from the wall at $x=1.0$ (say, $y^+ > \sim 260$) which causes $dp/dx > 0$ at this region. That is why an increase is observed for this region. RMS spanwise vorticity fluctuations presented in bottom figure of (4.19) seem to collapse well in the region around $y^+ \approx 30$ although the values at the wall are a little different.

RMS vorticity fluctuations, normalized by U_{ref}/L_x , between the bottom and top walls are presented in figure (4.20). The profiles close to the bottom wall display similar behaviour as figure (4.19). Streamwise and wall-normal vorticity fluctuations at $x = 0.7$ close to the top wall are very small compared with other locations at APG region, however, the spanwise vorticity fluctuation increase dramatically close to the top wall, due to the unsteady separation.

Turbulence, viscous and total shear stresses at four different streamwise locations are illustrated in figures (4.21) and (4.22) respectively. The figures indicate that both the peak turbulence shear stress and the region with significant turbulent shear stress increase as the flow moves from the FPG region to the APG region (from figure *a* to figure *e*). The total shear stress is not linear with the distance from the wall. The slope of total shear stress (normalized by the local wall shear stress) profile close to the wall increases from negative to positive values as the flow goes from the FPG region to the APG region. The slope of the total shear stress profile at $x = 1.0$ is negative close to the wall and then become positive away from the wall which is

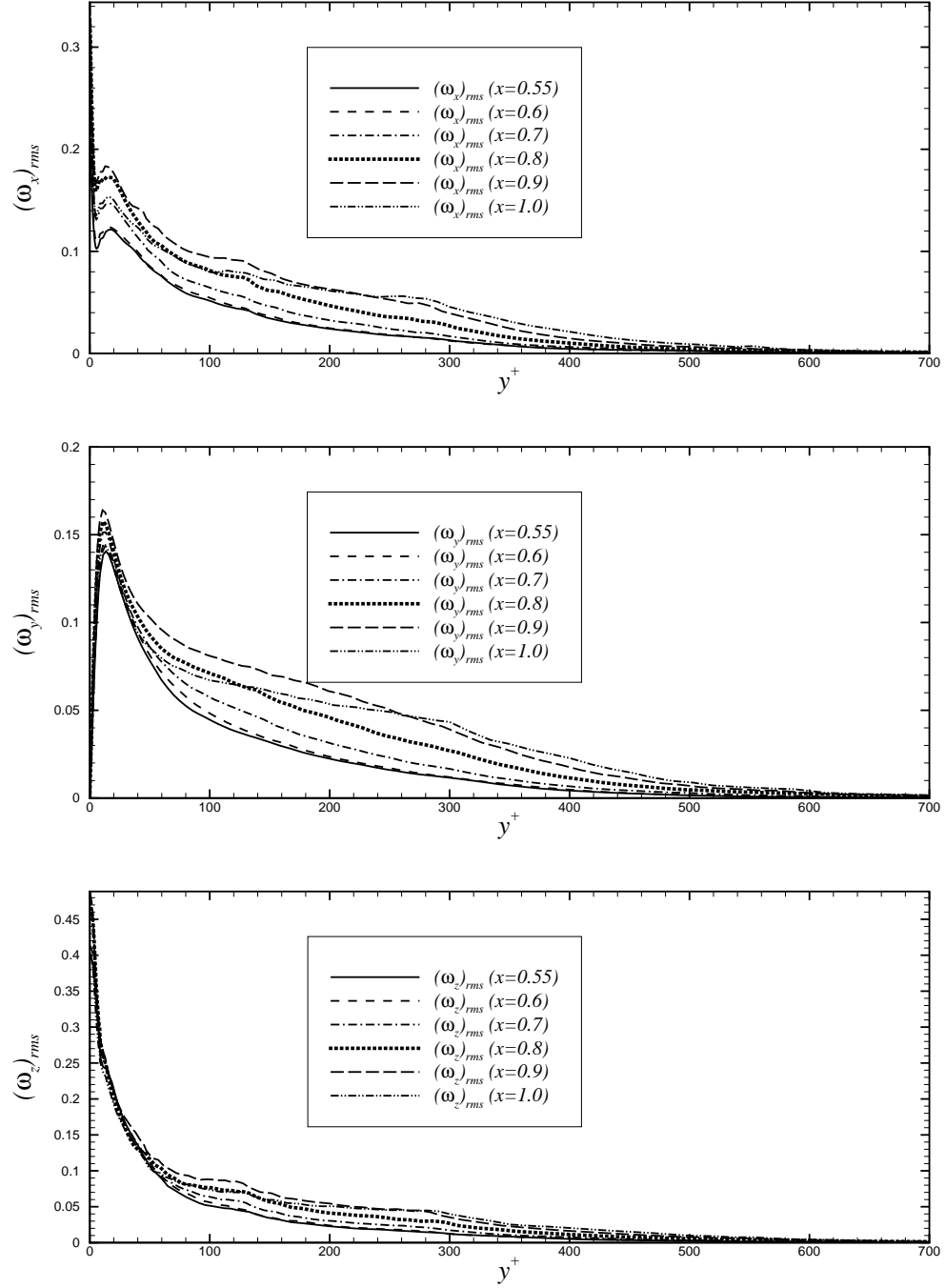


Figure 4.19: RMS streamwise (top), wall-normal (middle), and spanwise (bottom) vorticity fluctuations close to the bottom plane wall, normalized by the mean shear at the wall τ_w/μ_w in wall units.

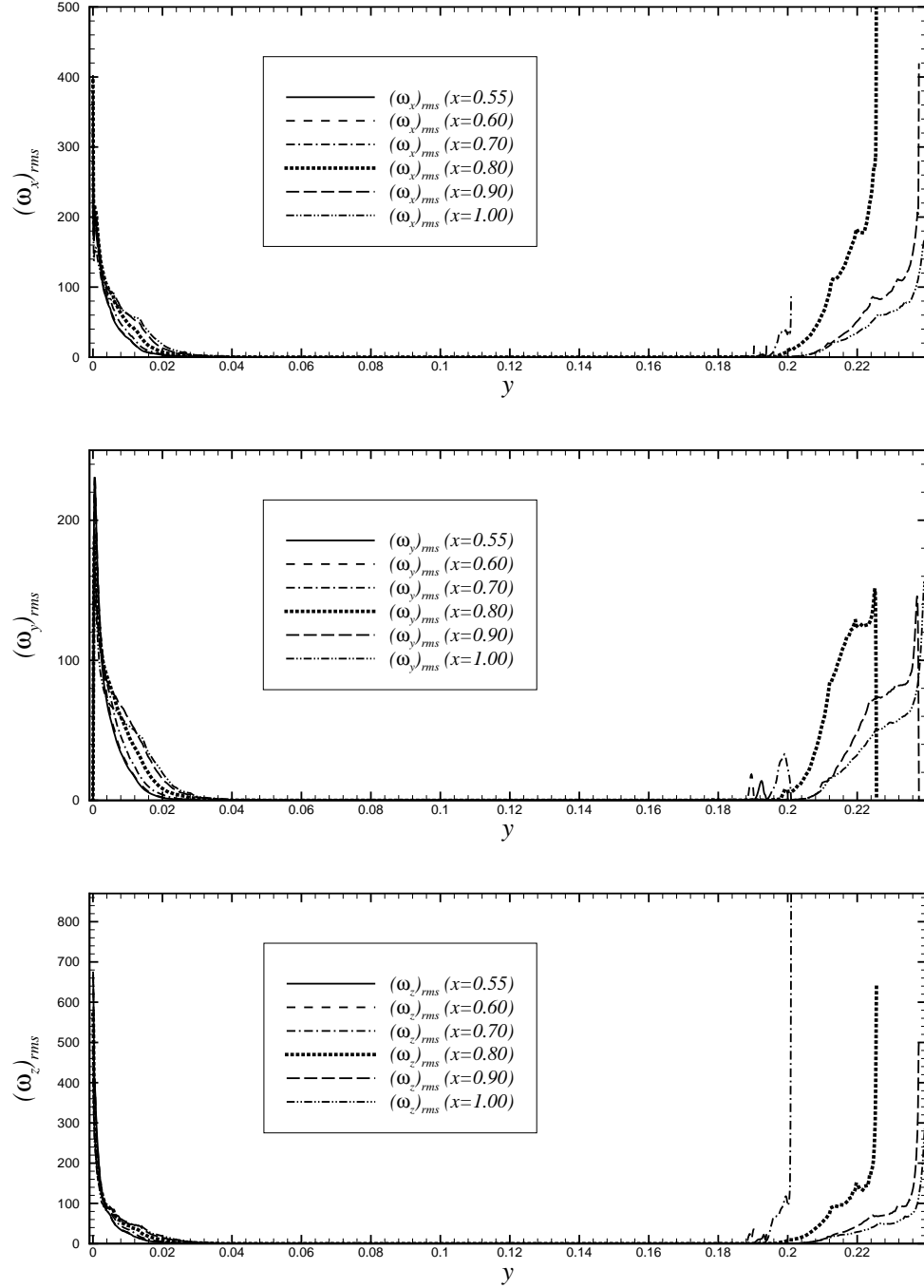


Figure 4.20: RMS streamwise (top), wall-normal (middle), and spanwise (bottom) vorticity fluctuations between the bottom and top walls, normalized by the U_{ref}/L_x in global units.

mainly because the region close to the wall at $x = 1.0$ is not in an APG region any more, see figure (4.13), but the region away from the wall is still influenced by the upstream flow in the APG region.

4.6 Vorticity and pressure gradients correlations

The cross-correlation coefficient (between variable a and variable b) is defined as:

$$\rho_{a:b} = \frac{\langle a' b' \rangle}{\langle a' a' \rangle^{0.5} \langle b' b' \rangle^{0.5}} \quad (4.2)$$

The momentum equation on an isothermal wall can be simplified as (see the previous chapter):

$$\frac{\partial p}{\partial x} = -\mu \frac{\partial \omega_z}{\partial y} + \frac{\partial u}{\partial y} \frac{\partial \mu}{\partial y} + \frac{4}{3} \mu \frac{\partial \Theta}{\partial x} + \rho f_x. \quad (4.3)$$

$$\frac{\partial p}{\partial y} = -\mu \frac{\partial \omega_x}{\partial z} + \mu \frac{\partial \omega_z}{\partial x} + \frac{4}{3} \mu \frac{\partial \Theta}{\partial y} + \frac{4}{3} \Theta \frac{\partial \mu}{\partial y} + \rho f_y. \quad (4.4)$$

$$\frac{\partial p}{\partial z} = \mu \frac{\partial \omega_x}{\partial y} + \frac{\partial w}{\partial y} \frac{\partial \mu}{\partial y} + \frac{4}{3} \mu \frac{\partial \Theta}{\partial z} + \rho f_z. \quad (4.5)$$

or in a more concise form:

$$\frac{\partial p}{\partial x} = -\frac{\partial \mu \omega_z}{\partial y} + \frac{4}{3} \frac{\partial \mu \Theta}{\partial x} + \rho f_x. \quad (4.6)$$

$$\frac{\partial p}{\partial y} = -\frac{\partial \mu \omega_x}{\partial z} + \frac{\partial \mu \omega_z}{\partial x} + \frac{4}{3} \frac{\partial \mu \Theta}{\partial y} + \rho f_y. \quad (4.7)$$

$$\frac{\partial p}{\partial z} = \frac{\partial \mu \omega_x}{\partial y} + \frac{4}{3} \frac{\partial \mu \Theta}{\partial z} + \rho f_z. \quad (4.8)$$

There is no driving force in the FPG and APG regions of the current computational domain, that is, $f_x = f_y = f_z = 0$. The dilatation Θ on the wall is actually equal to $\partial v / \partial y$ as $\partial u / \partial x = \partial w / \partial z = 0$. Then $\Theta' = \partial v' / \partial y$. Compared with fully developed

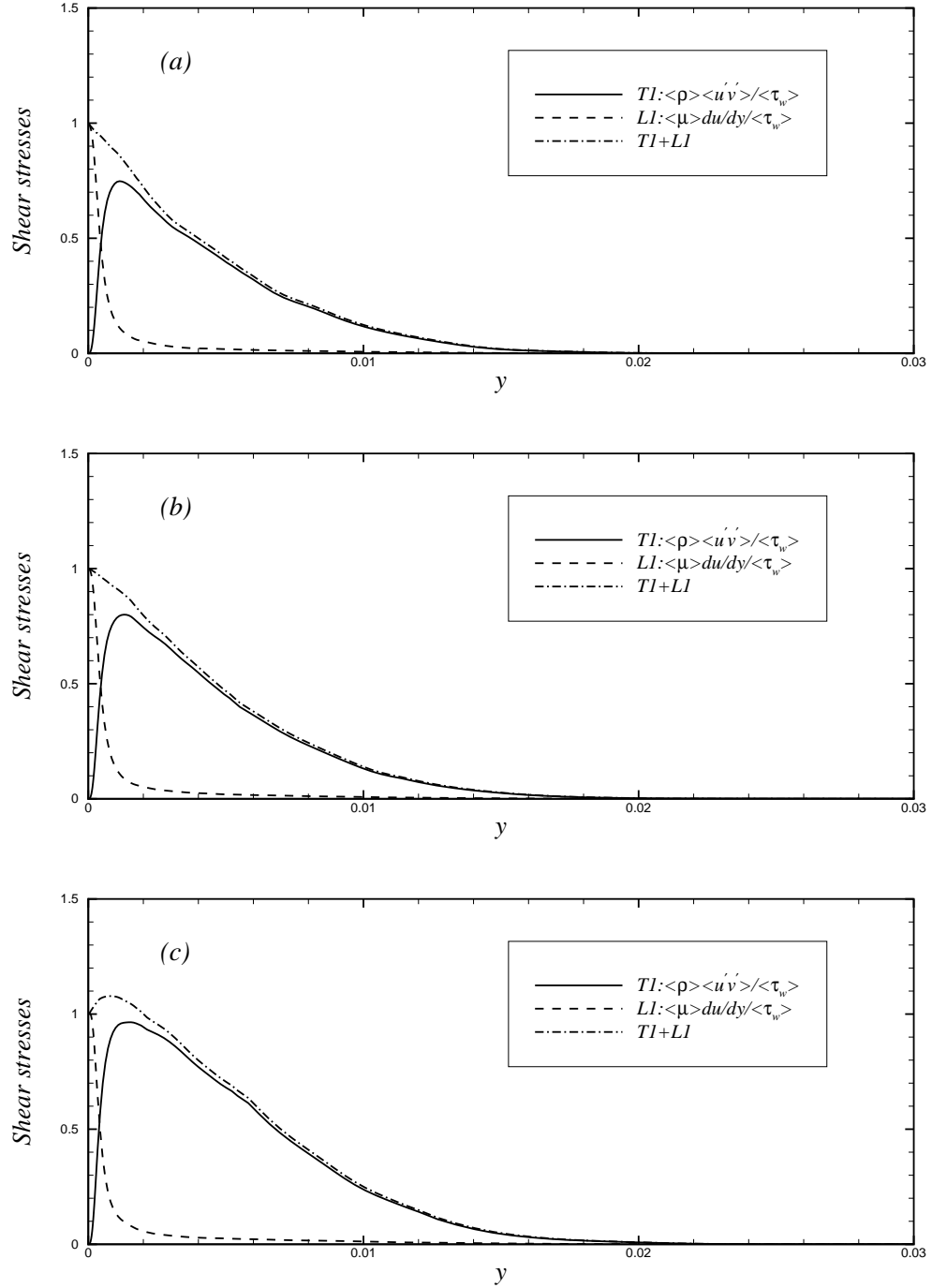


Figure 4.21: Turbulence, viscous, and total shear stresses normalized by the wall shear stress τ_w . (a) $x = 0.55$; (b) $x = 0.60$; (c) $x = 0.70$. Ll represents viscous shear stress; Tl represents turbulent shear stress $\langle \rho \rangle \langle u'v' \rangle / \tau_w$; $Ll + Tl$ represents the total shear stress.

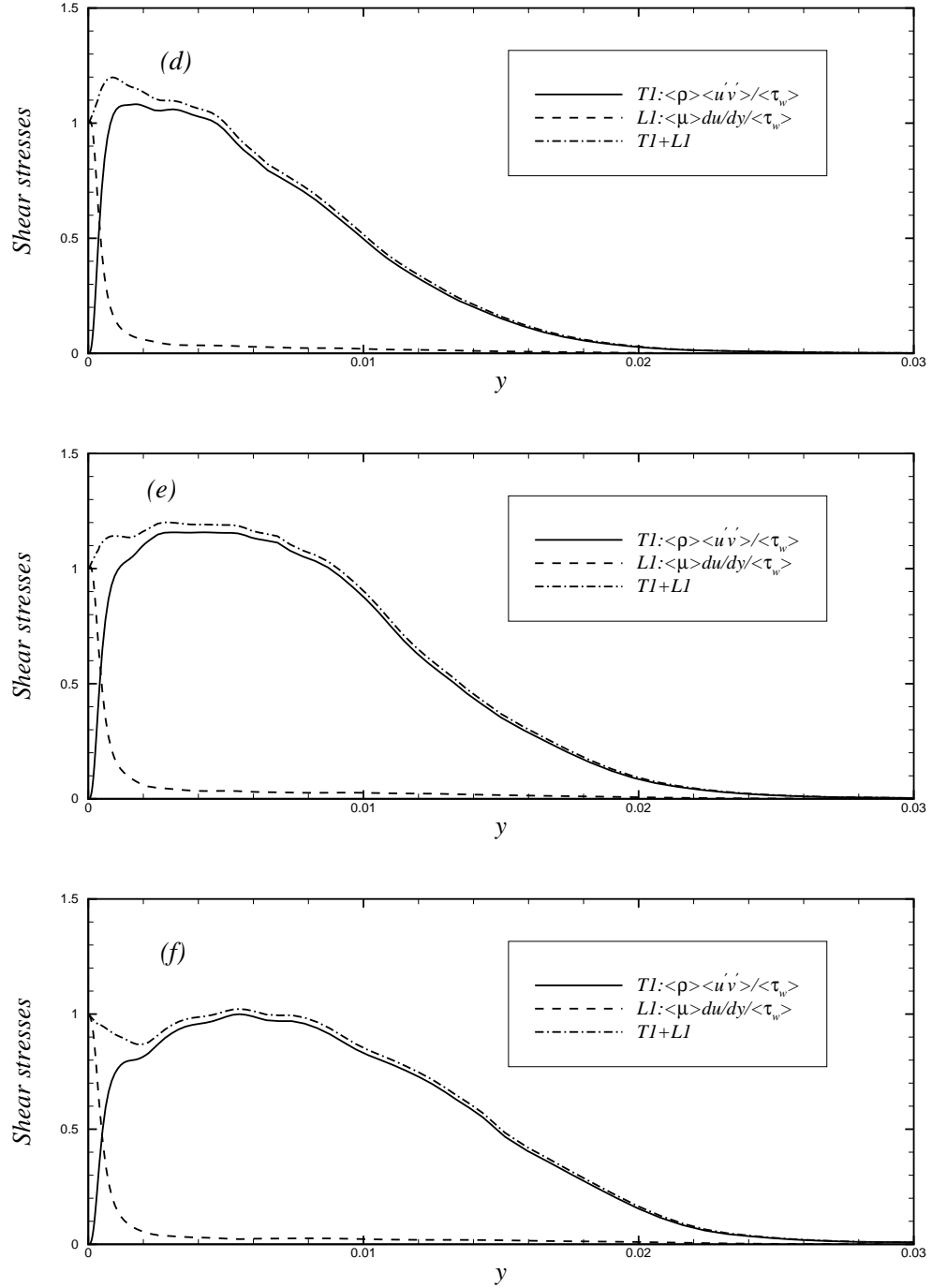


Figure 4.22: Turbulence, viscous, and total shear stresses normalized by the wall shear stress τ_w . (d) $x = 0.80$; (e) $x = 0.90$; (f) $x = 1.00$. Ll represents viscous shear stress; Tl represents turbulent shear stress $\langle \rho \rangle \langle u'v' \rangle / \tau_w$; $Ll + Tl$ represents the total shear stress.

turbulent channel flow, the mean dilatation gradient $\langle \partial\Theta/\partial x \rangle$ for turbulent flow with FPG and APG is not zero, see figure 4.14.

The cross-correlations between pressure gradients and two type of vorticity fluxes $\partial\mu\omega_i/\partial x_j$ and $\partial\omega_i/\partial x_j$ have been generated to investigate the influence of pressure gradients, dilatation, viscosity etc. It has been found that there is no difference for the correlation between pressure gradient and two fluxes for the current case. Only correlations between pressure gradients and vorticity fluxes $\partial\omega_i/\partial x_j$ are presented for simplicity.

The correlations between the pressure gradients and vorticity fluxes in above equations on both walls are presented in figure (4.23). Figure (a) shows the correlations on the bottom wall. It indicates that the influence of pressure gradient through FPG and APG regions on the correlations is very small, although it seems that the correlation in the APG region is slightly higher. It is high in either negative or positive sense for the correlation between the streamwise pressure gradient and spanwise vorticity flux in the wall normal direction $(\rho_{\partial p/\partial x:\partial\omega_z/\partial y})$, and the correlation between the spanwise pressure gradient and streamwise vorticity flux in the wall normal direction $(\rho_{\partial p/\partial z:\partial\omega_x/\partial y})$. This is similar as fully developed channel flow but with slightly lower values in the magnitude. However, the correlation between the wall-normal pressure gradient and streamwise vorticity flux in the spanwise direction $(\rho_{\partial p/\partial y:\partial\omega_x/\partial z})$, and as well as the correlation between wall-normal pressure gradient and spanwise vorticity flux in the streamwise direction $(\rho_{\partial p/\partial y:\partial\omega_z/\partial x})$ are rather poor. The magnitudes are smaller than the fully developed channel flow.

The above correlations between pressure gradients and vorticity fluxes show similar performance as those of fully developed turbulent channel flow case of $Ma = 0.2$ (see

the previous chapter), but with slightly lower values at the wall. The possible reason is the influence of dilatation term (Θ). As the flow evolves downstream, the density at the wall changes with changing pressure as the wall is isothermal. This causes the dilatation to vary, which weakens the correlation between pressure gradient and wall vorticity flux.

Figure (b) of (4.23) shows the correlations on the top wall. It indicates that the correlations on the top wall show similar performance as the bottom wall after the flow transitions to turbulence, or, in the region $\sim 0.8 < x < \sim 1.0$. The magnitudes of correlation ($\rho_{\partial p/\partial x:\partial \omega_z/\partial y}$) and ($\rho_{\partial p/\partial z:\partial \omega_x/\partial y}$) are higher in the region $x < \sim 0.7$ where the flow is unsteady laminar than the turbulence region.

The correlations close to the bottom and top walls are presented in the following paragraphs in order to study the influence of pressure gradients and separation on the flow.

The cross-correlation coefficient $\rho_{\partial p/\partial x:\partial \omega_z/\partial y}$ between both walls is shown in figure (4.24) both in wall units and global units. The two variables are highly correlated in a negative sense close to both bottom and top walls; however, the influence of the pressure gradient through the FPG and APG regions on the correlations is light. It is interesting to note that there is a small region with high positive correlation occurring near the flow separation bubble close to the top wall at $x = 0.7$.

The cross-correlation coefficient $\rho_{\partial p/\partial z:\partial \omega_x/\partial y}$ between both walls is presented in figure (4.25) both in wall units and global units. Again, high positive correlations are observed close to both walls. However, correlations at other locations are essentially small including the region close to the separation.

The cross-correlation coefficients $\rho_{\partial p/\partial y:\partial \omega_x/\partial z}$ and $\rho_{\partial p/\partial y:\partial \omega_z/\partial x}$ between both walls

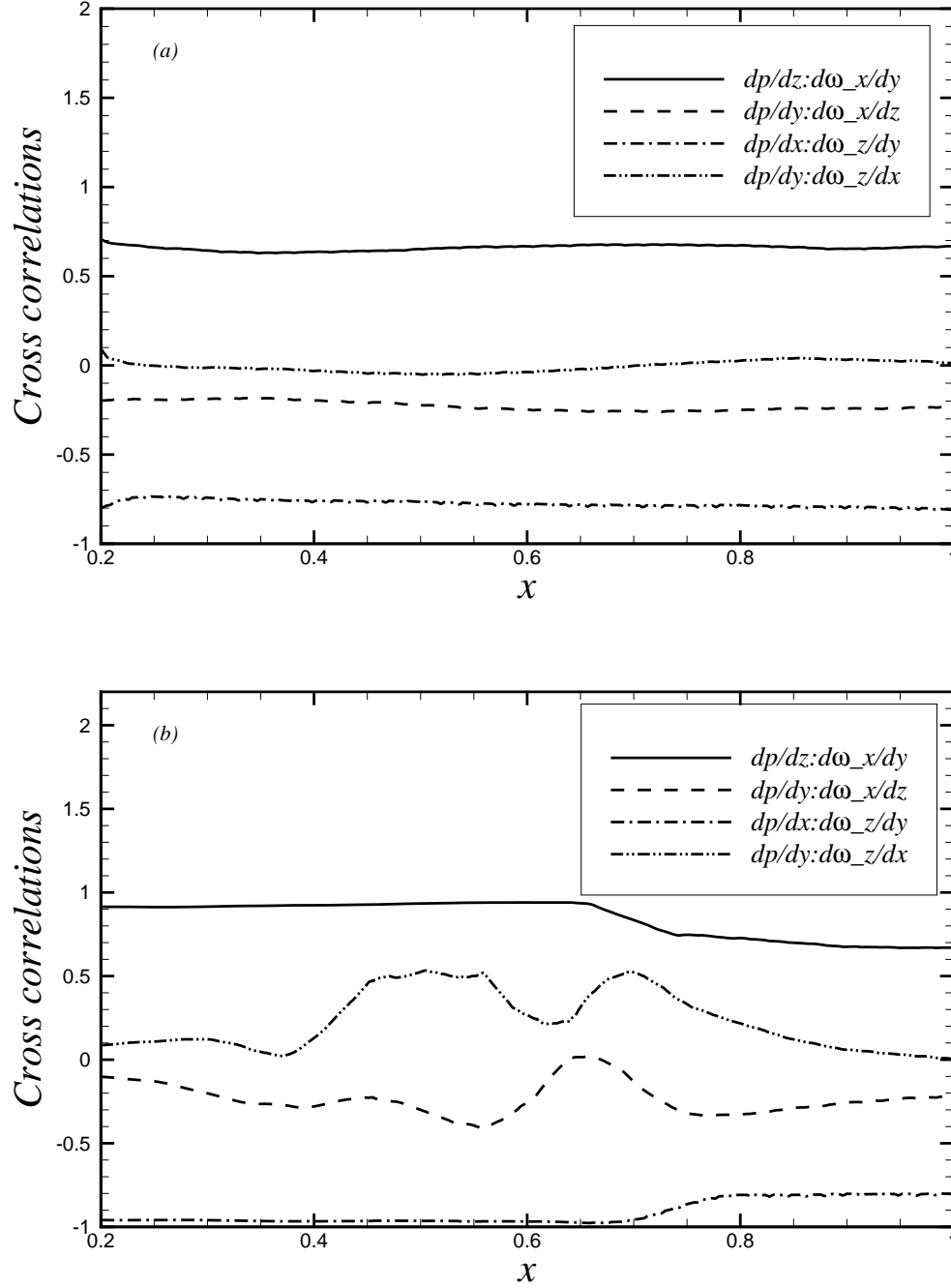


Figure 4.23: Cross-correlation coefficients between pressure gradients and vorticity fluxes on the wall. (a) bottom wall; (b) top wall. d denotes partial derivative, and $_$ denotes subscript.

are given in figures (4.26) and (4.27) respectively. The correlations in most inner regions between both walls are poor except for the correlation coefficient $\rho_{\partial p/\partial y:\partial \omega_z/\partial x}$ near separation close to the top wall at $x = 0.7$ where the correlation coefficient is high, shown in figure (4.27). It seems that there might be a correlation between the pressure gradient and spanwise vorticity near separation.

The correlations between pressure gradients and spanwise vorticity ($\rho_{\partial p/\partial x_i:\partial \omega_z}$) are sketched in figure (4.28). It can be seen that both streamwise and wall-normal pressure gradients are highly correlated with spanwise vorticity near separation at $x = 0.7$, although the correlation between the spanwise pressure gradient and spanwise vorticity is ≈ 0 . This provides an evidence of the influence of tangential pressure gradients on flow separation.

4.7 Near-wall turbulence structures

Near-wall streaks denote narrow regions of near-wall low speed fluid stretched in the streamwise direction (Smith & Metzler, 1983). Smith & Metzler (1983) studied near-wall streaks in a turbulent boundary layer for $740 < Re_\theta < 5830$ and found that the mean spanwise spacing of near-wall low speed streaks was 100 in wall units, independent of Reynolds number; however, the spanwise streak spacing was found to increase with increased distance from the wall. Numerical results of Kim, Moin & Moser (1987) confirmed these findings through the indication of spanwise auto-correlations of streamwise velocity fluctuations for fully developed turbulent channel flows.

The spanwise correlations of streamwise velocities close to the wall at different x locations are given in figures (4.29) and (4.29) in wall units. It can be seen that the

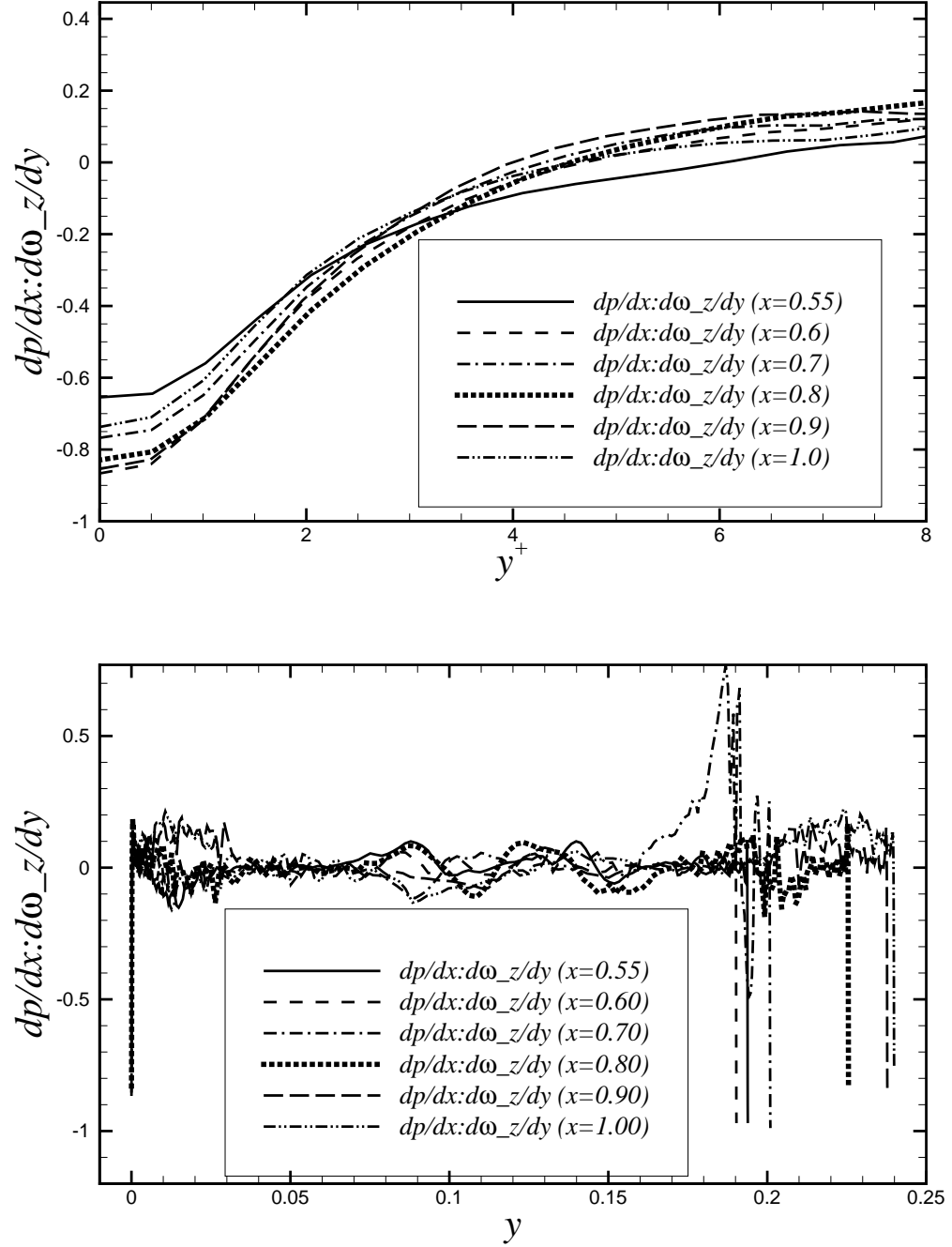


Figure 4.24: Cross-correlation coefficients between streamwise pressure gradient and spanwise vorticity fluxes in the wall normal direction at different streamwise locations, very near the wall in wall units (top), and global units (bottom). d denotes partial derivative, and $_z$ denotes subscript.

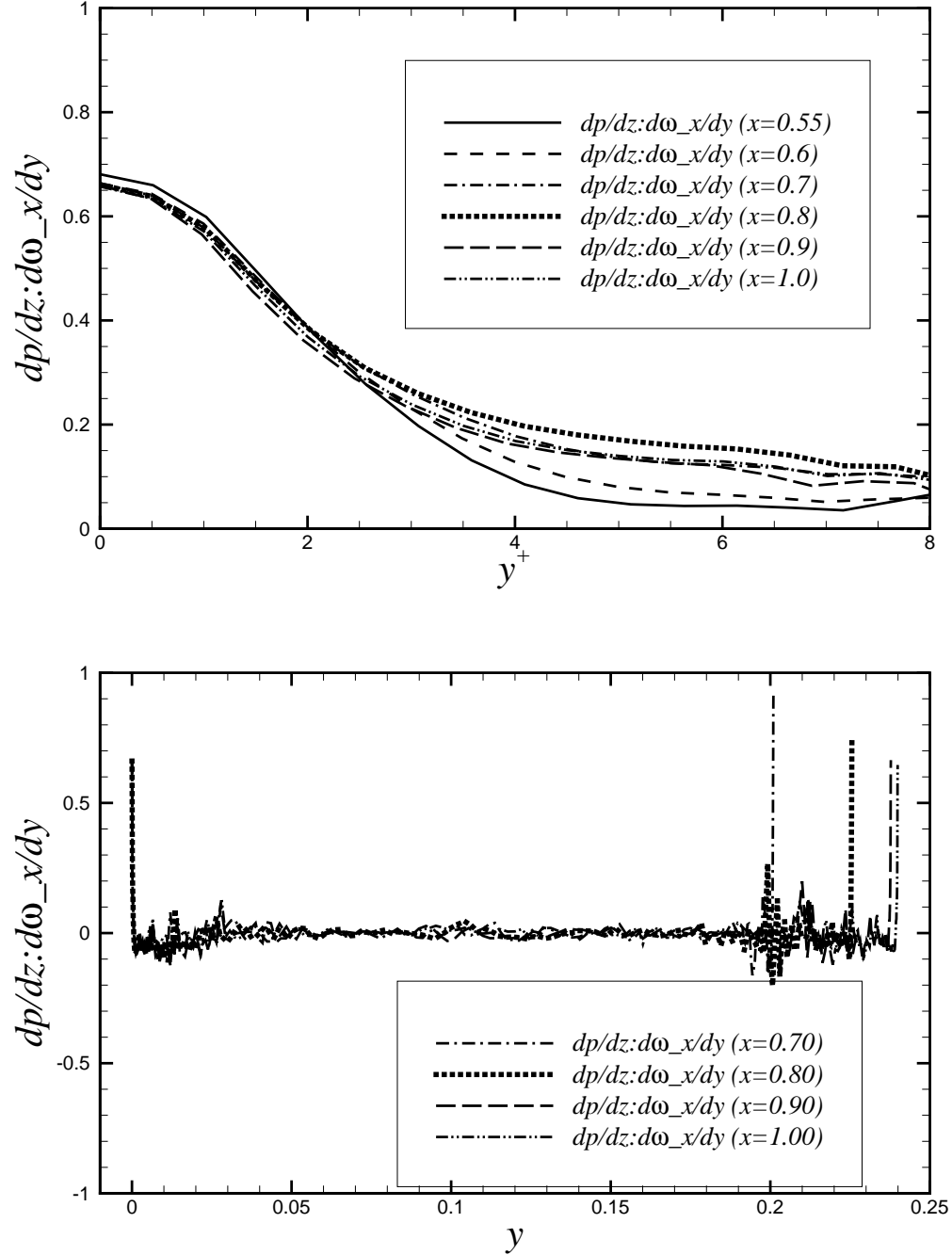


Figure 4.25: Cross-correlation coefficients between spanwise pressure gradient and streamwise vorticity fluxes in the wall normal direction at different streamwise locations, very near the wall in wall units (top), and global units (bottom). d denotes partial derivative, and $_x$ denotes subscript.

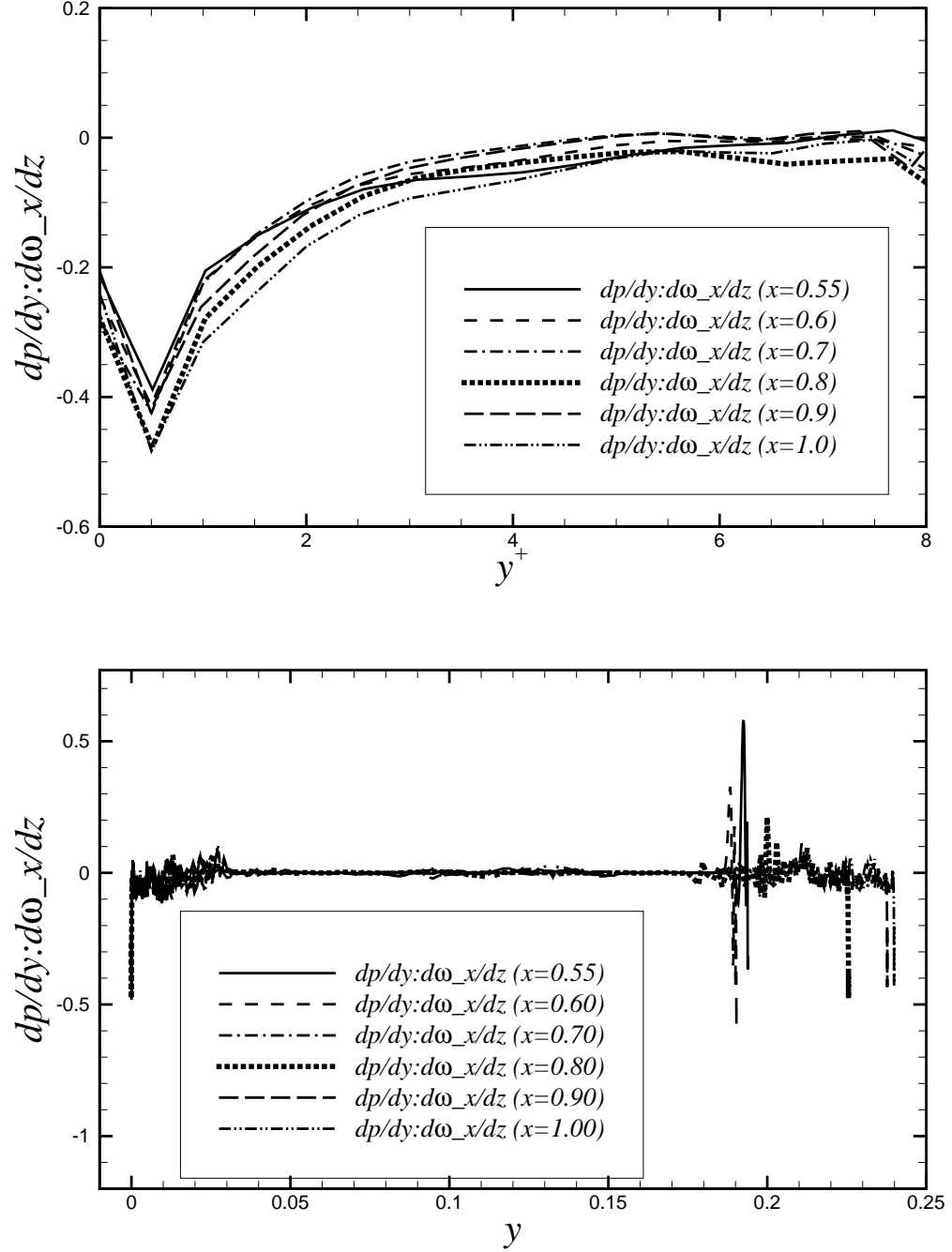


Figure 4.26: Cross-correlation coefficients between wall normal pressure gradient and streamwise vorticity fluxes in the spanwise direction at different streamwise locations, very near the wall in wall units (top), and global units (bottom). d denotes partial derivative, and $_$ denotes subscript.

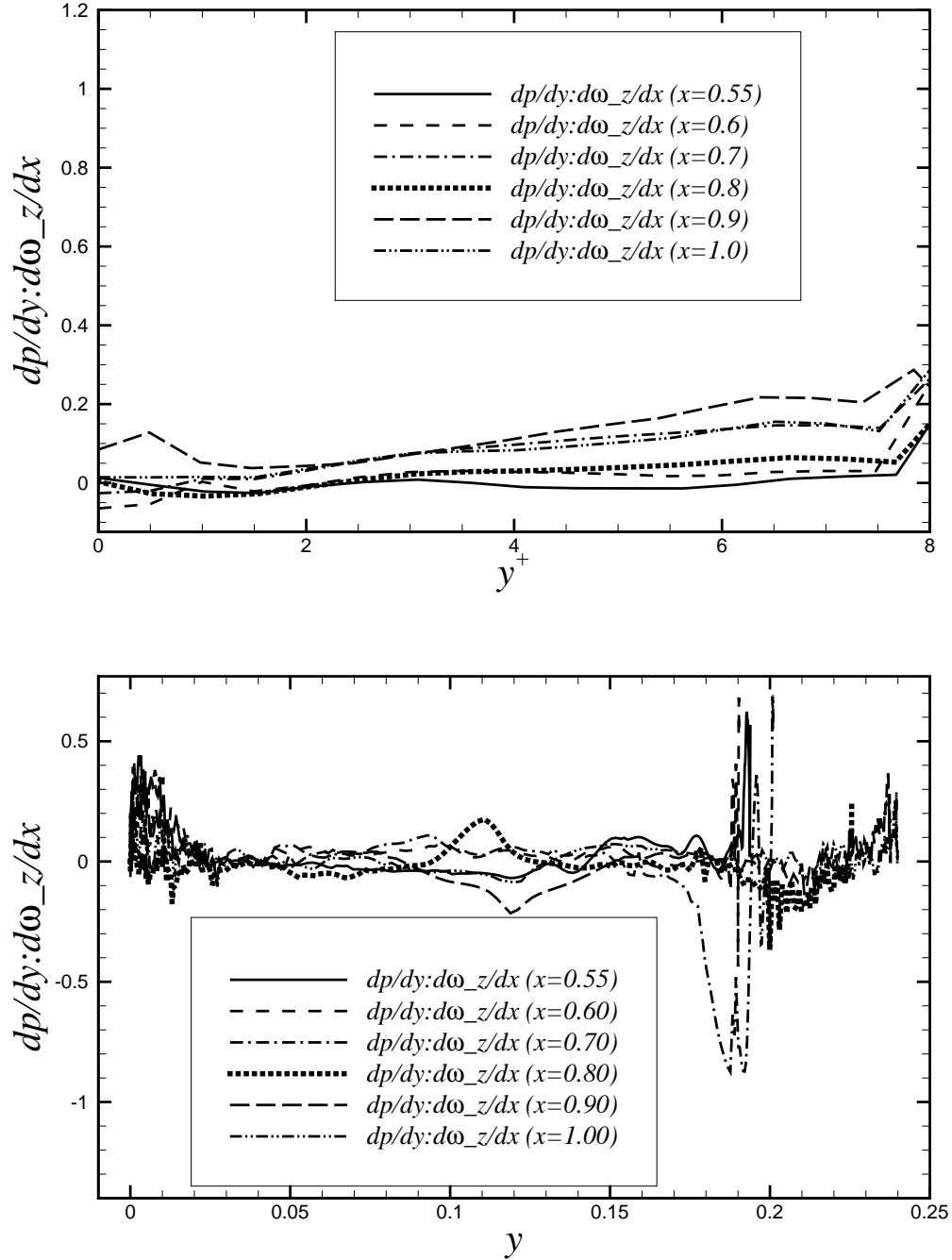


Figure 4.27: Cross-correlation coefficients between wall normal pressure gradient and spanwise vorticity fluxes in the streamwise direction at different streamwise locations, very near the wall in wall units (top), and global units (bottom). d denotes partial derivative, and $_z$ denotes subscript.

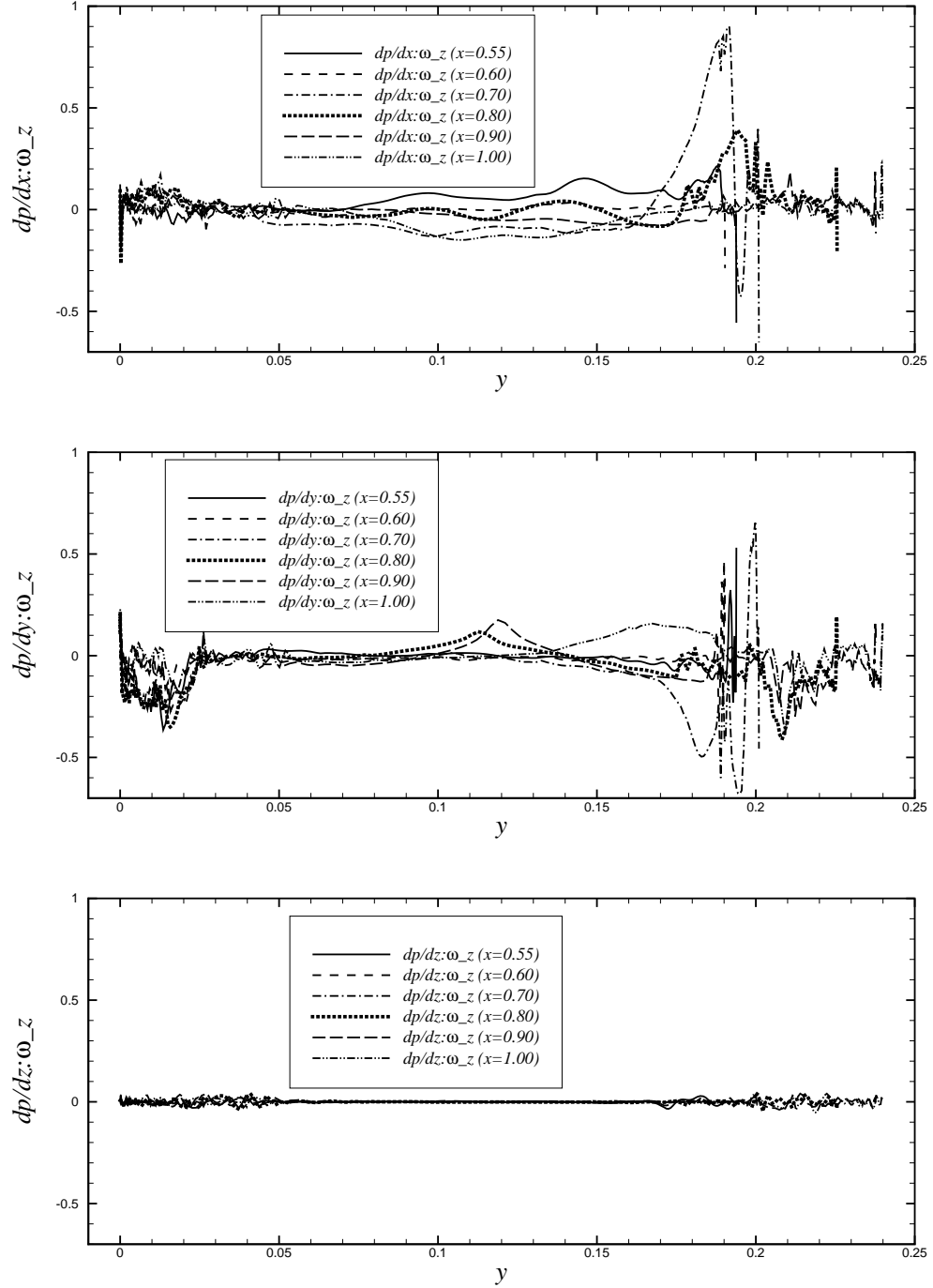


Figure 4.28: Cross-correlation coefficients between pressure gradients and spanwise vorticity at different streamwise locations. (top) streamwise pressure gradient; (middle) wall-normal pressure gradient; (bottom) spanwise pressure gradient. d denotes partial derivative, and $_z$ denotes subscript.

location of the minimum of the correlation very close to the wall ($y^+ \approx 8$) remains essentially the same: $\Delta z^+ \approx 50$ for the 4 streamwise locations, independent of pressure gradients, although the location of minimum increases with increase of y^+ , especially for the correlations at $x = 0.9$. The near-wall low speed streak spacings (twice of the location Δz^+ of minimum correlation of streamwise velocity fluctuations). It is found that the spacing is around 100 wall units, which agrees well with the incompressible experimental and numerical results reported by Kim *et al.* (1987) and Smith & Metzler (1983).

A snapshot of streamwise velocity fluctuations close to the bottom plane wall ($y^+ \approx 8$) is shown in figure (4.31). It is shown that the streaks are elongated in the streamwise direction in the FPG region due to the acceleration and shortened in the APG region because of the deceleration. However, the mean spanwise streak spacing is similar for both FPG and APG regions, which confirms the previous predictions based on spanwise correlations of streamwise velocities.

Second invariant of the velocity gradient tensor (denoted as Q) is usually used for the visualization of turbulent coherent structures. It is defined as (Chong, Perry & Cantwell, 1990)

$$Q = \frac{1}{2}(P^2 - S_{ij}S_{ji} - R_{ij}R_{ji}) \quad (4.9)$$

where $P = -\frac{\partial u_i}{\partial x_i}$ is zero for incompressible flows, $S_{ij} = \frac{1}{2}(\frac{\partial u_i}{\partial x_j} + \frac{\partial u_j}{\partial x_i})$, and $R_{ij} = \frac{1}{2}(\frac{\partial u_i}{\partial x_j} - \frac{\partial u_j}{\partial x_i})$.

Iso-surfaces of Q are shown in figures (4.32) and (4.33) with coloring based on the local streamwise velocity. It can be seen that the hairpin like structures start to grow after the trip and its inclined angle to streamwise direction of the bottom plane plate is generally smaller (flatter) in the FPG region than the APG region. The structures

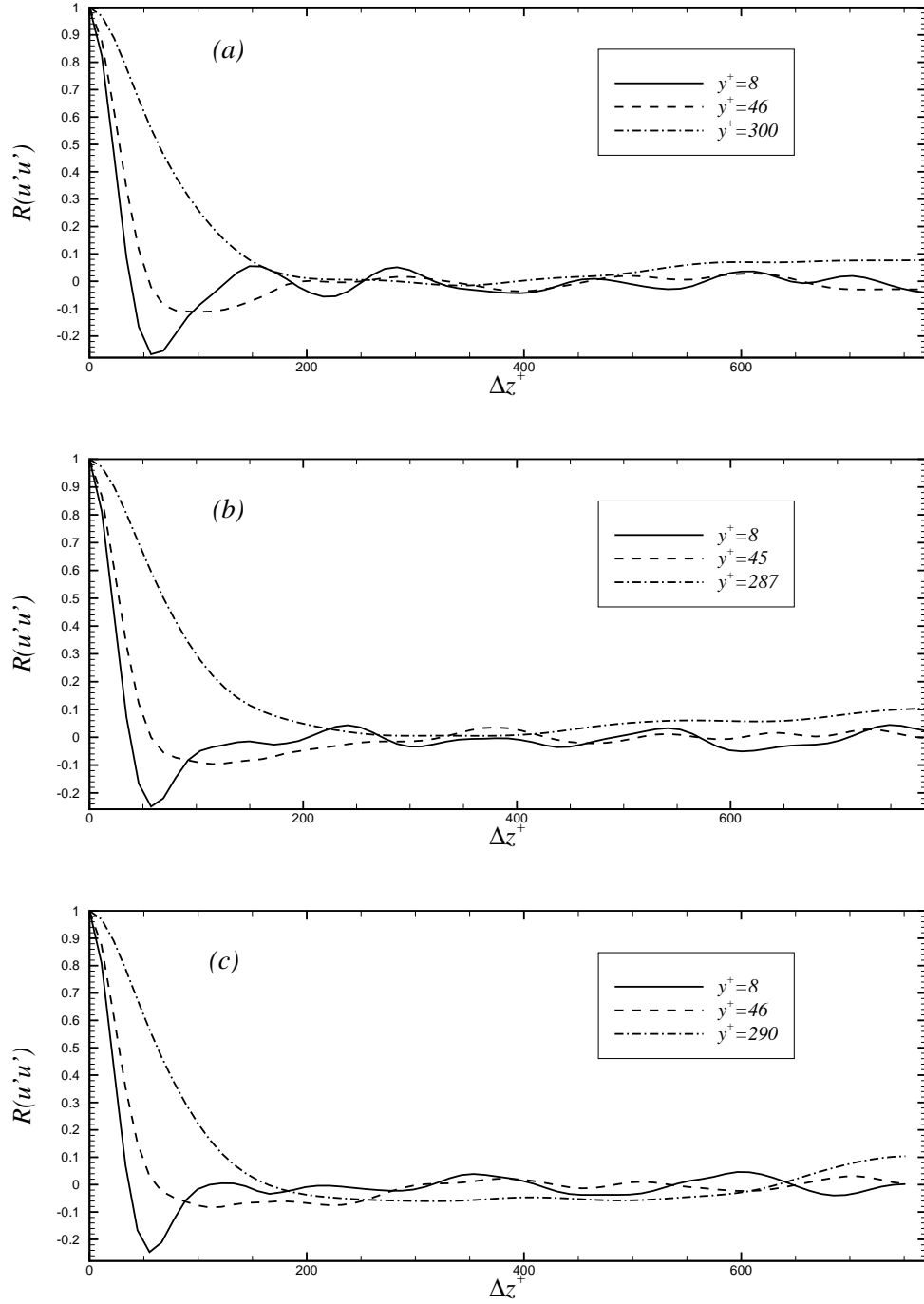


Figure 4.29: Correlations of streamwise velocity fluctuations close to the wall at different x locations: (a) $x = 0.50$; (b) $x = 0.60$; (c) $x = 0.70$.

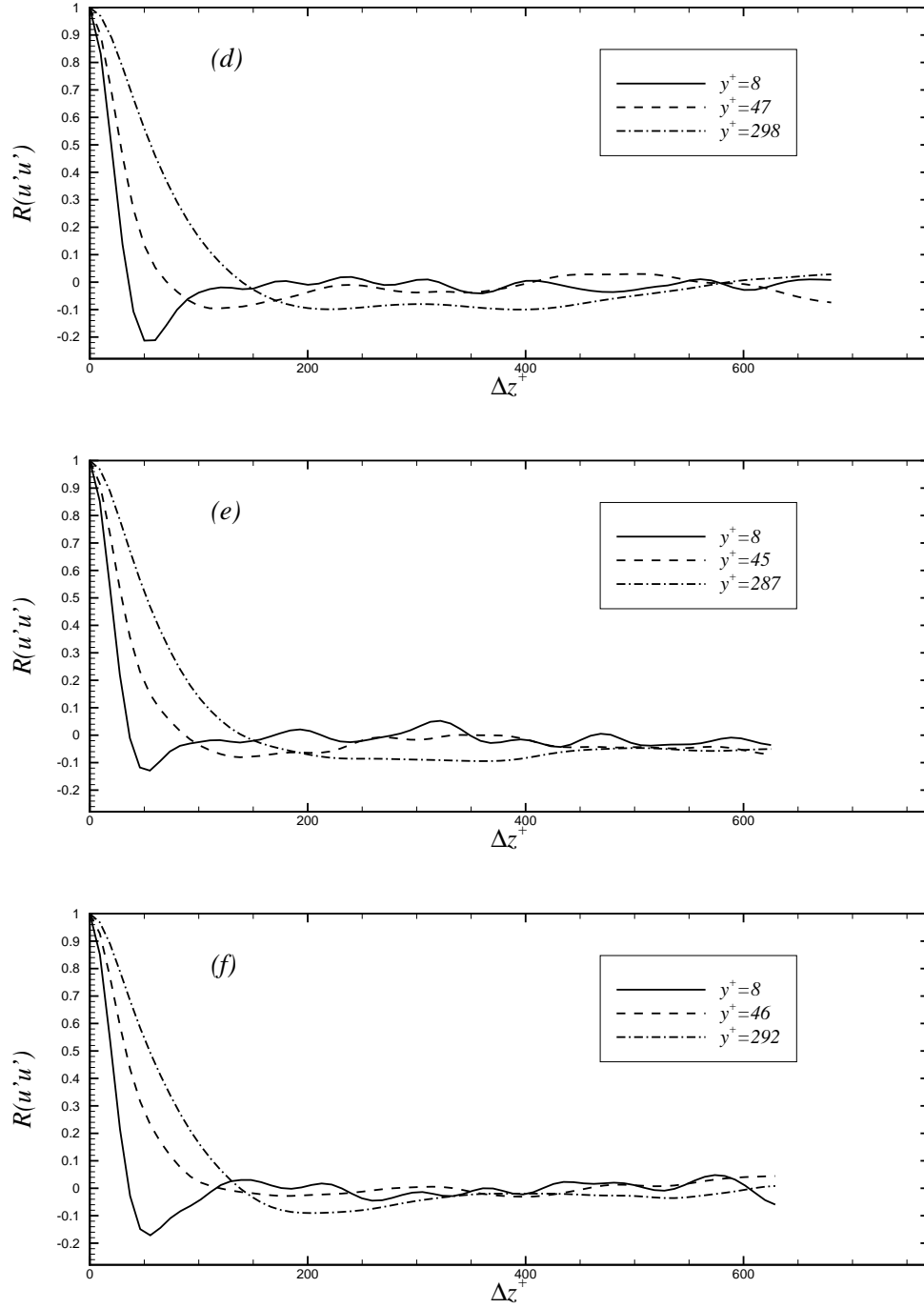


Figure 4.30: Correlations of streamwise velocity fluctuations close to the wall at different x locations: (d) $x = 0.80$; (e) $x = 0.90$; (f) $x = 1.00$.

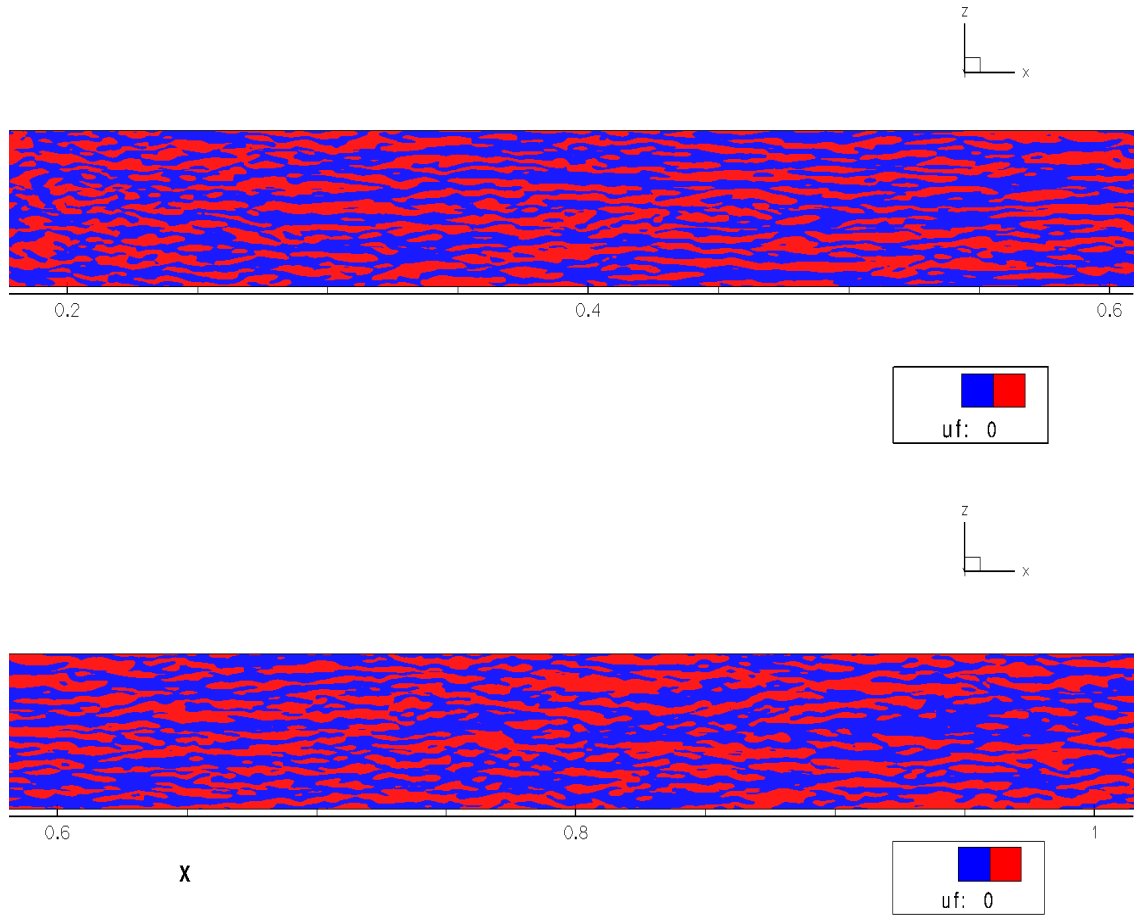


Figure 4.31: A snapshot of streamwise velocity fluctuations close to the bottom plane wall ($y^+ \approx 8$), in the FPG region (top), and APG region (bottom).

are more densely distributed in the downstream APG region than the upstream FPG region close to the bottom wall. There is a small separation region that occurs at the APG region of the top curved wall. But this separation bubble is not stable and changes with time and space, which can be seen from snapshots at different time instants. No structures are observed in the FPG region of the top curved wall, the region before the trip and the rear part of the fringe region, which in other words are laminar regions.

4.8 Concluding remarks

Direct numerical simulation of turbulent isothermal-wall bounded flow with FPG and APG at Mach numbers $Ma \approx 0.2$ and reference Reynolds number $Re \approx 428000$, based on the streamwise length of the bottom wall and inlet bulk velocity, has been performed using discontinuous Galerkin method with an addition of fringe region technique. The trip at the beginning of bottom plane wall makes the flow close to bottom wall transition to turbulence and turbulence develops well in the FPG region. The generated data have been compared with the SW case and the agreement is satisfactory. Many issues have been addressed and related physics has been analyzed.

Flow visualization and related analysis of turbulence transition has been made. The distance between the transition and the current trip device of triangular prism is compared with that of a cylinder. It is found that the triangular prism gives an earlier transition than the cylinder.

The mean profiles of velocities, pressure, and pressure gradients have been analysed. It is found that the pressure gradient has a great effect on profiles in the log-law region for the streamwise velocity: APG would push the low log-law layer down but

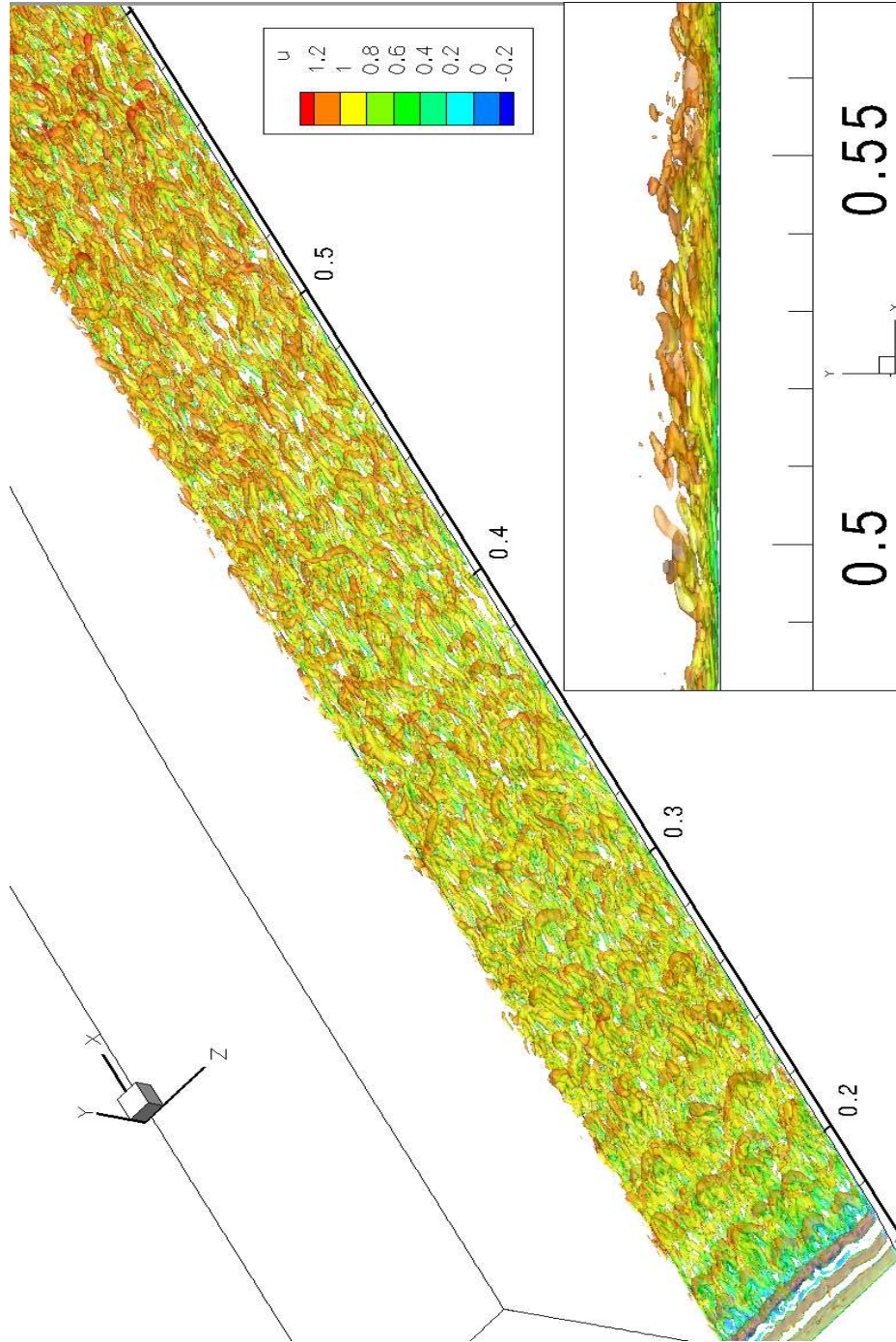


Figure 4.32: Iso-surfaces of the second invariant of the velocity gradient tensor (Q) in the FPG region. The coloring is based on the local streamwise velocity. The smaller figure at the bottom right is the side view of a thin slice in the z direction to show the inclined angle of the structures.

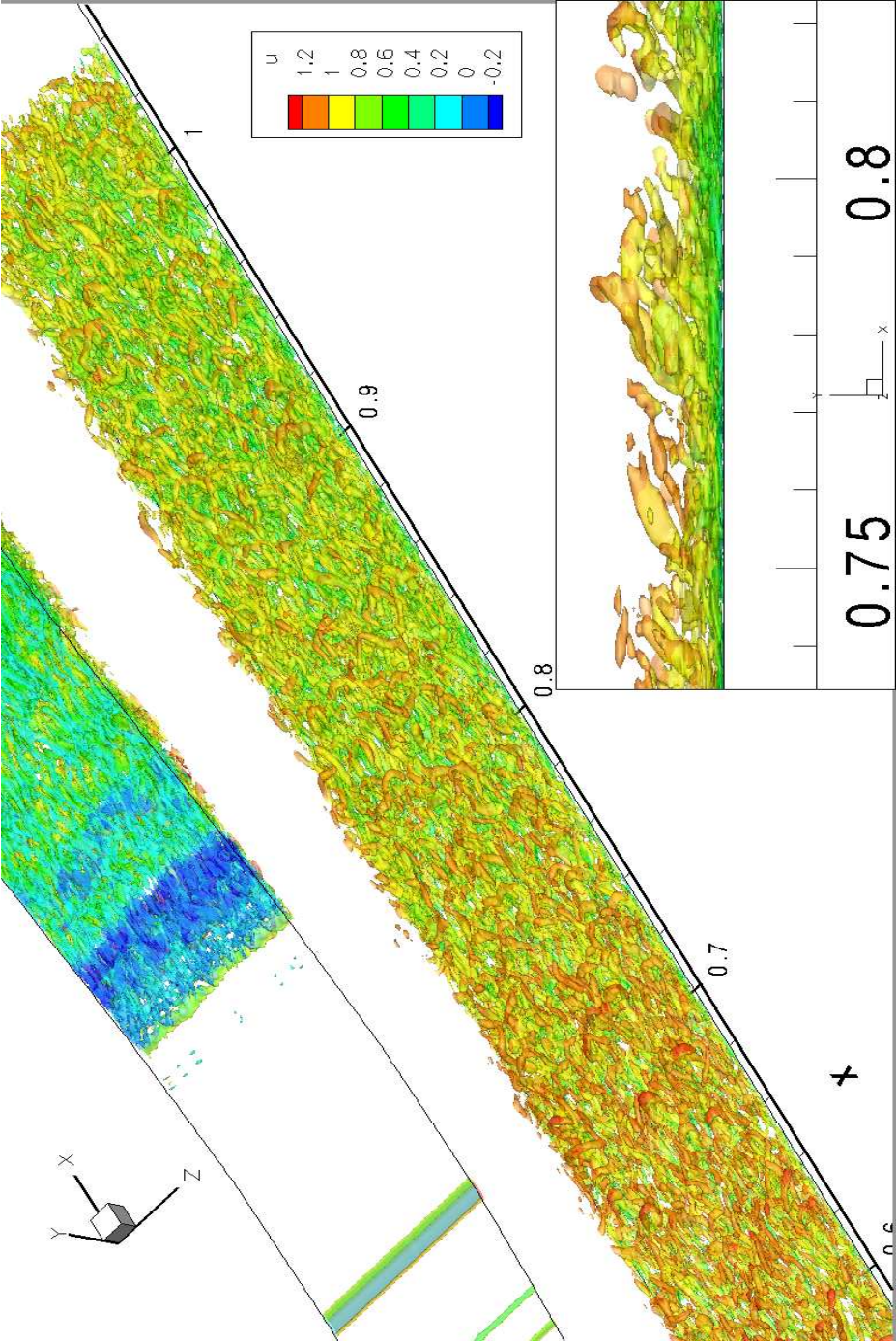


Figure 4.33: Iso-surfaces of the second invariant of the velocity gradient tensor (Q) in the APG region. The coloring is based on the local streamwise velocity. The smaller figure at the bottom right is the side view of a thin slice in the z direction to show the inclined angle of the structures.

lift the high log-law region up.

Second-order statistics such as velocity, pressure, vorticity fluctuations and shear stresses have been generated. Pressure gradient has a strong effect on both inner and outer scaling of RMS velocity, vorticities and inner scaling of RMS pressure, RMS shear stresses close to the wall. The influence of pressure gradient on outer scaling of RMS pressure is not much except for the region with flow separation close to the top wall and the APG wake region. Most profiles at $x = 1.0$, in the wake region of APG, display different behaviour close to the wall and away from the wall mainly due to different distribution of streamwise pressure gradients.

The cross-correlations between the pressure gradients and vorticity fluxes close to the wall have been obtained. It is found that the correlation between streamwise pressure gradient and spanwise vorticity flux in the wall normal direction, as well as the correlation between spanwise pressure gradient and streamwise vorticity flux in the wall normal direction are high close to the wall at both FPG and APG regions. The influence of pressure gradients through FPG and APG regions is very small. The correlations between streamwise/wall-normal pressure gradient and spanwise vorticity are boosted near separation close to the top wall.

Near-wall turbulence structures and spanwise correlations of streamwise velocity have been obtained. The pressure gradient has little effect on the near-wall spanwise spacings between low speed streaks. Iso-surfaces of second invariant of the velocity gradient tensor indicate that the angle of inclined hairpin structure to streamwise direction of the bottom plane plate is smaller (flatter) in the FPG region than the APG region and the structures are more densely distributed in the downstream APG region.

Future work will be presented in the next chapter.

Chapter 5

Conclusion and future work

5.1 Conclusion

The main objectives of this study were to:

- 1). Apply and assess to see suitability of the discontinuous Galerkin method (DGM) to calculate, via DNS, compressible turbulent channel flows and complex turbulent flows under favourable and adverse pressure gradients (FPG and APG).
- 2). Compute and study the effects of pressure gradients on vorticity generation from a solid wall for compressible and incompressible turbulent flows under zero, favourable, and adverse pressure gradients.
- 3). Provide a database for low Mach number turbulent flows subjected to favourable and adverse pressure gradients. This database may then be used to develop and test modifications to models of turbulence that can accurately predict aircraft-wing-type APG and separated flows, for example.

This thesis was mainly focused on direct numerical simulation (DNS) of compressible and incompressible fully developed turbulent flows between isothermal walls and DNS of low Mach number transitional turbulent flows with favourable and adverse pressure gradients and separation using DGM. The conclusions drawn from this work are as follows.

The formulation and implementation of DGM was introduced. Its attractive features, such as high order accuracy, high parallelizability, good stability, and good for complex geometries, were verified by the DNS cases in this study. The close-to-linear scaling was obtained from tests done on different architectures. The accuracy of results was validated by comparing the current simulation results with the data of published literatures.

DNS of fully developed turbulent flow between two isothermal plane walls, at Mach numbers $Ma = 0.2$, $Ma = 0.7$, $Ma = 1.5$ and Reynolds number $Re \approx 2800$ using DGM, referred to as the case A, and DNS of turbulent isothermal-wall bounded flow with FPG and APG at Mach number $Ma \approx 0.2$ and reference Reynolds number $Re \approx 428000$, based on the streamwise length of the bottom wall and inlet bulk velocity using DGM with fringe region technique, referred to as the case B, were performed. The data from the current simulations using DGM was found to be in good agreement with the corresponding incompressible DNS data of Moser *et al.* (1999) and compressible DNS data of Coleman *et al.* (1995) for the case A, and incompressible DNS data of Spalart & Watmuff (1993) for the case B, thereby verifying the utility of the DGM and fringe region technique for DNS.

The mean velocity profile is affected significantly by Mach number and pressure gradient. It departs from the log law as the Mach number increases. However, there

is a good fit in the viscous sublayer and buffer layer. The Van Driest transformation of the velocity profiles of compressible cases causes the profiles to get closer to the incompressible log law in the log-law region, but at the same time the velocity profile departs from the incompressible profile in the buffer layer region. APG would push the velocity profiles in the log-law layer down.

For the case A, compared with the log-law, a power law seems to better represent the scaling of mean streamwise velocity with Mach number, although the mean velocity profiles of the current cases do not exactly obey power law either.

Flow visualization and related analysis of turbulence transition was made. The distance between the transition and the current trip device of triangular prism was compared with that of a cylinder. It is found that the triangular prism gives an earlier transition than the cylinder.

The influence of Mach number and pressure gradients on the inner and outer scaling of turbulent statistics was analyzed. It is found for case A that the inner scaling of second-order statistics, such as turbulence velocity, density, temperature, shear stress and vorticity fluctuations, is dependent of Mach numbers; but outer scaling with Mach number shows a better collapse. However, the scaling of some higher-order statistics, such as skewness and flatness of density and temperature fluctuations, seems to collapse better when inner scaling is used. For the case B, both inner and outer scaling of RMS velocity, vorticities and inner scaling of RMS pressure, RMS shear stresses close to the wall are dependent of pressure gradient through FPG and APG regions. It seems that outer scaling of RMS pressure does not depend much on pressure gradient except for the region near flow separation close to the top wall and the APG wake region. Most profiles at $x = 1.0$, the wake of APG region, display

different behaviours close to the wall and away from the wall mainly due to different distribution of streamwise pressure gradients.

Turbulent kinetic energy (TKE) budget for the case A was reported. The related scaling and analysis of compressibility terms was analysed. The result shows that the inner scaling of TKE budget does not collapse well in the near-wall region, but the collapse of the outer scaling is satisfactory. The influence of compressibility terms on TKE budget is negligible.

The linkage between the pressure gradient and vorticity flux on the wall was derived and confirmed by their correlations of the current simulation results. The influence of Mach number, viscosity, dilatation, pressure gradient and separation was analyzed. It is found that the correlation between streamwise pressure gradient and spanwise vorticity flux in the wall normal direction, as well as the correlation between spanwise pressure gradient and streamwise vorticity flux in the wall normal direction are high very close to the wall for both case A and case B. Viscosity affects the correlation between streamwise pressure gradient and spanwise vorticity flux in the wall normal direction close to the wall as Mach number increases. The influence of pressure gradients on the correlations through FPG and APG regions is very small. The correlations between streamwise/wall-normal pressure gradient and spanwise vorticity are increased near separation close to the top wall.

The mean spanwise near-wall streak spacing is affected greatly by Mach number for case A but it is little affected by the pressure gradient through FPG and APG regions for the case B. The mean spanwise streak spacing, which is independent of Reynolds numbers, however, increases as Mach number increases, which is confirmed by the snapshot of near-wall streak contours. Isosurfaces of second invariant of the

velocity gradient tensor are more sparsely distributed and elongated as Mach number increases, which is similar to the distribution of near-wall low speed streaks. The angle of inclined hairpin structure to streamwise direction of the bottom plane plate is smaller (flatter) in the FPG region than the APG region and the structures are more densely distributed in the downstream APG region than the upstream FPG region.

5.2 Future work

Future work should include further extraction of data, such as the time dependent spanwise variations in pressure vorticity correlations, energy balance, higher order statistics, and related analysis for the regions with pressure gradients and especially separation, analysis based on other velocity scalings such as u_p , flow instability analysis regarding Taylor-Goertler vortices and Tollmien-Schlichting waves close to the top wall, etc, to complement the study of turbulent flows with FPG and APG.

Future work should also include an extensive study on similar cases of the case B as the current case is mainly concentrated on the influence of mild pressure gradients on transitional turbulent flows at a low Mach number. Cases at stronger pressure gradients could further investigate the influence of pressure gradient on turbulence statistics and physics. Physical trip device was only placed at $x = 0.15$ on the bottom plane wall for the current case. It would be interesting to study influence of location and size of the trip device on this type of flow. For example, the trip device could be placed at different x, z locations with different size or geometry, or a new trip element could be added to the curved top wall, which would transition the flow close to the top wall to turbulence earlier, such that the flow and separation would

change accordingly. Finally cases with higher Mach numbers would help to further understand the influence of Mach number and compressibility effects on turbulence statistics and separation.

Bibliography

- ALVING, A. & FERNHOLZ, H. 1996 Turbulence measurements around a mild separation bubble and downstream of reattachment. *J. Fluid Mech.* **322**, 297–328.
- ANTONIA, R. A. & KIM, J. 1994 Low-reynolds-number effects on near-wall turbulence. *J. Fluid Mech.* **276**, 61–80.
- BAGGAG, A., ATKINS, H. & KEYES, D. 1999 Parallel implementation of the discontinuous Galerkin method. *Tech. Rep.* 99-35. Institute for Computer Applications in Science and Engineering, NASA Langley Research Center, Hampton, VA, USA.
- BARENBLATT, G. I., CHORIN, A. J. & PROSTOKISHIN, V. M. 1997 Scaling laws for fully developed turbulent flow in pipes. *Applied Mechanics Reviews* **50**, 413–429.
- BASSI, F. & REBAY, S. 1997 A high-order accurate discontinuous finite element method for numerical solution of the compressible navier-stokes equations. *J. Comput. Phys.* **131**, 267–279.
- BAUMANN, C. E. & ODEN, J. T. 1999 A discontinuous hp finite element method for convection-diffusion problems. *Comp. Meth. Appl. Mech. Eng.* **175**, 311–341.
- BRADSHAW, P. 1977 Compressible turbulent shear layers. *Annu. Rev. Fluid. Mech.* **9**, 33–54.

- BRUN, C., BOIARCIUC, M. P., HABERKORN, M. & COMTE, P. 2008 Large eddy simulation of compressible channel flow: Arguments in favour of universality of compressible turbulent wall bounded flows. *Theor. Comput. Fluid Dyn.* **22**, 189–212.
- CHONG, M. S., PERRY, A. E. & CANTWELL, B. J. 1990 A general classification of three dimensional flow fields. *Phys. Fluids A* **2** (5), 765–777.
- COCKBURN, B. 2003 Discontinuous Galerkin methods. *Journal of Applied Mathematics and Mechanics* **83**, 731–754.
- COCKBURN, B., KARNIADAKIS, G. & SHU, C.-W. 2000 *Discontinuous Galerkin methods—theory, computation and applications*. Springer.
- COCKBURN, B. & SHU, C.-W. 1998 The local discontinuous Galerkin method for time-dependent convection diffusion problems. *SIAM Journal on numerical analysis* **35**, 2440–2463.
- COLEMAN, G. N., KIM, J. & MOSER, R. D. 1995 A numerical study of turbulent supersonic isothermal-wall channel flow. *J. Fluid Mech* **305**, 159–183.
- COLLIS, S. S. 2002 Discontinuous Galerkin methods for turbulence simulation. In *Proceedings of the summer program*. Center for Turbulence Research, California, USA.
- DÉLERY, J. M. 2001 Robert Legendre and Henri Werle: toward the elucidation of three-dimensional separation. *Annu. Rev. Fluid. Mech.* **33**, 129–154.
- DURBIN, P. & BELCHER, S. E. 1992 Scaling of adverse-pressure-gradient turbulent boundary layers. *J. Fluid. Mech.* **238**, 699–722.

- FOX, D. & LILLY, D. 1972 Numerical simulations of turbulent flows. *Rev. Geophys. Space. Phys.* **10**, 51–72.
- FOYSI, H., SARKAR, S. & FRIEDRICH, R. 2004 Compressibility effects and turbulence scalings in supersonic channel flow. *J. Fluid Mech* **509**, 207–216.
- GAD-EL-HAK, M. 1990 Control of low-speed airfoil aerodynamics. *AIAA Journal* **28** (9), 1537–1552.
- GALERKIN, B. 1915 Series solution of some problems in elastic equilibrium of rods and plates. *Engineers Bulletin* **19**, 897–908.
- GEORGE, W. K. & CASTILLO, L. 1993 Boundary layers with pressure gradient: another look at the equilibrium boundary layer. In *Near-Wall Turbulent Flows: Proceedings of the International Conference on Near-Wall Turbulent Flows, Tempe, Arizona, U.S.A., 15-17 March 1993* (ed. R. M. C. So, C. G. Speziale & B. E. Launder), pp. 901–910.
- GEORGE, W. K. & CASTILLO, L. 1997 Zero-pressure-gradient turbulent boundary layer. *Applied Mechanics Reviews* **50**, 689–729.
- GEURTS, B. J. 2004 *Elements of direct and large-eddy simulation*. R.T Edwards Inc.
- GUARINI, S. E., MOSER, R. D., SHARIFF, K. & WRAY, A. 2000 Direct numerical simulation of a supersonic turbulent boundary layer at Mach 2.5. *J. Fluid. Mech.* **414**, 1–33.
- HERBST, A. & HENNINGSON, D. 2006 The influence of periodic excitation on a turbulent separation bubble. *Flow, Turbulence and Combustion* **76**, 1–21.

- HUANG, P., COLEMAN, G. & BRADSHAW, P. 1995 Compressible turbulent channel flows: Dns results and modelling. *J. Fluid Mech.* **305**, 185–218.
- HUTTL, T., DENG, G., FRIEDRICH, R. & MANHART, M. 2001 Testing turbulence models by comparison with DNS data of adverse-pressure-gradient boundary layer flow. In *High performance computing in science and engineering 2000* (ed. E. Krause & W. Jäger), pp. 356–367. Springer-Verlag Berlin Heidelberg.
- KADER, B. & YAGLOM, A. 1978 Similarity treatment of moving-equilibrium turbulent boundary layers in adverse pressure gradients. *J. Fluid Mech.* **89**, 305–342.
- KARNIADAKIS, G. & SHERWIN, S. 2005 *Spectral/hp Element Methods for Computational Fluid Dynamics*, 2nd edn. Oxford Science Publications.
- KIM, J., MOIN, P. & MOSER, R. 1987 Turbulence statistics in fully-developed channel flow at low Reynolds number. *J. Fluid. Mech.* **177**, 133–166.
- KOUMOUTSAKOS, P. 1999 vorticity flux control for a turbulent channel flow. *Phys. Fluids* **11** (2), 248–250.
- LEE, C. & KIM, J. 2002 Control of viscous sublayer for drag reduction. *Phys. Fluids* **14** (7), 2523–2529.
- LELE, S. K. 1994 Compressibility effects on turbulence. *Annu. Rev. Fluid. Mech.* **26**, 211–254.
- LIGHTHILL, M. J. 1963 *Introduction. Boundary Layer Theory, chapter II in Laminar Boundary Layers*. Oxford University Press.

- MARQUILLIE, M., LAVAL, J. P. & DOLGANOV, R. 2008 Direct numerical simulation of a separated channel flow with a smooth profile. *J. Turbulence* **9**, 1–23.
- MELNIK, R. E. 1989 An asymptotic theory of turbulent separation. *Computers and fluids* **17**, 165–184.
- MENTER, F. 1993 Zonal two-equation $k - \omega$ models for aerodynamic flows. *AIAA 24th Fluid Dynamics Conference* **93**, 2906.
- MOIN, P. & MAHESH, K. 1998 Direct numerical simulation: a tool in turbulence research. *Annu. Rev. Fluid. Mech.* **30**, 539–578.
- MONTY, J. P., HUTCHINS, N., NG, H. C. H., MARUSIC, I. & CHONG, M. S. 2009 A comparison of turbulent pipe, channel and boundary layer flows. *J. Fluid Mech* **631**, 431–442.
- MORINISHI, Y., TAMANO, S. & NAKABAYASHI, K. 2004 Direct numerical simulation of compressible turbulent channel flow between adiabatic and isothermal walls. *J. Fluid Mech* **502**, 273–308.
- MORKOVIN, M. V. 1964 Effects of compressibility on turbulent flows. In *The Mechanics of Turbulence* (ed. A. Favre), pp. 367–380. New York: Gordon and Breach.
- MORRISON, J. F. 2007 The interaction between inner and outer regions of turbulent wall-bounded flow. *Phil. Trans. R. Soc. A* **365**, 683–698.
- MORRISON, J. F., MCKEON, B. J., JIANG, W. & SMITS, A. J. 2004 Scaling of the streamwise velocity component in turbulent pipe flow. *J. Fluid Mech* **508**, 99–131.

- MOSER, R. D., KIM, J. & MANSOUR, N. N. 1999 Direct numerical simulation of turbulent channel flow up to $Re_\tau \approx 590$. *Phys. Fluids* **11** (4), 943–945.
- MOSER, R. D. & MOIN, P. 1984 Direct numerical simulation of curved turbulent channel flow. *Tech. Rep.* NASA TM 85794, Department of Mechanical Engineering, Stanford University, Stanford, California, USA.
- NA, Y. & MOIN, P. 1996 Direct numerical simulation of turbulent boundary layers with adverse pressure gradient and separation. *Tech. Rep.* TF-68. Stanford University.
- NA, Y. & MOIN, P. 1998 Direct numerical simulation of a separated turbulent boundary layer. *J. Fluid Mech.* **374**, 520–533.
- NAGANO, Y., TAGAWA, M. & TSUJI, T. 1993 Effects of adverse pressure gradients on mean flows and turbulence statistics in a boundary layer. In *Turbulent Shear Flows 8*, pp. 7–21. Springer-Verlag.
- NAGANO, Y., TSUJI, T. & HOURA, T. 1998 Structure of turbulent boundary layer subjected to adverse pressure gradient. *International Journal of Heat and Fluid Flow* **19**, 563–572.
- NAGIB, H., CHRISTOPHOROU, C. & MONKEWITZ, P. 2006 High Reynolds number turbulent boundary layers subjected to various pressure-gradient conditions. In *IUTAM Symposium on One Hundred Years of Boundary Layer Research*, pp. 383–394. Springer Netherlands.
- ORSZAG, S. & PATTERSON, G. 1972 Numerical simulations of three-dimensional homogeneous isotropic turbulence. *Phys. Rev. Lett* **28**, 76–79.

- PERRY, A. & SCHOFIELD, W. 1973 Mean velocity and shear stress distributions in turbulent boundary layers. *Phys. Fluids* **16**, 2068–2074.
- POPE, S. B. 2000 *Turbulent flows*. Cambridge University Press.
- RADHAKRISHNAN, S., PIOMELLI, U. & KEATING, A. 2008 Wall-modeled large-eddy simulations of flows with curvature and mild separation. *J. Fluids Eng.* **130** (101203), 1–9.
- REED, W. H. & HILL, T. R. 1973 Triangular mesh methods for the neutron transport equation. LA-UR 479. Los Alamos Scientific Laboratory, Los Alamos, USA.
- RIDER, W. J. & LOWRIE, R. B. 2002 The use of classical Lax-Friedrichs Riemann solvers with discontinuous Galerkin methods. *Int. J. Numer. Meth. Fluids*. **40**, 479–486.
- ROBINSON, S. K. 1991 Coherent motions in the turbulent boundary layer. *Ann. Rev. Fluid Mech.* **23**, 601–639.
- ROGALLO, R. S. & MOIN, P. 1984 Numerical simulation of turbulent flows. *Annu. Rev. Fluid. Mech.* **16**, 99–137.
- SCHLICHTING, H. 1979 *Boundary-layer theory*, seventh edn. McGraw-Hill Book Company.
- SCHOFIELD, W. H. 1981 Equilibrium boundary layers in moderate to strong adverse pressure gradients. *J. Fluid Mech.* **113**, 91–122.
- SHAN, H., JIANG, L. & LIU, C. 2005 Direct numerical simulation of flow separation around a naca 0012 airfoil. *Computers and Fluids* **34**, 1096–1114.

- SHU, C.-W. 1987 TVB uniformly high-order schemes for conservation laws. *Math Comput* **49**, 105–121.
- SIMPSON, R. L. 1989 Turbulent boundary-layer separation. *Annu. Rev. Fluid. Mech.* **21**, 205–232.
- SIMPSON, R. L., CHEW, Y.-T. & SHIVAPRASAD, B. G. 1981*a* The structure of a separating turbulent boundary layer. Part 1. Mean flow and Reynolds stresses. *J. Fluid Mech* **113**, 23–51.
- SIMPSON, R. L., CHEW, Y.-T. & SHIVAPRASAD, B. G. 1981*b* The structure of a separating turbulent boundary layer. Part 2. Higher-order turbulence results. *J. Fluid Mech* **113**, 53–73.
- SIMPSON, R. L., STRICKLAND, J. & BARR, P. 1977 Features of a separating turbulent boundary layer in the vicinity of separation. *J. Fluid Mech.* **79**, 553–594.
- SKOTE, M., HENNINGSON, D. & HENKES, R. 1998 Direct numerical simulation of self-similar turbulent boundary layers in adverse pressure gradients. *Flow, Turbulence and Combustion* **60**, 47–85.
- SKOTE, M. & HENNINGSON, D. S. 2002 Direct numerical simulation of a separated turbulent boundary layer. *J. Fluid Mech.* **471**, 107–136.
- SMITH, C. R. & METZLER, S. P. 1983 The characteristics of low-speed streaks in the near-wall region of a turbulent boundary layer. *J. Fluid Mech* **129**, 27–54.
- SMITS, A. 1991 Turbulent boundary-layer structure in supersonic flow. *Phil. Trans. R. Soc. London Ser. A* **336**, 81–93.

- SPALART, P. 1988 Direct numerical simulation of a turbulent boundary layer up to $R_\theta = 1410$. *J. Fluid Mech.* **187**, 61–98.
- SPALART, P. & WATMUFF, J. 1993 Experimental and numerical study of a turbulent boundary layer with pressure gradient. *J. Fluid Mech.* **249**, 337–371.
- STRATFORD, B. S. 1959 The prediction of separation of the turbulent boundary layer. *J. Fluid Mech* **5**, 1–16.
- SURANA, A., GRUNBERG, O. & HALLER, G. 2006 Exact theory of three-dimensional flow separation. part 1. steady separation. *J. Fluid Mech.* **564**, 57–103.
- SURANA, A., JACOBS, G. B., GRUNBERG, O. & HALLER, G. 2008 An exact theory of three-dimensional fixed separation in unsteady flows. *Phys. Fluids* **20**, 1–22.
- TAMANO, S. & MORINISHI, Y. 2006 Effect of different thermal wall boundary conditions on compressible turbulent channel flow at $m=1.5$. *J. Fluid Mech* **548**, 361–373.
- TENNEKES, H. & LUMLEY, J. 1972 *A first course in turbulence*. The MIT Press.
- TOBAK, M. & PEAKE, D. 1982 Topology of three-dimensional separation. *Annu. Rev. Fluid. Mech.* **14**, 61–85.
- TORO, E. 1997 *Riemann Solvers and Numerical Methods for Fluid Dynamics*. Springer Verlag.
- TOWNSEND, A. A. 1956 *The structure of turbulent shear flow*, 1st edn. Cambridge University Press.
- TOWNSEND, A. A. 1961 Equilibrium layers and wall turbulence. *J. Fluid Mech.* **11**, 97–120.

- TOWNSEND, A. A. 1976 *The structure of turbulent shear flow*, 2nd edn. Cambridge University Press.
- VAN DRIEST, E. R. 1951 Turbulent boundary layer structure in compressible fluids. *J. of Aero. Sci* **18**, 145–160.
- WANG, K. C. 1972 Separation patterns of boundary layer over an inclined body of revolution. *AIAA J.* **10**, 1044–1050.
- WANG, K. C. 1974 Boundary layer over an blunt body at high incidence with an open-type separation. *Proc. R. Soc. Lond A* **340**, 33–55.
- WARBURTON, T. C. & KARNIADAKIS, G. E. 1999 A discontinuous Galerkin method for the viscous MHD equations. *J. Comput. Phys.* **152**, 608–641.
- WOSNIK, M., CASTILLO, L. & GEORGE, W. K. 2000 A theory for turbulent pipe and channel flows. *J. Fluid Mech.* **421**, 115–145.
- WU, J. Z. & WU, J. M. 1998 Boundary vorticity dynamics since Lighthill’s 1963 article: review and development. *Theoret. Comput. Fluid Dynamics* **10**, 459–474.
- WU, J. Z., WU, J. M. & WU, C. J. 1988 A viscous compressible flow theory on the interaction between moving bodies and flow field in the (ω, ϑ) framework. *Fluid Dynamics Research* **3**, 203–208.
- WU, J. Z., WU, X. H. & WU, J. M. 1993 Streaming vorticity flux from oscillating walls with finite amplitude. *Phys. Fluids A* **5**, 1933–1938.
- WU, X. & MOIN, P. 2009 Direct numerical simulation of turbulence in a nominally zero-pressure-gradient flat-plate boundary layer. *J. Fluid Mech* **630**, 5–41.

- ZHAO, R. & SMITS, A. J. 2007 Scaling of the wall-normal turbulence component in high-Reynolds-number pipe flow. *J. Fluid Mech.* **576**, 457–473.

Appendix A

Favre average and TKE budget

The Reynolds average is the classical time average. The Favre average is density based time average. For example,

The Reynolds average of the quantity ϕ is denoted as $\langle \phi \rangle = \frac{1}{T} \int_T \phi dt$;

' denotes the fluctuation with respect to Reynolds average. $\phi' = \phi - \langle \phi \rangle$

The Favre average of the quantity ϕ is denoted as $\{\phi\} = \frac{\langle \rho \phi \rangle}{\langle \rho \rangle}$;

" denotes the fluctuation with respect to Favre average: $\phi'' = \phi - \{\phi\}$

Some relations between these two averages are,

$$\langle \phi'' \rangle = \langle \phi \rangle - \{\phi\} \quad (\text{A.1})$$

$$\{\phi'' \psi''\} = \langle \phi' \psi' \rangle - \langle \phi'' \rangle \langle \psi'' \rangle + \frac{\langle \rho' \phi' \psi' \rangle}{\langle \rho \rangle} = \{\phi \psi\} - \{\phi\} \{\psi\} \quad (\text{A.2})$$

$$\langle \phi' \psi'' \rangle = \langle (\phi - \langle \phi \rangle) (\psi - \frac{\langle \rho \psi \rangle}{\langle \rho \rangle}) \rangle = \langle \phi \psi \rangle - \langle \phi \rangle \langle \psi \rangle = \langle \phi' \psi' \rangle \quad (\text{A.3})$$

The conservation form of continuity, momentum, and total energy equations can be written as the following equations (A.4) (A.5) (A.6) respectively.

$$\frac{\partial \rho}{\partial t} + \frac{\partial \rho u_j}{\partial x_j} = 0 \quad (\text{A.4})$$

$$\frac{\partial \rho u_i}{\partial t} + \frac{\partial (\rho u_i u_j + p \delta_{ij})}{\partial x_j} = \frac{\partial \tau_{ij}}{\partial x_j} + \rho f_i \quad (\text{A.5})$$

$$\frac{\partial E}{\partial t} + \frac{\partial (E + p) u_j}{\partial x_j} = \frac{\partial (\tau_{ij} u_i - q_j)}{\partial x_j} + \rho f_i u_i \quad (\text{A.6})$$

where,

δ_{ij} is Kronecker's delta;

τ_{ij} is the viscous stress tensor: $\tau_{ij} = \mu \left(\frac{\partial u_i}{\partial x_j} + \frac{\partial u_j}{\partial x_i} \right) - \frac{2}{3} \mu \delta_{ij} \frac{\partial u_k}{\partial x_k}$;

f_i is the driving force (e.g. $f_i = -\tau_{w_{av}} \delta_{i1} / (h \rho_m)$ where h is the channel half width, for fully developed turbulence plane channel flow);

E is the total energy per unit volume, defined as $E = \rho e_0 = \rho c_v T + \frac{1}{2} \rho u_i u_i = \frac{p}{\gamma - 1} + \frac{1}{2} \rho u_i u_i$, where e_0 is the total energy per unit mass;

q_j is the heat flux: $q_j = -\kappa \frac{\partial T}{\partial x_j}$.

Equation (A.5) can also be written as,

$$\rho \frac{\partial u_i}{\partial t} + u_i \frac{\partial \rho}{\partial t} + \frac{\partial (\rho u_i u_j + p \delta_{ij})}{\partial x_j} = \frac{\partial \tau_{ij}}{\partial x_j} + \rho f_i \quad (\text{A.7})$$

Considering equation (A.4), eq. (A.7) becomes,

$$\rho \frac{\partial u_i}{\partial t} - u_i \frac{\partial \rho u_j}{\partial x_j} + \frac{\partial (\rho u_i u_j + p \delta_{ij})}{\partial x_j} = \frac{\partial \tau_{ij}}{\partial x_j} + \rho f_i \quad (\text{A.8})$$

After a little rearrangement, eq. (A.8) becomes,

$$\rho \frac{\partial u_i}{\partial t} + \rho u_j \frac{\partial u_i}{\partial x_j} = -\frac{\partial(p\delta_{ij})}{\partial x_j} + \frac{\partial\tau_{ij}}{\partial x_j} + \rho f_i \quad (\text{A.9})$$

Eq. (A.9) * $\frac{1}{2}u_i$ + eq. (A.5) * $\frac{1}{2}u_i$ gives the kinetic energy equation,

$$\frac{\partial(\frac{1}{2}\rho u_i u_i)}{\partial t} + \frac{\partial(\frac{1}{2}\rho u_i u_i u_j)}{\partial x_j} = -u_i \frac{\partial(p\delta_{ij})}{\partial x_j} + u_i \frac{\partial\tau_{ij}}{\partial x_j} + \rho u_i f_i \quad (\text{A.10})$$

Favre-averaged mean kinetic energy per unit mass is defined as: $\{K\} = \frac{1}{2}\{u_i\}\{u_i\} = \frac{1}{2} \frac{\langle \rho u_i \rangle}{\langle \rho \rangle} \frac{\langle \rho u_i \rangle}{\langle \rho \rangle}$

Favre-fluctuation mean kinetic energy per unit mass is defined as: $K'' = K - \{K\} = \{u_i\}u_i''$

Favre-averaged turbulent kinetic energy per unit mass is defined as: $\{k\} = \frac{1}{2}\{u_i'' u_i''\} = \frac{1}{2}(\{u_i u_i\} - \{u_i\}\{u_i\}) = \frac{1}{2}(\frac{\langle \rho u_i u_i \rangle}{\langle \rho \rangle} - \frac{\langle \rho u_i \rangle}{\langle \rho \rangle} \frac{\langle \rho u_i \rangle}{\langle \rho \rangle})$

Favre-fluctuation turbulent kinetic energy per unit mass is defined as: $k'' = \frac{1}{2}u_i'' u_i'' - \frac{1}{2}\{u_i'' u_i''\}$

Favre-averaged internal energy per unit mass is defined as: $\{e\} = c_v \{T\}$

Favre-fluctuation internal energy per unit mass is defined as: $e'' = c_v \{T''\}$

Favre-averaged total energy per unit mass is defined as $\{e_0\} = c_v \{T\} + \frac{1}{2}\{u_i u_i\} = \{e\} + \{K\} + \{k\}$

Favre-fluctuation total energy per unit mass is defined as $e_0'' = e'' + K'' + k'' = c_v T'' + \{u_i\}u_i'' + \frac{1}{2}(u_i'' u_i'' - \{u_i'' u_i''\})$

The time-averaged continuity, momentum, total energy, and kinetic energy equations (A.4, A.5, A.6, A.10) become (Huang *et al.*, 1995; Morinishi *et al.*, 2004)

$$\frac{\partial \langle \rho \rangle \{u_j\}}{\partial x_j} = 0 \quad (\text{A.11})$$

$$\frac{\partial \langle \rho \rangle \{u_i\} \{u_j\}}{\partial x_j} = -\frac{\partial \langle \rho \rangle \{u_i'' u_j''\}}{\partial x_j} - \frac{\partial \langle p \rangle \delta_{ij}}{\partial x_j} + \frac{\partial \langle \tau_{ij} \rangle}{\partial x_j} + \langle \rho \rangle f_i \quad (\text{A.12})$$

$$\begin{aligned} \frac{\partial \langle \rho \rangle \{e_0\} \{u_j\}}{\partial x_j} = & -\frac{\partial \langle \rho \rangle \{e_0'' u_j''\}}{\partial x_j} - \frac{\partial \langle p \rangle \{u_j\}}{\partial x_j} - \frac{\partial \langle p \rangle \langle u_j'' \rangle}{\partial x_j} - \frac{\partial \langle p' u_j'' \rangle}{\partial x_j} \\ & + \frac{\partial (\langle \tau_{ij} \rangle \{u_i\} + \langle \tau_{ij} \rangle \langle u_i'' \rangle + \langle \tau_{ij}' u_i'' \rangle - \langle q_j \rangle)}{\partial x_j} + \langle \rho \rangle \{u_i\} f_i \quad (\text{A.13}) \end{aligned}$$

$$\begin{aligned} \frac{\partial \frac{1}{2} \langle \rho \rangle \{u_i u_i\} \{u_j\}}{\partial x_j} = & -\frac{\partial \langle \rho \rangle (\{u_i\} \{u_i'' u_j''\} + \frac{1}{2} \{u_i'' u_i'' u_j''\})}{\partial x_j} - \{u_i\} \frac{\partial \langle p \rangle \delta_{ij}}{\partial x_j} - \\ & \langle u_i'' \rangle \frac{\partial \langle p \rangle \delta_{ij}}{\partial x_j} - \langle u_i'' \frac{\partial p'}{\partial x_j} \delta_{ij} \rangle + \{u_i\} \frac{\partial \langle \tau_{ij} \rangle}{\partial x_j} + \langle u_i'' \rangle \frac{\partial \langle \tau_{ij} \rangle}{\partial x_j} + \langle u_i'' \frac{\partial \tau_{ij}'}{\partial x_j} \rangle + \langle \rho \rangle \{u_i\} f_i \quad (\text{A.14}) \end{aligned}$$

Considering equation (A.11), equation (A.12) can be written as,

$$\langle \rho \rangle \{u_j\} \frac{\partial \{u_i\}}{\partial x_j} = -\frac{\partial \langle \rho \rangle \{u_i'' u_j''\}}{\partial x_j} - \frac{\partial \langle p \rangle \delta_{ij}}{\partial x_j} + \frac{\partial \langle \tau_{ij} \rangle}{\partial x_j} + \langle \rho \rangle f_i \quad (\text{A.15})$$

Eq. (A.12) * $\frac{1}{2} \{u_i\}$ + eq. (A.15) * $\frac{1}{2} \{u_i\}$ gives,

$$\begin{aligned} \frac{\partial \frac{1}{2} \langle \rho \rangle \{u_i\} \{u_i\} \{u_j\}}{\partial x_j} = & -\{u_i\} \frac{\partial \langle \rho \rangle \{u_i'' u_j''\}}{\partial x_j} - \{u_i\} \frac{\partial \langle p \rangle \delta_{ij}}{\partial x_j} + \{u_i\} \frac{\partial \langle \tau_{ij} \rangle}{\partial x_j} + \langle \rho \rangle \{u_i\} f_i \quad (\text{A.16}) \end{aligned}$$

After some arrangements, the mean kinetic energy (MKE) equation (A.16) becomes,

$$\begin{aligned} \frac{\partial \frac{1}{2} \langle \rho \rangle \{u_i\} \{u_i\} \{u_j\}}{\partial x_j} = & \langle \rho \rangle \{u_i'' u_j''\} \frac{\partial \{u_i\}}{\partial x_j} + \langle p \rangle \delta_{ij} \frac{\partial \{u_i\}}{\partial x_j} - \langle \tau_{ij} \rangle \frac{\partial \{u_i\}}{\partial x_j} + \\ & \frac{\partial (-\langle \rho \rangle \{u_i\} \{u_i'' u_j''\} - \langle p \rangle \delta_{ij} \{u_i\} + \langle \tau_{ij} \rangle \{u_i\})}{\partial x_j} + \langle \rho \rangle \{u_i\} f_i \quad (\text{A.17}) \end{aligned}$$

(Eq.A.14 – eq.A.16) gives the turbulent kinetic energy (TKE) equation:

$$\begin{aligned} \frac{\partial \frac{1}{2} \langle \rho \rangle \{u_i'' u_i''\} \{u_j\}}{\partial x_j} = & -\frac{\partial (\frac{1}{2} \langle \rho \rangle \{u_i'' u_i'' u_j''\} - \langle u_i'' \tau_{ij}' \rangle + \langle u_i'' p' \delta_{ij} \rangle)}{\partial x_j} - \\ & \langle \rho \rangle \{u_i'' u_j''\} \frac{\partial \{u_i\}}{\partial x_j} - \langle u_i'' \rangle \frac{\partial \langle p \rangle \delta_{ij}}{\partial x_j} + \langle p' \delta_{ij} \frac{\partial u_i''}{\partial x_j} \rangle + \langle u_i'' \rangle \frac{\partial \langle \tau_{ij} \rangle}{\partial x_j} - \langle \tau_{ij}' \frac{\partial u_i''}{\partial x_j} \rangle \quad (\text{A.18}) \end{aligned}$$

The TKE equation (A.18) can be rewritten as:

$$\begin{aligned} \frac{\partial \frac{1}{2} \langle \rho \rangle \{u_i'' u_j''\} \{u_j\}}{\partial x_j} = & - \frac{\partial (\frac{1}{2} \langle \rho \rangle \{u_i'' u_i'' u_j''\} - \langle u_i'' \tau_{ij}' \rangle + \langle u_j'' p' \rangle)}{\partial x_j} \\ & - \langle \rho \rangle \{u_i'' u_j''\} \frac{\partial \{u_i\}}{\partial x_j} - \langle u_i'' \rangle \frac{\partial \langle p \rangle \delta_{ij}}{\partial x_j} + \langle p' \frac{\partial u_j''}{\partial x_j} \rangle + \langle u_i'' \rangle \frac{\partial \langle \tau_{ij} \rangle}{\partial x_j} - \langle \tau_{ij}' \frac{\partial u_i''}{\partial x_j} \rangle \quad (\text{A.19}) \end{aligned}$$

The terms in the TKE equation (A.19) can be denoted as,

$$\begin{aligned} \text{Advection: } A_k &= \frac{\partial \frac{1}{2} \langle \rho \rangle \{u_i'' u_j''\} \{u_j\}}{\partial x_j} \\ \text{Production: } P_k &= - \langle \rho \rangle \{u_i'' u_j''\} \frac{\partial \{u_i\}}{\partial x_j} \\ \text{Diffusion: } D_k &= - \frac{\partial (\frac{1}{2} \langle \rho \rangle \{u_i'' u_i'' u_j''\} - \langle u_i'' \tau_{ij}' \rangle + \langle u_j'' p' \rangle)}{\partial x_j} \\ \text{Dissipation: } \epsilon_k &= \langle \tau_{ij}' \frac{\partial u_i''}{\partial x_j} \rangle \\ \text{Compressibility: } C_k &= - \langle u_i'' \rangle \frac{\partial \langle p \rangle \delta_{ij}}{\partial x_j} + \langle p' \frac{\partial u_j''}{\partial x_j} \rangle + \langle u_i'' \rangle \frac{\partial \langle \tau_{ij} \rangle}{\partial x_j} \end{aligned}$$

The equation (A.19) is the traditional Favre-averaged TKE equation. A different form of TKE equation, proposed by Huang *et al.* (1995), can be obtained by using Favre average only on the convective terms and the traditional Reynolds average on the other terms. The final equations can be obtained from a similar but simpler way of the above deductions.

Finally the second form of TKE equation follows,

$$\begin{aligned} \frac{\partial \frac{1}{2} \langle \rho \rangle \{u_i'' u_j''\} \{u_j\}}{\partial x_j} = & - \frac{\partial (\frac{1}{2} \langle \rho \rangle \{u_i'' u_i'' u_j''\} - \langle u_i' \tau_{ij}' \rangle + \langle u_j' p' \rangle)}{\partial x_j} \\ & - \langle \rho \rangle \{u_i'' u_j''\} \frac{\partial \{u_i\}}{\partial x_j} - \langle u_i'' \rangle \frac{\partial \langle p \rangle \delta_{ij}}{\partial x_j} + \langle p' \frac{\partial u_j'}{\partial x_j} \rangle + \langle u_i'' \rangle \frac{\partial \langle \tau_{ij} \rangle}{\partial x_j} - \langle \tau_{ij}' \frac{\partial u_i'}{\partial x_j} \rangle \quad (\text{A.20}) \end{aligned}$$

Similarly, the terms in the TKE equation (A.19) can be denoted as,

$$\begin{aligned} \text{Advection: } A_k &= \frac{\partial \frac{1}{2} \langle \rho \rangle \{u_i'' u_j''\} \{u_j\}}{\partial x_j} \\ \text{Production: } P_k &= - \langle \rho \rangle \{u_i'' u_j''\} \frac{\partial \{u_i\}}{\partial x_j} \\ \text{Diffusion: } D_k &= - \frac{\partial (\frac{1}{2} \langle \rho \rangle \{u_i'' u_i'' u_j''\} - \langle u_i' \tau_{ij}' \rangle + \langle u_j' p' \rangle)}{\partial x_j} \end{aligned}$$

$$\text{Dissipation: } \epsilon_k = \langle \tau'_{ij} \frac{\partial u'_i}{\partial x_j} \rangle$$

$$\text{Compressibility: } C_k = -\langle u''_i \rangle \frac{\partial \langle p \rangle \delta_{ij}}{\partial x_j} + \langle p' \frac{\partial u'_j}{\partial x_j} \rangle + \langle u''_i \rangle \frac{\partial \langle \tau_{ij} \rangle}{\partial x_j}$$

However, the two forms are the same for TKE equation as $\langle \phi' \psi'' \rangle = \langle \phi' \psi' \rangle$, shown in the equation (A.3).

Appendix B

The Database

The data generated and used in this thesis will be available upon request. The following are the details of the database.

The database for compressible and incompressible wall-bounded flows ($Ma \approx 0.2$, 0.7 and 1.5) include mean streamwise velocity, density, and temperature, Van Driest transformation of the mean velocity profiles, RMS velocities, density, temperature, pressure, pressure gradients, vorticities profiles, skewness and flatness of velocities, density and temperature profiles, shear stresses profiles, turbulent kinetic energy budget, cross-correlations between velocities and temperature, cross-correlations between pressure gradients and vorticity flux, one dimensional spectra and autocorrelations of velocities, density and temperature etc.

The database for low Mach number ($Ma \approx 0.2$) wall-bounded flows with pressure gradients and separation include global quantities, such as wall pressure coefficient, skin friction, nondimensional pressure gradient parameter, and local profiles, such as mean velocities, pressure coefficient and streamwise pressure gradient profiles, RMS velocities, pressure, vorticities profiles, shear stresses, cross-correlations between

pressure gradient and vorticity flux, cross-correlations between pressure gradient and spanwise vorticity, spanwise autocorrelations of streamwise velocities, etc. at different streamwise locations.